Imaging, Spectroscopy and Manipulation of C_{60} Molecules on Semiconductor Surfaces

Cristina Chiutu, BSc.

Thesis submitted to the University of Nottingham for the degree of Doctor of Philosophy

October 2013

Abstract

Scanning probe microscopy techniques were employed to investigate C_{60} molecules adsorbed on Si(111)-(7x7) and Ag-Si(111)-($\sqrt{3}$x$\sqrt{3}$)R30^{o} using imaging, spectroscopy, and manipulation methods. First, dynamic scanning tunnelling microscopy revealed the lowest unoccupied molecular orbital features of C_{60} molecules adsorbed on Si(111)-(7x7) with extremely high resolution at 77 K. Experimental data were compared with Hückel molecular orbital theory simulations to determine the orientation of the molecules on these surfaces. Second, C_{60} molecules were imaged with a qPlus atomic force microscope, in the attractive force regime and appeared as bright spherical protrusions. The potential energy of interaction between the AFM tip and C_{60} molecules adsorbed on Si(111)-(7x7) was quantified by force spectroscopy.

Furthermore, a C_{60} molecule was transferred to the scanning probe microscope tip and used as molecular probe to image the Si(111)-(7x7) surface and other C_{60} molecules. The on-tip C_{60} molecule was imaged with high precision. Hückel molecular orbital theory calculations accurately predicted the shape and characteristics of molecular orbitals observed with dynamic scanning tunnelling microscopy, which were strongly dependent on molecular symmetry, orientation, and adsorption angle. Using qPlus atomic force microscopy, chemical reactivity was probed close to or at the carbon atom positions in the C_{60} cage. Density functional theory simulations showed that an (iono)covalent bond formed between a carbon atom and the underlying Si adatom was responsible for contrast formation.

The pair potential for two C_{60} molecules was also determined experimentally and found to be in very good agreement with the Girifalco potential (Girifalco, L.A., *J. Phys. Chem.*, 1992. 96(2): p. 858). Using Hückel molecular orbital theory, the mutual orientation of a C_{60} molecule adsorbed on the STM/AFM tip and a C_{60} molecule adsorbed on the Si(111)-(7x7) surface was determined via comparison of simulated images to the experimental data. Individual C_{60} molecules were also manipulated with qPlus atomic force microscopy.

Manipulation of single C_{60} molecules was performed on the Ag-Si(111)-($\sqrt{3}$x$\sqrt{3}$)R30^{o} surface using scanning tunnelling microscopy at room temperature and at 100 K. The interaction was predominantly attractive. Due to weak molecule-substrate interaction, a short-range chemical force between the C_{60} molecule and the tip was considered to be responsible for the manipulation process.

List of Publications

"Recovering molecular orientation from convoluted orbitals"

A. J. Lakin, C. Chiutu, A. M. Sweetman, P. Moriarty, and J. L. Dunn

Phys. Rev. B 88 (2013) 035447

"Precise orientation of a single C_{60} molecule on the tip of a scanning probe microscope"

C. Chiutu, S. Jarvis, A. Lakin, A. Stannard, A. M. Sweetman, L. Kantorovich, J. Dunn, P. Moriarty

Phys. Rev. Lett. 109 (2012) 079901

"Mono- and multi-layer adsorption of an ionic liquid on Au(110)"

R. Foulston, S. Gangopadhyay, C. Chiutu, P. Moriarty, and R. G. Jones

Phys. Chem. Chem. Phys. 14 (2012) 6054

"Measuring Si–C_{60} chemical forces via single molecule spectroscopy "

C. Chiutu, A. Stannard, A. M. Sweetman, and P. Moriarty

Chem. Commun. 47 (2011) 10575

Acknowledgements

First of all, I express my gratitude to my supervisor, Prof. Philip Moriarty, who gave me the opportunity to study for a Ph.D. in Physics at the University of Nottingham. He was to me a teacher, scientific guide, lab mate and friend. Many thanks for the long patience and immense moral support. Without his guidance for the experiments and his encouragement I would not have achieved as much during this Ph.D. course.

Grateful and sincere acknowledgement for completion of the thesis are addressed to Prof. Peter Beton and Prof. Steven D. Aird, who provided their kind help, instructions, and supervision with regard to the content, organization, and writing of the thesis.

I express my appreciation and special thanks to Dr. Subhashis Gangopadhyay, Dr. Alex Saywell, Dr. Richard Foulston, Dr. Peter Sharp, Dr. Adam Sweetman, Dr. Andrew Stannard, Dr. Andrew Lakin, Dr. Rosanna Danza, Dr. Haya Alhummiany, Dr Luis Perdigao, Dr. Julian Stirling, Dr. Adrian Ghita for their essential help, for the time and patience invested to teach me lab skills and physics knowledge on the ultrahigh vacuum systems, sample/tip preparation, scanning techniques, or computer simulations. For many stimulating discussions and helpful suggestions I would like to thank also to the other members of the Nanoscience Group.

For the Hückel molecular orbital theory simulations presented in this thesis I would like to thank Dr. Andrew Lakin and Dr. Janette Dunn, who did a fast and reliable computation of the scanning tunnelling microscope images leading to a fruitful and pleasant collaboration. The same appreciation is also addressed to Prof. Lev Kantorovich, Dr. Sam Jarvis and Dr. Joseph Bamidele who produced the SIESTA Code AFM calculations included in the present work.

I would like to offer thanks and acknowledgment to the professors and members of staff from the School of Physics and Astronomy for being always amiable, and ready to help me with my studies and research requirements. I have been honoured and truly happy for the funding received from Marie Curie Actions and University of Nottingham.

My profound gratitude is offered to my mother, Eng. Maria Chiutu, for all her love and moral encouragement. Many thanks for the endless prayers and tears raised to God for my blessing and success. I am also deeply grateful to the people of Christ's church in Bals, Romania, who remembered me continuously in their prayers. My praise and worship are dedicated to God and the Lord Jesus for the gift of this Ph.D. and the experimental results coming from it.

“Fair is what we see,

Fairer what we have perceived,

Fairest what is still in veil.”

Nicolas Steno

Table of Contents

ABSTRACT ..... **I**

LIST OF PUBLICATIONS ..... **II**

ACKNOWLEDGEMENTS ..... **III**

TABLE OF CONTENTS ..... **V**

1 INTRODUCTION **8**

1.1 MOTIVATION FOR THE RESEARCH 8

2 THEORETICAL BACKGROUND **11**

2.1 COVALENT BONDING 11

2.2 HYBRIDIZATION 12

2.3 CHEMISORPTION 15

2.4 SCANNING TUNNELLING MICROSCOPY 16

2.4.1 Quantum Tunnelling *16*

2.4.2 Imaging Modes in STM *20*

2.4.3 Tersoff-Hamann Theory of STM Imaging and Spectroscopy *22*

2.5 ATOMIC FORCE MICROSCOPY 25

2.5.1 Forces Sensed by AFM *26*

2.5.2 Girifalco Potential *29*

2.5.3 Modes of Operation *30*

2.5.3.1 Dynamic AFM 30

2.5.3.2 FM-AFM Set-up 36

2.5.3.3 Phase-locked Loop 36

2.5.3.4 Dynamic STM 37

2.5.3.5 Q Factor 38

2.5.3.6 Force Spectroscopy 39

2.5.3.7 Cross-talk 41

2.6 HÜCKEL MOLECULAR ORBITAL THEORY 42

2.7 DENSITY FUNCTIONAL THEORY 48

2.7.1 Modelling AFM Experiments with DFT *51*

2.8 SURFACE RECONSTRUCTION 53

2.8.1 Si(111)-(7x7) *53*

2.8.2 Ag-Si(111)-(√3x√3)R30^{o} *56*

2.8.2.1 STS on Ag-Si(111)-(√3x√3)R30° 61
2.9 BUCKMINSTERFULLERENE 62
2.9.1 Geometry and Properties of C_{60} Molecules 62
2.9.2 SPM Research on C_{60} Molecules – Brief History 66
2.9.2.1 Imaging C_{60} Molecules using STM on Si(111)-(7x7) 66
2.9.2.2 STS of C_{60} Molecules on Si(111)-(7x7) 68
2.9.2.3 STM Imaging and STS of C_{60} Molecules on Au(111) 70
2.9.2.4 C_{60} Islands on Au(111) 70
2.9.2.5 C_{60} Islands on Ag-Si(111)-(√3x√3)R30° 71
2.9.2.6 C_{60} Molecule Manipulation on Si(100)-(2x1) with STM 74
2.9.2.7 Manipulation of C_{60} Molecules on Si(111)-(7x7) with STM 76
2.9.2.8 Imaging C_{60} Molecules with AFM 77
2.9.2.9 Sub-molecular Resolution of C_{60} Molecules with AFM 78
2.9.2.10 Bond Discrimination in C_{60} Molecules with AFM 79
2.9.2.11 "Sub-atomic" and Sub-molecular Imaging of SPM Tip 80
2.9.2.12 Manipulation of C_{60} Molecules using AFM 83
2.9.2.13 Force Required to Move an Adsorbate 84

3 EXPERIMENTAL METHODS 86

3.1 VARIABLE TEMPERATURE STM/AFM SYSTEM 86
3.1.1 Sample Cooling Procedure for VT STM 88
3.1.2 Tip Preparation-Electrochemical Etching 89
3.1.3 Sample Preparation in VT System 90
3.1.3.1 Si(111)-(7x7) 90
3.1.3.2 Ag-Si(111)-(√3x√3)R30° 91
3.1.3.3 C_{60} Molecule Deposition 91
3.2 LOW TEMPERATURE SYSTEM 92
3.2.1 LT System Set-up Details 92
3.2.2 Sample Preparation in LT System 95
3.2.2.1 Si(111)-(7x7) 95
3.2.2.2 C_{60} Molecule Deposition 95

4 STUDY OF C_{60} MOLECULES ON SI(111)-(7X7) WITH DYNAMIC STM AND QPLUS AFM 96

4.1 INTRODUCTION 96
4.2 C_{60} MOLECULE IMAGING USING DYNAMIC STM 96
4.3 MEASUREMENTS ON C_{60} MOLECULES USING QPLUS AFM 105
4.3.1 Force Spectroscopy on Si(111)-(7x7) 105
4.3.2 Imaging C_{60} Molecules using qPlus AFM 106
4.3.3 Force Spectroscopy of a Si-terminated Tip and C_{60} Molecules 109

4.3.4 Force Required to Move a C_{60} Molecule on Si(111)-(7x7) using AFM 113

4.4 SUMMARY AND OUTLOOK 117

5 SUB-MOLECULAR RESOLUTION AND ORIENTATION OF ON-TIP C_{60} MOLECULE: MEASURING THE C_{60}-C_{60} PAIR INTERACTION 119

5.1 INTRODUCTION 119

5.2 C_{60} MOLECULE TRANSFER TO THE SPM TIP 120

5.3 SUB-MOLECULAR IMAGING OF ON-TIP C_{60} WITH DYNAMIC STM 122

5.4 SUB-MOLECULAR IMAGING OF ON-TIP C_{60} WITH QPLUS AFM 127

5.5 CONTRAST FORMATION IN AFM 130

5.6 C_{60}-C_{60} PAIR POTENTIAL 132

5.7 STM IMAGING OF C_{60} MOLECULES WITH A C_{60} PROBE 133

5.8 SUMMARY AND OUTLOOK 136

6 MANIPULATION OF C_{60} MOLECULES ON AG-SI(111)-(√3X√3)R30^{o} USING STM 138

6.1 INTRODUCTION 138

6.2 MANIPULATION OF C_{60} MOLECULES ON AG-SI(111)-(√3X√3)R30^{o} AT ROOM TEMPERATURE 138

6.3 MANIPULATION OF C_{60} MOLECULAR ISLANDS AT 100 K 142

6.4 SUMMARY AND OUTLOOK 146

7 CONCLUSIONS 148

APPENDIX - IONIC LIQUID ON AU(110)-(2X1) 151

A.1 INTRODUCTION 151

A.2 AU(110)-(2X1) SAMPLE PREPARATION 152

A.3 IONIC LIQUID DEPOSITION 152

A.4 AU(110)-(2X1) RECONSTRUCTION 153

A.5 IMAGING OF IONIC LIQUID ON AU(110)-(2X1) USING STM 154

A.6 SUMMARY AND OUTLOOK 158

LIST OF REFERENCES 159

LIST OF FIGURES 167

1 Introduction

1.1 Motivation for the Research

The relatively large size and perfect symmetry of the C_{60} molecule, the possibility of tuning its electric conductance from insulator to superconductor with doping and connecting with derivatives, as well as its capacity as an electron acceptor, are some characteristics which explain the importance of the C_{60} molecule for fundamental science and for development of molecular electronics [1]. The C_{60} molecule has played a significant role in molecular electronic devices, as an individual acceptor or when incorporated into various carbon nanostructures [2, 3]. C_{60} has also been exploited in single-molecule devices, electron transport, or as a tunnelling junction in transistors [4-6]. Therefore, the elucidation of its properties, including binding energy, bonding configurations, force of interaction, and charge transfer, are essential to understand the interactions in intermolecular and molecule-substrate systems.

Over twenty years of intensive research have been carried out to investigate the electronic properties of C_{60} molecule and its behavior on various substrates. Scanning probe microscopes (SPM) permit visualization of single molecules and also enable detailed investigations of the self-assembly of molecules into well-ordered structures or thin layers. By means of SPM, a wide range of properties - electronic, chemical, and mechanical - can be investigated.

Scanning tunnelling microscopy (STM) and atomic force microscopy (AFM) have been improved dramatically over the past decades and transformed into powerful techniques, not only for revealing topographic features at the atomic scale but also for surface structuring and modification, along with atomic and molecular manipulation [7-21]. STM and AFM have also been used for characterisation of the electronic and chemical properties of surfaces. The study of individual atoms and molecules has played a key role in the development of functional molecular design,

supramolecular chemistry, quantum effects for building electronic devices, integrated circuits and chips, biochips, and various electromechanical systems [22-26].

Fullerenes have been imaged with STM and non-contact AFM at room and low temperature, on semiconductor and metallic surfaces. At room temperature they appeared as bright spherical protrusions [27-29], while at low temperature, their intramolecular structure was revealed [30, 31]. The sub-molecular features of C_{60} observed in SPM experiments have been interpreted using theoretical calculations relating to their electronic characteristics, orientations and bonding configurations on various surfaces [30, 31]. The probability density of both the highest occupied molecular orbital (HOMO) and lowest unoccupied molecular orbital (LUMO) of C_{60} molecule have been imaged with STM. The sub-molecular structure varies substantially with bias voltage and adsorption site [30].

On low free energy surfaces C_{60} molecule will self-assemble into close-packed islands, with well-ordered domains [30, 31] whose packing can be dictated by molecular orientation [32-35]. On reactive substrates, however, such as the Si(111)-(7x7) surface discussed at length in this thesis (Chapters 4 and 5), C_{60} molecule interacts strongly with the underlying dangling bonds and is effectively "pinned" in place. In this work we use both the Si(111)-(7x7) and Ag-Si (111)-($\sqrt{3}$x$\sqrt{3}$)R30^{o} surfaces as complementary 'platforms' for C_{60} adsorption, due to their very different reactivities.

Sub-molecular contrast in STM varies dramatically depending on both molecular orientation and, importantly, the tip state [32]. In addition to a study of the adsorption state and chemomechanical properties of C_{60} on silicon surfaces, precise characterisation of the tip state in SPM measurements is a central theme of this thesis, and an increasingly important aspect of state-of-the-art scanning probe microscopy. Although imaging of C_{60} molecules adsorbed on the tip apex of an STM has been also reported [36, 37], a key advance reported in Chapter 5 of this thesis is the ability to image a tip-adsorbed C_{60} with *atomic* resolution.

A detailed understanding of the nature and effect of chemical forces in interactions at the nanoscale is crucial in nanophysics. A key aim of the work

described in this thesis was to determine the force and potential due to Si-C_{60} and C_{60}-C_{60} interactions, which had hitherto not been determined experimentally. The results of our experimental and theoretical investigations into the nature of the Si-C_{60} and C_{60}-C_{60} interactions, on both a highly reactive (Si(111)-(7x7)) and a weakly interacting (Ag-Si (111)-($\sqrt{3}$x$\sqrt{3}$)R30^{o}), substrate are described in Chapter 4, 5, and 6. Before discussing those results in detail, it is appropriate to describe the basic physics and chemistry underpinning the experiments and calculations described in this thesis.

2 Theoretical Background

2.1 Covalent Bonding

In a covalent bond, two atoms, which may be same or different elements, share a pair of electrons. One shared pair forms a single bond and two pairs form a double bond. Different types of covalent bonds are formed depending upon the types of orbitals involved (Figure 2-1) [38, 39]. A σ bond can be formed by overlap of two *s* or the 'end-to-end' overlap of two p_x orbitals. A π bond is formed when two p_z orbitals overlap in a 'side-by-side' configuration. One *s* orbital and one p_x orbital can also form a σ bond. Both σ and π bonds are covalent bonds.

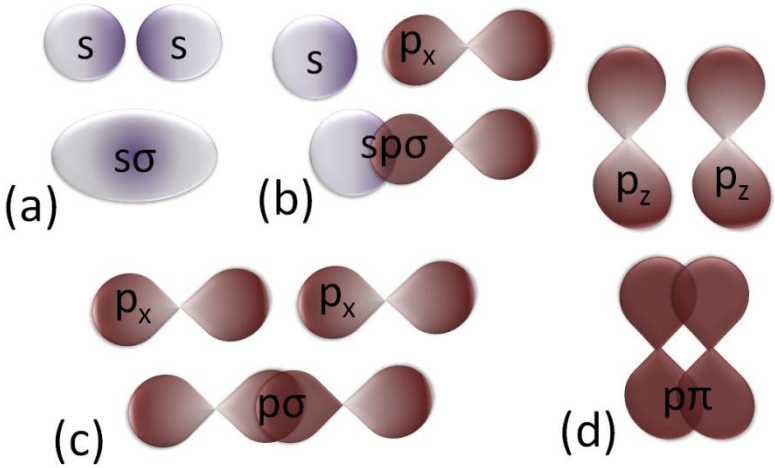

Figure 2-1. Four fundamental bonding configurations. A σ bond can be formed by two *s* orbitals **(a)**, one *s* orbital and one p_x orbital **(b)** or two p_x orbitals **(c)**. A π bond can be built by two p_z orbitals **(d)**.

Typical double bonds consist of one σ bond and one π bond. The double bonds pull the two atoms closer, and, therefore, double bonds are shorter than single bonds. The single bonds are of σ type. These bonds are the strongest because the density of electronic orbitals is highest along the axis that connects the nuclei of the two atoms. In contrast, in π bonds, overlapping occurs in a plane away from the

internuclei axis. These bonds tend to be weaker than σ bonds because the amount of orbital overlap is decreased.

Bonding is stronger in a structure with a combination of σ and π bonds compared to a structure with either σ or π bonds alone. Alternating single and double bonds in a structure also confers interesting electronic properties, as in the benzene ring. Overlapping of *p* orbitals in a planar cyclic structure produces delocalization of electrons. This means that electrons are not localized between the two atoms, but their density is spread across and above/below the whole ring. Molecules with a cyclic structure, which contain π bonds and in-plane overlap of *p* orbitals, are aromatic.

2.2 Hybridization

Hybrid orbitals are formed by mixing *s* and *p* states (Figure 2-2). This provides higher stability for various structures [39, 40].

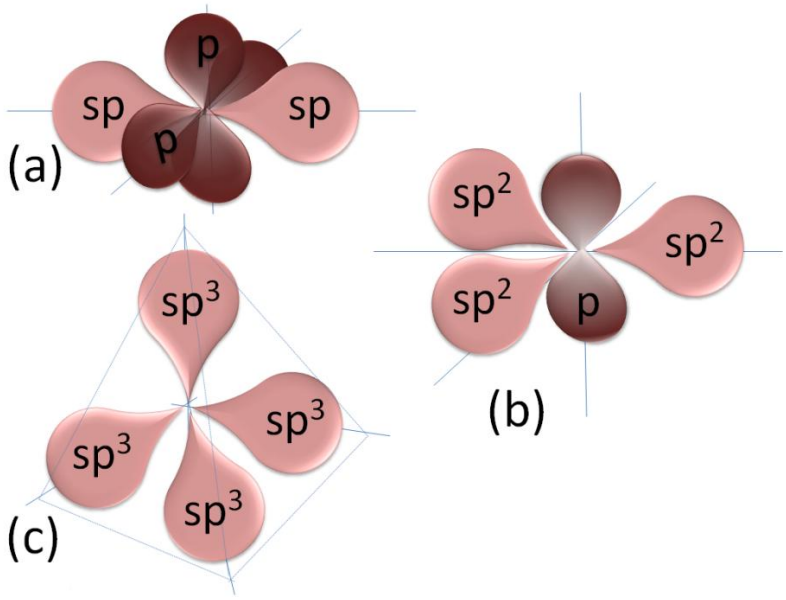

Figure 2-2. Hybrid orbitals **(a)** *sp* with two *p* orbitals left over, **(b)** in-plane sp^2 with 120^o angle between orbitals and one *p* orbital left over, and **(c)** tetrahedral sp^3 with 109.5^o angle between orbitals.

C and Si have four valence electrons, two in an *s* state and two in a *p* state. These electrons can combine to form hybrid states. The electronic

configuration of C in its ground state is $1s^2 2s^2 2p_x^1 2p_y^1$, while for Si it is $1s^2 2s^2 2p^6 3s^2 3p_x^1 3p_y^1$. Bonding energy of the σ bonds leads to sp^3 hybridization by passing an electron from *2s* to *2p* (Figure 2-3).

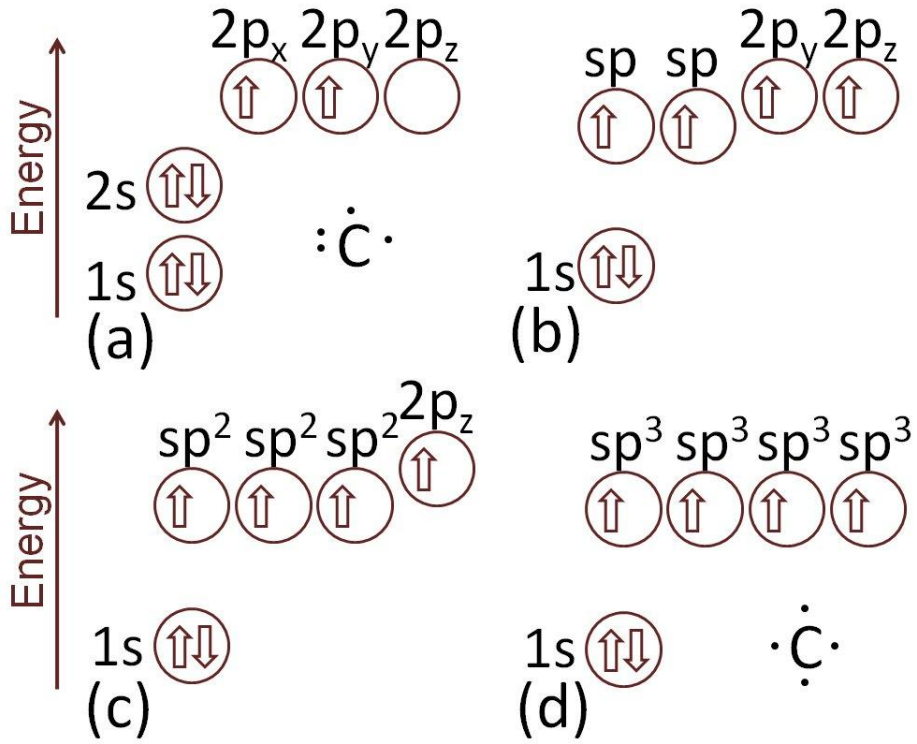

Figure 2-3. Distribution of electrons and energy levels for a C atom in its ground state **(a)**, *sp* bonding **(b)**, sp^2 bonding **(c)**, and sp^3 bonding **(d)**. Electrons of *2s* orbital are shared with *2p* orbitals giving rise to the hybrids sp^i. (Figure reproduced from ***lsc.ucdavis****.edu/~holliste/Jim2A/****Hybridization****Carbon.pdf*)

Atoms share a pair of electrons and form σ bonds in diamond and Si crystals [38, 41]. C and Si exhibit a tetrahedral bonding geometry in the crystalline state (Figure 2-4). Electron orbitals are distributed along tetrahedral axes. On the Si surface, one sp^3 orbital of the sp^3 hybrid points out perpendicular to the surface giving rise to a dangling bond. A dangling bond is a broken covalent bond. Diamond [42] is an insulator and its hardness is derived from the σ bonds and by the electrons which are locked in the tetrahedral arrangement of crystal bonding.

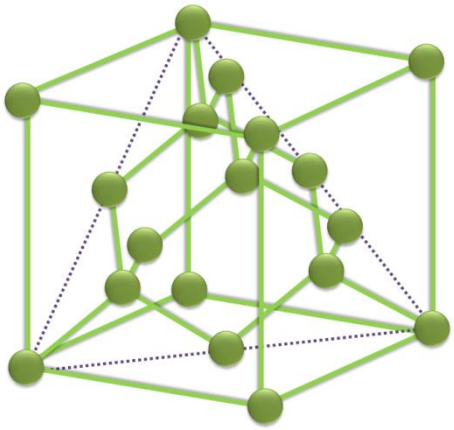

Figure 2-4. Tetrahedral arrangement of atoms in a face-centred cubic unit cell of Si and diamond crystals. Dashed blue triangle marks the (111) plane.

The graphite structure is completely different to the tetrahedral configuration of a diamond crystal. In-plane bonds of the graphite sheet are sp^2 hybrids. Each C atom forms σ bonds with three neighbours making a bond angle of 120^o. This bonding offers strength to the graphite sheet. However, the interaction between sheets is weak, van der Waals type, conferred only by the remaining p_z orbital of sp^2 hybrids. This p_z orbital forms a π bond with an orbital from the next sheet. Therefore, C atoms form a π bond and a σ bond at the same time. Due to formation of these double bonds, there are no dangling bonds, leaving the surface inert.

For C_{60} molecules, the bonding type is not well defined. In simulations, because each C atom binds to three others via covalent bonds and forms a ring structure, sp^2 hybridization with a p_z orbital left over is assumed. However, in reality, C bonding is not planar and the angle between bonds is not exactly 120^o. This difference results from the angle strain that occurs when planar graphite bends to close the C_{60} cage. Another phenomenon that occurs when the C_{60} cage builds is the electrophilic addition at the 6-6 double bonds, a reaction that consists of breaking a π bond into two σ bonds. For this reason, some sp^2 hybrids are changed to sp^3 and the bonding configuration in C_{60} molecules is sp^2- sp^3. In addition, as there are no double bonds in the pentagonal rings, electrons in the hexagonal rings are not delocalized over the entire C_{60} molecule. This poor electron delocalization makes C_{60} molecules non-aromatic.

2.3 Chemisorption

When interacting with a substrate, the energy levels of a free molecule suffer significant changes due to the character of interaction [43]. The process which takes place can be physisorption or chemisorption [44]. When adsorbed on a surface, energy levels of a molecule broaden and shift with reference to the Fermi level.

In physisorption, valence energy levels of a molecule broaden slightly from the free molecule phase and its potential energy has a short attractive trend (Figure 2-5). A stronger interaction with the surface produces a splitting of both filled and empty molecular orbitals. The closer the molecule is to the surface, the larger the separation is between newly formed orbitals. This electronic reaction is produced by the overlap between surface and molecular wavefunctions.

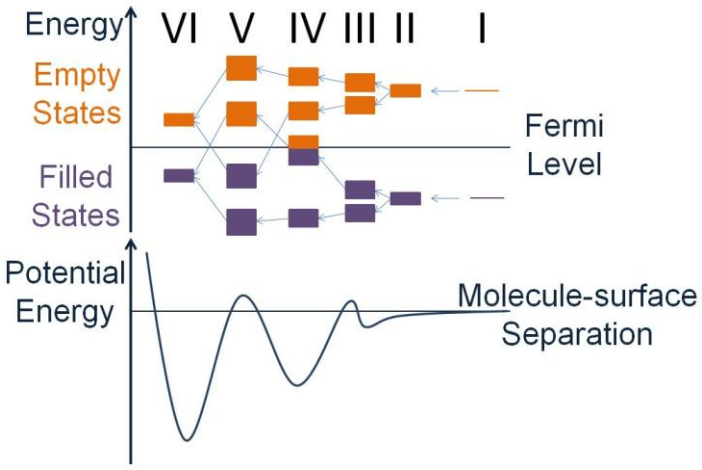

Figure 2-5. Interaction with a substrate yields significant changes in the energy states of an adsorbate. **(I)** Energy levels in a free molecule. **(II)** Physisorption. **(III-V)** Chemisorption. **(IV)** Charge transfer. **(VI)** Dissociation of the molecule. (Figure reproduced from [43])

If a molecule has enough activation energy to form a chemical bond with a surface, there will be greater overlap or hybridization between the surface and the molecule, leading to a charge transfer. In this state of chemisorption, filled molecular orbitals shift slightly above Fermi level indicating that a charge transfer to the surface occurred (Figure 2-5IV). Depending on the strength of the interaction and on the nature of the chemical bond, an unoccupied molecular level can be filled with electrons and may drop below the Fermi level. This chemisorption phase may weaken bonding in the molecule, allowing it to dissociate.

On most surfaces, significant chemical interaction occurs, leading to chemisorption. Physisorption is possible only for very inert surfaces, such as graphite and passivated semiconductors.

2.4 Scanning Tunnelling Microscopy

2.4.1 Quantum Tunnelling

The scanning tunnelling microscope was designed by Binnig and Rohrer [45] to visualize features much smaller than the wavelength of visible light. STM employs a totally different principle than that of an optical microscope [46, 47], and the object is magnified to such a degree that "sub-atomic" structures, *i.e.* features arising from the charge density of single orbitals, can be seen.

A phenomenon called "quantum mechanical tunnelling" makes it possible to image surfaces with extremely high resolution. Tunnelling has no counterpart in classical physics, but can be explained in terms of quantum mechanics. Tunnelling is the penetration of the electron wavefunction beyond a classically forbidden region (Figure 2-7) [40]. In STM, when the gap between the tip and the sample is thin enough (on the order of a few nanometers), an electron tunnels through a classically forbidden region (in a vacuum, air, or fluid) from one surface to another of lower potential (Figure 2-6).

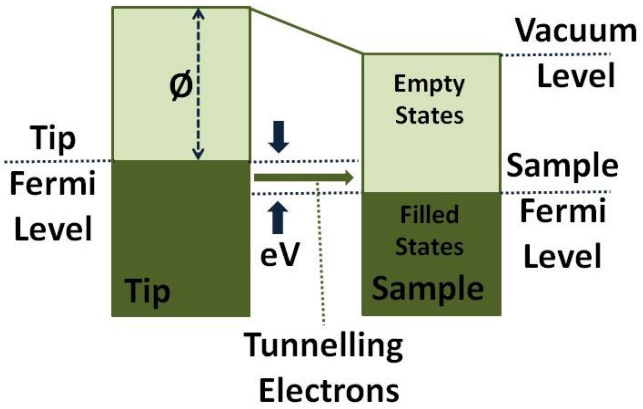

Figure 2-6. A simple energy level diagram for a metallic surface and a tip, the tip having a negative bias voltage relative to the surface. With a positive tunnelling voltage (+eV) applied to the sample, electrons from the occupied states in the valence band of the tip travel through the barrier to the unoccupied states of the sample. Φ is the work function of the tip.

By approximating the STM gap with a 1D tunnelling barrier of finite dimensions (Figure 2-7) [23, 41, 46], the transmission probability can be quantified starting from the time-independent Schrödinger equation [48, 49]:

$$\hat{H}\psi(z) = E\psi(z)$$

Eq. 2-1

where $\hat{H}$ is the Hamiltonian operator, $\psi(z)$ is the electron wavefunction, and E is the total energy of the electron. The wavefunction of the electrons has three components: incident, reflected and transmitted wave [40].

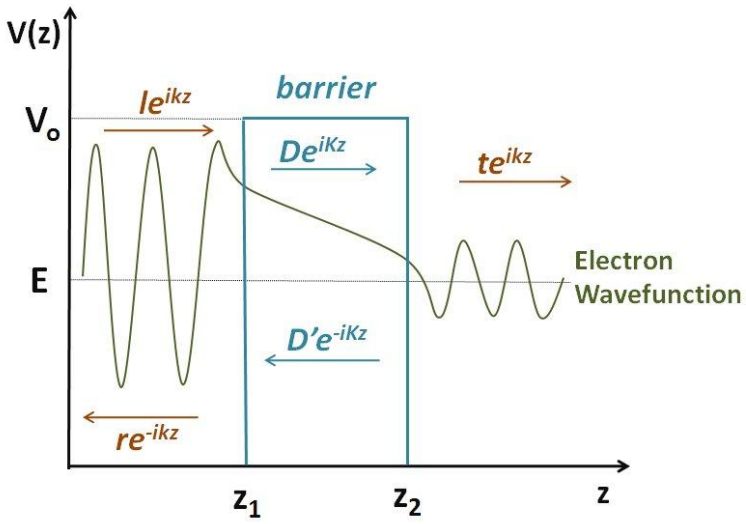

Figure 2-7. Schematic diagram describing wavefunction's behavior for an electron incident to a barrier le^{ikz}. Electron's wavefunction decays or varies inside the barrier $De^{iKz}, D'e^{-iKz}$, according to the probability of penetrating the barrier, and has a reflected component re^{-ikz}. Transmitted wave is the remaining component of the wavefunction and represents the motion of the electron on the other side of the barrier te^{ikz}. In this figure V_o is the height of the barrier, $d = z_2\text{-}z_1$ is the width of the barrier, E is the energy of the electron, k is the wavevector of the wavefunction outside the barrier, K is the wavevector of the wavefunction inside the barrier, l,r,t,D, and D' represent wave amplitude. (Figure after [48])

For an electron moving in one dimension the Schrödinger equation takes the form:

$$-\frac{\hbar^2}{2m}\frac{d^2\psi(z)}{dz^2} + V(z)\psi(z) = E\psi(z)$$

Eq. 2-2

with the first term representing the kinetic energy of the electron and $V(z)$ is a step function and represents the height of the potential barrier, $\hbar$ is Boltzmann constant and *m* is the mass of the electron. The potential *V(z)* can be defined as

$$V(z) = \begin{cases} 0, & for\ z \le z_1, leftside\ of\ barrier \\ V_o, & for\ \ z_1 \le z \le z_2, inside\ the\ barrier \\ 0, & for\ z \ge z_2, rightside\ of\ barrier \end{cases}$$

Eq. 2-3

where V_o is the height of the potential barrier.

In this case, the general solution of the Equation 2-2 is a wavefunction of the electron given by the form

$$\psi(z) = \begin{cases} le^{ikz} + re^{-ikz}, z \le z_1, \dfrac{\hbar^2 k^2}{2m} = E \\ De^{iKz} + D'^{e^{-iKz}}, z_1 \le\ z \le z_2, \dfrac{\hbar^2 K^2}{2m} = E - V_o \\ te^{ikz}, z \ge z_2, \dfrac{\hbar^2 k^2}{2m} = E \end{cases}$$

Eq. 2-4

where *E* is the energy of the electron, *k*, *K* are the wavevectors, *l,r,t,D*, and *D'* represent the amplitudes in the wave's equation.

The transmission, *T*, and reflection, *R*, coefficients can be calculated from the boundary conditions at $z = z_1$ and $z = z_2$, knowing that

$$T + R = \left|\frac{t}{l}\right|^2 + \left|\frac{r}{l}\right|^2 = 1$$

Eq. 2-5

A relationship can be drawn for the transmission coefficient

$$\frac{1}{T} = \left|\frac{l}{t}\right|^2 = 1 + \frac{1}{4}\left(\frac{k^2 - K^2}{kK}\right)^2 sin^2(2Kd)$$

Eq. 2-6

where *d* is the barrier width. Introducing the dependence of the wavevectors *k* and *K* of *E* and V_o and considering that for $E < V_o$ *K* is pure imaginary [48], $iK = \kappa$, the expression for transmission coefficient becomes

$$\frac{1}{T} = 1 + \frac{1}{4}\frac{{V_o}^2}{E(V_o - E)} sinh^2(2\kappa d)$$

Eq. 2-7

In case of wide barriers and low transmission probability $\kappa d >> 1$, $sinh(\kappa d) \approx 1/2$ and $e^{\kappa d} >> 1$, the transmission decays exponentially with the barrier width *d* [49]

$$T \approx \frac{16E}{V_o} e^{-2\kappa d}$$

Eq. 2-8

Therefore, the transmission coefficient represents the finite probability for an electron with a low energy $E < V_o$ to penetrate and tunnel through the barrier. κ^{-1} is called the characteristic decay length, measures the decay of the wavefunction inside the barrier and is given by the formula

$$\kappa^{-1} = \hbar/\sqrt{2m(V_o - E)}$$

Eq. 2-9

where $(V_o\text{-}E)$ is the effective barrier height.

In terms of current densities, transmission coefficient can be defined as the ration of transmitted probability current density in the transmitted wave, j_t, to the probability current density, j_i, in the incident wave [50]:

$$T = \left|\frac{j_t}{j_i}\right|$$

Eq. 2-10

The probability current density *j* for a quantum mechanical particle is

$$j = \frac{\hbar}{2mi}\left(\psi^* \frac{\partial \psi}{\partial z} - \psi \frac{\partial \psi^*}{\partial z}\right)$$

Eq. 2-11

and it can be calculated by substituting the wavefunction $\psi(z)$ from Equation 2-4.

In STM, the transmission coefficient is defined as "the ration of the tunnelling current at the tip surface *d* to the impinging current at *d = 0*" [51]

$$T \equiv \frac{I(d)}{I(0)} = e^{-2\kappa d}$$

Eq. 2-12

Thus, the tunnel current depends exponentially on the tip-surface separation. The rapid decay of the current with distance *d* is due to the very small probability of tunnelling across a vacuum barrier at large distances and provides high sensitivity with small changes of distance, which enables to the atomic resolution sensitivity of the STM.

2.4.2 Imaging Modes in STM

In STM, a sharp tip approaches a conducting surface to achieve a separation distance on the order of nanometers. Both the tip and the sample must be made of conducting or semiconducting materials. When they are close enough, the electron wavefunctions overlap and by applying a bias voltage a tunnelling current is caused to flow.

The current is monitored using a computer. A preamplifier is used to amplify the tunnel current to a level that can be measured. The computer controls tip movement via a negative feedback loop which holds the current at constant level, by

increasing or decreasing the tip-sample separation. This is made possible by piezodrive construction.

The tip is mounted on a piezoelectric tube, which enables movement when a voltage is applied at its electrodes (Figure 2-8). Piezoelectric crystals expand or contract depending on the voltage applied to the piezo, allowing tip/sample movement in the *x*, *y* and *z* directions. The voltage is recorded and converted into a displacement using the known/calibrated piezo sensitivity. STM does not measure atomic (nuclear) positions. Rather, it measures the local density of electronic states within an energy window defined by the sample (or tip) bias voltage.

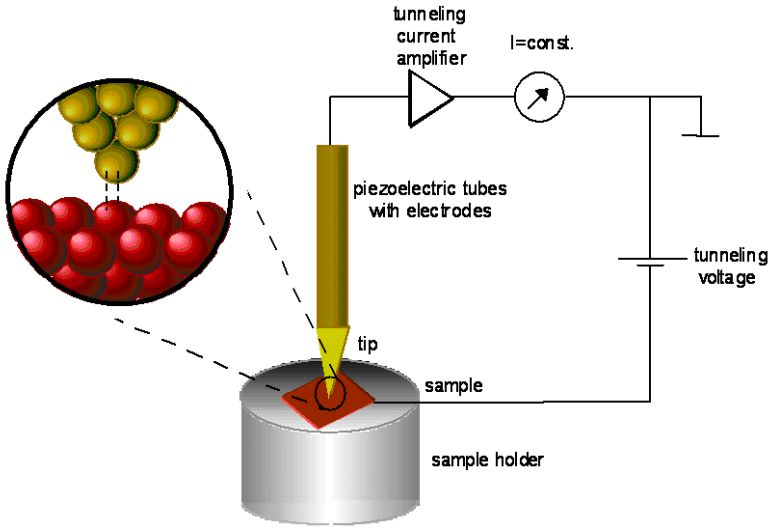

Figure 2-8. Schematic diagram of the scanning tunnelling microscopy principle.

STM uses two important scanning modes: constant-height mode and constant-current mode [46]. Constant-height mode (Figure 2-9a) represents a fast method for visualising surfaces, but provides reasonable data only for flat, smooth substrates. In the constant-height mode, the tip is held at constant height, set before the scan begins, and the tunnelling current is measured. The tunnelling current varies with the topographic and electronic characteristics of the sample.

Although constant-current mode (Figure 2-9b) requires longer time, it is often preferable because it offers precise detection and monitoring of irregular features of rough surfaces. The control system uses a feedback loop to adjust the height, based upon a preset value for the tunnelling current. When the tunnelling current registers an increase, above the set-point value, the gap between tip and

sample is automatically increased. If the tunnelling current is smaller, the tip is brought closer to the substrate. In this way, the desired tunnelling current is maintained. The computer gathers signals and displays a two- or three-dimensional plot, generated from the tunnelling current or piezo voltage at every point of the raster scan.

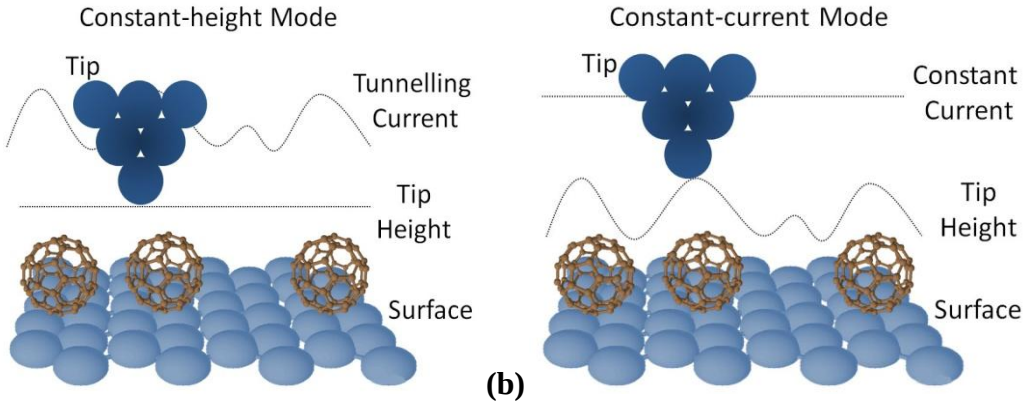

Figure 2-9. Comparison between constant-height mode **(a)** and constant-current mode **(b)** of STM. In constant-current mode the scanner is moved up and down, but the irregular surfaces can be measured with high precision, while the constant-height mode can provide useful information only for very smooth surfaces.

2.4.3 Tersoff-Hamann Theory of STM Imaging and Spectroscopy

For realistic models a more complex theoretical description is necessary in order to interpret STM images. In the Tersoff and Hamann model [52], electron transmission is described by the matrix element which can be determined from first-order perturbation theory, where the tunnelling current is of the form:

$$I = \frac{2\pi e}{\hbar}\sum_{\mu,\nu}\{f(E_\mu)[1-f(E_\nu)] - f(E_\nu)[1-f(E_\mu)]\}|M_{\mu\nu}|^2\delta(E_\nu - E_\mu + eV)$$

Eq. 2-13

This equation consists of a sum over tip (μ) and sample (ν) states, $M_{\mu\nu}$ matrix element and $\delta(E_\nu - E_\mu + eV)$ term, which ensures energy conservation. In the

limit of zero temperature the Fermi functions *f(E)* can be approximated by unit step function and the Equation 2-13 is simplified to:

$$I = \frac{2\pi e^2}{\hbar} V \sum_{\mu,\nu} \left|M_{\mu\nu}\right|^2 \delta(E_\mu - E_\nu)\delta(E_\nu - E_\mu)$$

Eq. 2-14

The crucial and most difficult point in Tersoff-Hamann theory is to determine the tunnelling matrix elements. The Bardeen model [53] can be used to evaluate the matrix elements.

Assuming elastic tunnelling $E_\mu = E_\nu$, matrix elements can be calculated with the formula:

$$M_{\mu\nu} = -\frac{\hbar^2}{2m}\int dS(\psi_\nu^* \frac{\partial \psi_\mu}{\partial z} + \psi_\mu \frac{\partial \psi_\nu^*}{\partial z})$$

Eq. 2-15

Matrix elements are fully dependent on the wavefunctions of tip and sample. In order to calculate the tunnelling matrix, one needs to know the structure of the tip precisely. Tersoff and Hamann introduced a model for the wavefunction of the tip. They considered an ideal STM tip with the apex approximating a sphere:

$$\psi_\mu = \Omega_t^{-\frac{1}{2}} c_t kR e^{kR} e^{-k|r-r_0|}(k|r-r_0|)^{-1}$$

Eq. 2-16

where Ω_t is the volume of the tip, c_t is the normalization term, k is the wavevector, R is the radius of curvature, and $r = r_o$ the centre of the sphere.

Assuming an *s*-wave state for the tip wavefunction [52], for the model described above, the matrix element can be written:

$$M_{\mu\nu} = \frac{4\pi\hbar^2}{2mk}\Omega_t^{-\frac{1}{2}} kR e^{kR}\psi_\nu(r_0)$$

Eq. 2-17

Furthermore, the tunnelling current can be reduced to a simpler form:

$$I \sim \sum_{v} |\psi_v(r_0)|^2 \delta(E_v - E_F)$$

Eq. 2-18

where $|\psi_v(r_0)|^2$ represents the probability density of states of the sample at position $r = r_o$. The term $\delta(E_v - E_F)$ restricts the sum to states at the Fermi level for the ideal case when the tip is limited to a point probe and its wavefunctions are arbitrarily localized. Therefore, the tunnelling current is produced by the local density of states of the surface arose from the states at Fermi level at the position of the tip.

In conclusion, the tunnelling current can be approximated to the local density of states at the Fermi level and at the position of the tip:

$$I \sim \rho_v(r_0, E_F)$$

Eq. 2-19

Equation 2-19 is an ideal relation between tunnelling current and local density of states at the surface. However, in actual STM experiments, electronic and chemical interaction between tip and sample is much stronger and the voltage can be significantly higher than is assumed in the Tersoff-Hamann model. Formula 2-19 applies reasonably well to metallic surfaces.

Instead, for semiconductor samples and molecular adsorbates, Equation 2-19 should be modified for the case of finite voltages to:

$$I \sim \int_{E_F}^{E_F+eV} \rho_v(r_0, E) T(E, eV) dE$$

Eq. 2-20

where *T(E,eV)* is the transmission coefficient and depends on the energy of the electrons *E*. However, the transmission coefficient *T* will be approximated as voltage independent.

From Equation 2-20, for small bias voltages and a narrow range of energies, which contribute to tunnelling,

$$\frac{dI}{dV} \sim \rho_v(r_0, E_F + eV)$$

Eq. 2-21

However, this expression is an approximation for non-metals or molecular adsorbates. Illustrative experimental data obtained via scanning tunnelling spectroscopy (STS) are presented in Figure 2-10. Spectra were measured on C_{60} molecules adsorbed on Si(100)-(2x1) [54]. There is an energy gap of ~2 eV between LUMO and HOMO. Peaks in the graph representing the orbitals correspond to the theoretical energy levels of a free C_{60} molecule.

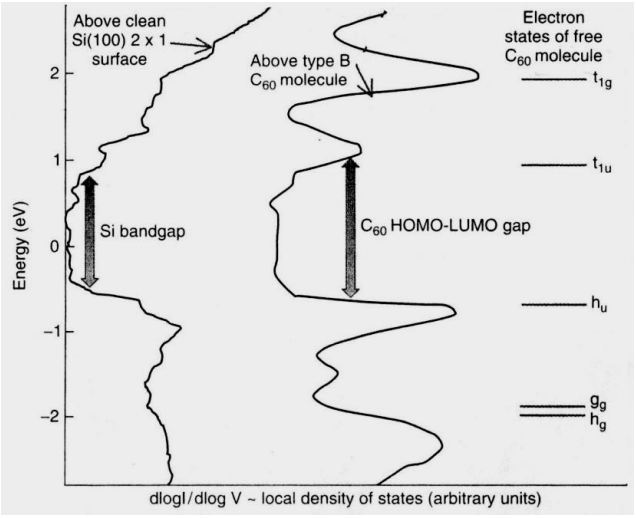

Figure 2-10. Scanning tunnelling spectroscopy data acquired on clean Si(100)-(2x1) and on C_{60} molecules deposited on this substrate. Theoretical energy levels calculated for a free C_{60} molecule are compared to the peaks resulted from experimental measurement. Once the molecule is adsorbed on the surface, due to covalent bonding, its energy levels maintain their position with slight deviation, but they broaden significantly. (Figure from [54])

2.5 Atomic Force Microscopy

The atomic force microscope [55] was developed with the purpose of measuring interaction forces present at the atomic scale and to extend surface imaging allowed in STM to non-conducting materials. Soon after its invention, AFM was employed in many scientific fields, but only after a considerable period of development was it possible to resolve atomic contrast. For the first time, Franz Giessibl resolved the atoms on a Si(111)-(7x7) surface using dynamic-mode, non-

contact AFM in ultrahigh vacuum (UHV) [56]. Since then, AFM has provided high-resolution analysis on semiconductors, insulators, ionic crystals, metals, adsorbed atoms and molecules [17, 21, 47, 57]. Moreover, the ability of AFM to quantify forces was used to measure chemical bond forces and to discriminate between different types of atoms [20].

In addition, AFM measures tip-sample forces acting at a distance from less than 0.1 nm to more than 100 nm. Atomic force microscopy uses mechanical responses and draws a 3D map of true atomic resolution based on the force acting at atomic level. Both atomic and molecular forces can be measured with high precision and used to manipulate atoms or molecules.

2.5.1 Forces Sensed by AFM

Interactions at the nanoscale can be classified as short- or long-range forces, and as attractive or repulsive [46, 47, 58]. When a tip is located in the proximity of the surface, interacting forces are superimposed. AFM senses interactions such as covalent forces, electrostatic forces, repulsive interaction forces and van der Waals forces.

Covalent forces are defined as short-range chemical forces (0.1-0.2 nm, F=1-9 nN), that tightly bind the atoms in a crystal or a molecule. Chemical forces can be described by the negative derivative of the Lennard-Jones potential (Figure 2-11) $F = -dU/dz$ [59]:

$$F(z) = \frac{12E_0}{r_0}\left[\left(\frac{r_0}{z}\right)^{13} - \left(\frac{r_0}{z}\right)^{7}\right] ,$$

Eq. 2-22

where E_0 represents the binding energy, r_0 is the equilibrium distance of the Lennard-Jones potential and z is the tip-sample separation.

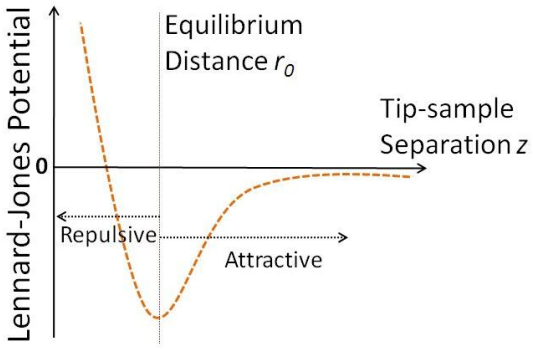

Figure 2-11. Lennard-Jones potential describing a short-range interaction.

At the atomic level in any kind of material, when the atoms are very close to each other, short-range repulsive forces are manifested. These forces can be explained by hard sphere repulsion, Pauli exclusion interaction and electron-electron Coulomb interactions. Their strength decays with increasing separation. Between neutral atoms van der Waals forces act based on dipole-dipole interaction [60]. They are caused by fluctuations in the electric dipole moment of atoms and by their mutual polarization. If the sample and the tip are composed of the same material and/or vacuum is the working environment, van der Waals forces are always attractive. The van der Waals interaction between a spherical tip and a flat surface is mathematically described by the van der Waals potential, V_{vdW}:

$$V_{vdW} = -\frac{A_H R}{6z}.$$

Eq. 2-23

or force, F_{vdW} :

$$F_{vdW} = -\frac{dV_{vdW}}{dz} = -\frac{A_H R}{6z^2},$$

Eq. 2-24

where R is the tip radius, z the tip-sample distance and A_H the Hamaker constant (which is determined by the physical properties of the material).

The force curve in AFM, describing tip-sample interactions is composed of the long-range force term (for example, van der Waals) and the short-range force

term (Figure 2-12). The two terms can be summed up in the following equation giving the total tip-sample interaction force, F_{ts}:

$$F_{ts}(z) = -\frac{A_H R}{6z^2} + \frac{12E_0}{r_0}\left[\left(\frac{r_0}{z}\right)^{13} - \left(\frac{r_0}{z}\right)^{7}\right],$$

Eq. 2-25

where A_H is the Hamaker constant, E_0 represents the binding energy, r_0 is the equilibrium distance of the Lennard-Jones potential, z is the tip-sample separation and R is the tip radius.

The short-range chemical forces are obtained after removing the long-range force contribution (Figure 2-12). However, this procedure is not trivial. Long range forces are higher in magnitude and have a long, smooth decay [20]. Short range forces are small in magnitude and have a sharp decay.

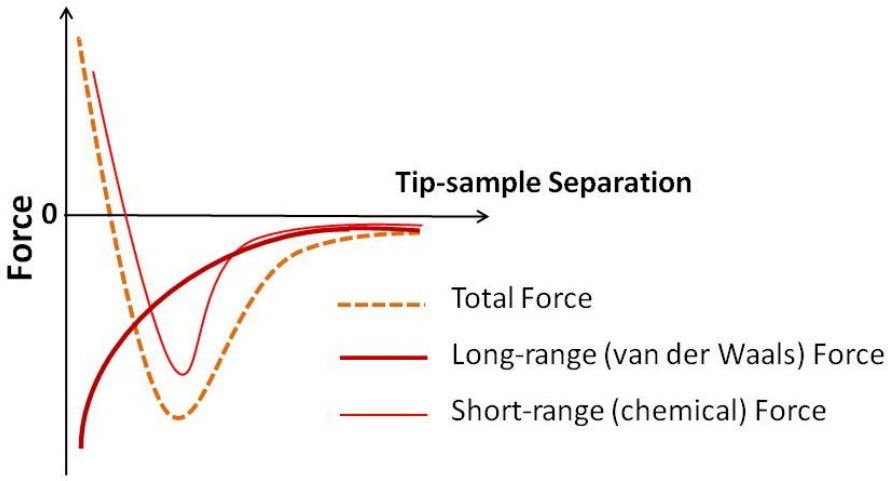

Figure 2-12. The total interaction force is composed of the long- and short-range forces. Long-range forces have a smooth monotonic decay. The forces deriving from the chemical bond occur only very close to the sample. In this case, the attractive force increases sharply.

Short-range forces are used to image the atomic structure with high resolution. From several nm to 100 nm distance between probe and substrate, the total force is derived almost entirely from long-range forces, such as van der Waals, and other electrostatic/electromagnetic forces.

The force is zero for large tip-sample separations (Figure 2-13). With decreasing distance between tip and sample the attractive force increases (negative region of force). The maximum attractive force is reached at the minimum of the graph. Decreasing the distance even further, the attractive force weakens until it is dominated by the repulsive force (positive region of force).

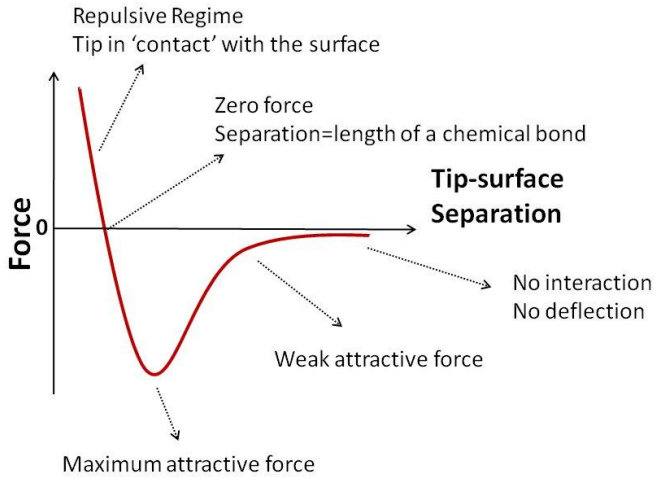

Figure 2-13. Example of force versus tip-sample separation curve, measured with AFM.

2.5.2 Girifalco Potential

The Girifalco potential [61] is a Lennard-Jones type potential which describes van der Waals interaction between two C_{60} molecules. In gas and solid, due to high thermal energy, C_{60} molecules rotate freely. Therefore, for the interaction of two C_{60} molecules, the sum of interactions arising from individual carbon atoms cannot be considered. Consequently, the C_{60} molecules are approximated as hard spheres of uniform density of carbon atoms. Using this 'smeared out spherical approximation', the potential energy of interaction between the two C_{60} molecules is calculated by integrating an inverse power function over the surfaces of the two spheres. The result of this integration applied to the 6-12 potential leads to the form of the Girifalco interaction potential:

$$\emptyset(r) = -2\alpha\left[\frac{1}{s(s-1)^3} - \frac{1}{s(s+1)^3} - \frac{2}{s^4}\right] + 2\beta\left[\frac{1}{s(s-1)^9} - \frac{1}{s(s+1)^9} - \frac{2}{s^{10}}\right]$$

Eq. 2-26

where α and β are constants, $s = r/a$, r is the intermolecular separation and a is the diameter of the C_{60} molecule.

The force of interaction between two C_{60} molecules is the derivative of the Girifalco potential with molecular separation, r,

$$F = -\frac{d\emptyset}{dr}$$

Eq. 2-27

According to the Girifalco potential, at long-range, attractive forces dominate, while, at short-range, there is a strong repulsive interaction between molecules. This conclusion provides information on how separation can be chosen to perform attractive or repulsive manipulation. However, one cannot rely only on this theory, because, in experiments, the manipulation process also depends on other types of forces, the tip shape, and the direction of applied force.

2.5.3 Modes of Operation

The simplest mode of AFM is contact mode, also called static. The second main group of modes, named dynamic, can be divided into non-contact and intermittent contact, involving the collection of measurements for amplitude, frequency or phase. The discussion in this section will focus only on non-contact dynamic mode of operation as this is the method of choice for work under ultrahigh vacuum conditions.

2.5.3.1 Dynamic AFM

In dynamic mode the cantilever is deliberately vibrated (Figure 2-14) at its resonant frequency. The resonance of the cantilever is characterized by amplitude, phase, and frequency. These parameters can each be used to monitor the force of interaction (or, more precisely, the force gradient).

In dynamic AFM [62], two modes of operation can be distinguished: first, amplitude modulation, which also includes phase imaging, and second, frequency modulation, combined with the use of phase-locked loop electronics.

When measurements are taken using amplitude modulation, either oscillation amplitude or phase of the cantilever oscillation is controlled by a feedback signal, while the excitation frequency remains constant. Changes of amplitude or phase are registered and used to adjust the *z* position of the tip.

Frequency modulation [63] is used to measure the cantilever resonant frequency, while oscillation is kept constant. The cantilever is always driven on-resonance.

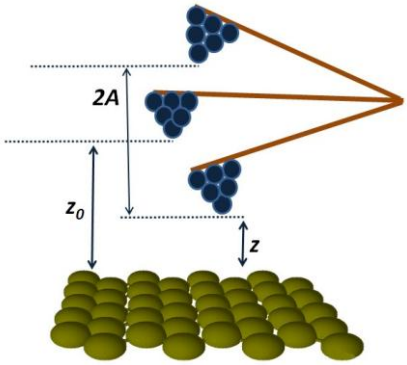

Figure 2-14. Tuning fork vibrated at its resonant frequency with an amplitude, *2A*. *Z* is the minimum tip-sample separation. At distance z_o the fork is not deflected.

Similar to STM (Section 2.4.2), frequency modulation AFM (FM-AFM) can be operated in two scanning modes: constant-height mode and constant-frequency shift mode. In constant-height mode, the cantilever travels above the surface at a fixed tip-sample distance. At each point, changes in the frequency shift are recorded. When using this operation mode it is essential to scan over very flat areas with minimum corrugation and, preferably, a step and defect-free surface, in order to avoid tip crashes. Constant-frequency shift mode is the analogue of the constant-current mode in STM. The frequency shift, which is analogous to the tunnelling current in STM, is the parameter to be monitored. A set-point value is set for the frequency shift and a feedback circuit moves the tip up and down to maintain

the pre-set value constant. Frequency shift refers to the change in the resonant frequency of the cantilever [57].

The cantilever has a harmonic oscillation and a sinusoidal motion when the tip is not in interacting with the surface. If the tip is close enough to interact with the surface, the force between tip and surface will cause an anharmonic oscillation of the cantilever and the frequency of the oscillation will be modified. The frequency shift is actually the difference between this new frequency and the resonant frequency of the cantilever (Figure 2-15).

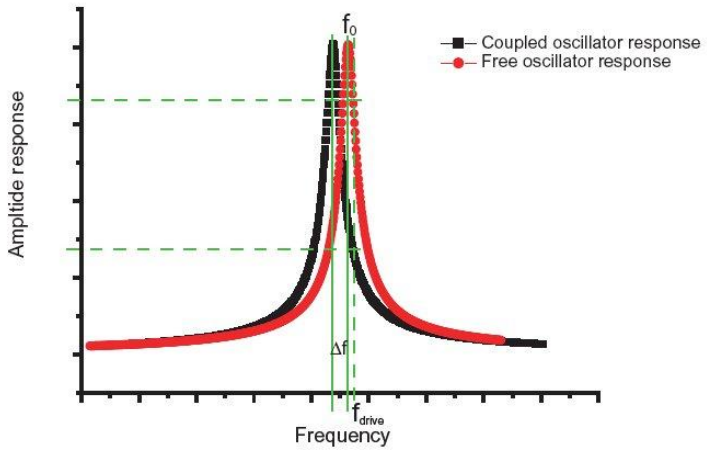

Figure 2-15. Representation of frequency profile as a function of amplitude. Due to interaction with the substrate a shift in the frequency Δf of the cantilever with respect to resonant frequency f_0 is recorded at constant amplitude A. (Figure by Dr Adam Sweetman)

If the interaction is elastic, conservative forces produce a frequency shift in the cantilever oscillation. On the other hand, if the interaction is inelastic and forces non-conservative, energy dissipation and damping of the cantilever occur. Furthermore, this will yield a sharp decay in the amplitude.

The cantilever behaves like a damped harmonic oscillator [57]. The equation of motion for this one-dimensional system is given by the formula:

$$m\frac{d^2z(t)}{dt^2} + \frac{m\omega_0}{Q}\frac{dz(t)}{dt} + kz(t) - F_{ts}(x, y, z_0 + z) = F_d(t)$$

Eq. 2-28

where F_{ts} is the total force of interaction between tip and surface, F_d is the driving force that maintains cantilever's oscillation, m is the effective mass of the cantilever, Q represents the quality factor, k equals the spring constant, $\omega_0 = 2\pi f_0$ the natural frequency of the cantilever, z is the displacement of the cantilever, and z_o is the undeflected position. In the absence of tip-surface interaction, $F_{ts} = 0$.

The motion of the cantilever is assumed to be perpendicular to the sample plane. Lateral speed is neglected because it is much slower than the oscillation sequence, therefore the force over one oscillation cycle depends only on tip-sample separation. The first term in Equation 2-28 represents inertia, the second term, damping, and the third term, restoring force.

The driving force F_d is given by

$$F_d(t) \sim A\cos(\omega_0 t)$$

Eq. 2-29

The response of the cantilever is an equation of form

$$A(t) \sim A_{max}\cos(\omega_0 t - \varphi)$$

Eq. 2-30

where φ is the phase shift between oscillation and excitation (always $\pi/2$ on resonance in our experiments).

A relation between frequency shift and force gradient can be obtained from the equation of motion 2-28 by simplifying the term for tip-sample interaction through a linear expansion [24, 47, 64]. Assuming no damping and conservative forces, Equation 2-28 becomes

$$m\frac{d^2z}{dt^2} + k(z-d) = F_{ts}(z)$$

Eq. 2-31

Total force $F_{ts}(z)$ can be expanded into a Taylor series:

$$F_{ts}(z) \approx F_{ts}(d_0) + \frac{dF_{ts}(d_0)}{dz}(z - d_0) + \ ...$$

Eq. 2-32

For small oscillation amplitudes in the range (d_o-A, d_o+A), with d_0 as equilibrium position, no deflection, Equation 2-32 can be reduced to

$$F_{ts}(z) = F_{ts}(d_0) + \frac{dF_{ts}(d_0)}{dz}(z - d_0)$$

Eq. 2-33

Therefore, Equation 2-31 becomes

$$m\frac{d^2z}{dt^2} + k(z - d) = F_{ts}(d_0) + \frac{dF_{ts}(d_0)}{dz}(z - d_0)$$

Eq. 2-34

Solving Equation 2-34 yields:

$$z(t) = z_0 + Acos(2\pi(\omega_0 + \Delta\omega)t)$$

Eq. 2-35

From Equation 2-34, a modified spring constant can be written

$$k_{eff} = k - \frac{dF}{dz}$$

Eq. 2-36

The change in resonant frequency is given by

$$\Delta\omega = (\frac{k_{eff}}{m})^{1/2} - \omega_0 \approx -\frac{1}{2}\omega_0\frac{dF/dz}{k}$$

Eq. 2-37

Rearranging the terms in Equation 2-37 and assuming low oscillation amplitude approximation, the relationship between frequency shift and force gradient is

$$\frac{\Delta\omega}{\omega_0} = -\frac{1}{2k}\frac{dF}{dz}$$

Eq. 2-38

Dynamic modes represent non-contact scanning methods and are advantageous for avoiding damage to both tip and sample. However, sometimes, a 'jump-to-contact' phenomenon can occur for large interaction forces, especially in the repulsive regime.

In order to avoid contact with the surface, the energy of the oscillating cantilever must overcome attractive forces acting between the tip and sample which may lead to chemical bond formation. For this, the spring constant *k* of the cantilever and the oscillation amplitude, *A*, play an important role and must satisfy the following relationship

$$kA > \max(-F_{ts})$$

Eq. 2-39

meaning that for good stability either *k* or *A*, or both, must be large. However, for optimal resolution small amplitudes are required. These two parameters can be related to the energy loss per cycle ΔE_{ts}

$$\frac{k}{2}A^2 \geq \Delta E_{ts}\frac{Q}{2\pi}$$

Eq. 2-40

where *Q* is the quality factor [47, 64]. If the energy loss is larger, the amplitude cannot be controlled.

2.5.3.2 FM-AFM Set-up

In frequency modulation AFM, the cantilever is oscillated at constant amplitude and at its resonant frequency. The frequency shift based on tip-sample interaction is the feedback parameter. The, so-called, Automatic Gain Control block (Figure 2-16) uses a controlled positive feedback circuit to maintain the oscillation amplitude at a given set-point. The output signal from the Automatic Gain Control loop is fed into an actuator which drives the oscillation of the cantilever. The excitation amplitude of the driving signal is recorded and provides information on the energy dissipation of the system via the damping signal.

Frequency shift output signal from the phase-locked loop (discussed in Section 2.5.3.3) is used by *Z* feedback controller (Figure 2-16) to modulate the tip-sample separation in order to maintain the frequency shift set-point constant.

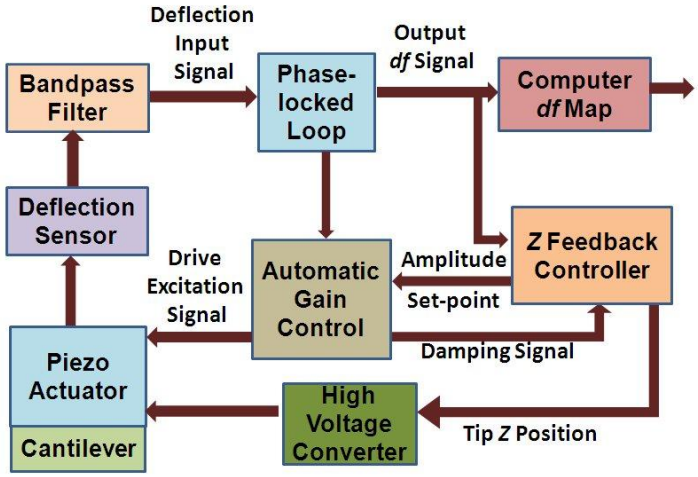

Figure 2-16. FM-AFM set-up diagram.

2.5.3.3 Phase-locked Loop

The phase-locked loop (PLL) [65] is an electronic circuit used in the *frequency modulation* mode as a detector for phase and frequency. The PLL provides a feedback mechanism to maintain the cantilever oscillation at its resonant frequency [66]. In most non-contact AFM systems, the output of the PLL is used to drive the oscillation of the cantilever [57].

This device plays a central role in controlling cantilever dynamics (Figure 2-17). It receives a deflection signal from the cantilever and reads its phase and frequency. At the same time, the PLL outputs a signal which is in-phase with cantilever oscillation. The frequency shift signal detected by the PLL is fed into a computer which plots the topography of the surface. The same signal is sent to the feedback electronics. The feedback circuit adjusts the frequency to the resonant frequency of the cantilever and the new signal is transmitted to the voltage controller oscillator, which is used to drive cantilever excitation. The phase angle between the excitation signal and the oscillation of the cantilever must be $\pi/2$, to ensure that the cantilever oscillates on resonance.

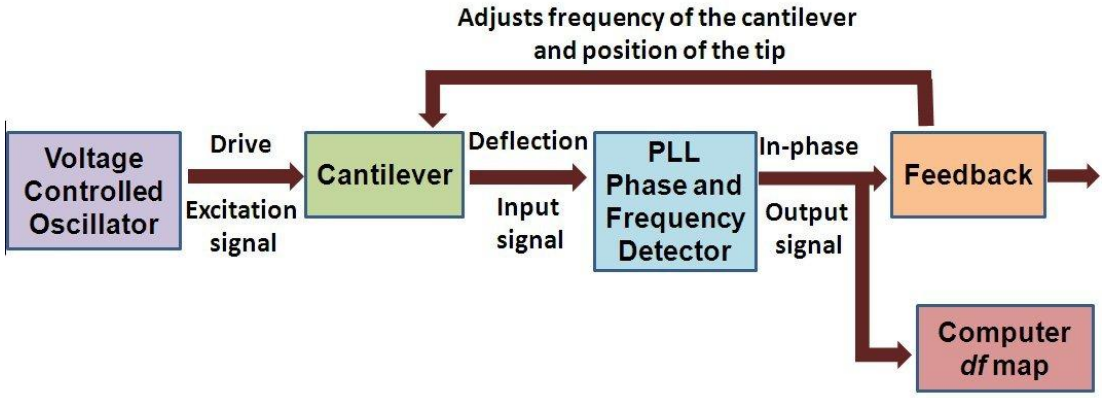

Figure 2-17. Diagram of AFM circuit including the PLL block.

2.5.3.4 Dynamic STM

Simultaneous STM and frequency modulation AFM measurements can be performed in dynamic STM. The cantilever is deliberately vibrated at its resonant frequency in constant-amplitude mode using PLL. Both tunnelling current and frequency shift are monitored and displayed. The set-point parameter in dynamic STM is the average tunnelling current over one oscillation cycle given by

$$< I(z, A) > \approx \frac{I(z, 0)}{\sqrt{4\pi kA}}$$

Eq. 2-41

where *z* is the tip-sample separation, *A* represents the oscillation amplitude and *k* is the spring constant [56]. According to Equation 2-32, an increase in tunnelling current signal is produced for small amplitudes. Therefore, contrast in dynamic STM measurements is strongly improved by employing low oscillation amplitudes. At the same time, signal-to-noise ratio for current measurements is improved.

2.5.3.5 Q Factor

Key properties of the cantilever are its stiffness, resonant frequency, quality factor and variation of the resonant frequency with temperature. The quality factor is a measure of the amount of dissipation. The stiffness is given by the spring constant, a parameter determined by the geometry and material of the cantilever. The resonant frequency is expressed by the following formula:

$$f_0 = \frac{1}{2\pi}\sqrt{\frac{k}{m}},$$

Eq. 2-42

where *k* is the spring constant and *m* is the effective mass. High stiffness produces a high resonant frequency, which is an advantage to minimize frequency noise.

The quality factor *Q* determines the height and the width of the response peak (Figure 2-18). The sharper the peak, the higher the quality factor, thus sensitivity is improved.

$$Q \sim \frac{\omega_0}{\Delta\omega}$$

Eq. 2-43

When the cantilever is driven by an external excitation at its resonant frequency, the response decays after the excitation has stopped. More exactly, the amplitude follows an exponential decay from its highest peak, *A*, to zero, by a constant $Q/2\pi f_0$.

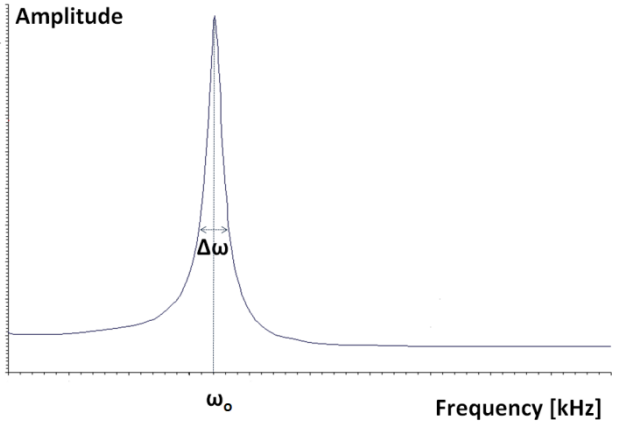

Figure 2-18. Amplitude versus frequency resonance curve. ω_o is the resonant frequency where the amplitude is maxim. $\Delta\omega$ is the width of the resonance peak. High *Q* factor – sharp narrow tall peak. Low *Q* factor – wide short peak.

The quality factor is directly proportional to the decay time and resonant frequency. High *Q* results from many cycles in a characteristic decay time, *i.e.*, little damping. This results in a tall, narrow peak in frequency space (Figure 2-18). The *Q* factor is correlated with the energy loss and the damping mechanism in the system by

$$Q = \frac{2\pi E}{\Delta E_c}$$

Eq. 2-44

where $E = kA^2/2$ is energy stored in the cantilever and ΔE_c is energy loss per cycle [56].

There are a multitude of factors which determine the quality factor, including, the physical and geometric properties of the cantilever, pressure, temperature, noise, and how the sensor is mounted in the AFM.

2.5.3.6 Force Spectroscopy

Force spectroscopy is an important application of AFM [57, 67]. In the static mode, spectroscopic data are acquired by applying to the sample or tip, a movement along the *z*-direction, approaching and retracting, while cantilever

deflection is kept under observation. This mode facilitates a straightforward interpretation of the interaction. However, the graph does not have a monotonic trend, but shows hysteresis loops, attributed to 'jump-to-contact' and 'jump-off-contact' phenomena.

Non-contact AFM offers advantages for force spectroscopy. The quality of the experiment is improved by increased sensitivity and stable force measurements. In FM-AFM, spectroscopic data are acquired by measuring the frequency shift at preset points between tip and sample. The force of interaction is the parameter of interest. The conversion from *df* to force is far from trivial. Sader and Jarvis [68] calculated a formula that gives a direct relationship between the frequency shift and force. The formula is applicable for arbitrary oscillation amplitudes. Their theory is based on a formula given by Giessibl *et al.* [59] which describes a relationship between the measured frequency shift and force:

$$\frac{\Delta\omega}{\omega_{res}} = -\frac{1}{\pi a k}\int_{-1}^{1} F(z + a(1+u))\frac{u}{\sqrt{1-u^2}}du \ ,$$

Eq. 2-45

where k is the spring constant, F is the force of interaction, ω_{res} is the resonant frequency, $\Delta\omega$ is the change in the resonant frequency, a is the amplitude of oscillation, and z is the tip-sample separation, and $u = cos(2\pi f_o t)$.

The force extraction from Equation 2-45 cannot be accurate for all amplitudes, or all length scales of force. This formula is limited and may provide significant errors upon conversion. The formula derived by Sader and Jarvis [68] is valid for constant amplitude independent of the distance between tip and sample and gives the force expression in terms of frequency shift:

$$F(z) = 2k\int_{z}^{\infty}\left(1 + \frac{a^{\frac{1}{2}}}{8\sqrt{\pi(t-z)}}\right)\Omega(t) - \frac{a^{\frac{3}{2}}}{\sqrt{2(t-z)}}\frac{d\Omega(t)}{dt}dt,$$

Eq. 2-46

where $\Omega(z)=\Delta\omega(z)/\omega_{res}$.

The energy of interaction between tip and sample is obtained by integrating Equation 2-46 and results in:

$$U(z) = 2k\int_z^\infty \Omega(t)((t-z) + \frac{a^{\frac{1}{2}}}{4}\sqrt{\frac{t-z}{\pi}} + \frac{a^{\frac{3}{2}}}{\sqrt{2(t-z)}})dt.$$

Eq. 2-47

2.5.3.7 Cross-talk

The interference, so-called cross-talk, usually arising from the tunnelling current, produces supplementary modulation in the quartz fork tuning, with effects on amplitude and phase of oscillation. Cross-talk arises from capacitive coupling between the current channel and the deflection channel. The current induced in the deflection signal is given by

$$I = C\frac{dV_g}{dt}$$

Eq. 2-48

where *C* is capacitance and *Vg* is virtual ground potential [69]. Cross-talk was observed by Weymouth *et al.* [70] to produce effects on AFM imaging, reflected in a "phantom" atomic contrast. This phenomenon occurred when a bias voltage was applied between tip and sample in order to reduce the attractive electrostatic force. The bias voltage induced a tunnel current with influence on the electrostatic force. This "phantom" force was reflected in artifacts in the AFM images.

Cross-talk varies with instrument design. For example, qPlus sensors used in the experiments described in this thesis, did not have separate connections to the tip for the tunnelling current. For this generation of qPlus sensors, even for voltages of tens of mV, preamplifier input may result in uncontrolled vibration of the tuning fork. This phenomenon, called "self-excitation" occurs often in STM

measurements after tip-surface contact or voltage pulses, or just for applying higher bias voltages.

Frequency shift spectroscopy can be significantly influenced by cross-talk between the tunnel current, frequency shift and damping channels [71, 72]. The objective in the experiments using the qPlus AFM is for the tunnelling current to have no influence on the frequency shift data. For this reason the bias voltage was reduced to zero during measurements. Tests have proven that for very small tunnel currents (~pA) there is negligible cross-talk between tunnel current and frequency shift or damping channels (see Supplementary Information Material for Chiutu *et al.* [73]). However, zero bias voltage can generate an appreciable contact potential difference and a long-range electrostatic force.

2.6 Hückel Molecular Orbital Theory

For interpretation of sub-molecular features seen in experiments, Hückel molecular orbital theory was used to compute simulated STM and dynamic-STM images [74]. Simulations were carried out by Dr. Andrew Lakin and Dr. Janette Dunn. Hückel molecular orbital theory is an analytical method which allows fast modelling of electronic orbitals. Bardeen's approach [53] (see also Section 2.4.3) was used to construct the overlap integral for the interaction between tip and sample. The tunnelling current is proportional to the tunnelling matrix element (Equation 2-15) and is given by the density of states at position r_o (Equation 2-19). The matrix element is an integral depending on the wavefunction that describes the molecular/atomic orbital (Section 2.4.3).

In simulations, lower symmetry of the molecule due to adsorption on the tip or the surface is accounted for by a new Hamiltonian acting on the molecular orbital wavefunction. The energy change is considered to be lowered along a single axis and varies inversely and proportionally to the distance between molecule and substrate. Thus, there is no atomistic consideration of the C_{60}-tip or C_{60}-sample interaction (unlike density functional theory (DFT)).

For C_{60}, the LUMO/HOMO is considered a linear combination of sixty *p* orbitals pointing outward from each C atom. The wavefunction of the LUMO/HOMO is the sum of the individual atomic orbitals. Each atomic orbital is multiplied by a coefficient c_i which indicates the contribution of the atomic orbital ψ_i to the LUMO/HOMO:

$$\Psi = \sum_i c_i \psi_i$$

Eq. 2-49

The coefficients c_i satisfy the conditions for normalizing and orthogonalizing the molecular orbitals (Equation 2-50). The wavefunction Ψ of the molecular orbital is substituted in the overlap integral:

$$\int \Psi^* \Psi d\tau = \delta_{mn} = \begin{cases} 0, m \neq n, orthogonalizong \\ 1, m = n, \quad normalizing \end{cases}$$

Eq. 2-50

Hückel molecular orbital theory aims to determine the expectation value expression for the energy of the molecular orbital

$$E_\Psi = \sum_i e_i \varepsilon_i$$

Eq. 2-51

where e_i is the number of electrons in orbital *i* and ε_i is the energy of the *p* orbital *i*. The energy ε_i is found by solving one-electron Schrödinger equation

$$H\,\psi_i = \varepsilon_i \psi_i$$

Eq. 2-52

where Hamiltonian *H* describes the interaction of one orbital with the rest of the molecule, ε_i is the energy eigenvalue of the orbital *i*, corresponding to the eigenfuction ψ_i of orbital *i*.

The energy ε_i of each *i* orbital is given by

$$\varepsilon_i = \int \psi_i^* H \psi_i d\tau$$

Eq. 2-53

Hamiltonian *H* is considered in the form of a diagonal matrix. Elements of this matrix are constants. The diagonal will be a set of 60 α coefficients corresponding to each carbon atom in the C_{60} molecule. The other elements in the matrix describe the interaction between orbitals and will equal constant β if the atoms are neighbours or *0* in any other case. Energy ε_i will be an expression in terms of α and β.

According to Chen's rule [75], in the Hückel molecular orbital theory simulations presented in this thesis, the tunnel current, *I*, results from all components of the HOMO

$$I \propto \sum_i \left(\frac{\partial \psi_i}{\partial z}\right)^2$$

Eq. 2-54

where *z* is the direction in which the *p* orbital of a carbon atom points.

Hückel molecular orbital theory was employed to analyze C_{60} molecules in three cases: **A.** C_{60} adsorbed on Si(111)-(7x7); **B.** C_{60} adsorbed on a Si tip interacting with Si adatoms; **C.** C_{60} adsorbed on a Si tip interacting with another C_{60} adsorbed on Si(111)-(7x7). Simulations were done both in constant-height and constant-current modes and also for higher current values. This method is not at all as time-intensive as methods such as density functional theory-based methods. On the contrary, it allows images to be calculated in several minutes.

In the first case, **A.**, a rich variety of intramolecular features arise from the orientation of the C_{60} molecule on the Si(111)-(7x7) surface in STM. In order to determine the origin of the molecular orbitals, a range of orientations were analyzed

(Section 4.2). A C_{60} molecule adsorbs with a pentagon, hexagon, double-bond, single-bond or apex-atom prone to the surface. Furthermore, the symmetry axis can be either perpendicular to the surface or can form angles at various degrees. In both cases, a reduction in the symmetry and degeneracy of the molecule is expected due to the interaction with the surface. In simulations, a weak interaction of the molecule with the substrate was assumed to assure simple splitting of the HOMO, LUMO and LUMO+1 orbitals. In experiments at different bias voltages, orbitals can be well defined, if separated in energy, or, otherwise, orbitals overlap. In the case of an isolated molecule, the LUMO and LUMO+1 orbitals are in three-fold degenerate states, while the HOMO is five-fold degenerate.

When the C_{60} molecule is involved in an external interaction, such as bonding with tip/surface, a reduction in the symmetry and a difference in the energy occurs. Molecular orbitals split according to the new energy of the molecule. As a consequence, singlets and doublets are formed. In the terminology used in this thesis, a singlet state represents a single molecular orbital at a particular energy and a doublet represents two molecular orbitals at the same energy. Splitting of molecular orbitals is strongly determined by the orientation of the C_{60} molecule. Different orientations yield different splitting.

In case **B.**, (see Figure 2-19), to compare simulated STM data to experimental dynamic STM images, two assumptions were made. In calculations, on the one hand, it was considered that the sp^3 orbital of each adatom did not penetrate beyond the regime where the molecular orbital function decays exponentially. In addition, the rate of decay for the region of the molecule being imaged was approximated with a constant in the *z* direction. These assumptions were validated by good agreement between theory and experimental data.

The interaction between a Si adatom and C_{60} was studied for the three main high symmetry orientations: C_2 - double bond down, C_3 - hexagon down, and C_5 - pentagon down, and also for single bond prone. Both experimental and theoretical data represent the empty states of the sample, so the molecular orbitals discussed in Section 5.3 correspond to the HOMO of C_{60}. When the molecule is attached to the tip, a lower symmetry would be considered in calculations. In these

calculations, the distortion was chosen along the axis which joins the center of the molecule and the point at which C_{60} binds on the tip. Basically, C atoms of the C_{60} cage were pulled toward the tip along this axis. The on-tip C_{60} is expected to be distorted which will eliminate some of the degeneracy. The effect of molecule-surface interaction or bonding will produce a change in the energy of the *p* orbitals. Starting from a lower symmetry, finding the characters of the matrices which act on molecular orbitals, for each symmetry case, the splitting of the degenerate orbitals can be calculated. In case of a hexagon or a pentagon interacting with the surface, the HOMO of the C_{60} molecule was reduced to two doublets and a singlet, while for a single or double bond, HOMO reduced to five singlets. The image that shows single bond orientation was formed by tunnelling current contributed from two singlets, but predominantly from one singlet, while for hexagon and pentagon, the electronic contribution was considered from the two doublets. Regarding Si(111)-(7x7) surfaces, an sp^3 hybridized orbital is associated to each adatom. Therefore, each Si adatom participates with a sp^3 orbital in the interaction with C_{60} molecule.

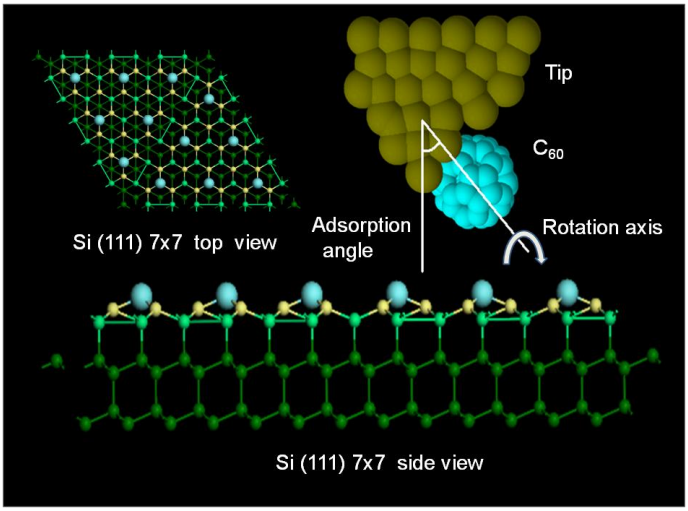

Figure 2-19. Diagram showing a C_{60} molecule attached to the tip, scanning across a Si(111)-(7x7) surface. Molecules adsorb on the tip/surface with symmetry axis parallel or at an angle to the normal surface. Depending on the molecular orientation, atomic contrast for Si adatoms changes in dynamic STM and qPlus AFM.

In the third case, **C.**, Hückel molecular orbital theory simulations were used for analysis of more complicated systems such as the interaction between two C_{60} molecules (Figure 2-20). The calculations help to elucidate the orientation of

both molecules. New electronic density features measured in dynamic STM may also arise from probing the states of a C_{60} molecule adsorbed on the surface with another C_{60} molecule as probe, attached on the tip apex.

In simulations it was assumed that electrons would tunnel from the HOMO of the tip-molecule into LUMO of the sample-molecule because all experimental data were recorded at positive bias voltage (Section 5.7). The molecule adsorbed on the tip was mapped by surface atoms. The orientation of the molecule on the tip was determined by comparing it to theoretical simulations. Once the orientation of the on-tip molecule was known, using a "trial-and-error" process, this information was used as input to calculate the orientation of the molecule adsorbed on the surface. By these means, a reliable match for the experimental image was obtained. However, selection of the best match is qualitative, because it is done visually and it cannot be quantified.

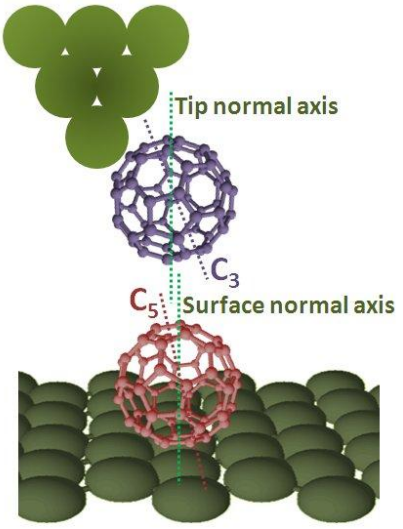

Figure 2-20. Interaction of two C_{60} molecules. The molecule adsorbed on the tip plays role of a probe and images the molecule adsorbed on the surface. The molecule on the surface is adsorbed with a pentagon down. The five-fold symmetry axis C_5 forms an angle with surface normal. The on-tip C_{60} molecule faces downward with a hexagon tilted from normal axis of the tip.

In calculating the position of the molecule, the adsorption angle with the normal axis to the surface and the rotation angle around the symmetry axis were taken into account. Electronic density across the molecule varies dramatically with very small changes of the angle.

The adsorbed C_{60} molecule interacts with both the surface and the tip. The molecule no longer behaves as a free molecule and suffers deformations and distortions of the cage structure. These changes were reflected in a lower symmetry and, implicitly, a split in the energy of the orbitals. As a consequence of this phenomenon the change in energy to lower values was taken into account when implementing the simulations. Therefore, the HOMO of C_{60} molecule was reduced to five singlets for single and double bonds, and to two doublets and one singlet for pentagon and hexagon.

Although the simulations were run for STM conditions, a direct comparison with the dynamic STM images was possible. The tip was treated as a simple harmonic oscillator because it vibrated during measurements, and the mean tunnelling current observed in dynamic STM differed by a constant factor from the STM current set-point (see Supplementary Information Material for Chiutu *et al.* [73]). The constant current technique used throughout simulations has shown that this constant did not strongly influence the qualitative results of the calculations.

For two C_{60} molecules, there are 3600 individual interactions between 120 *p* orbitals. However, most of these interactions, due to the distance between atoms, produce minimal orbital overlap. Therefore, their contribution can be neglected. The simulation presented in this work considered only 36 interactions from the nearest six atoms. This helped to reduce computation time.

2.7 Density Functional Theory

Density functional theory is a modelling technique that allows calculations of structural, chemical and electronic properties of materials. This method is widely implemented in solid state physics, surface science, and computational chemistry.

The core of density functional theory [76] is represented by calculation of the electron density. Mathematical demonstration of this theory shows that once the electron density is known, wavefunction, potential, total energy, forces of interaction,

and all other properties of the system in the ground state can be determined. This method is simplified because it works with electron density and does not need to deal with the wavefunction, which depends on many variables and on a large number of electrons. Even so, calculations for systems with high number of atoms are time-expensive.

In principle, this theory attempts to solve the many-body time-independent Schrödinger equation for a system with *M* nuclei and *N* electrons:

$$H\Psi(r_1, r_2 \dots r_N, R_1, R_2 \dots R_M) = E\Psi(r_1, r_2 \dots r_N, R_1, R_2 \dots R_M)$$

Eq. 2-55

where *H* is the Hamiltonian, Ψ is the many-body wavefunction, and *E* represents the total energy of the system.

The Hamiltonian in this case is a sum of five kinetic and potential energy terms arising from interactions of electrons and nuclei: kinetic energy of the electrons, kinetic energy of the nuclei, attractive electrostatic potential between electrons and nuclei, repulsive electrostatic potential between electrons, repulsive electrostatic potential between nuclei.

In this form the wavefunction has *3(N+M)* coordinates, where *M* is the number of nuclei and *N* is the number of electrons. However, for real systems, this high number of variables makes the equation almost impossible to solve. For this reason, the Born-Oppenheimer approximation is used. This theory assumes that, because electrons are much lighter than nuclei, their motion can be decoupled from the nuclei which can be regarded as fixed. In this way, the Hamiltonian will be reduced to three terms by removing the kinetic energy of the nuclei-nuclei interaction potential.

Even after this approximation, finding a solution for the many-body Schrödinger equation remains a difficult task due to the number of variables on which, the wavefunction depends. Therefore, in density functional theory, the wavefunction is replaced by the electron density. The theorem elaborated by

Hohenberg and Kohn [77] built the foundation for density functional theory. It holds that the electron density alone can determine the Hamiltonian, the energy and all other properties of a system. The first Hohenberg and Kohn theorem says: "For any system of electrons in an external potential V_{ext}, that potential is determined uniquely, except for a constant, by the ground state density $\rho(r)$". This allows the ground state total energy to be written as:

$$E[\rho(r)] = \int \rho(r) V_{ext}(r) dr + F[\rho(r)]$$

Eq. 2-56

where $F[\rho(r)]$ is the functional, unknown.

The second theorem states: "A universal functional for the energy $E[\rho]$ of the density $\rho(r)$ can be defined for all electron systems. The exact ground state energy is the global minimum for a given V_{ext}, and the density $\rho(r)$ which minimizes this functional is the exact ground state density". Therefore, to determine the minimum energy of the system E_o, the input of the density of the ground state $E[\rho]$ is required:

$$E_0 \leq E[\rho]$$

Eq. 2-57

The Kohn-Sham equation given in the Equation 2-58 below offers an approximation to construct $E[\rho]$ functional. Kohn and Sham considered a non-interacting electron system and showed that $\rho(r)$ can be obtained from the one-electron Schrödinger equation:

$$\{-\nabla^2(\mathrm{r}) + \mathrm{V_{ks}}[\rho(\mathrm{r})]\}\Psi_i(r) = \varepsilon_i \Psi_i(r)$$

Eq. 2-58

where V_{ks} is Kohn-Sham potential.

To construct the Hohenberg-Kohn functional *F[ρ(r)]* is very challenging and the system requires further approximations. The local density approximation (LDA) and generalized gradient approximation (GGA) have been introduced to calculate the exchange correlation energy functional. LDA assumes the system is a uniform electron gas. GGA is an improved version of LDA. In this case, the functional depends only on the electron density at each point and its gradient. The exchange correlation energy functional in GGA is given by

$$E_{xc}^{GGA}[\rho] = \int f\left(\rho_\alpha, \rho_\beta, \nabla\rho_\alpha, \nabla\rho_\beta\right) dr$$

Eq. 2-59

where α and β indicate the spin.

2.7.1 Modelling AFM Experiments with DFT

The SIESTA Code was employed by Dr. Samuel Jarvis and Prof. Lev Kantorovich to model short-range chemical forces between C_{60} molecules and Si adatoms. Chemical forces are responsible for the atomic contrast. Atomic scale interactions consist of covalent bonding, electrostatic forces, short-range repulsive forces, and van der Waals forces. The SIESTA Code offers a realistic modelling for constant-frequency shift imaging leading to a good interpretation of contrast formation in AFM.

There are three main steps in modelling an AFM experiment: (a) build a realistic model for the surface; (b) make a realistic model for the tip; (c) calculate the force between tip and sample as a function of the tip-sample separation and of the lateral position.

The cantilever is considered a weakly damped, harmonic oscillator, described by Equation 2-28 [59, 78]. In the case of an ideal oscillator when no damping of the cantilever occurs, the equation has a simpler form

$$m\frac{d^2z(t)}{dt^2} + kz(t) - F_{ts}(x, y, z_0 - z) = 0$$

Eq. 2-60

The frequency shift *Δf* can be determined from solution *z(t)* of Equation 2-60. In the case of large oscillation amplitudes and a tip trajectory larger than the tip-surface force range, the frequency shift *Δf* can be calculated from the tip-surface force using classical first-order perturbation theory:

$$\Delta f(A_0, f_0, kz_0) = -\frac{f_0}{2\pi k A_0}\int_0^{1/f_0} F_{ts}\left(z_0 + A_0\cos(2\pi f_0 t)\right)\cos(2\pi f_0 t)\,dt$$

Eq. 2-61

where A_0, f_0, k, z_0 are experimental parameters.

To model the C_{60}-Si interaction with DFT, the SIESTA code was run to simulate force spectroscopy using a C_{60} molecule as a probe, and a cluster of Si adatoms approximating the local configuration of a Si adatom, instead of an entire (7x7) unit cell (Figure 2-21). In the experiment presented in this thesis, the C_{60} was adsorbed on the tip and suffered a local deformation, but this may not affect the fundamental interaction between the bottom part of the C_{60} cage and Si adatoms or the imaging mechanism. For this reason the C_{60}-tip interaction was excluded in DFT calculations. The system was simplified this way in order to avoid very long time and expensive computations resulting from the enormous number of atoms (>300). Even this model required very time-consuming calculations. Simulations were carried out to test the validity of the C_{60}-Si cluster system also against the entire (7x7) unit cell and accurate results were obtained, providing reliable data for comparisons with experimental data (see Supplementary Information Material for Chiutu *et al.* [73]).

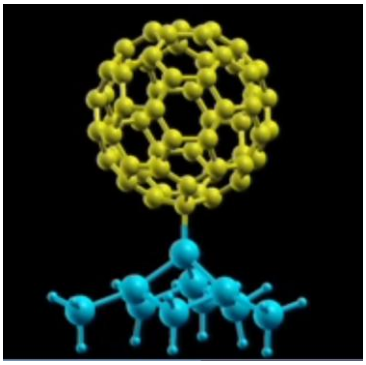

Figure 2-21. Ball and stick model of interaction between a C_{60} molecule and a Si cluster (blue balls). This Si cluster approximates position of a Si adatoms in (7x7) unit cell. (Figure by Dr Sam Jarvis)

2.8 Surface Reconstruction

Surfaces and interfaces break the 3D periodicity of crystals, leaving a highly reactive surface with free dangling bonds, vacancies, adatoms, steps, and kinks. Reconstruction is driven by energetic characteristics of the system, where atoms rearrange and build a surface with a new periodicity. Therefore, surfaces and interfaces exhibit morphological and electronic properties beyond simple bulk structure. The experimental data presented in this section were recorded using the VT Omicron STM as part of this Ph.D. project.

2.8.1 Si(111)-(7x7)

By heating a Si(111) sample up to 1200^{o} C, the native oxide layer is removed and the C diffuses into the bulk crystal. At the same time a (1x1) reconstruction is formed on the top layer of Si. Each Si atom has an unsatisfied, dangling bond that arises from its sp^3 orbital. For this reason, the free energy of the surface is very high. Therefore, atoms need to rearrange at the surface and in bulk to reduce the density of dangling bonds and implicitly, to decrease their free energy. The unit cell of this atomic arrangement is a supercell of (7x7) and exhibits 49 free dangling bonds in a high energetic state. When the sample temperature decreases, for different ranges of temperature, Si atoms reposition themselves forming unit cells of

various sizes: (5x5), (7x7), (9x9), of these the (7x7) is the most energetically favourable [46, 47, 51].

A theoretical model called the dimer-adatom stacking model (DAS) [46, 47, 51] was developed to explain the (7x7) reconstruction. The 49 dangling bonds in the (7x7) supercell are reduced to 19 bonds per cell. Three dangling bonds will be reduced to one partially filled dangling bond, corresponding to each of the twelve adatoms of (7x7). Six dangling bonds come from the first layer of rest atoms and one dangling bond (per unit cell) from the corner hole (Figure 2-22). The DAS model of the (7x7) supercell has the shape of a parallelogram and splits into a faulted and an unfaulted half. The first layer of the reconstruction is formed by Si adatoms. The second layer is build by rest atoms, while the third and the fourth layer are Si bulk layers. The fourth layer is formed only by the Si atoms in the unfaulted half. Adatoms form three covalent bonds with three neighbours in the rest atoms layer in sp^3 hybridization. Each adatom has a sp^3 orbital pointing outward the surface [79].

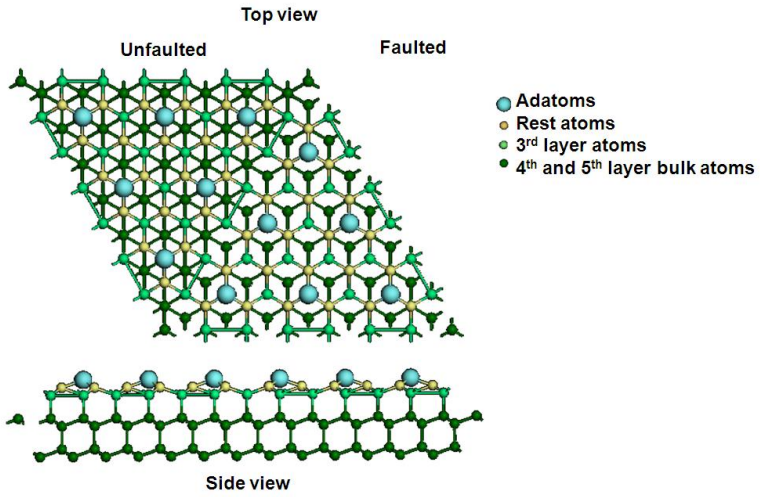

Figure 2-22. Si(111)-(7x7) DAS model: Top view and side view.

This complex structure has several pecularities: missing corner atoms, which appear as dark regions, dimers along the edges and along the central line of the mesh, adatoms on top layer, and a faulted arrangement of rest atoms (stacking fault). About 200 atoms of the Si crystal participate in the reconstructed of Si(111)-(7x7) unit cell [80, 81]. Steps, domain boundaries and various defects can be observed on Si(111)-(7x7) (Figure 2-23).

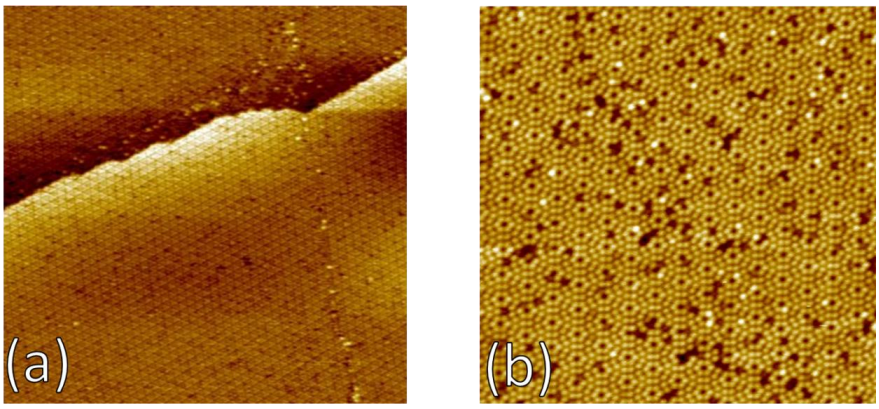

Figure 2-23. Si(111)-(7x7). **(a)** 200 nm image shows a step, always seen on a Si sample, good resolution of the unit cells and a domain boundary crossing the terrace. Image recorded at -2 V, 400 pA. **(b)** 40 nm empty states image – dark and bright spots represent missing atoms and adatoms/adsorbates, respectively, all considered defects of the reconstruction. Scanning parameters: 1 V, 20 pA.

Due to the partially filled dangling bonds, the adatoms appear in both empty and filled state STM images, regardless of the polarity of the bias voltage, but with a difference of contrast between the two halves of the unit cell in the filled- state image (Figure 2-24b). The adatoms appear brighter in the faulted half. The dark edges of the parallelogram are the result of dimer structures that remove the dangling bonds. In optimal atomic resolution the six rest atoms of the first layer can also be observed in filled state images (Figure 2-24c). According to the DAS model, the bright protrusions correspond to the positions of adatoms in STM images of Si(111)-(7x7).

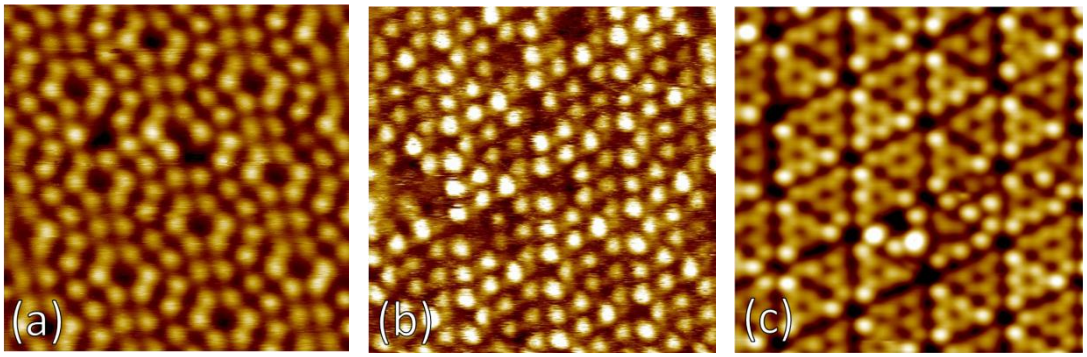

Figure 2-24. Si(111)-(7x7). **(a)** Empty states image, 10 nm, 1 V, 100 pA; **(b)** Filled states at room temperature, -0.9 V, 1 nA; **(c)** Filled states at 77 K with high resolution of rest atoms, 0.5 V, 0.6 nA.

2.8.2 Ag-Si(111)-(√3x√3)R30°

The (√3x√3) structure of the Ag-Si(111)-(√3x√3)R30° surface has proven to be very difficult to interpret. Theoretical simulations were carried out to clarify the STM data with regard to atomic positions and electronic states of the (√3x√3) reconstruction. Two models, the honeycomb-chain-trimer (HCT) and the inequivalent triangle (IET) structures were developed [51, 82]. The oldest and most widely observed structure was the honeycomb network, observed in both empty and filled states images (Figure 2-26a) [46, 83-85]. The HCT is a hexagonal network formed with Ag 'trimers' (Figure 2-25). The triangles are equivalent and equally sized. Two Ag triangles form the mesh of the (√3x√3) reconstruction, which is a rhombus with the four corners right above the Si atoms in the third layer.

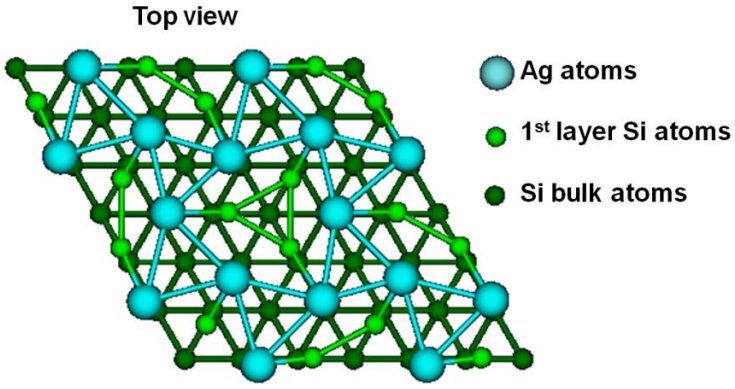

Figure 2-25. Model of honeycomb-chain-trimer. Two Ag triangles (blue balls) form the unit cell of the (√3x√3) reconstruction. Each Ag 'trimer' is imaged as a bright protrusion in STM. Si 'trimers' are formed by light green balls in the first layer. Dark green balls represent the second layer of Si atoms.

The honeycomb-chain-trimer model [82] explains the bright protrusions of the honeycomb network seen in STM images as the centres of Ag 'trimers' and not as Ag atoms. The central distribution of *5s* and *5p* orbitals in the Ag triangle can explain the image formation [86]. Two bright protrusions form a rhombus shaped unit cell. The dark centres corresponding to the corners of the unit cell were assigned to the centres of Si 'trimers', each Si 'trimer' being surrounded by six Ag 'trimers'. Therefore, the Ag triangles are imaged as bright maxima which build a hexagonal network, the so-called honeycomb reconstruction.

Inequivalent contrast between the two ‘trimers’ composing the hexagonal structure was first revealed in low temperature experiments [87]. In the beginning, the asymmetric appearance was considered a different kind of reconstruction given by a shift in the position of Ag atoms, which could be measured only at low temperature. A second model called the inequivalent-triangle structure (Figure 2-26b) [82] was introduced to clarify the asymmetric hexagonal structure and was found to differ from the HCT model by a slight rotation and displacement of the topmost Ag atoms. In STM images of IET model, brighter protrusions come from the ‘small’ Ag ‘trimers’, while the darker ones come from the ‘large’ Ag ‘trimers’. The difference in intensity is dictated by the distribution of density of states across the Ag ‘trimer’ [88, 89].

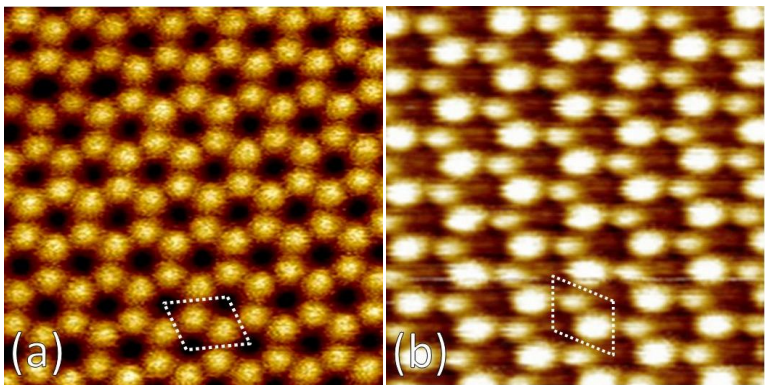

Figure 2-26. Ag-Si(111)-(√3x√3)R30^{o} reconstruction. **(a)** HCT and **(b)** IET room temperature STM images. One Ag ‘trimer’ gives rise to a maximum. Si ‘trimers’ are located in the dark centre of each hexagon. Two Ag ‘trimers’ build a unit cell, the dashed, white rhombus with the vertices on Si ‘trimers’. Image parameters: HCT: 10 nm, 0.4 V, 1 nA, IET: 4 nm, -0.2 V, 50 pA.

When a Ag layer is deposited on a Si surface, the substrate is held at high temperature. Monovalent Ag atoms each bind to one Si atom of each ‘trimer’ at the surface, leaving no free dangling bonds and energetically terminating the Si substrate. The Ag layer forms flat terraces with a long-range ordered network (Figure 2-27).

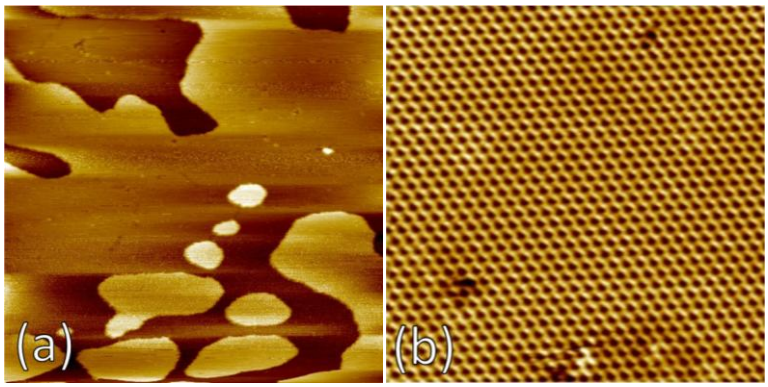

Figure 2-27. (a) Flat Ag terraces and islands on the Ag-Si(111)-(√3x√3)R30° substrate, 150 nm, -2 V, 10 pA. **(b)** Honeycomb network, 25 nm, -2 V, 100 pA.

Kirchner *et al.* [84] presented theoretical calculations where they demonstrated that between the Ag layer and the Si substrate there is a significant charge transfer and each Si atom forms a strong covalent bond with a Ag atom. The Ag-Ag interaction in the Ag layer is weak, being a simple interaction between *p* orbitals. However, the interaction between Ag and Si is not trivial because it has bonding character. According to the theory of Aizawa *et al.* [90], a Ag *5p* orbital interacts with a Si sp^3 orbital and forms a bond which reflected in the so-called S_1 surface state. Previously, it was considered that the *5s* orbital produces the S_1 state (Figure 2-28) [91].

Chen *et al.* [88] produced experimental *dI/dV* images and performed theoretical calculations to determine the electronic structure of Ag-Si(111)-(√3x√3)R30°. They found three surface-state bands S_1, S_2 and S_3, in the Brillouin zone of the unit cell which were also confirmed by other research groups (Figure 2-28). Moreover, two resonance surface bands, SR_1 and SR_2, were reported in Chen *et al.*'s paper [88]. According to their analysis, the S_1 state is determined mainly by the contribution of Ag p_x and p_y orbitals, while S_2 arises primarily from *s* orbitals. In principle, the S_3 state derives from Ag p_x and p_y orbitals with some contribution from Ag *5s* orbitals. Experimental *dI/dV* measurements provide information on how atomic contrast varies with different bias voltage. Electrons tunnel in different state bands giving specific features to each orbital contribution.

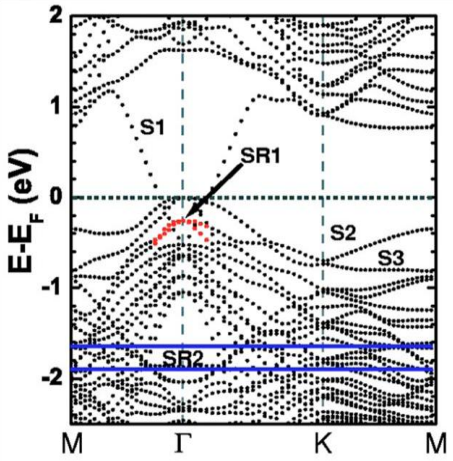

Figure 2-28. Calculation of band structure for Ag-Si(111)-(√3x√3)R30°. Depending on the bias voltage employed in STM imaging, tunnelling can be tuned for different surface states S_1, S_2, S_3. Resonance states SR_1 (black arrow) and SR_2 (parallel blue lines) are labelled on the graph. (Figure from [88])

To the surface states SR_1 and SR_2, which come mainly from the Ag *5s* states, there can be added a significant contribution from the sp^3 orbitals of Si 'trimers' in the layer below. Because sp^3 orbitals have long tails they extend in the vacuum and may dominate the *5s* orbital and produce the bright contrast resolution of Si triangles. Loenen *et al.* [92] carried STM scans with the purpose of achieving atomic contrast arising from Ag *d* orbitals. This was not possible to achieve, perhaps because of the short decay length of *d* wavefunctions at the surface compared to *s* and *p* orbitals.

The geometrical and electronic structure of Ag-Si(111)-(√3x√3)R30° was thus rather controversial. Different reconstruction phenomena were better understood in STM measurements at room temperature. Both HCT and IET structures appeared in the same STM image [82]. Tunnelling into different tip states was considered the reason for the switch between the two models in the same scan. In experiments carried out on a VT Omicron STM system at room temperature as part of this thesis work, both honeycomb reconstruction and the inequivalent-triangle models were routinely observed. The switch between the two models did not seem to be influenced by the polarity of the bias voltage or by the magnitude of the tunnelling current. The variations in the hexagonal lattice were attributed to rearrangements of the atoms located at tip apex, leading to tunnelling into different electronic states

[82]. In some cases, changes in the local density of states were registered in STM as a consequence of the dependence on the voltage polarity (Figure 2-29a).

Thus, for certain tip states, in the filled-state images, the pattern observed is a regular array of bright spots arranged in parallel rows. By switching the bias from positive to negative, the scan again showed the honeycomb network. White arrows show the line where the voltage polarity was reversed. Further measurements on the Ag-Si(111)-($\sqrt{3}$x$\sqrt{3}$)R30^o sample demonstrated that the dark centres of the Ag 'trimers' can also be resolved (Figure 2-29b). This was also observed by Zhang *et al.* [82]. They interpreted the centered bright spots as Si 'trimers', usually imaged as dark centres in HCT or IET models.

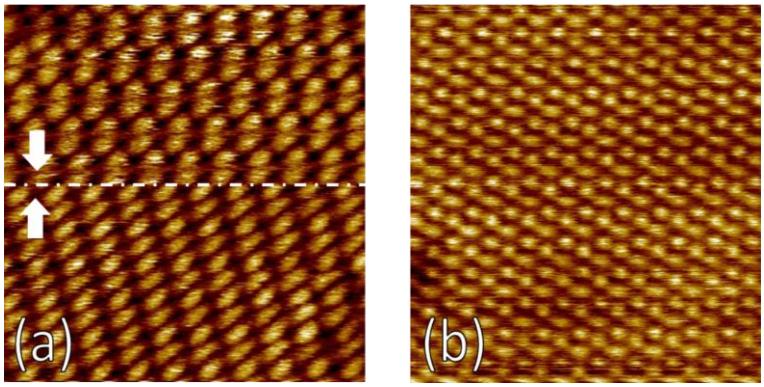

Figure 2-29. Tip state-dependent images of a ($\sqrt{3}$x$\sqrt{3}$) reconstruction of Ag-terminated Si obtain with STM at room temperature. In image **(a)** at 0.2 V, data show parallel lines of individual bright spots. At the dashed line, also marked by white arrows, when the bias voltage is set at -0.2 V, scanning shows again the honeycomb network. Imaging parameters: 10 nm, 500 pA. In image **(b)** the Si 'trimers' were imaged as bright spots. Together with the protrusion of the Ag 'trimers', they form a hexagonal network. Imaging parameters: 7 nm, 0.1 V, 1.5 nA.

Starting with the basic idea that STM senses only the tails of the wave functions that protrude in the vacuum, atomic resolution can be measured only by an atomically sharp tip. In these experiments, the terminal atom at the apex could be Si, Ag or tungsten. Zhang *et al*. considered that a Ag atom may be more sensitive into interaction with the Ag 'trimer' giving rise to an IET pattern [82]. A tungsten atom with a d_z state produces less interaction and yields the frequently observed honeycomb pattern [93]. The Si 'trimer' may be resolved with a tip having a Si atom with a sp^3 orbital as termination. Experimental data demonstrate that the tip state

plays a determinant role in resolving the electronic density of the Ag-Si(111)-($\sqrt{3}$x$\sqrt{3}$)R30^o surface.

2.8.2.1 STS on Ag-Si(111)-($\sqrt{3}$x$\sqrt{3}$)R30^o

I(V) and *dI/dV* spectroscopic data were measured on a clean Ag-Si (111)-($\sqrt{3}$x$\sqrt{3}$)R30^o surface, with a VT Omicron STM, at room temperature. Using a lock-in amplifier, a relatively high frequency modulation voltage is added to the DC bias voltage. The AC component of the tunnelling current, in phase with the modulation voltage, is recorded to yield the *dI/dV* signal. The derivative *dI/dV* of the *I(V)* curve is proportional to the density of states present at the sample surface (Equation 2-21) [94].

STS measurements on clean Ag-Si (111)-($\sqrt{3}$x$\sqrt{3}$)R30^o were single point acquisitions, up to twenty repetitions on various spots of a 10x10 nm^2 area. The *I(V)* and *dI/dV* profiles presented in Figure 2-30 are mean curves calculated from more than one hundred measurements. The *I(V)* curves are similar for all data sets, intersecting the axes only at the (0,0) point, and thus showing the metallic character of the substrate. Spectroscopic curves show a nearly metallic continuum and almost structureless metallic density of states, for most *dI/dV* spectra in Figure 2-30. A plateau – a slight change of the slope – indicating extra charge in the empty band of the surface was located in the valence band, close to the Fermi level (located at 0 V), with a peak at -0.2 V. This most likely corresponds to the surface state S_1 [87, 93].

The metallic character observed in STS experiment is consistent with previously published STS data [87, 94], but is inconsistent with the first principle calculation [86] and some measurements [95], which explained a semiconductive character for the honeycomb reconstruction. This apparent contradiction between the theoretical and experimental results is almost certainly due to a small excess of rapidly diffusing Ag adatoms [94].

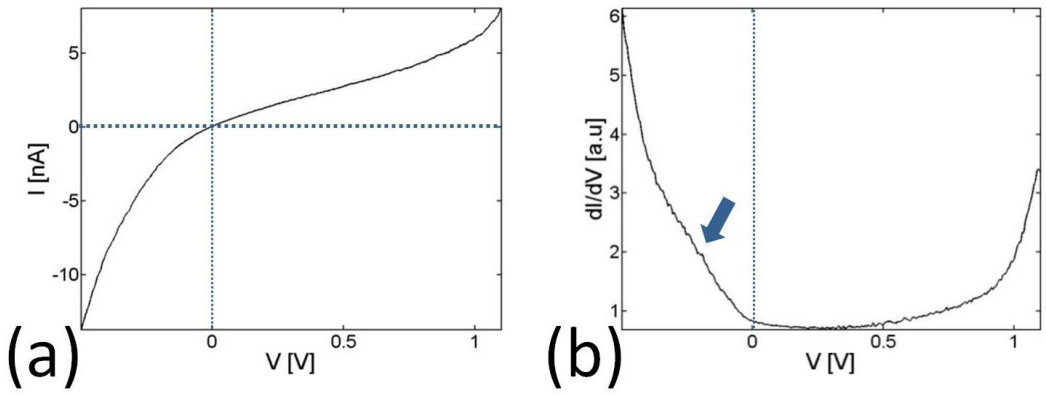

Figure 2-30. (a) *I(V)* and (b) *dI/dV* spectroscopic profiles of clean Ag-Si(111)-($\sqrt{3}$x$\sqrt{3}$)R30°. The curves represent the average of three sets of measurements recorded using the same tip and sample. (a) The graph intersects the axes only at the (0,0) point. (b) The curves show a featureless metallic character of the surface. Blue dashed vertical line marks the Fermi level, while the blue arrow shows potential S_1 state.

2.9 Buckminsterfullerene

2.9.1 Geometry and Properties of C_{60} Molecules

The existence of fullerenes was theoretically predicted many decades before their experimental discovery. In 1966, David Jones introduced the idea of hollow balloons for a new carbon form designed from a graphene sheet curled up by adding pentagon rings [96]. Osawa (1970) [97] and Davidson (1981) [98] ran simple calculations suggesting that the C_{60} structure could be found in nature. In 1984, the first spectroscopic evidence was achieved by Rohlfing *et al.* [99]. Finally, in 1985 Kroto *et al.* discovered and produced the first C_{60} molecules [25, 96, 100]. For this discovery they were awarded the Nobel Prize in Chemistry in 1996. The experimental setup leading to the discovery of C_{60} consisted of a laser irradiating a rotating disk of graphite [25]. The evaporated C species were filtered and analyzed using a mass spectrometer. Today, a simple method to produce C_{60} molecules is to apply an arc discharge in an inert atmosphere between two graphite electrodes [25, 100].

Along with graphite and diamond, fullerenes comprise a third allotrope of carbon [4]. They exhibit interesting properties that can be explored at nanoscale.

Fullerenes are a family of closed-cage molecules having only C atoms in a number varying from 20 to 548 or higher. The C atoms bind in a pentagon-hexagon structure, forming, according to Euler's theorem [96], twelve pentagonal rings and any number of hexagonal faces.

Generally, fullerenes are closed-shell molecules, denoted as C_n, where *n* is the number of C atoms (Figure 2-31). Threefold-coordinate atoms comprise fullerenes, which contain twelve pentagons and (*n*/2-10) hexagons, with *n* equal or higher than 20 [100]. Twenty is the smallest number that can contain the twelve pentagons required to close the shell [96]. Molecules with fewer than 32 atoms are unstable. The most stable fullerene has proven to be C_{60}. More complex fullerenes are of interest because of their complicated symmetry or orientation and their temperature dependence or physical properties [100].

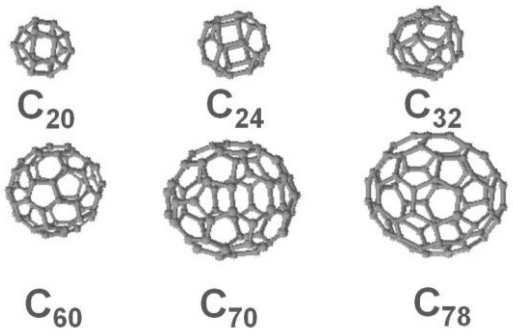

Figure 2-31. Small and large fullerenes.

The C_{60} molecule is of special interest because of its remarkable chemical and physical properties. In C_{60}, the bond shared by two hexagonal faces is a short double bond with a length of ~1.38 Å and the bond connecting a hexagonal and a pentagonal face is a single bond of ~1.45 Å length [2, 4, 101]. The molecule has an almost spherical shape and an average diameter of ~7.1 Å. C_{60} is a truncated regular icosahedron which is very rare in nature because of their icosahedral symmetry [101]. C_{60} possesses 120 different symmetry elements, including rotation around the two-fold, three-fold and five-fold symmetry axes (Figure 2-32). Two-fold rotation derives from the C_2 axes crossing the double bond edge between two hexagons. The C_3 axes piercing the centers of the hexagons determine three-fold symmetry (but not six-fold symmetry because of single-double bond alternation). The five-fold rotation

axis, C_5, crosses the centers of the pentagons. Each pentagon, hexagon or bond matches another one on the opposite side of the molecule.

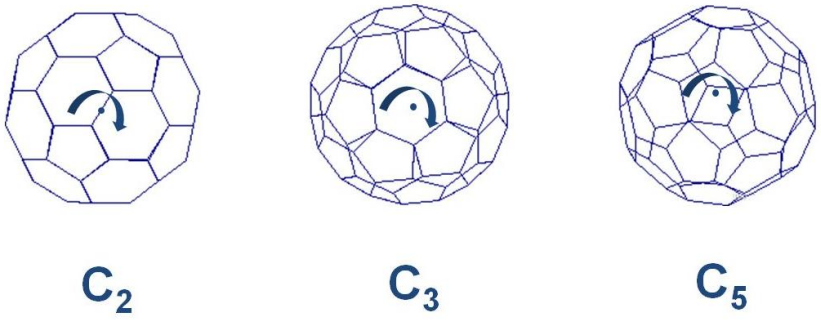

Figure 2-32. Rotation axes and symmetry of C_{60}.

Studies of molecular orbitals and vibrational dynamics of C_{60} have elucidated its optical and electronic behavior. C_{60} is a relatively large molecule, so it exhibits a wide range of energetic states and vibrational modes. In C_{60}, each C atom is bonded to three others, predominantly in an sp^2 configuration mixed with sp^3 hybridization [4]. The HOMO, the LUMO, and the next LUMO (LUMO+1) are the most important in reactions and interactions of fullerenes. The HOMO and LUMO are separated by an energy gap which underpins the optoelectronic behavior of the molecule.

The HOMO, h_u, is five-fold-degenerate and is occupied by ten electrons, while the LUMO, t_{1u}, and LUMO+1, t_{1g} [102], are triply degenerate and can accept up to six electrons each (Figure 2-33) [4, 101]. When the molecule interacts with a substrate or other chemical elements, orbitals can be shifted or modified leading to different values for the discrete energy levels. These orbitals describe energetically the chemical and physical properties of the molecule.

Properties of the molecule can be modified in a controllable manner. Due to the rich number of functionalization possibilities, and with the use of supramolecular chemistry, novel molecular materials can be created [1]. The electronic character of the molecule can be varied from insulator/semiconductor to metal or superconductor simply by doping the fullerene with guest atoms, chemical radicals or various foreign molecules, which can be both electron acceptors and donors. For example, by doping C_{60} with K or Rb atoms, three electrons are added to

the three-fold-degenerate LUMO transforming the fullerene into a superconductor with an optimum metal behavior (a half-filled band) [3].

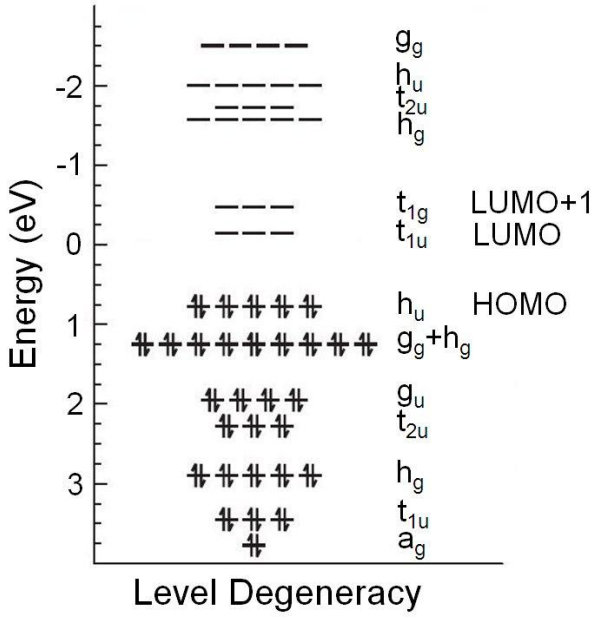

Figure 2-33. Energy-level diagram in C_{60}.

There are several modes of doping C_{60}: (a) from inside with encapsulated guest species, creating endohedral fullerenes; (b) by substituting any C atom of the molecule with other elements, forming heterofullerenes; (c) by adding various functional groups to the outside of the cage, exohedral fullerenes are obtained. Electronic transport properties of C_{60} and its siblings have been at the core of fullerene research. Fullerenes are very good electron acceptors in intermolecular and intramolecular interactions [2]. C_{60} can accept electrons by photoinduced and photoexcited electron transfer. The molecule has been successfully imaged, manipulated, and investigated electronically, demonstrating great potential for applications in molecular electronics.

Electronic and physiochemical properties of fullerene on surfaces have been extensively studied by single-molecule manipulation techniques and spectroscopy. Interaction of C_{60} molecules with metal and semiconductor substrates has been widely investigated [27-29, 103]. The next section will review the history of previous experimental work on imaging, spectroscopy, and manipulation of C_{60} using STM and non-contact AFM.

2.9.2 SPM Research on C_{60} Molecules – Brief History

Since the discovery of C_{60}, various surface science techniques have been used to investigate its characteristics and its interaction with metal and semiconductor substrates. Research carried out with scanning probe microscopes has contributed massively to the understanding of fullerene structure and properties. Adsorption configurations, intramolecular structure, and electronic properties of C_{60} have been analyzed with SPM [104] on surfaces such as Si(100) and Si(111), Ge(100) and Ge(111), Au(111) and Au(110), Ag(111), Cu(111), HOPG(0001), Ag-Si(111)-($\sqrt{3}$x$\sqrt{3}$)(R30^o), and many others.

2.9.2.1 Imaging C_{60} Molecules using STM on Si(111)-(7x7)

Strongly reactive substrates, such as Si, generally bind at the site where the fullerene contacts the surface. C_{60} has a chemical interaction with the Si(111) surface and forms an (iono)covalent bond [105, 106]. The molecule is thus chemisorbed [107]. Coverage of C_{60} by less than one monolayer results in randomly distributed molecules, because they do not diffuse. Molecules attached in this fashion also do not rotate: thus, the adsorption geometry can be ascertained via STM [108].

Intramolecular contrast of C_{60} has been successfully obtained with STM at low temperatures using for adsorption both Si [30] and metals [109]. Experimental data show good agreement with theoretical calculations [110, 111]. The symmetry and orientation of C_{60} can be clearly determined by STM imaging. Each of the two-fold, three-fold and five-fold symmetries has been resolved on single molecules [112] or on molecules inside islands [32].

Hou *et al*. [30] studied the orientation of C_{60} molecules on Si(111)-(7x7) at low temperature. They observed using STM measurements that the intramolecular features of adsorbed C_{60} are strongly influenced by the adsorption site and the bias voltage. Adsorption geometries of C_{60} were analyzed and correlated with the orientation of the cage using local density approximation calculations, which provided a good approximation of the molecular orientation. Hou *et al.* determined

that when molecules were adsorbed on different sites, the internal molecular characteristics changed under different bias voltages.

An example of two molecules is presented in Figure 2-34. The C_{60} molecules adsorbed at two different positions in the unit cell of Si(111)-(7x7) and were imaged at different bias voltage. Theoretical calculations showed that one molecule (Figure 2-34a-a4) adsorbed with a 5-6 bond down above a three Si atom site in the faulted half and a second molecule (Figure 2-34b-b2) adsorbed with an edge atom down on a corner hole.

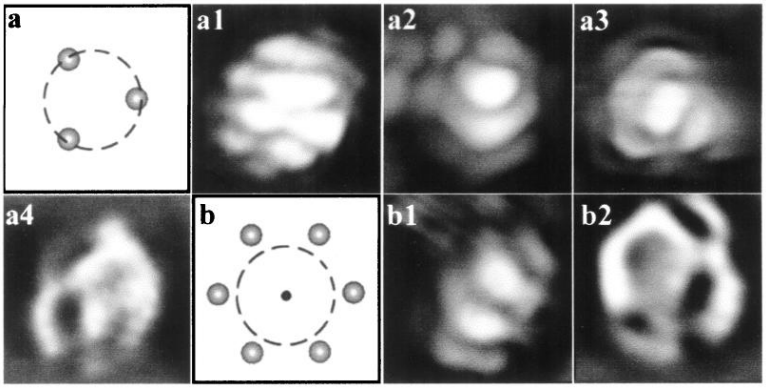

Figure 2-34. (a1)-(a4) – molecule adsorbed on the faulted half of a (7x7) unit cell on top of three Si adatoms **(a)** imaged at different bias voltages. (a1) *Vs* = -1.8 V, (a2) *Vs* = 1.5 V, (a3) *Vs* = 1.8 V, (a4) *Vs* = 2.5 V; **(b1)-(b2)** – molecule sitting on the corner hole, between six Si adatoms **(b)**. (b1) *Vs* = -1.8 V, (b2) *Vs* = 2.3 V. Electronic features change significantly for different voltages. (Figure from [30])

Investigation of the orientation and molecular binding of C_{60} on Si(111)-(7x7) were carried out by Pascual *et al*. [31]. When C_{60} molecules are imaged at high resolution with STM, detailed features of the molecular orbitals are revealed (Figure 2-35a-d). SIESTA DFT calculations (Figure 2-35e-h) were run by Pascual *et al*. in order to interpret the intramolecular structure observed in the experiments. Simulations were performed for HOMO of a free molecule, but slightly compressed along the symmetry axes. The simulated C_{60} structures agree well with experimental data.

Molecular orbital-derived features, revealed with STM, arise from the electronic states of the molecule, which depend upon the sample state and its partial coupling to the STM tip. Pascual *et al.* observed that depending on the local C_{60}-Si

interaction, C_{60} molecules exhibit apparently variable size and height. Some molecules, that appear larger (~0.6 nm high and ~2.0 nm wide), were claimed to be slightly mobile; hence they may look fuzzy and noisy. It is also very difficult to resolve internal features on these molecules. Other molecules appear smaller (~0.5 nm high and ~1.5 nm wide), and seem strongly anchored to Si. These molecules reveal the complex electronic structure of C_{60}.

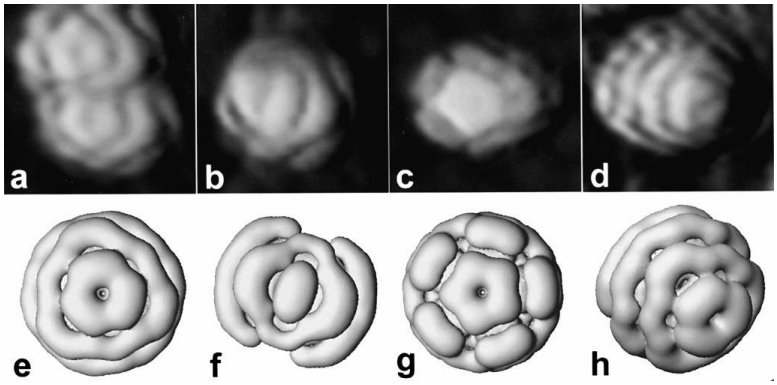

Figure 2-35. Intramolecular structure of C_{60} on Si(111)-(7x7). Experimental data (a-d) and analog DFT simulations (e-h). Imaging parameters: **(a)** 2 V, 0.2 nA. The molecule has three-fold symmetry and is adsorbed onto Si with a hexagon down; **(b)** -1.5 V, 0.2 nA. The molecule has its two-fold axis perpendicular to the surface; **(c)** 2 V, 1 nA. The molecule has a pentagon on top, and on the bottom as well; **(d)** -2 V, 1 nA. The molecule has three-fold symmetry, but its axis is tilted by 40^{o}. Corresponding DFT orientation: **(e)** three-fold, **(f)** two-fold, **(g)** five-fold, **(h)** three-fold symmetry axis of the molecule tilted 40^{o}. (Figure from [31])

2.9.2.2 STS of C_{60} Molecules on Si(111)-(7x7)

The electronic structure of adsorbed C_{60} molecules can be revealed by *I(V)* and *(dI/dV)(V)* spectra measured with scanning tunnelling spectroscopy in STM. C_{60} is a semiconductor with discrete energy levels (HOMO and LUMO) and a bandgap of ~1.8 V [4]. In order to obtain spectra representative of a single, isolated molecule it is necessary to choose an inert surface that does not interact with the adsorbed molecule. If interaction with the substrate is significant, STS data will be the result of an overlap of the states of the C_{60} molecule and the local density of states of the substrate.

Wang *et al*. [113] studied C_{60} on Si(111)-(7x7) using STM at low temperature. They showed that the STS data are dependent on the adsorption site, suggesting that the electronic states of the surface intermix with the molecular orbitals of C_{60}. Mixing between the molecule and surface states is observed from normalized *dI/dV* spectra (Figure 2-36).

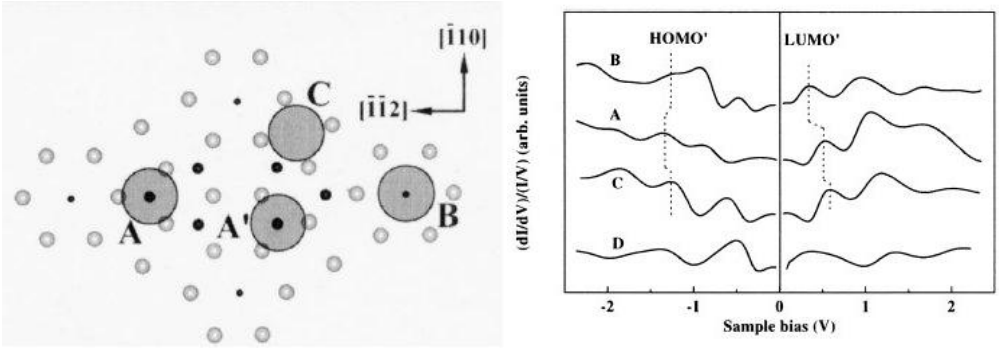

Figure 2-36. STS spectra recorded on C_{60} molecules adsorbed at sites A, B and C on the Si(111)-(7x7) unit cell. The shift of the main orbitals peaks, HOMO and LUMO, and additional peaks measured in the gap denote a strong electronic contribution from the surface states to interaction with the molecule. Spectrum D is the average of the other spectra. For C_{60} adsorbed on the faulted half of Si(111)-(7x7) unit cell, on top of three Si adatoms, (site A) the gap is the largest (~1.4 eV). For site B, a molecule on the corner hole, the gap is slightly smaller (~1.3 eV). The smallest gap was measured for a molecule adsorbed on top of four adatoms, including the dimer line – site C, and was ~0.8 eV. These values are considerably smaller than the energy gap of free C_{60} (1.6-1.9 eV). (Figure from [113])

From STS spectra of C_{60} bound to Si adatoms (Figure 2-36), a number of additional peaks and broadening of the HOMO-LUMO peaks are also observed, as compared to STS spectra of free C_{60}. Differences occur due to influence of the substrate state. Still, because C_{60} is a relatively large molecule, it is expected that the fundamental electronic characteristics of the free molecule are maintained. In this way, the position of HOMO and LUMO levels on the spectra can be determined. The shift and split of energy levels in the adsorbed molecule arise due to the strong interaction of the molecule with the substrate. The cage is distorted and C_{60} symmetry is reduced. Extra peaks present in the gap in the STS spectra are induced by the Si substrate, demonstrating that the occupied states of C_{60} mix with the Si to a larger degree than the unoccupied states.

2.9.2.3 STM Imaging and STS of C_{60} Molecules *on Au(111)*

Individual C_{60} molecules have also been studied on metallic surfaces. Lu *et al.* [112] observed five orientations of C_{60} molecules on Au(111) with STM, at 7 K. (Figure 2-37). Analyses of ~90 molecules with different tips have revealed only these orientations. The C_{60} adsorbs on Au(111) in the following positions with a hexagon down, a double bond down - formed between two hexagons - , a single bond down - formed between a pentagon and a hexagon - , an apex atom down and a pentagon down. The hexagon down and the double bond down configurations were prevalent on the surface in proportion (~35 % each). STS data have been also acquired for single C_{60} molecules on Au(111). Electronic features do not vary significantly with orientation, but for spectra recorded on different spots across one molecule, heights of the HOMO and LUMO peaks change radically (Figure 2-37).

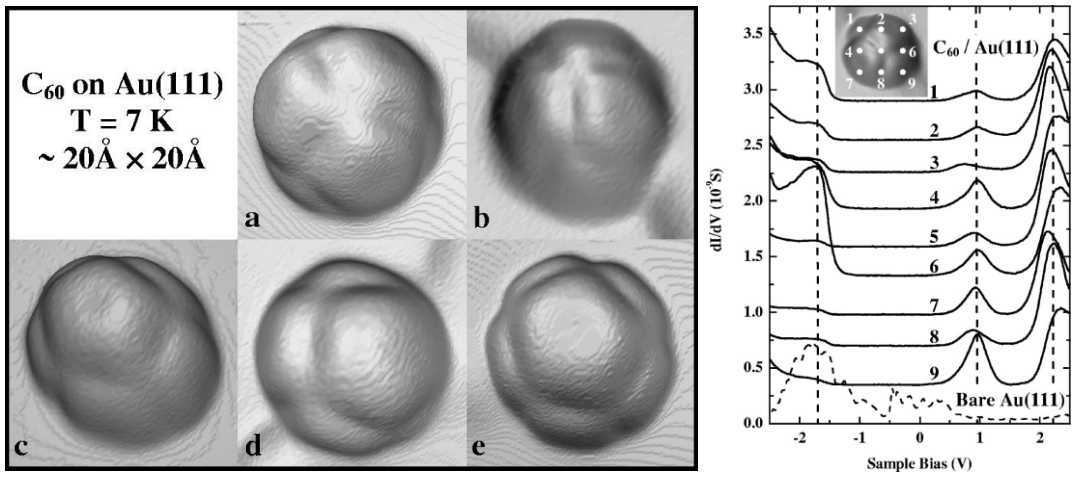

Figure 2-37. Single C_{60} molecules imaged on Au(111) at 7 K. Scanning parameters: V = 2.0 V, I = 0.3 nA. The molecule is oriented with a hexagon **(a)**, double bond **(b)**, single bond **(c)**, apex atom **(d)**, and pentagon **(e)** prone to the surface. STS *dI/dV* spectra were acquired at nine different points on a single molecule adsorbed on Au(111). At each point, peaks' height varies depending on the electronic states. In conclusion, density of states is not distributed uniform but varies across the molecule. Tunnelling parameters: V = 2.0 V, I = 1.0 nA. (Figure from [112])

2.9.2.4 C_{60} Islands on Au(111)

Schull and Berndt [32] investigated self-assembly of C_{60} molecules on Au(111) at 5.7 K. They were first to observe a long range complex superstructure of

a C_{60} assembly (Figure 2-38). Low temperature imaging offers the advantage of probing internal features of the molecules when they self-assemble in closely-packed structures. This is possible because rotation and vibration of the molecules are minimized. The internal structure of the molecules reveals sub-domains with different directional ordering and different orientation for the molecules inside the hexagonal islands [29, 32, 114].

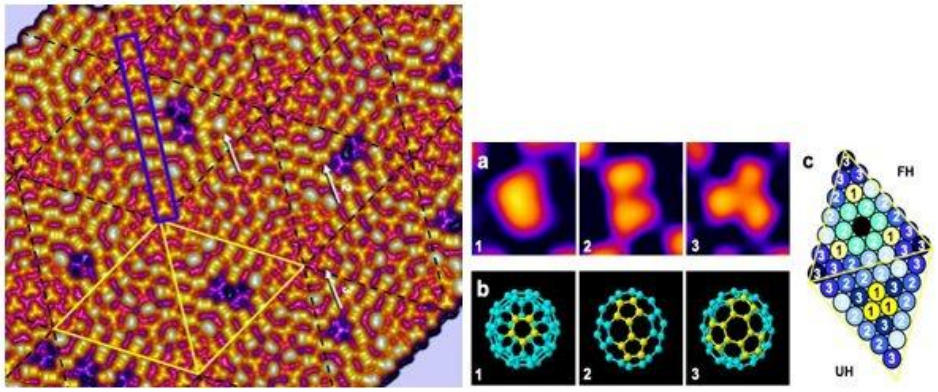

Figure 2-38. C_{60} superstructure. The yellow rhombus is the unit cell formed by 49 molecules. The unit cell has a faulted and an unfaulted half. Arrows highlight the molecules with C_5 **(1)**, C_2 **(2)** and C_3 **(3)** symmetry. They indicate a five-fold symmetry (pentagon up appearing as one-fold (first case)), two-fold symmetry (double bond up (second case)), and three-fold symmetry of C_{60} (hexagon up). Defects seen in the molecular lattice were mainly dark molecules. They appear lower than the other molecules and always in the faulted half of the unit cell. The approximate orientation of each molecule in the mesh of C_{60} assembly is also indicated. (Figure from [32])

After deposition of C_{60} molecules on an alkylthiol, self-assembled monolayer, Hou *et al.* have also obtained ordered 2D domains separated by boundaries [33-35]. In the closely-packed hexagonal islands, one or more domains formed with molecules exhibiting a single orientation.

2.9.2.5 C_{60} Islands on Ag-Si(111)-($\sqrt{3}$x$\sqrt{3}$)R30^o

On non-reactive surfaces, at room temperature, C_{60} molecules diffuse until they find a reactive spot at a defect, a step edge or another molecule. For example, on Ag-Si(111)-($\sqrt{3}$x$\sqrt{3}$)R30^o, they assemble into close-packed islands. Adsorbed Ag atoms in the honeycomb-chained-trimer structure of the Ag-Si(111)-($\sqrt{3}$x$\sqrt{3}$)R30^o reconstruction, form covalent bonds with Si atoms, leaving no dangling

bonds on the surface (apart from step edges and phase boundaries) and greatly reducing surface reactivity. C_{60} adsorbates are located on top of Si 'trimers' or in the middle of neighbouring Ag 'trimers' [29].

C_{60} molecules sit preferentially on top of Ag 'trimers' and only ~30 % reside above a Si 'trimer' [27] (Figure 2-39). The hexagonal lattice is the schematic representation of Ag-Si(111)-($\sqrt{3}$x$\sqrt{3}$)R30^o reconstruction. The center of each hexagon corresponds to a Si 'trimer', while each vertex is associated with an Ag 'trimer'. The rhombus unit cell of the Ag reconstruction comprises a Si 'trimer' and an Ag 'trimer'. Black circles represent C_{60} molecules.

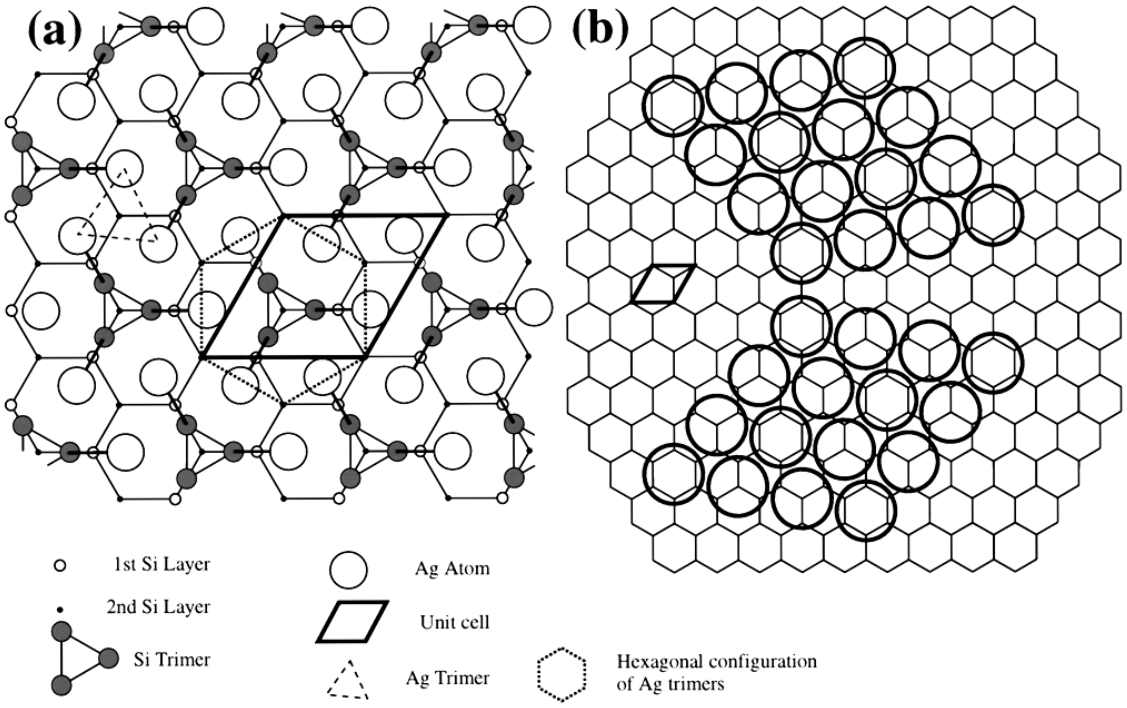

Figure 2-39. (a) Model of ($\sqrt{3}$x$\sqrt{3}$) reconstruction. The rhombus unit cell encloses an Ag 'trimer' and a Si 'trimer'. **(b)** Position of C_{60} (circles) on Ag-Si(111)-($\sqrt{3}$x$\sqrt{3}$)R30^o. Molecules sit on a Si 'trimer' (the hexagon) or on an Ag 'trimer' (the vertex). (Figure from [27])

Experiments revealed that molecules self-assemble in ordered domains (Figure 2-40), with ($\sqrt{21}$x$\sqrt{21}$)(R±10.9^o) symmetry [28, 29]. C_{60} molecules also self-assemble into (3$\sqrt{3}$x3$\sqrt{3}$)(R30^o) domains, but in this case the molecules sit mainly at asymmetric sites which leads to a high density of defects [28, 29].

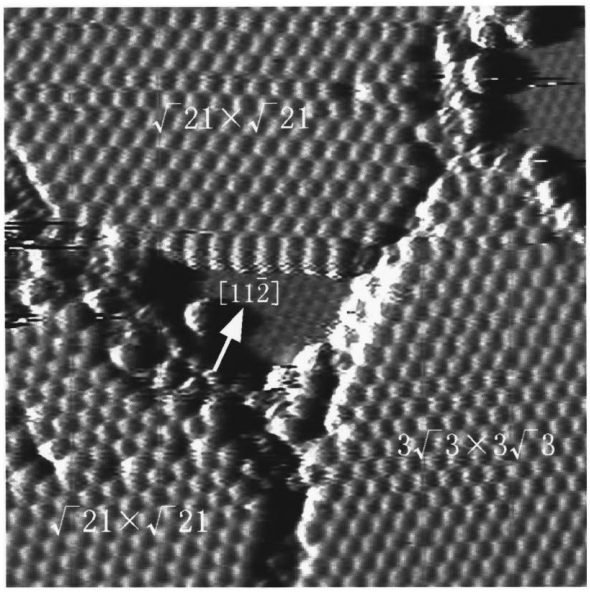

Figure 2-40. Ordered domains formed by ~0.8 monolayers of C_{60} on Ag-Si(111)-($\sqrt{3}$x$\sqrt{3}$)R30°. (Figure from [29])

For C_{60} molecules deposited on Ag-Si(111)-($\sqrt{3}$x$\sqrt{3}$)R30°, the intermolecular spacing between molecules is ~1 nm [27-29]. Separation between adjacent molecules varies slightly due to the tensile or compressive strain fields caused by missing molecules or by the surface energy landscape. If the molecules are adsorbed on Ag terraces they are free to rotate [29]. Only at low temperature is rotation suppressed. Due to the very small amount of charge transfer between molecules and substrate, C_{60} molecules are weakly bound to Ag-Si(111)-($\sqrt{3}$x$\sqrt{3}$)R30°, but the interaction type is not pure van der Waals. On the other hand, C_{60} molecules are strongly bound to substrate steps. The binding energy of a single molecule on the Ag-Si(111)-($\sqrt{3}$x$\sqrt{3}$)R30° surface has been determined from the desorption temperature to be 0.8-0.9 eV [28].

Molecular islands are not perfectly assembled. Tensile or comprehensive strain and surface corrugation, lead to defects which result in missing molecules (Figure 2-41). The distance between two adjacent molecules varies (Figure 2-41b), straining the lattice.

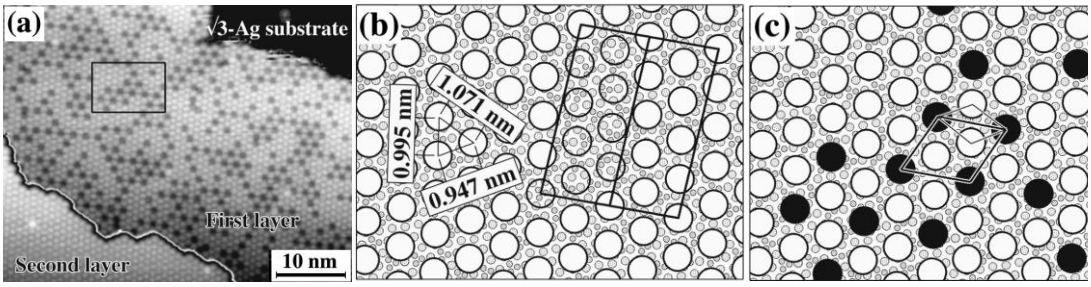

Figure 2-41. (a) Experimental image of C_{60} layers showing the defect distribution. **(b)-(c)** Diagram of the first layer indicating the spacing between molecules and the periodicity of defects, respectively. **(c)** is a schematic representation of the rectangle marked on (a). The two parallelograms on (c) show a local short range periodicity of the defective sites. (Figure from [28])

2.9.2.6 C_{60} Molecule Manipulation on Si(100)-(2x1) with STM

Beside molecular organization, "orbital imaging" and single molecule spectroscopy, controlled manipulation of C_{60} has also been achieved with STM. By controlling the tunnelling current, molecules can be pushed, pulled or rolled [115, 116]. In particular, C_{60} molecules were manipulated [117-119] on Si(100)-(2x1) and Si(111)-(7x7) surfaces at room temperature [120, 121]. In order to move them, a threshold force must be reached to break the chemical bonds with the substrate [115, 122].

Manipulation consists of a few simple steps [115]. The STM tip is placed close to the target molecule and tip-sample separation is reduced by decreasing the voltage and/or increasing the current, maintaining active the feedback response. The tip is then moved in the chosen direction, usually in sub-angstrom steps, the height being adjusted after each step by the feedback control.

Using attractive and repulsive manipulation, molecules can be pushed or pulled or moved by sliding, rolling or hopping (Figure 2-42). Details of this complex translation-rotation displacement can be interpreted from tip trajectory traces. In the attractive regime (Figure 2-42a), the tip travels toward the target molecule, then follows the contour of the molecule, due to the feedback control. The moment when the molecule is attracted to the tip is marked by a sharp increase in the line profile height. The molecule will be pulled in the direction of the tip. Then the tip continues

its trajectory along the molecule profile until C_{60} is attracted again and moves forward.

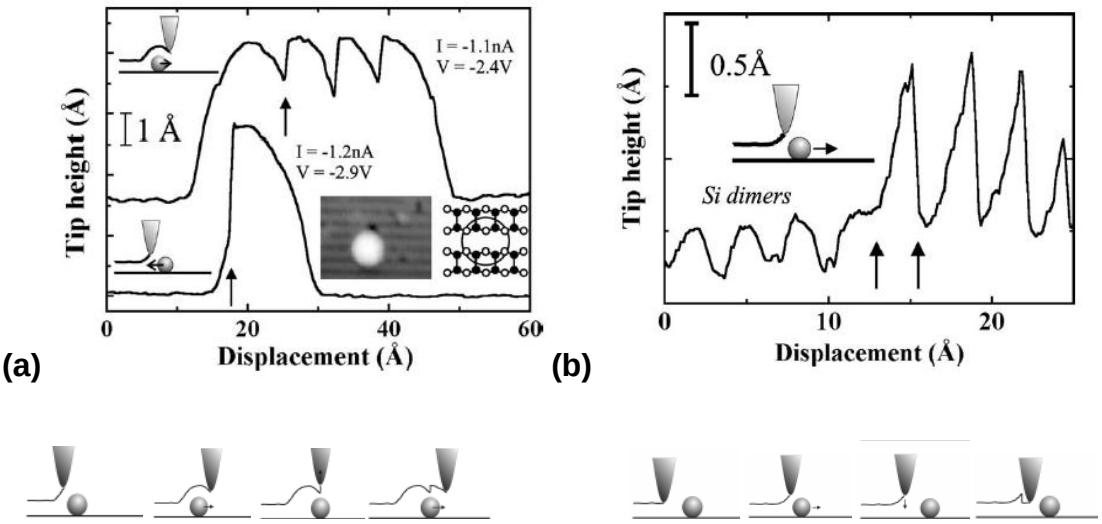

Figure 2-42. Line scan showing attractive **(a)**, and repulsive **(b)** manipulation. The first arrow indicates the moment when the tip approaches the molecule and the second arrow the point where the molecule is moved. In the repulsive mode (b), the tip is placed near the target molecule, within 2 nm distance. The tip position is lowered by modifying the current set-point or the bias voltage. Next, the tip follows the molecule profile till the point where the molecule is pushed away by the tip interaction. At this moment, an increase is recorded in the tip-sample separation profile. The feedback loop then drives the tip towards the sample surface. (Figure from [115]).

By exploiting the SPM-induced manipulation, molecule-substrate interactions and intermolecular interactions can be studied [120]. Short range forces, such as chemical interaction with the tip, are responsible for attractive interaction, while electrostatic and van der Waals forces make only a very weak contribution. The maximum distance for the attractive interaction is suggested from the transition from repulsive to attractive forces. Both types of interaction occur for both positive and negative voltages. Most manipulation experiments have been done in the repulsive mode, while the attractive mode has proven to be random, and occasionally successful, possibly reflecting tip atomic structure [115]. Tip height variations are recorded along the manipulation line scan.

Making use of the manipulation method described above, C_{60} molecules were translated on Si(100)-(2x1) [120] parallel to the dimer rows (Figure 2-43a-c) or perpendicular to the rows (Figure 2-43d-e). Manipulation along the rows had a high

success rate of ~95 %. The potential energy landscape of the surface in this direction facilitates overcoming the diffusion barrier, producing controlled, unidirectional movement. Manipulation across rows produced a success rate of only ~15 %.

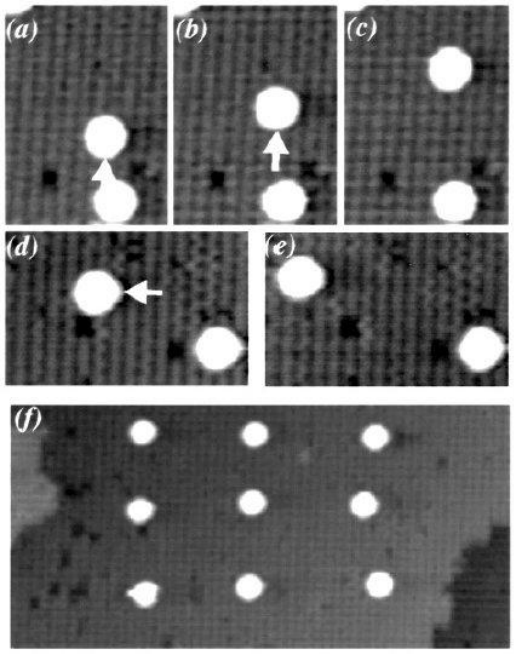

Figure 2-43. Manipulation of C_{60} on Si(100)-(2x1). **(a)-(c)** Parallel to the dimer rows, **(d)-(e)** Perpendicular to the dimer rows, **(f)** An array of C_{60} formed by positioning individual molecules. The white arrows show the direction of the tip trajectory. **(e)** Indicates a small deviation of the molecule from the perpendicular direction. This lateral displacement from the set trajectory shows the natural trend of the molecule to relax in the potential well along the dimer rows. **(f)** Possibility to form ordered pattern is illustrated, such as molecular arrays, based on the molecule translation along or across the rows of Si(100)-(2x1). Manipulation parameters were -1.0 V bias voltage and 1.0 nA tunnelling current. The imaging was acquired at -3.5 V and 0.1 nA. (Figure from [120])

2.9.2.7 Manipulation of C_{60} Molecules on Si(111)-(7x7) with STM

C_{60} molecules have also been manipulated successfully on Si(111)-(7x7) (Figure 2-44). By means of STM, at room temperature, individual C_{60} molecules were moved precisely from a set position to another predetermined site. The purpose was to clear a specific area on the surface [121] or to create a simpler or a more complex pattern with C_{60} molecules [118, 123].

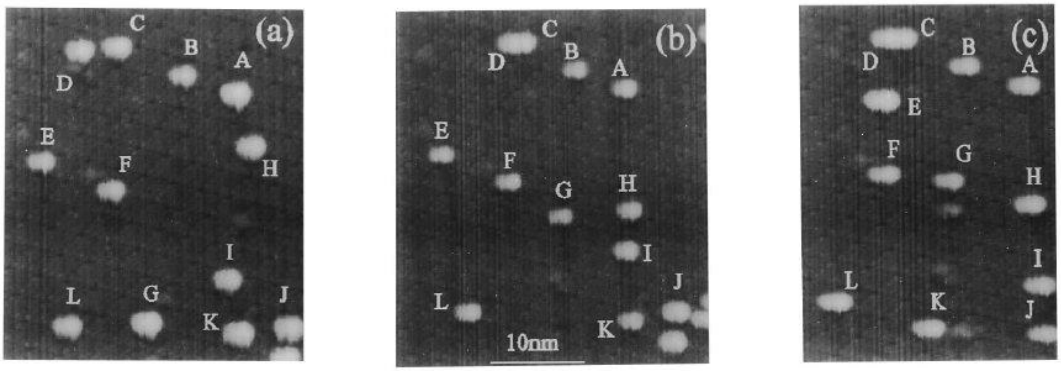

Figure 2-44. Manipulation of C_{60} molecules by "sweeping" method on Si(111)-(7x7). Labels help to track the molecules, showing how their positions changed from the initial scan (a). The pattern was built with five segments in the shape of letter '*S*'. Manipulation parameters: -0.4 V, 4 nA. (Figure from [118])

2.9.2.8 Imaging C_{60} Molecules with AFM

C_{60} molecules have also been imaged with non-contact AFM, both on semiconductors [124] and metals [125]. Molecular resolution was previously observed in non-contact AFM on Si(111)-(7x7) [124], Au(111) [125] or on rutile TiO_2 [126, 127], for example. C_{60} molecules appear as spherical, bright features with a diameter of 1 nm [124]. Lattice spacing within the molecular islands was measured as 1 nm on Au(111) [125].

Molecular resolution was achieved using a thin film of C_{60} on Si(111)-(7x7) and Au(111) (Figure 2-45a,b). Isolated molecules on Si(111)-(7x7) were also resolved individually, but with very poor contrast relative to the (7x7) background [124]. Molecules were imaged as bright protrusions, but the scanning conditions were unstable (Figure 2-45c). Possibly the tip was too close to the surface or molecules, leading to a strong interaction that produced changes in the tip apex. Molecular corrugation measured in both cases, C_{60}/Au(111) and C_{60}/Si(111)-(7x7), was 30-40 pm.

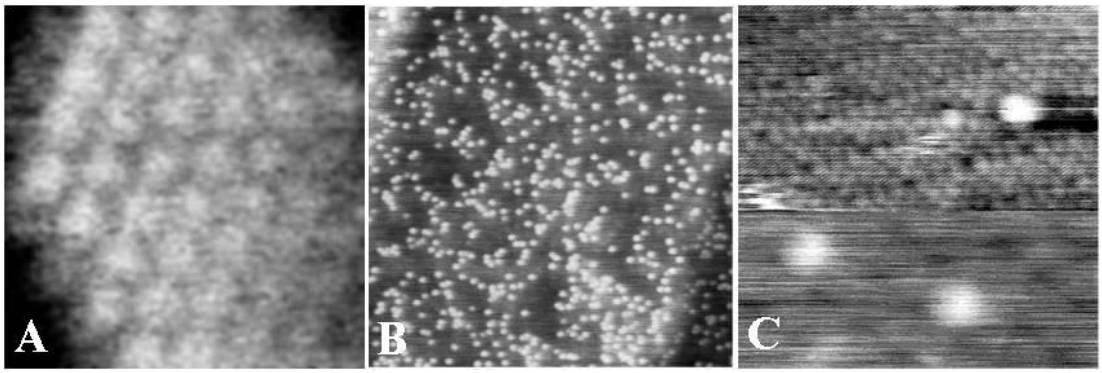

Figure 2-45. Individual C_{60} molecules resolved with non-contact AFM on Au(111) **(a)** and Si(111)-(7x7) **(b-c)**. (Figure (a) from [125] and (b-c) from [124])

2.9.2.9 Sub-molecular Resolution of C_{60} Molecules with AFM

Intramolecular contrast of C_{60} molecules using qPlus AFM was only recently achieved [128, 129] on Cu(111) (Figure 2-46a). More than one monolayer of molecules was deposited, and C_{60} molecules were imaged with AFM using a tuning fork sensor, in constant-height mode, at 5 K. AFM measurements revealed a new pattern of intramolecular features, compared to the molecular orbitals usually observed with STM. The structure of the tops of the molecules showed polygons and edges. Pentagon and hexagon rings on the sides of the molecules could not be clearly resolved and appeared as facets. Several different orientations could be observed in relation to neighbouring molecules. To achieve sub-molecular resolution in AFM was very difficult because scanning the molecules at constant-height mostly resulted in manipulating the molecules rather than achieving internal contrast. Repulsive force was considered to be the source for the intramolecular contrast that resulted from the force map recorded on the molecules.

Force spectroscopy measurements (Figure 2-46b) indicated toward Pauli repulsive interaction responsible for intramolecular contrast. Images acquired in repulsive mode enabled high resolution of C_{60} molecules and emphasized their orientation on the surface. Repulsive force recorded between C_{60} molecules and the Cu-terminated tip, varied across the molecule. The force was dependent on positions of C atoms, with the smallest values recorded in the centre of the pentagonal or hexagonal rings (Figure 2-46b, red curve).

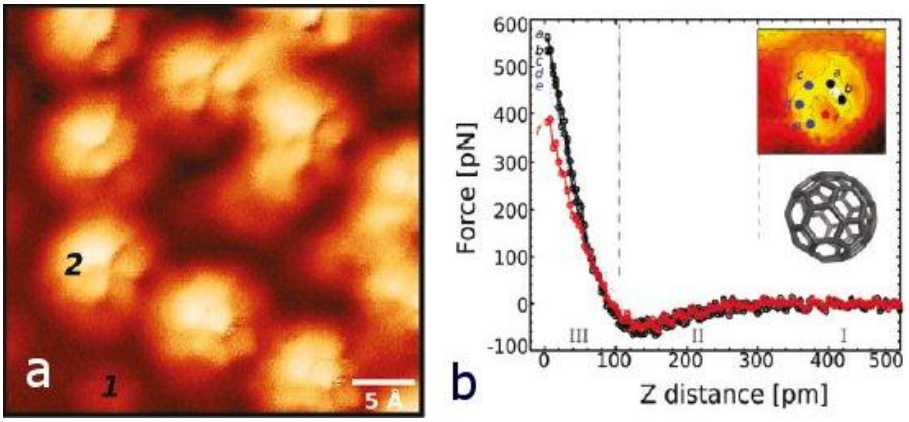

Figure 2-46. (a) Sub-molecular contrast of C_{60} using qPlus AFM, in constant-height mode, at 5 K. Only intramolecular structure of C_{60} molecules in the second layer (2) could be resolved. **(b)** Force spectra acquired on several points on a single C_{60} molecule. (Figures taken from ref. [128])

2.9.2.10 Bond Discrimination in C_{60} Molecules with AFM

Gross *et al.* used a carbon monoxide (CO)-functionalized tip in qPlus AFM, constant-height mode, to image the bond structure of C_{60} and other polycyclic aromatic molecules [130]. Bond order and length in a C_{60} hexagon could be distinguished based on the Pauli exclusion principle [131]. The proposed mechanism for contrast formation was founded on this principle. Due to Pauli repulsion, increased local electron density produced enhanced brightness for bonds of higher order. Bond order discrimination is essential to understand chemical structure and reactivity in organic molecules. Bond length, which decreases with increasing bond order [132] plays a determining role in bond discrimination.

For a C_{60} molecule adsorbed with a hexagon prone to the Cu(111) surface, using AFM Gross *et al.* observed two alternating types of bonds with different lengths in the hexagonal ring parallel to the surface (Figure 2-47), (double bonds are shorter than single bonds). DFT simulations performed by Gross *et al.* showed that the tilt of the CO molecule from a vertical adsorption position on the tip, led to apparent experimental bond lengths much larger than the theoretically predicted values.

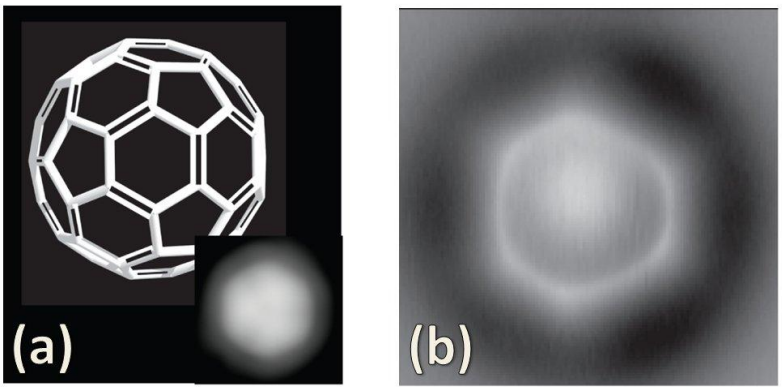

Figure 2-47. Bond discrimination in a hexagon ring of a C_{60} molecule using AFM. **(a)** Stick model of the C_{60} cage showing single and double bonds. Inset: STM image of the C_{60} molecule which confirmed its three-fold orientation on Cu(111). **(b)** AFM image of the same C_{60} molecule with two types of bonds in the hexagon, shorter bonds alternating with longer bonds. (Figures from [130])

2.9.2.11 "Sub-atomic" and Sub-molecular Imaging of SPM Tip

Franz Giessibl and co-workers performed experiments using frequency modulation AFM and dynamic STM to achieve high resolution of "sub-atomic" features or atomic orbitals [133, 134]. In the AFM experiment [133], Giessibl *et al.* used a boron-doped (*p*-type) Si(111) sample and a quartz tuning fork with a tungsten tip. Si was first scanned in STM to find large, clean areas of good (7x7) reconstruction. At the same time the tip apex was reshaped by controlled collision with the surface. When clear resolution of Si adatoms was achieved the tip was withdrawn and feedback was switched from tunnelling-current to frequency-shift control. The frequency-shift set-point was then decreased to reach the optimum corrugation for the image. After a few scans, the images showed distinctive features, that is, two maxima per Si adatom (Figure 2-48a).

Due to controlled collisions with the Si surface (in order to gain atomic resolution) it was believed that the end of the tip was covered with a Si cluster pointing toward the Si surface with a single Si atom. The split observed in the Si adatom shape on the surface was interpreted as having arisen from an sp^3 bond of a surface atom imaging the two free bonds of the hybrid orbital of the Si atom on the end of the tip (Figure 2-48b).

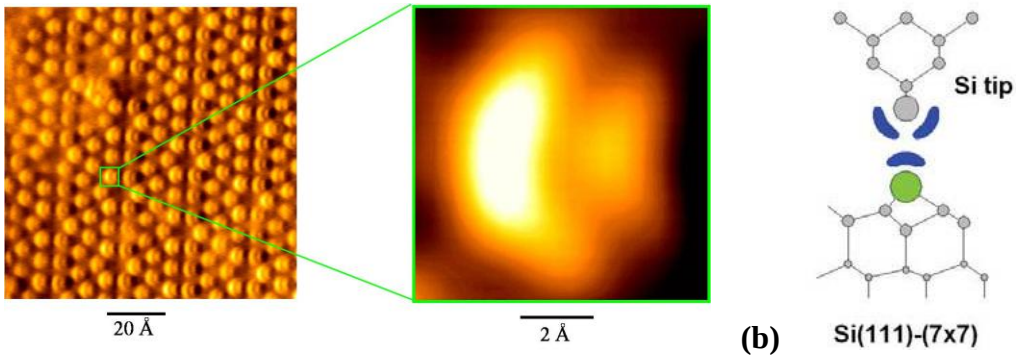

Figure 2-48. (a) AFM image of Si(111)-(7x7) surface. Each adatom exhibits sub-atomic 'double lobe' semispherical features. **(b)** Theoretical model representing the interaction between one sp^3 orbital of a Si adatom and two free, dangling bonds of the Si atom on the tip end. (Figure from [133])

From these experimental data, various theoretical models were proposed for the tip apex. Giessibl *et al.*'s results have been regarded as controversial. For example, the theoretical simulation in Giessibl *et al.*'s publication was contradicted by Caciuc *et al.* in a later publication [135]. They used *ab initio* DFT calculations to look at Si tips of various shapes. It was proposed that the tip described by Giessibl *et al.* is not a realistic model.

Herz *et al.* [134] scanned a Si surface using dynamic STM equipped with a qPlus sensor and employing various tip materials. Very high resolution imaging was achieved with a samarium tip, yielding atomic orbital visualization (Figure 2-49).

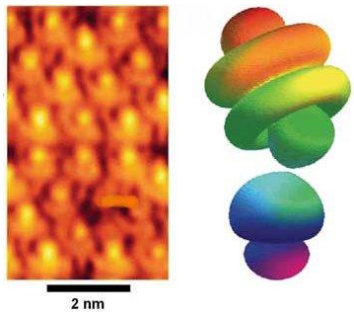

Figure 2-49. Dynamic STM scan of a Si(111)-(7x7) surface imaged with a samarium tip. Sub-atomic features reveal the structure of the samarium *f* orbital tilted at 37°. A schematic model shows the interaction between an *f* orbital and a p_z orbital. As explained by Bardeen [53], both tip and sample contribute to the tunnelling junction. Current recorded is a convolution of the electronic states of the two electrodes. Therefore, the sharp dangling bond of the Si adatoms maps the apex of the tip. (Figure from [134])

The calculations which simulate the interaction between a Si atom $3p_z$ state and a samarium atom with a $4f_z^3$ electronic state accurately predicted the experimental data when the samarium atom was tilted at 37°. The shape of the Si adatom seen in the experimental data was actually due to the samarium *f* state on the tip.

Tip functionalization with CO molecules demonstrated high resolution imaging and new sub-molecular features in STM and AFM [131, 136]. However, precise orientation and detailed characteristics of the probe molecule have not been achieved. Schull *et al.* [36, 37] demonstrated that Au/Cu adatoms or clusters deposited on surfaces may resolve C_{60} molecules adsorbed on the STM tip. They resolved two-fold and three-fold symmetry of the on-tip C_{60} via constant-current 'reverse' imaging (Figure 2-50a,h). Single bond orientation was also reported (Figure 2-50b). By applying a high current set-point, orientation of the on-tip C_{60} molecule could be changed (Figure 2-50c-f).

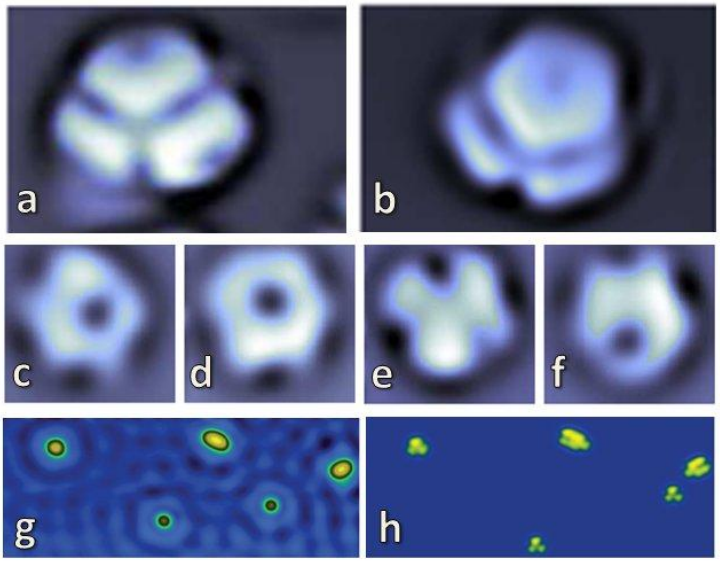

Figure 2-50. STM images of on-tip C_{60} molecule resolved by Au/Cu adatoms. **(a)** Hexagon down orientation of on-tip C_{60}. **(b)** Single bond down orientation of C_{60} adsorbed on the tip. **(c-f)** Various orientations of on-tip molecules imaged after controlled rotation by applying a high set-point current. **(g)** Adatoms imaged with a metal tip. **(h)** The same adatoms imaged with a C_{60} tip, showing three-fold symmetry. (Figures from [36, 37])

2.9.2.12 Manipulation of C_{60} Molecules using AFM

AFM is a promising tool for controlled manipulation of molecules. Mativetsky *et al.* [125] and Loske *et al.* [126] reported the first manipulation of C_{60} at room temperature. Hexagonal islands of C_{60} have been reshaped on Au(111) [125] by removing edge molecules with every scan across. Removal of molecules was considered to be tip-induced. The remaining molecules diffused and rearranged into close-packed islands. At the same time, the hexagonal network symmetry was preserved. Loske *et al.* [126] observed island manipulation on rutile TiO_2 substrate. By successive scanning over the same area, edge molecules of a C_{60} island were driven to diffuse to nearby islands. Thermal effects were considered to support the manipulation process, but the mechanism is not clearly understood.

Images of consecutive scans over the same island with non-contact AFM show that with every scan a number of molecules are stripped from the island (Figure 2-51). For this reason, the original number of molecules in island, 19, was reduced gradually to 18, then 16, 14, and finally 7 in the last image. The manipulated island changed size and shape, taking the form of a hexagon, triangle, rhombus, or circle. The new shape was related to the number of molecules remained in the island which self-assembled after each scan. The manipulation is not the result of spontaneous dissociation, but was induced by the tip.

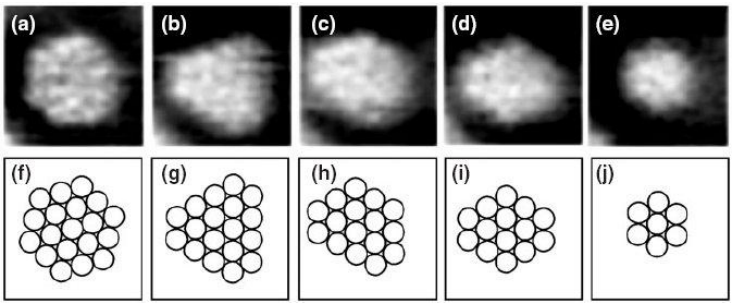

Figure 2-51. Close-packed island of C_{60} on Au(111). **(a-e)** Consecutive scans at room temperature with non-contact AFM. With every scan the molecular island changed its shape after losing a few molecules. **(f-j)** Schematic of the molecular island. (Figure from [125])

Using tip-induced manipulation, it is possible to create holes inside the islands in a centered rectangular superstructure of C_{60} molecules on a rutile TiO_2(110) surface (Figure 2-52). For manipulation of the island the *df* set-point was

decreased stepwise. The tip-sample distance was reduced and the interaction of the tip with the molecular island was sufficiently strong to produce displacement and removal of the molecules.

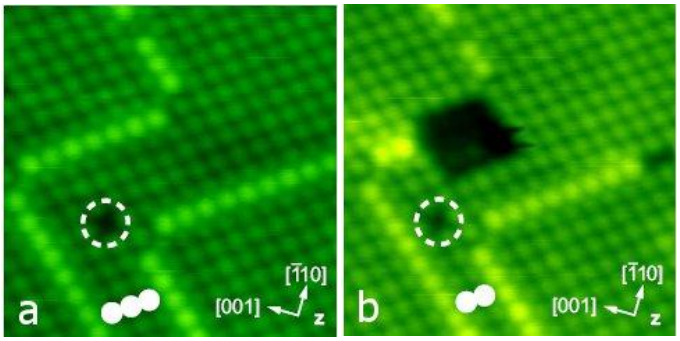

Figure 2-52. Manipulation of the C_{60} inside a close-packed island on rutile TiO_2(110). The dotted circle marks a defect (a missing molecule) used as reference point. Image **(a)** was taken before the manipulation. Image **(b)** shows the result of the manipulation. **(a)** The bright molecular segments are domain boundaries. The three full white circles indicate three molecular rows separating the domain boundaries at the bottom of the image. **(b)** A square hole in the center of the image resulted from removal of twelve C_{60} molecules from the island and five molecules from the domain boundary. At the same time, domain boundaries at the right were shifted by one molecular row, so the separation between the boundaries at the bottom of the image is two molecular rows marked by white circles. (Figure from [126])

2.9.2.13 Force Required to Move an Adsorbate

In AFM experiments, the force required to move an atom or a molecule can be quantified. Ternes *et al.* [137] calculated the force necessary to move an adsorbed Co atom on a Cu(111) surface, and found that a lateral force of 17 pN was in principle responsible for the manipulation process, independent of vertical force. This result contrasted with the manipulation procedure proposed by Sugimoto *et al.* [18], who found that vertical force was responsible for moving Si adatoms on a Si(111)-(7x7) surface.

In order to determine the lateral force, the potential energy *U(x,y,z)* was differentiated in the *x* direction. The differentiation yielded the lateral force F_x (Figure 2-53). (The potential *U(x,y,z)* had been calculated by integration of F_z in the *z* direction.) When the tip was directly above the adsorbate, the lateral force F_x was

zero. As the tip moved away from the adsorbate, the lateral force F_x increased to a maximum and decreased again to zero with increasing the tip-sample separation. Ternes *et al.* concluded that the force required to move an adsorbate was strongly dependent on the nature of adsorbate-substrate interaction and on chemical bonding.

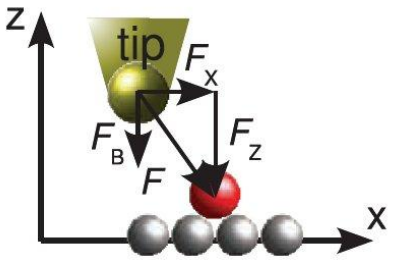

Figure 2-53. Interaction between an AFM tip and an adsorbate on the surface. F is the total force. F_x is the lateral force in the x direction. F_z is the remaining vertical force after the background force F_B was removed. (Figure from [137])

3 Experimental Methods

3.1 Variable Temperature STM/AFM System

A variable temperature (VT) Omicron system (Figure 3-1) was used for imaging, spectroscopy, and manipulation of various organic molecules on semiconductor and metallic surfaces by means of STM. *In situ* preparation of Si and Au surfaces, as well as Ag and organic material (C_{60}, ionic liquid) deposition, was achieved using this system.

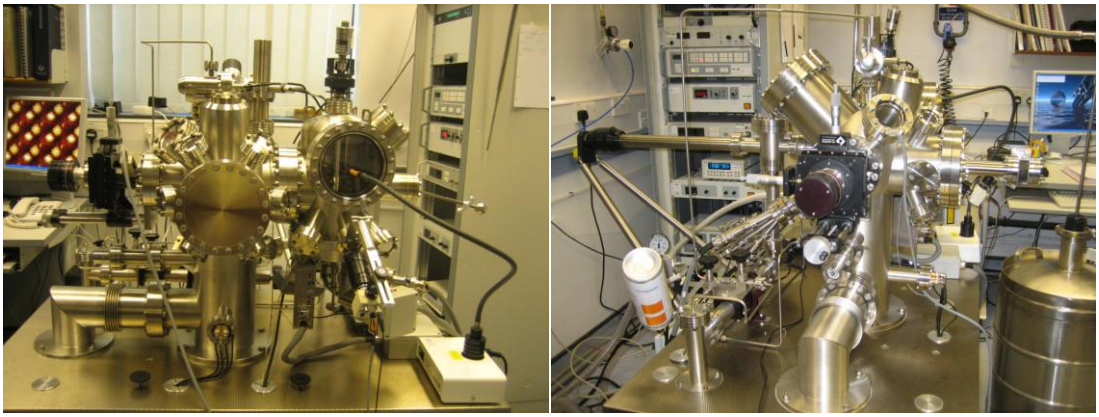

Figure 3-1. Omicron UHV VT AFM set-up (front view and side view). The system consisted of a transfer chamber and an STM/AFM chamber. To achieve UHV, the VT system was fitted with four pumps through the transfer chamber.

The VT STM/AFM system consisted of two main vacuum chambers. Fitted with a turbo molecular pump and an ion pump, the system is capable of attaining a pressure of $\leq 10^{-10}$ mbar. The main chamber enabled transfer and manipulation of the sample, with the help of a sample manipulator, mounted on the left-hand side of the set-up (Figure 3-1). A sister chamber supporting the scanning probe microscope was attached to the main chamber. On the VT Omicron system, measurements were run at room or low (~80 K) temperature. Sample transfer into the system increased the microscope chamber background pressure ~10^{-8} mbar (without

baking the transfer arm), but within a few hours after sample or probe transfer, the pressure returned to UHV conditions.

For successful high-resolution scanning probe microscopy, a high quality vibration decoupling system is essential. In this system, the STM/AFM base plate was suspended by four soft springs which were protected by surrounding columns. The resonant frequency of the spring suspension system was about 1 Hz. Vibrations of the suspension system were damped using an eddy current mechanism. For this, the STM/AFM base plate was surrounded by a ring of Cu plates, which passed down between permanent magnets.

The slip-stick motor was controlled by a handset and is monitored using a video camera which permitted observation of the movement of the tip. A video camera was set to view the sample. Tip and sample were mounted in the STM/AFM head (Figure 3-2).The tip was approached until its reflection was seen in the sample surface. This was the coarse approach. The fine approach was automatically made by the slip-stick motor until a tunnelling current was detected.

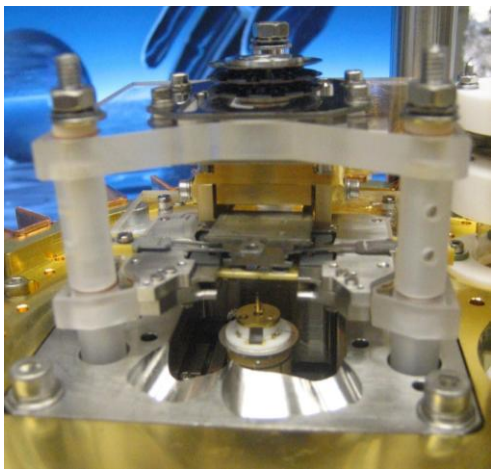

Figure 3-2. The head of the STM/AFM. The tip holder was mounted on the piezo tube scanner and the sample holder was inserted into the sample stage.

During measurements, the computer read the tunnel current from a pre-amplifier (an *I-V* converter) attached to the tip. The computer applied voltages to the piezotube to adjust the tip-sample separation and so keep the current constant. The Matrix software recorded and processed the signals to form an image based on the movement of the tip piezo as it scanned the sample.

3.1.1 Sample Cooling Procedure for VT STM

The Omicron VT STM/AFM was equipped with a continuous flow cryostat that allowed cooling of the sample to 80 K. This temperature was attained using liquid nitrogen. The dewar was connected to the cryostat through a transfer tube (Figure 3-3). This quantity of liquid nitrogen was sufficient to support ~50 h of low temperature operation at ~80 K.

Valve A on the transfer tube (Figure 3-3) allowed control of nitrogen flow. Liquid nitrogen exited from the cryostat through a metallic bellows to a rotary pump, which pumped out the nitrogen gas. The metallic bellows was connected to the pump bellows by a gas flow control block (valve B, Bypass and barometer).

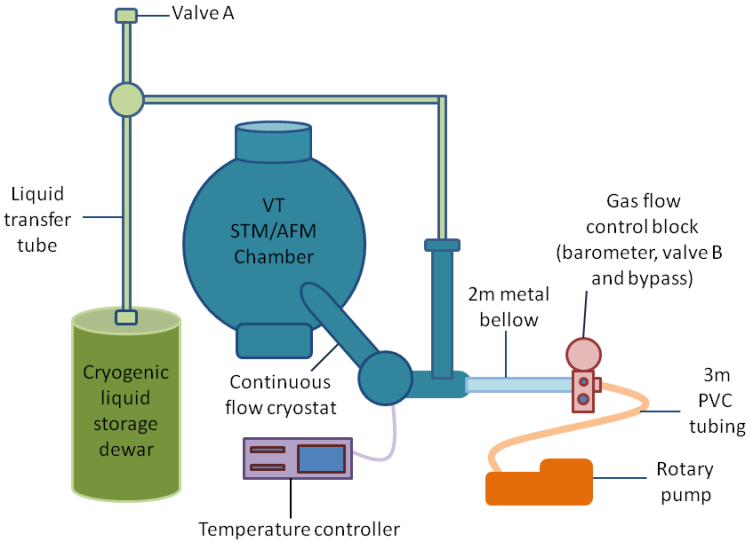

Figure 3-3. Schematic set-up for sample cooling on the VT Omicron STM/AFM.

Thermal transfer from the cryostat to the sample was realized by a Cu braid and a mobile cooling block. The reference temperature set by an integral counter heating element was read from the temperature controller. The heating element was mounted with a Si diode at the top of the cryostat and was used as

the temperature sensor for the flow cryostat. For direct current sample holders, at 80 K for example, there was a temperature offset of 15-20 K between the temperature measured by the silicon diode at the sample stage, the real temperature of the sample being higher. Flow cooling reduced usage of cryogenic liquid and made it possible to cool the sample to any temperature between room temperature and 77 K. A major disadvantage of the VT system was that the tip remained at room temperature.

3.1.2 Tip Preparation-Electrochemical Etching

Imaging using scanning probe microscopes has proven difficult in the effort to acquire high resolution images of surfaces. Therefore, strategies have been developed to improve the quality of tips and to optimize conditions for preparation, treatment, and conditioning of probes.

For experiments on the VT system, tungsten tips were prepared using electrochemical etching. Basic components of the etching system were a 2-7.5 M KOH or NaOH solution and an electronic circuit. A tip wire served as the anode, and a stainless steel ring, closing the circuit was the cathode. Both electrodes were immersed in electrolyte.

For tungsten, a direct current etch proved favourable because this yielded a hyperboloid tip. Moreover, with the direct current method the amount of current fluctuation can be considerably reduced [138]. To optimize the result, the current was maintained at the initial value during the process. A sudden decrease in the current was recorded prior to the “drop-off” [139]. Voltages in the range of 6-13 V were applied to the electrochemical system, since lower or higher values caused instabilities that lead to poor definition of the tips, or to bubble formation.

At the instant of tip breaking, the electric circuit was shut off so as to prevent further etching, which would have caused blunting of the tip. Because of the criticality of timing, an automatic cut-off circuit with a feedback signal was employed in order to synchronize current shut-off with the dropping moment [139]. The etching mechanism always leaves residuals and contaminants on the freshly

formed tip interface, so, at the end of the process, tips were rinsed in de-ionized water and cleaned in acetone or methanol in an ultrasonic bath.

The result of the tip fabrication methods outlined above was not always optimal. In many cases, the procedure did not leave an atomically sharp tip apex, so imaging with high resolution was not immediately possible with a freshly made probe tip. The tip produced by electrochemical etching was often covered by a set of miscellaneous contaminants including oxides and hydrocarbons [140-142]. These were removed before actual tunnelling to assure rapid success in scanning surfaces at nanoscale. An oxide layer increases the tunnelling apparent barrier height and represents a crash danger for the tip before detecting the tunnelling current in the barrier region. Moreover, because of complex electrical characteristics abnormal instabilities in the current signal are recorded and this makes imaging hard to achieve. Therefore, after the etching process, to clean the tip, voltage pulses were applied between tip and sample [138, 143-149] or tip-substrate controlled collisions [51, 138] were employed during scanning.

3.1.3 Sample Preparation in VT System

3.1.3.1 Si(111)-(7x7)

The silicon wafers used for the experiments had the following characteristics: *p*-type semiconductor, boron doped, 0.01-0.02 Ωcm, 1x10 mm^2 laser cut. Prior to their introduction to UHV, to remove contaminants, Si samples were sequentially ultrasonicated for a few minutes in three different solvents: acetone, methanol, and isopropanol.

Sample holders were degassed and flashed prior to mounting. The resistance for a Si sample mounted on the holder was of the order of tens of ohms. Once introduced in UHV, the Si was left to degas overnight by direct heating at 600^o C. This temperature caused the sample to glow a dark red at 0.6-0.8 A and 4.5-5.0 V. The pressure was maintained in the low 10^{-10} mbar range, never increasing above the low 10^{-9} mbar during flashing.

A flash annealing procedure was used to produce the (7x7) reconstruction [46, 47, 51, 150, 151] and involved heating the sample for 10-20 seconds at 1200^{o} C (a number of times). Then the Si was maintained at 600-700^{o} C for a few minutes. Cooling was carried out over a period of 5-10 min, since rapid cooling would have led to incomplete and poorly ordered reconstruction of the surface. For new samples, a lower flashing temperature was initially used, usually corresponding to 3.2 A and 5.5 V. The pressure was maintained in the 10^{-10} mbar range. When the pressure recovered and the sample temperature was close to room temperature, STM scanning was started.

3.1.3.2 Ag-Si(111)-(√3x√3)R30^{o}

Ag deposition was carried out by thermal evaporation in UHV from a crucible using an Omicron evaporator EFM 3T. Ag was evaporated onto a Si(111)-(7x7) reconstructed sample. In order to achieve the (√3x√3) reconstruction, the Si surface was maintained at 450-550^{o} C during evaporation [150-154].

Ag atoms which reach the substrate arrange themselves into a (√3x√3) reconstruction. The flux of the evaporated material was monitored. After three minute deposition time the sample temperature was slowly decreased to room temperature. The pressure did not rise above ~2.0x10^{-9} mbar during deposition. When the pressure was restored to 10^{-10} mbar, data acquisition was initiated.

3.1.3.3 C_{60} Molecule Deposition

An Omicron EFM 3T evaporator was used to deposit C_{60} on Ag-terminated Si surfaces. Compared to metal evaporation, the deposition of organic materials requires lower voltages and currents, due to the lower sublimation temperature. During the 13 min deposition, pressure in the preparation chamber was kept in the low 10^{-9} mbar range. When the base pressure in the system returned to ~2.0x10^{-10} mbar, the experiment was started.

3.2 Low Temperature System

3.2.1 LT System Set-up Details

The low temperature (LT) Omicron STM/AFM (Figure 3-4) was a commercial system, especially designed for very sensitive experiments at nanoscale. Imaging, spectroscopy and manipulation of C_{60} molecules were performed at 77 K using dynamic STM and qPlus AFM.

The system had two main vacuum chambers: the preparation chamber and the LT chamber. A long travel automated manipulator allowed the transfer of tips and samples between the two chambers. The preparation and LT chambers were separated by a gate valve. Vacuum in the chambers was achieved using a turbomolecular pump.

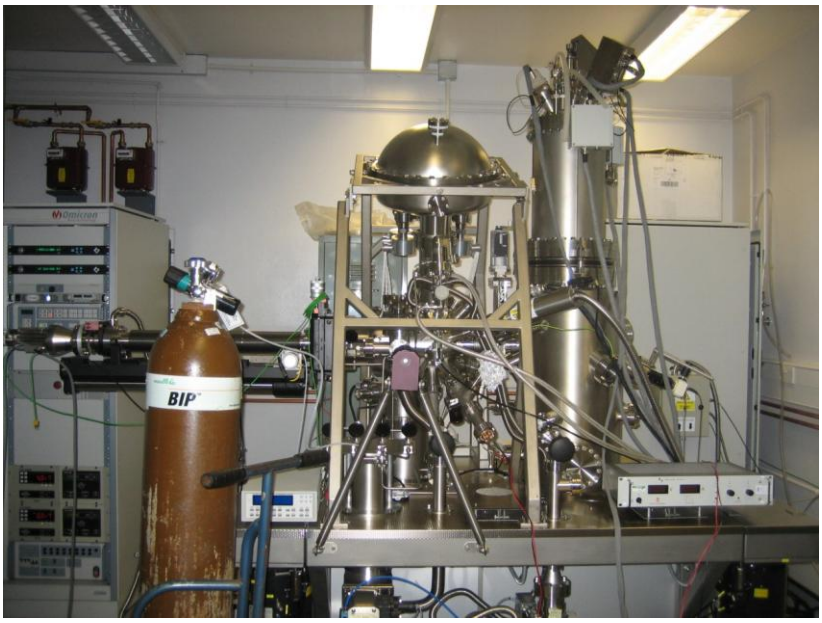

Figure 3-4. Omicron LT STM/ qPlus AFM.

Each chamber was equipped with an ion pump and a titanium sublimation pump to maintain vacuum. Two ion gauge devices monitored the vacuum in the two chambers. Base pressure in the LT chamber was $\leq 1.0 \times 10^{-11}$ mbar, while in the preparation chamber it was $\sim 1.0 \times 10^{-10}$ mbar.

A fast lock entry was attached to the preparation chamber. Through the load lock, the tips and sample were easily transferred in and out the system without

breaking the vacuum. Sample preparation took place in the preparation chamber. Samples were annealed in the manipulator head by direct heating. In case of sample degassing, which required a few hours, the manipulator was cooled to prevent a rise in LT temperature. The cooling procedure for the manipulator was the same as that used on the VT system (Section 3.1.1).

The LT chamber contained two cryogenic baths: the inner and the outer cryostat. The STM/AFM stage was hanging by the inner cryostat and was in direct mechanical and thermal contact with it. Each cryostat was fitted with a 60^{o} rotatable Cu cylinder that behaved as a shield and allowed access to the SPM stage when rotated. During the measurements, both shields were kept closed. In this fashion, temperature was maintained and the sample remained uncontaminated for weeks. The whole system was levitated on five air legs.

In experiments run on the LT system, commercially-prepared qPlus sensors with tungsten tips were used. Data were recorded using the newest Matrix version, called Twin Custom, which allowed transition from STM to dynamic STM and to AFM within the same application without having to retract the tip or to restart the software.

STM was used in constant-current mode and dynamic STM in constant-frequency mode. In both modes, tunnelling current was monitored as feedback parameter. Additionally, in dynamic STM, the tuning fork was oscillated and the frequency shift was measured using a frequency modulation method. During measurements the tip was continuously vibrated, driven by controlled excitation in dynamic STM and most of time by "self-excitation" in STM. The tip was vibrated in dynamic STM at constant amplitude, at its resonant frequency. A typical value for the resonant frequency of this sensor was 22.8 kHz, and the measured Q was ~10000. Imaging in dynamic STM was done in attractive mode with a measured frequency shift in the range of -30 to -150 Hz. During experiments, a positive bias voltage was used for both STM and dynamic STM, imaging the empty states of the sample.

A LabView program written by Prof. P. Moriarty was used to determine the frequency f_0 for which the amplitude peak was maximal (Figure 3-5). The

program also calculated and displayed the quality factor *Q* of the sensor. A slip-stick motor was used to mechanically excite the sensor. The sensor behaved as a harmonically-damped oscillator. The response was transformed to Fourier space and yielded a Lorentzian function. By fitting this function the resonant frequency and quality factor were extracted.

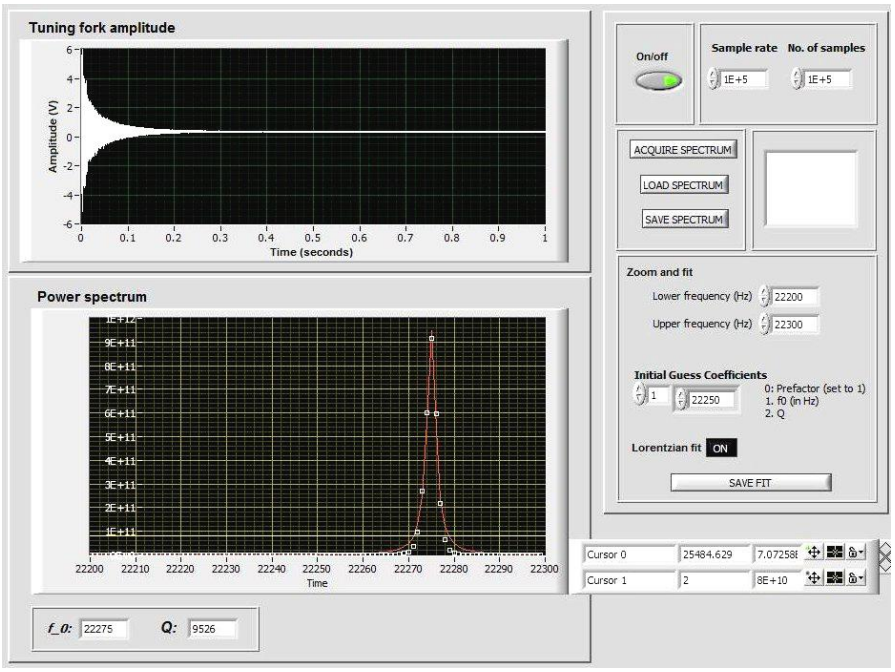

Figure 3-5. In-house LabView software used to measure resonant frequency, f_0, and quality factor, *Q*, of tuning fork (f_0 = 22275 Hz. *Q* = 9526).

The direct switch from dynamic STM to AFM allowed the user to image the same place on the surface within the limit of low thermal drift/creep. Before transfer to AFM the scan speed was considerably reduced. The scan angle was modified to reduce surface tilt. This was essential due to the slow feedback response in the AFM. Scan size was decreased because scanning was very slow for large images. After switching to AFM mode, the bias voltage was slowly reduced to 0 V (20 mV/sec) and the frequency shift set-point was increased in magnitude until regular features were observed. AFM images were recorded using frequency modulation, at constant amplitude, in the attractive regime at 0 V bias voltage.

3.2.2 Sample Preparation in LT System

3.2.2.1 Si(111)-(7x7)

Si samples used in the low temperature Omicron system had the same characteristics as the samples used for room temperature experiments (Section 3.1.3.1). The size was bigger (3x10 mm^2) and the sample was mounted on plates especially designed for the LT system. Samples were introduced into the preparation chamber via the fast entry lock and degassed a few hours in the manipulator. The Si sample was outgassed, during which it glowed dark red. For degassing the sample, the manipulator was cooled down by a liquid nitrogen flow. When the pressure in the preparation chamber was stabilized at ~$2.0x10^{-10}$ mbar the sample was flashed.

3.2.2.2 C_{60} Molecule Deposition

A homemade thermal evaporator was used to sublime C_{60} in the LT system. C_{60} molecules were contained in a tantalum pocket. The two ends of the pocket were in contact with two electrodes. A C-type thermocouple was attached to the metallic pocket and allowed monitoring of the deposition temperature. The evaporator was connected to a source able to supply a current of 20 A.

Before the first deposition, the source and the molecule pocket were degassed at a temperature lower than C_{60} sublimation for many hours, until the pressure decreased to ~$2.0x10^{-9}$ mbar. For the deposition of C_{60} molecules, the metallic pocket was first warmed for 10-20 min. When the pressure in the chamber reached a constant value the deposition was initiated.

4 Study of C_{60} Molecules on Si(111)-(7x7) with Dynamic STM and qPlus AFM

4.1 Introduction

C-Si nanostructures comprise an important research area in fullerene-based science. Applications of C-Si integrated compounds for electronic devices have been numerous [155]. Interest has focused primarily on the control of dimensionality and bonding interactions in C-Si structures, such as C_{60} molecules adsorbed on Si surfaces [156] or Si atoms/clusters attached to a C_{60} cage [106, 157, 158]. In addition, theoretical simulations have been employed to analyze various structures that can be formed with Si_mC_{60} clusters [106, 157-159]. However, to date, the chemical force or the energy potential between Si and C_{60} has not been determined experimentally.

This chapter includes a study of single C_{60} molecules adsorbed on Si(111)-(7x7) at 77 K. Dynamic STM resolved internal features of C_{60} molecules. Direct comparisons with theoretical simulations enabled interpretation of molecular orientation. Individual C_{60} molecules were resolved and manipulated with qPlus AFM. Force of interaction and potential energy between Si-terminated tips and C_{60} molecules were also investigated.

4.2 C_{60} Molecule Imaging using Dynamic STM

Using dynamic STM to study the interactions of molecules with metallic or semiconducting surfaces has been a very important step in the investigation of the spatial distribution of electronic states and of charge exchange in molecule-substrate systems [30, 31]. At low temperatures, dynamic STM can probe individual molecular orbitals giving approximate information on the geometric shape of the molecule and also of its internal structure. Dynamic STM measures the probability density

associated with molecular orbitals whose energy falls within the energy "window" defined by the tip-sample bias voltage.

Charge transfer between C_{60} molecules and substrates, their apparent height on the surface, and the electronic structure of the molecules, strongly depend on the adsorption site, molecular orientation, or bond type [30, 31]. In dynamic STM experiments, molecules appeared with different apparent height and some looked fuzzy, depending upon their orientations (Figure 4-2).

There are three primary sites in the silicon (7x7) unit cell where C_{60} molecules preferentially adsorb (Figure 4-1): (a) the corner hole (*CH*); (b) on top of three Si adatoms and above a rest atom (*R, C*); (c) on three Si adatoms, but not on a rest atom (*M*) [108].

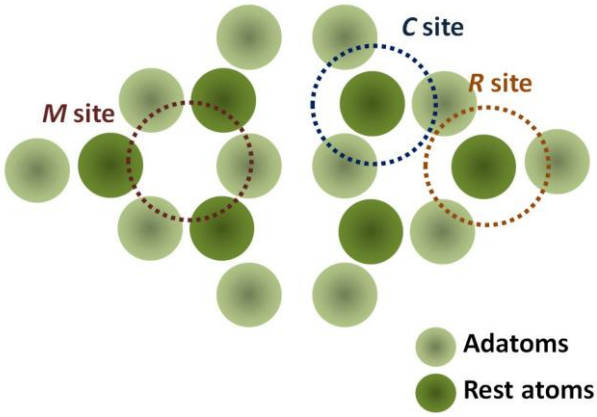

Figure 4-1. Schematic diagram of adsorption sites within a (7x7) unit cell. (Figure reproduced from [108])

In theoretical calculations, Rurali *et al.* concluded that the corner-hole site is the most energetically stable for an adsorbed molecule mainly for geometrical considerations [108]. The corner-hole is a large, symmetric site where the C_{60} molecule can fit in with minimal deformation. In the dynamic STM experiment presented in this section, a few molecules adsorbed at corner holes (Figure 4-2B). Their apparent heights and sizes are visibly smaller than those of molecules adsorbed at other sites, due to the bond formation, which held the molecule closer to the Si atoms [31, 108]. These molecules also looked "fuzzy".

The bonding configuration means that the apparent size of a C_{60} molecule varies from site to site across the surface. For example, the C_{60}–Si bond length is increased at *M* sites. When the C_{60} molecule forms a single C-Si bond with the substrate Rurali *et al.* find that the bond length is ~0.3 nm [108]. This weak bonding configuration could also cause some molecules to be slightly moved, attracted, or repelled by the tip during scanning. As a result, some molecules appear "noisy" or blurred (Figure 4-2).

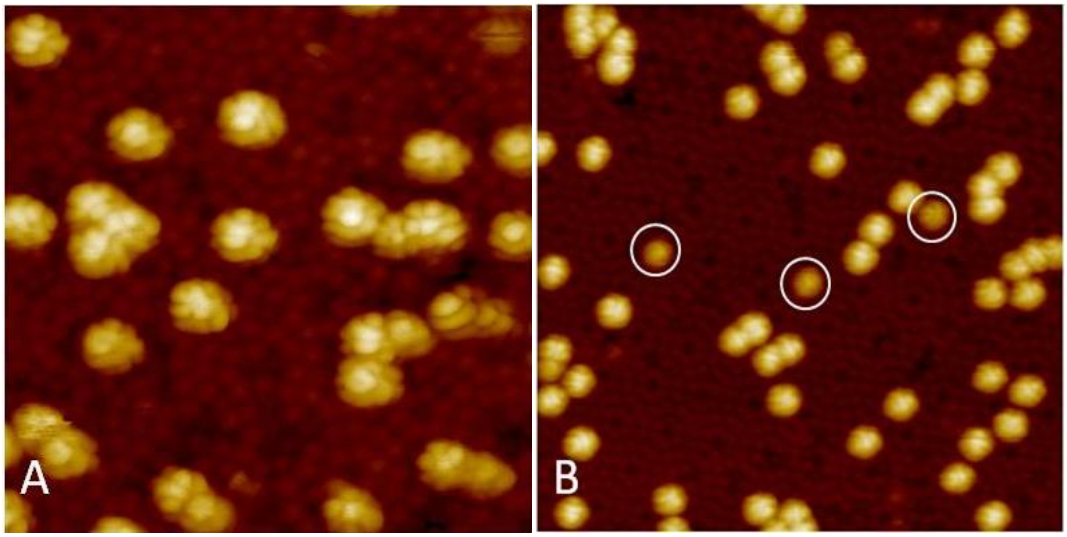

Figure 4-2. C_{60} molecules adsorbed on Si(111)-(7x7). Dynamic STM images recorded with a qPlus sensor at 77 K. **(A)** Intramolecular features show different orientations. V = 2.3 V, I = 2 nA. **(B)** Molecules adsorbed at corner holes have a lower apparent height than the others (marked by white circles). V = 2.8 V, I = 400 pA, A = 6.2 nm. Weakly bound molecules appear fuzzy during scanning.

The vast majority of molecules appeared stable, however, with reproducible intramolecular features, meaning that the Si(111)-(7x7) reconstruction is an appropriate substrate to enable visualization of intramolecular structures. C_{60} molecules undergo deformation from their icosahedral symmetry due to the bonding configuration with Si adatoms. Depending on how many C atoms bind with the substrate, the symmetry of the C_{60} molecule will be lifted in different ways. Due to the relatively large size of the C_{60} cage, however, only a few atoms will be affected by this interaction. Therefore, the degeneracy of energy levels of the molecular orbitals would be only partially lifted, the molecular orbitals preserving most of the characteristics of a free molecule. A detailed study on how the molecules adsorb on

various sites, the number and types of bonds, has been carried out by Rurali *et al.* [108].

The internal structure of a C_{60} molecule adsorbed on Si(111)-(7x7) has been studied previously using STM and theoretical simulations [30, 31]. Many of the results described in this section are consistent with those reported previously (Figure 4-3). However, a number of new, previously unreported, intramolecular features (Figure 4-4:6) have also been observed and have been interpreted using the Hückel molecular orbital theory simulations (Section 2.6).

The shapes and energies of molecular orbitals varied dramatically, depending on interactions in the tip-molecule-substrate system, and displayed a wide variety of internal features. The charge density of C_{60} molecules imaged with dynamic STM was defined by the electronic convolution of tip states and the electronic response of the molecule-substrate interaction. Electrons from the tip tunnel into different electronic states with particular energies. This in principle can reveal the intramolecular structure but it must always be borne in mind that every STM or AFM image – like any image acquired with *any* imaging technique – is a convolution of the imaging system and the object. In this case, the features we observe are due to a convolution of the electronic and chemical structure of the tip with that of the adsorbed molecules. As will be discussed in later chapters, when the tip is terminated by a C_{60} molecule this gives rise to a rich variety of complicated patterns of intramolecular contrast.

Molecular features observed in dynamic STM were not directly related to atomic positions in the C_{60} cage [30, 74]. Consequently, internal structures of C_{60} molecules imaged at positive bias voltage did not depend heavily on the adsorption site, but orientation of the molecule contributed significantly to intramolecular structure measured with dynamic STM [30, 74]. However, due to interaction with the surface, molecular orbitals broaden and overlap. As a consequence, molecular orbitals with energies far from Fermi level also participate in image formation.

Rurali *et al.* [108] used DFT to analyze the behavior of C_{60} on Si(111)-(7x7). STM images have been simulated by varying the bias voltage for molecules

adsorbed at seven different positions on the unit cells, assuming a sharp platinum-iridium tip or a blunt tungsten tip with a Si apex. Hands *et al.* [74] used Hückel molecular orbital theory to calculate the internal structure for HOMO, LUMO and LUMO+1 of C_{60} for three main orientations (a pentagon, a hexagon, and a double bond 'down'). Lee *et al.* carried out bias voltage-dependent calculations for different orientations of C_{60} on Si(111)-(7x7) on the adsorption site *M* [160]. Experimental results with regard to the electronic structure and orientation of C_{60} molecules on Si(111)-(7x7) could be interpreted by direct comparison to theoretical simulations (Figure 4-3:6).

Regardless of the nature of the substrate, experimentally, five main orientations for C_{60} molecules have been observed, relating to binding configurations due to a pentagon, a hexagon, a single bond, a double bond, or an apex atom prone to the surface. The experimental images show features which are in many cases broadly comparable to those observed in the theoretical simulations.

Hückel molecular orbital theory-simulated STM images were employed to understand the experimental dynamic STM images of C_{60} molecules on Si(111)-(7x7). This is a key novel feature of the work here – by forgoing a detailed density functional theory study, at the cost of losing atomistic detail, we can theoretically simulate a wide range of different bonding configurations for comparison with experiment. This has both enabled a study of sub-molecular contrast which has not been reported in the literature, and has allowed us to elucidate the origin of previously observed intramolecular features. As discussed above, the C_{60} molecules exhibited various orientations and symmetries in experiment (Figure 4-3:6). They can adsorb with the symmetry axis perpendicular to the surface, but can also be tilted with respect to, and rotated about, the surface normal. All the features presented in these experimental images arise from the LUMO of C_{60} molecules [74]. A number of the images can be "mapped" to the molecular cage and the orientation can be distinguished from the position of the pentagonal faces (Figure 4-3).

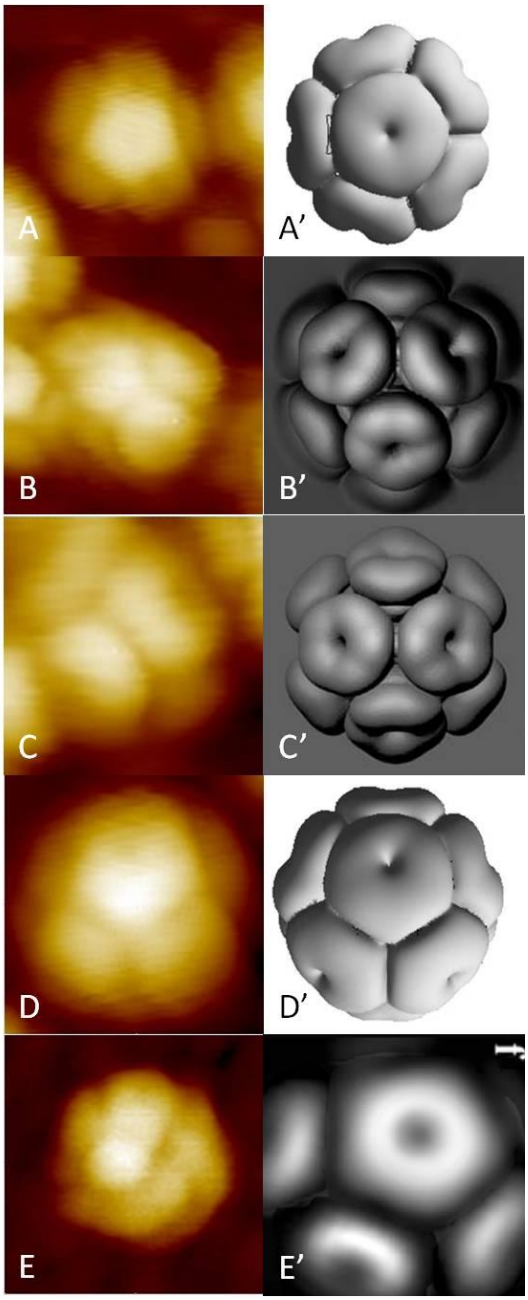

Figure 4-3. (A-E) Dynamic STM images of single C_{60} molecules. Hückel molecular orbital theory simulations showing orientations which produce images closest to those observed in experiment. molecular orientation **(A'-D')**. **(A)** A pentagon prone to the surface, 2.57 V, 200 pA, *A* = 8 nm. **(A')** LUMO. **(B)** A hexagon prone to the surface, 2.9 V, 300 pA. **(B')** LUMO+1 [74]. **(C)** A double bond prone to the surface, 2.9 V, 300 pA. **(C')** LUMO+1 [74]. **(D)** A single bond prone to the surface, 2.57 V, 200 pA, *A* = 8 nm. **(D')** LUMO. **(E)** An apex atom prone to the surface. 2.8 V, 400 pA, *A* = 6.2 nm. **(E')** simulation, 2.5 V [30]. A tip doubling effect can be noticed in all images due to a C_{60} molecule on the tip.

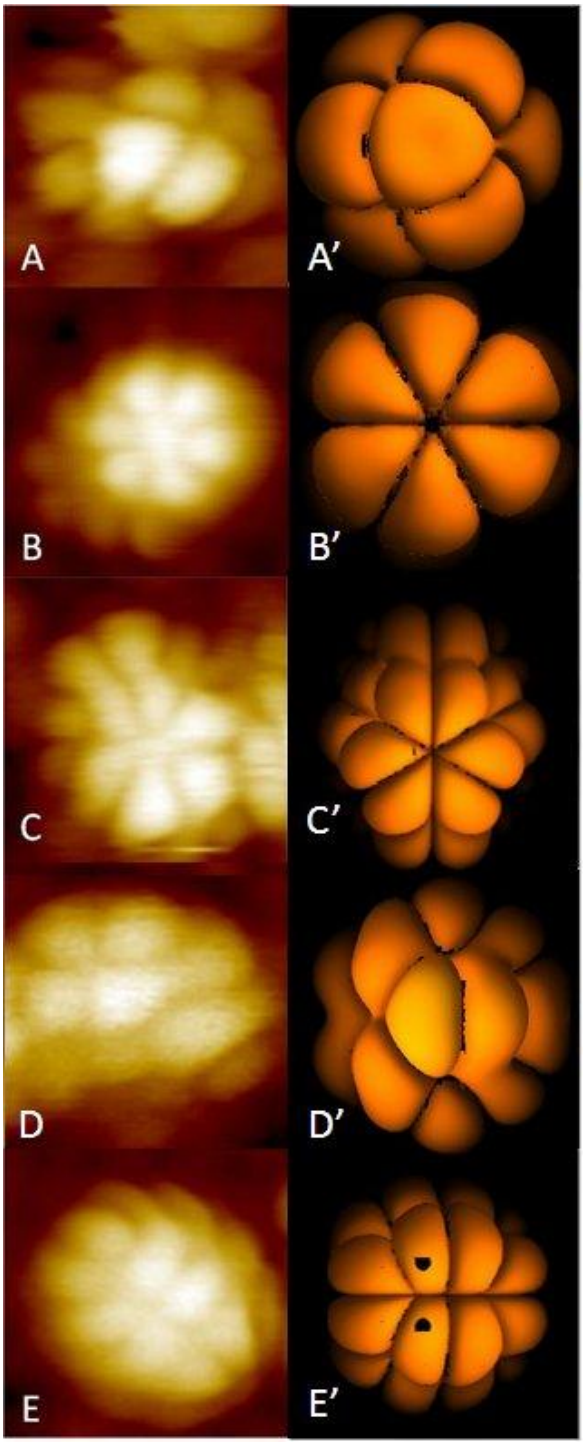

Figure 4-4. Dynamic STM images of C_{60} molecules **(A-E)**. Various internal features compared to Hückel molecular orbital theory images **(A'-E')**. A hexagon prone to the surface: **(A)** 2.1 V, 300 pA **(A')** LUMO. **(B)** 2.3 V, 2 nA. **(B')** LUMO. **(C)** 2.3 V, 2 nA. **(C')** LUMO. A single bond prone to the surface: **(D)** 2.1 V, 300 pA. **(D')** LUMO. A double bond prone to the surface: **(E)** 1.6 V, 400 pA. **(E')** LUMO. A tip doubling effect can be noticed in all images due to a C_{60} molecule on the tip.

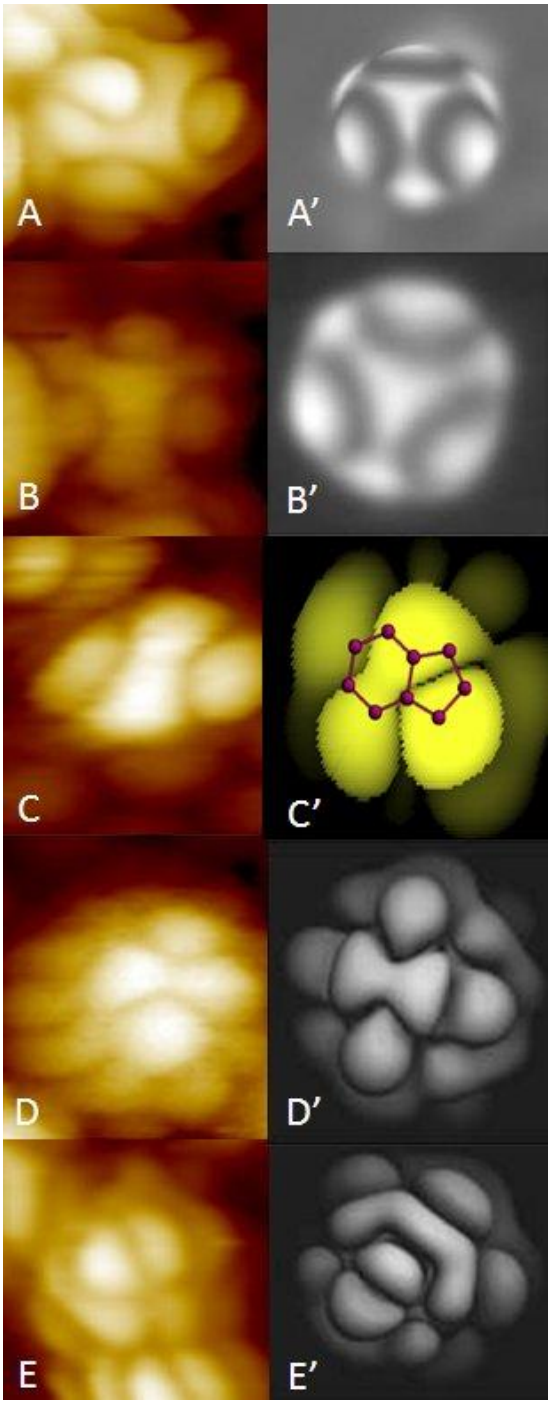

Figure 4-5. Dynamic STM images of C_{60} molecules **(A-E)**. Associated simulation images **(A'-E')**. A hexagon prone to the surface: **(A)** 2.1 V, 300 pA. **(A')** *dI/dV* map, 1 V [112]. **(B)** 2.1 V, 300 pA. **(B')** *dI/dV* map, 0.8 V [161]. A single/double bond prone to the surface: **(C)** 2.1 V, 300 pA. **(C')** DFT -0.4 V [160]. **(D)** 3 V, 300 pA. **(D')** DFT, -0.4 V [162]. Unidentified orientation: **(E)** 2.1 V, 300 pA. **(E')** DFT 1.5 V [162]. A tip doubling effect can be noticed in all images due to a C_{60} molecule on the tip.

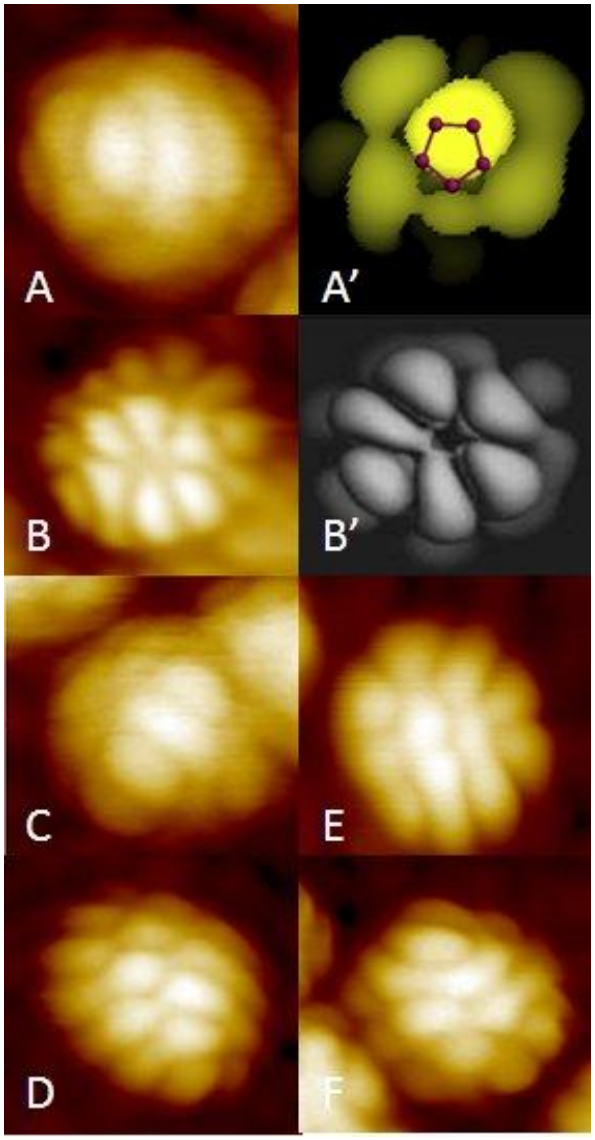

Figure 4-6. A pentagon prone to the surface: **(A)** 2.3 V, 300 pA, **(A')** DFT 0.3 V [160]. A hexagon prone to the surface: **(B)** 2.1 V, 300 pA, **(B')** DFT, -0.4 V [162]. **(C-F)** Dynamic STM images of C_{60} molecules: unidentified orientations. Probably, these images are the result of imaging with a C_{60} probe.

Some patterns of intramolecular contrast arising from the LUMO which was observed in experiment were remarkably similar to the HOMO spatial distribution predicted by theory (Figure 4-5C,D and Figure 4-6B). According to Hands *et al.* [74] low resolution, low current, surface-induced splitting or site-specific perturbation may explain this phenomenon. Similarities between HOMO and LUMO structures were also reported by Pascual *et al.* [31] and explained by an energy shift of the molecular orbitals due to molecule-substrate bonding. However,

there is now evidence beside STM images to confirm this hypothesis. Unknown tip state or a C_{60} molecular probe may yield these similar features. The C_{60} molecules in dynamic STM images in Figure 4-3:6 look blurry, with distorted symmetry and slight doubling, most likely due to other C_{60} molecules adsorbed on the tip. This complicates the direct comparison to theoretical calculations. Some of the molecular structures imaged with a C_{60} probe will be discussed in Section 5.7.

4.3 Measurements on C_{60} Molecules using qPlus AFM

4.3.1 Force Spectroscopy on Si(111)-(7x7)

Before deposition of C_{60} molecules the quality of the Si(111)-(7x7) surface was checked. The (7x7) reconstruction must be clean, with a low density of defects across large regions. Imaged with AFM, Si adatoms appear as bright features arranged as in the DAS model of Si(111)-(7x7) (Figure 4-7). The apparent size of the adatoms is also significantly smaller than observed in STM [19].

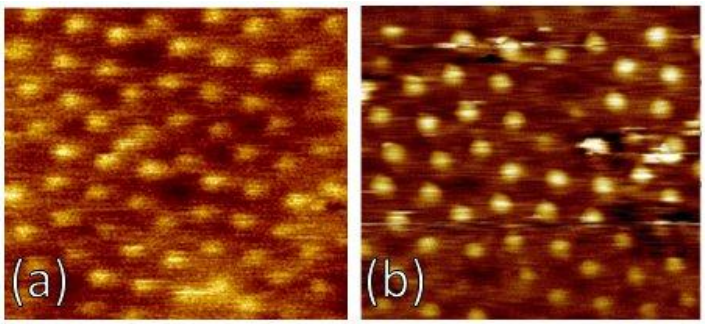

Figure 4-7. qPlus AFM images of Si(111)-(7x7). (a) 6x6 nm^2, *df* = -7.5 Hz, *V* = 0 V, *A* = 1 nm. (b) 5x5 nm^2, *df* = -26 Hz, *V* = 0 V, *A* = 2 nm. Tip-sample separation was decreased in image (b) to achieve sharper resolution. Unfortunately, this often resulted in strong interactions or contact with the surface leading to a total loss of resolution.

AFM imaging with atomic resolution was somewhat more challenging than in STM. In order to acquire stable and high resolution images in AFM, the tip must be rigid and sharply structured. Even minor changes in the tip apex, arising from an interaction with the surface, strongly affected the imaging process. Instability could also result from very slow feedback response in AFM. When the tip

lost the ability to provide atomic resolution, scanning was switched to STM to proceed with tip recovery.

Force spectroscopy measurements were carried out on clean Si(111)-(7x7) (Figure 4-8) to ensure reliability of the spectroscopy data. These force spectroscopy data were used as a control for the background, long-range force measured on clean Si surfaces before taking spectra on C_{60} molecules. They were consistent with previous measurements on Si(111)-(7x7) [163]. This method provided evidence that the tip was properly Si-terminated. Analysis of tips was also carried out using scanning electron microscopy and energy dispersive X-ray analysis to confirm the presence of Si.

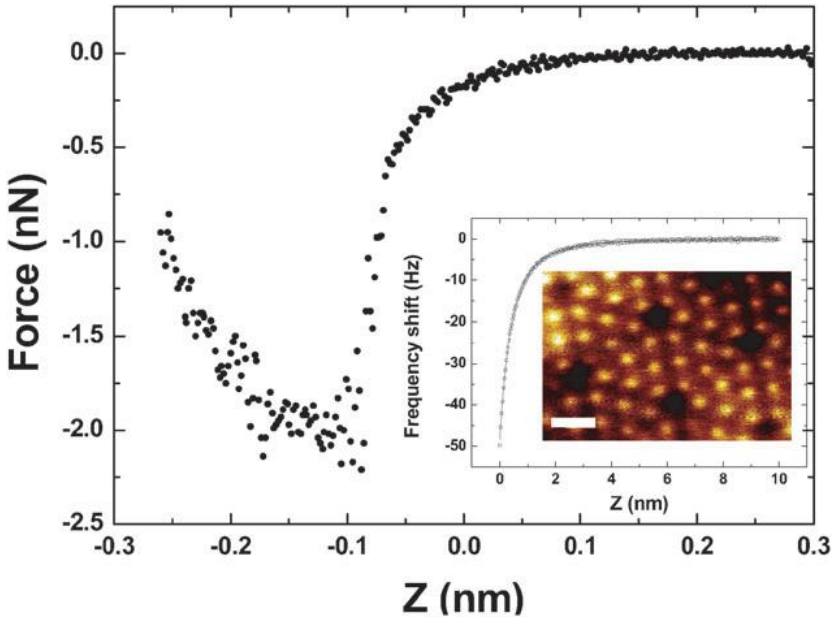

Figure 4-8. Force curve measured above Si adatoms. Short-range chemical force curve indicated a maximum attractive force at ~2 nN. The inset shows a long-range frequency shift curve acquired above a corner hole on Si surface. Imaging parameters: *df* = -21.6 Hz, *V* = 0 V, *A* =1 nm.

4.3.2 Imaging C_{60} Molecules using qPlus AFM

In qPlus AFM images, C_{60} molecules appeared as bright spherical protrusions (Figure 4-9). The C_{60} molecular diameter in AFM was close to the hard sphere diameter of C_{60} (~1 nm). Depending on the tip radius, some molecules had an apparent diameter of ~1.5 nm. The apparent height of C_{60} molecules was measured at

~0.01-0.08 nm. In AFM, the tip could not approach closely enough to the surface to image the Si atoms, because at that tip-sample separation the C_{60} molecules would have been moved.

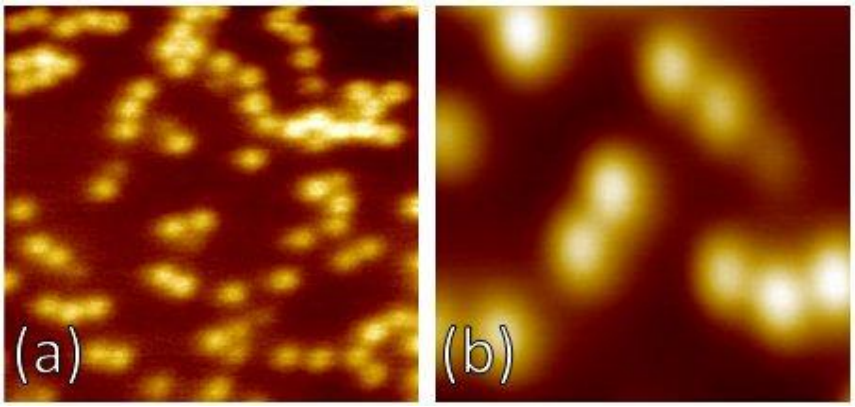

Figure 4-9. AFM images of individual C_{60} molecules, recorded at 0 V bias voltage. **(a)** 15x15 nm^2, *A* = 6.4 nm, *df* = -10.5 Hz. **(b)** 8x8 nm^2, *A* = 1 nm, *df* = -59 Hz.

In dynamic STM images Si adatoms and molecular orbitals of C_{60} molecules could be clearly resolved (Figure 4-10A). The diameter of a molecule was measured to be 1.5-2 nm. The frequency shift (*df* image) image in dynamic STM showed similar features to those seen in the topographic STM image: the molecules had the same apparent size, but small features appeared less sharp (Figure 4-10B). The imaging set-up was then switched to AFM mode and same area was imaged (Figure 4-10C).

Cross-talk issues in dynamic SPM measurements (Section 2.5.3.7), especially for simultaneous tunnelling current and frequency shift measurements, can give rise to artefacts and data with ambiguous interpretation. For example, "a phantom force" phenomenon, recently observed in experiments by Weymouth *et al.* [70, 164] was thought to have been induced by tunnelling currents on semiconductor surfaces. Frequency shift measurements, in this case, were dominated by electronic contributions so that measurements were no longer related to the real force interaction (Figure 4-10B).

In addition to the instrumentation design which induces a capacitive coupling into the deflection channel [164, 165] for simultaneous measurements in

dynamic STM, cross-talk between the frequency shift and tunnelling current may also occur in the feedback response while mapping the surface [164].

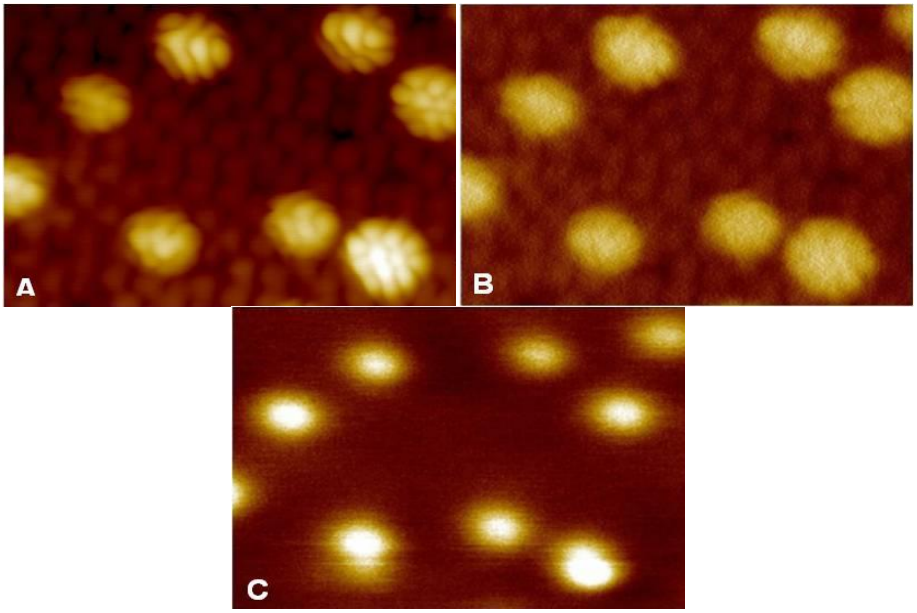

Figure 4-10. (A)-(B) Dynamic STM images 9x6 nm^2 , V = 2.3 V, I = 300 pA, A = 6 nm, df = -59 Hz. **(A)** Z image showing topography. **(B)** Frequency shift image. **(C)** AFM Z image recorded on the same area in constant-frequency shift mode, V = 0 V, A = 1 nm, df = -11 Hz. A great difference was evident between the df image in D-STM and the AFM Z image due to cross-talk. The df measured by PLL in dynamic STM was on the order of tens of Hz, much higher than in AFM, due to the bias voltage of more than 2 V. Therefore, the tunnelling current apparently dominated the force of interaction producing df images as seen in (B).

Scanning C_{60} molecules in the attractive force regime of qPlus AFM, was proven to be stable for both 'small' (~1 nm peak to peak or smaller) and 'large' (~6 nm peak to peak) amplitudes. In addition to this type of constant frequency shift imaging, we also carried out a number of 'pseudo constant-height' measurements. In this case, the forward scan was set on constant-frequency shift mode (Figure 4-11a) (*i.e.* the feedback loop was on), while the backward scan had the feedback loop turned off and the variation in the frequency shift was recorded. Sub-molecular features are clearly observed in the df image (Figure 4-11b). In this fashion, contrast was increased and sub-molecular features were more clearly seen. In "pseudo constant-height" mode the intramolecular contrast arises from the repulsive force originating from Pauli exclusion principle, also described by Pawlak *et al.* [128] and

Gross *et al.* [130, 131]. (For more details on constant-height imaging and Pauli repulsion see Sections 2.9.2.9 and 2.9.2.10.)

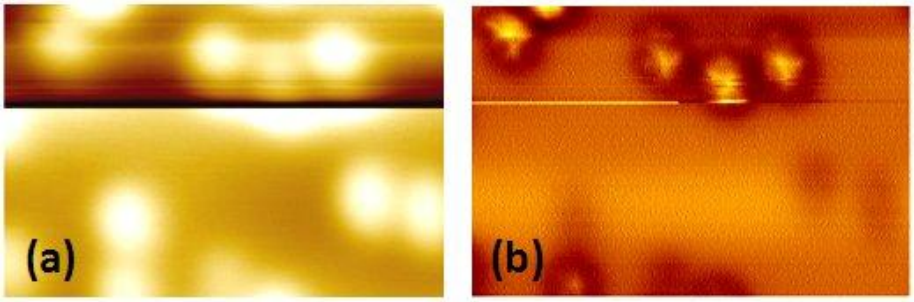

Figure 4-11. (a) AFM topography *Z* image, forward scan, constant-frequency shift mode, 6.6x4.8 nm^2, V = 0 V, A = 1 nm, df = -18 Hz. **(b)** df image, backward scan, pseudo-constant height/contact mode. Above the horizontal line the df set-point was increased to -18.75 Hz. Molecules appeared sharper and sub-molecular contrast was more intense.

4.3.3 Force Spectroscopy of a Si-terminated Tip and C_{60} Molecules

The interaction between Si-terminated tips and C_{60} molecules adsorbed on Si(111)-(7x7) was also studied via FM-AFM force spectroscopy. The force spectroscopy experiment presented in this section measured both short- and long-range forces generated by both Si substrate and C_{60} molecules. The frequency shift was measured at each defined point between tip and sample for a given *z* range as the tip approached and retracted from the sample. The force was then calculated from df measurements [68].

First, long-range spectra were recorded above Si and C_{60} molecules. Tip-sample separation *z* was usually ramped from 30-50 nm to 0. These spectra were measured to fit and remove the long-range background contribution. Then several spectra were acquired for separations less than 5-10 nm, each time increasing the lower limit, so as to decrease the tip-sample distance. Force spectra were successively acquired on Si and on C_{60} molecules. Si spectra represented the contribution of long-range forces to the total force (Figure 4-12).

Spectra acquired on clean Si were subtracted from spectra measured on C_{60} to remove the long-range force contribution (Figure 4-12 and Figure 4-13). When

Si spectra were subtracted from C_{60} molecule spectra, the resulting graph showed the contribution of the short-range chemical force, corresponding only to the interaction between tip and a C_{60} molecule. On the spectra presented in this chapter $z = 0$ represents the tip-sample separation at the *df* set-point selected for scanning when the cantilever is not deflected.

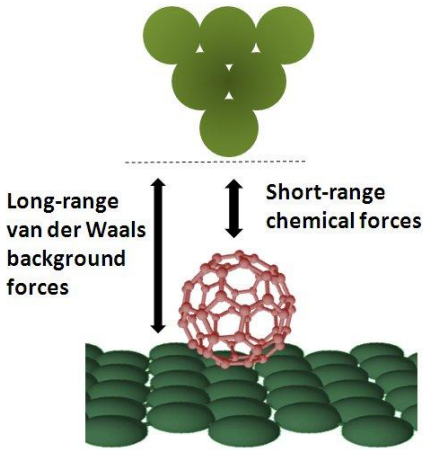

Figure 4-12. When the tip was positioned above the molecule the interaction consisted of contribution of both short- and long-range forces. (Figure reproduced from [166])

Calculation of the total force derived from *df* measurements was performed by Dr. Andrew Stannard using a mathematical algorithm based on the theory method described by Sader and Jarvis [68]. First, the potential energy curve was calculated from the raw *df* data. Then this was differentiated to obtain the force. The method for force conversion was described in detail in Section 2.5.3.6.

Extraction of the long-range background was extremely sensitive. The offset in *z* of the spectrum taken above Si was corrected to align with the spectrum acquired on a C_{60} molecule. Special care was given because even for very small (~10 pm) offsets in *z*, the short-range *df* curve could vary significantly. To assure a suitable value for the offset, residuals in fitting of the long-range background were carefully examined.

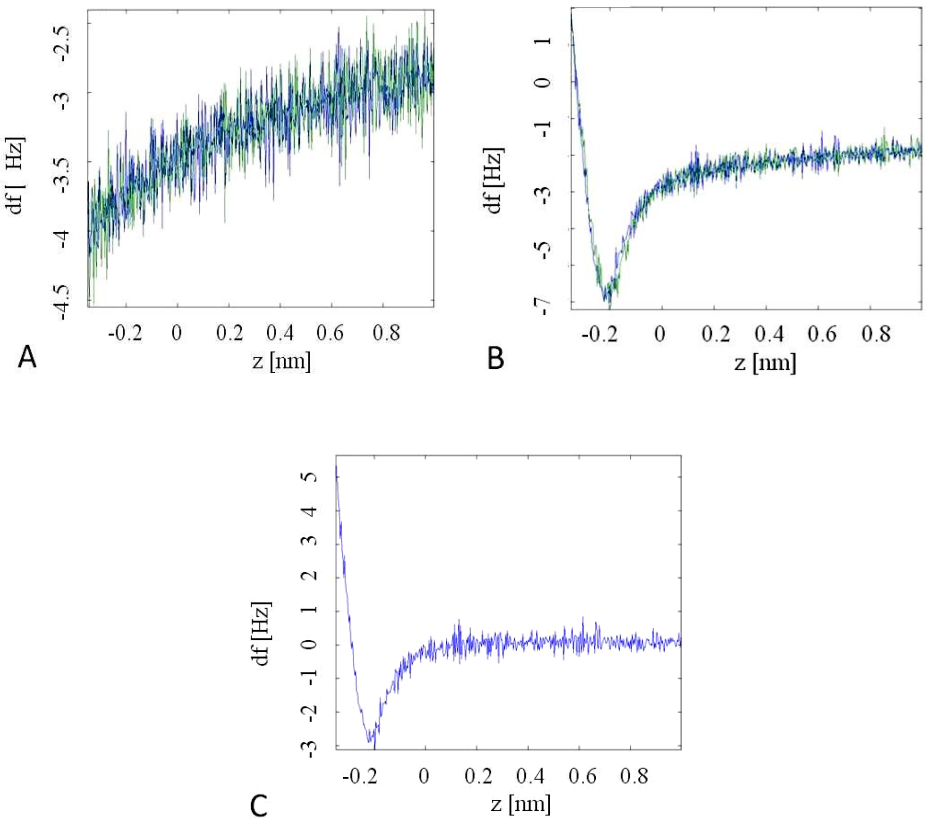

Figure 4-13. (A) Raw *df(z)* spectra measured above clean Si, *df* = -4.14 Hz. **(B)** Raw *df(z)* spectra measured above a C_{60} molecule, *df* = -4.14 Hz. **(C)** Spectrum obtained from the curve in (B) after subtraction of the *df* spectrum measured on Si. The short-range chemical force was calculated from (C).

The maximum attractive force between a Si-terminated tip and a C_{60} molecule adsorbed on Si(111)-(7x7) was measured as ~1(±0.2) nN (Figure 4-14). Significant efforts were made to ensure that the tip was terminated by Si but we cannot rule out that the tip was terminated by C_{60}, although the magnitude of the forces would suggest otherwise. This value was lower than the DFT prediction made by Hobbs and Kantorovich [166]. They determined the maximum attractive force to be in the range of 1.5-2 nN for a C_{60} molecule adsorbed on Si(001). Moreover, the force spectra in Figure 4-14 were shallower than those predicted with DFT.

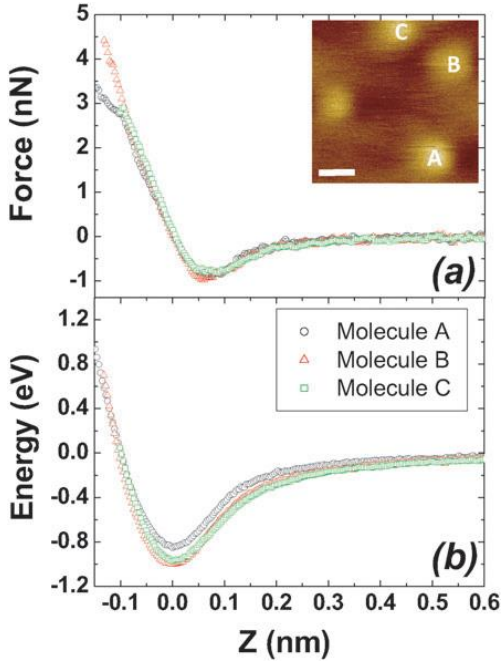

Figure 4-14. (a) Experimental short-range force versus *z* spectra acquired with qPlus AFM above C_{60} molecules labelled in the inset, *df* = -3.65 Hz. **(b)** Binding energy was calculated in the lower graph for each of the molecules *A*, *B* and *C*.

The binding energy between the Si apex and a C_{60} molecule determined in the experiment (Figure 4-14) was lower than that predicted in the work of Masenelli *et al.* for the bonding of a Si atom to a C_{60} cage [106, 158]. However, in their experiment, neither the Si atom nor the C_{60} cage was 'free'. Therefore, the bonding mechanism and thus the bond energy were severely constrained by the arrangement of the outermost Si atoms at the tip apex and by the bond C_{60} forms with the Si(111)-(7x7) surface.

The configuration of Si atoms at the end of the tip can dramatically influence the Si-C_{60} chemical bond and the strength of the interaction (Figure 4-15a). Many *df(z)* spectra were recorded above the same C_{60} molecule – we show four examples in Figure 4-15. Modifications occurring at the tip apex are visible in the curves due to hysteresis and the very different line-shapes. We interpret this large amount of hysteresis as arising due to changes in the atomic structure of the tip apex caused by chemical bonding with the adsorbed C_{60} molecule. Various Si-C_{60} chemical bonds were also marked by different force magnitudes. The maximum attractive force varied widely from ~0.6 nN to > 2.5 nN (Figure 4-15b).

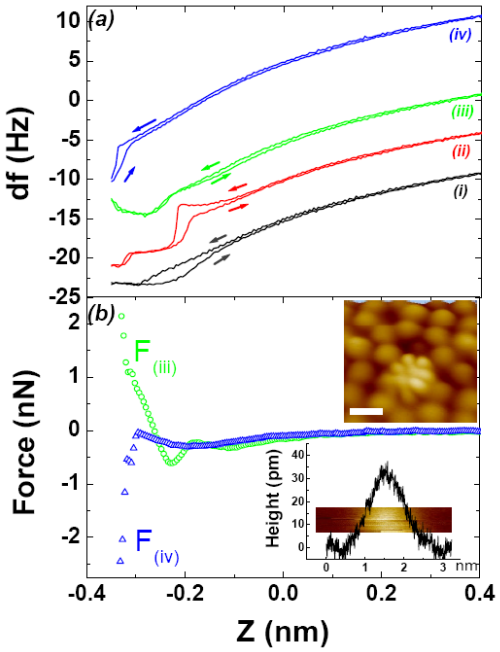

Figure 4-15. (a) Frequency shift spectra showing the strong dependence of Si-C_{60} bonding on the structure of the apex of the tip, *df* = -15.4 Hz. Arrows indicate the approach and retraction *df(z)* curves. The hysteresis observed in spectra denotes rearrangement of the atoms on the tip. Spectra were recorded on the molecule presented in the dynamic STM image in the inset in (b). **(b)** Force calculated from the (iii) and (iv) *df(z)* curves shown in (a). Inset: height profile of the same C_{60} molecule.

All measurements in AFM were performed at 0 V bias voltage in order to avoid cross-talk. Force spectroscopy curves were acquired for both low and high oscillation amplitude on clean Si areas and on top of C_{60} molecules. The force was also measured on several points across C_{60} molecules. Hundreds of spectra were recorded with very high reproducibility on multiple C_{60} molecules.

4.3.4 *Force Required to Move a C_{60} Molecule on Si(111)-(7x7) using AFM*

During AFM scanning, while increasing the *df* set-point, a strong molecule-tip interaction was produced such that the C_{60} molecule followed the tip. The molecule picked up by the tip could be released at a desired position by reducing the *df* set-point to the initial value. Therefore, tip-sample separation was decreased during scanning until a C_{60} molecule was moved (Figure 4-16 and Figure 4-18).

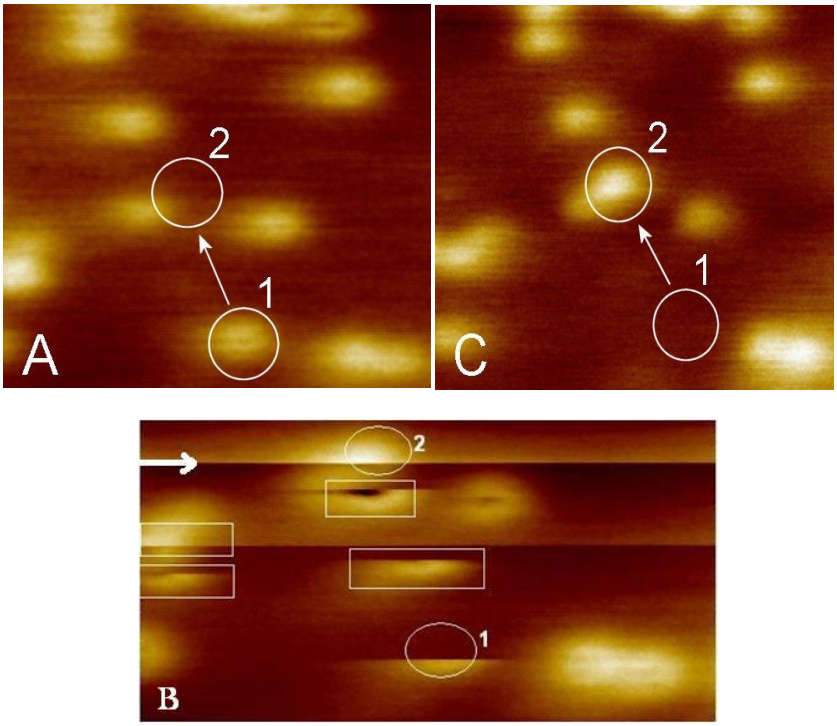

Figure 4-16. Manipulation of a C_{60} molecule with AFM. Images showing a C_{60} molecule moved from Position 1 to Position 2. Imaging parameters: A = 7.2 nm, V = 0 V, 9x9 nm^2 image size. First image **A** was recorded at df = -6.1 Hz. Second, image **B** was recorded by decreasing the tip-surface separation by changing the set-point to -6.25 Hz. The C_{60} molecule located in Position 1 was removed by the tip. In the positions marked with rectangles the molecule appeared to interact repeatedly with the tip, four times. At the line indicated by the white arrow, the df set-point was reduced to -6.1 Hz and the molecule was released in Position 2. Scanning followed well. Image **C** was a check scan. In this image, the molecule disappeared from Position 1 and it was located in Position 2 just at the spot where the set-point was set back to its initial value. (Image A was recorded downward. Image B was recorded upward and stopped after the molecule dropped. Image C was recorded upward after restart.)

If the df set-point magnitude was high enough, such that the tip-sample distance was small enough or when the oscillation amplitude of the qPlus sensor was too large, the top of the molecule was recorded as a black spot and some molecules were picked up or pushed. The black spot or depression recorded in the centre of the C_{60} molecules was an artifact and represented inverted contrast. This effect occurred at the point where measured frequency shift changed from attractive to repulsive interaction [124, 127].

In order to estimate the force necessary to move a molecule and to determine the molecule-Si interaction, force spectra were measured before

manipulation on both Si and C_{60} (Figure 4-17 and Figure 4-19). Correlation of the *df* set-point with the *df* curves provided a very rough approximation of the threshold vertical force required to move the molecule.

The first manipulation was performed with set-point *df* = -6.25 Hz (Figure 4-16). The reading on the raw *df* curve measured on the C_{60} molecule, *df* = -6.25 Hz was registered at *z* ~ -0.18 nm tip-sample separation (Figure 4-17A). The force corresponding to this position in the short-range force graph was in the range of 0.5-1 nN in the attractive regime (Figure 4-17B). This value is slightly lower than the magnitude calculated for manipulation of C_{60} molecules on Si(100)-(2x1) [115]. Note that this method for force approximation provided information on the vertical force, but not on the lateral force. An approach similar to that used by Ternes *et al.* [137] is necessary in order to extract the lateral force, and this will be the subject of future work.

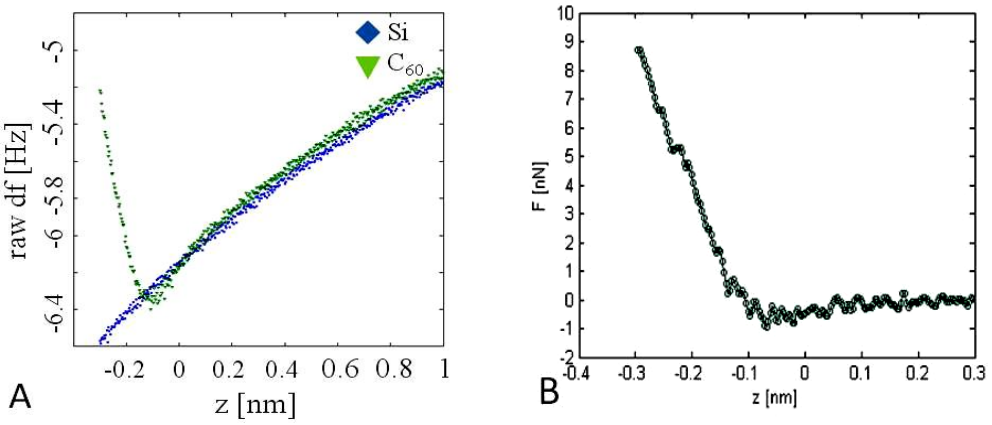

Figure 4-17. (A) Raw *df(z)* spectra acquired on C_{60} molecules and on clean Si surfaces. *V* = 0 V, *A* = 7.2 nm, *df* = -6.1 Hz. **(B)** Force versus *z* curve showing the short-range interaction between the tip and a C_{60} molecule calculated after subtraction of the *df* taken on Si from the *df* taken on C_{60}. These spectra were recorded before the manipulation presented in Figure 4-16.

Force spectroscopy curves were measured at the same oscillation amplitude with the amplitude used for manipulation. Short-range chemical force was considered responsible for manipulation [115]. Other molecules on the surface were not moved at these parameters, thus, a stronger force would be required to remove them. A second manipulation was recorded at *df* = -4.14 Hz (Figure 4-18). The

manipulation procedure was the same as described for Figure 4-16. The *df* set-point in image B was set to -4.25 Hz.

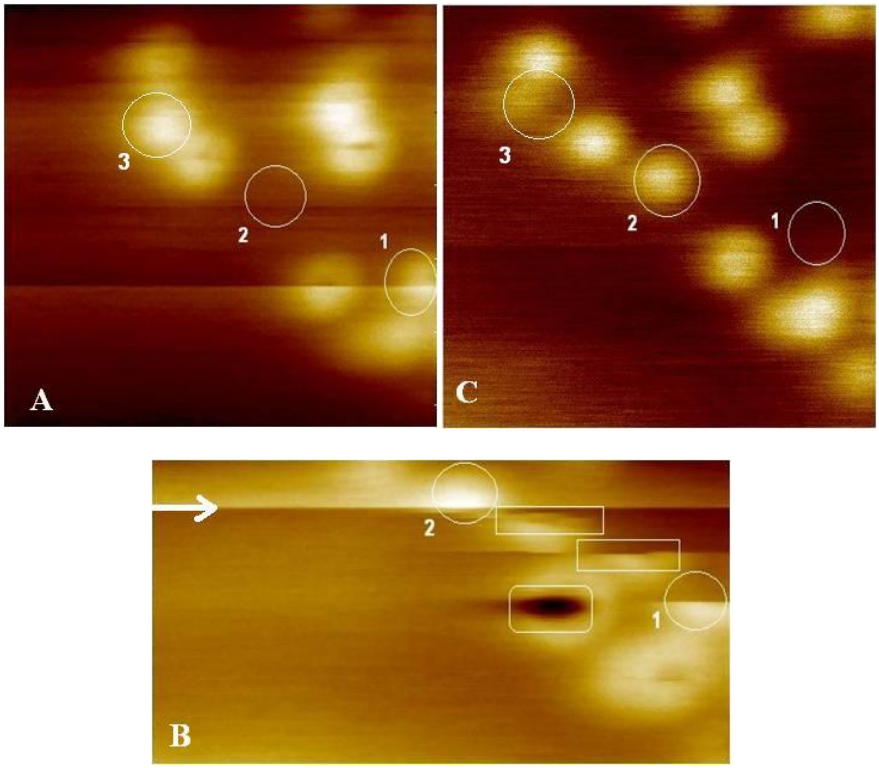

Figure 4-18. An example of manipulation of a C_{60} molecule with AFM. The molecule was moved from Position 1 to Position 2. A rounded rectangle surrounds a black spot on a C_{60} molecule. Imaging parameters: A = 7 nm, V = 0 V, df = -4.14 Hz, 8x8 nm^2 image size. (Description of figures in text.)

One possible interpretation of the data is as follows. The C_{60} molecule located in Position 1 was picked up by the tip and pushed in the scanning direction. In the positions marked with rectangles, the molecule was transferred twice between tip and surface. At the point marked with the white arrow the *df* set-point was set back to -4.13 Hz and the molecule was 'released' in Position 2. The result was checked in image C. Position 3 marked a molecule that was picked up while acquiring a force spectrum on top of it. This occurred before the manipulation experiment described above. The vertical force estimated for this case using the method described above was again 0.5-1 nN. As stated above, this is one interpretation. However, it is important to consider that the tip may be covered by C_{60} molecules and during tip-substrate interaction, at the positions marked by rectangles, may drop a different molecule than the C_{60} molecule originally picked in

Position 1. Therefore, the drop in Position 2 may be of a different molecule which was initially on the tip.

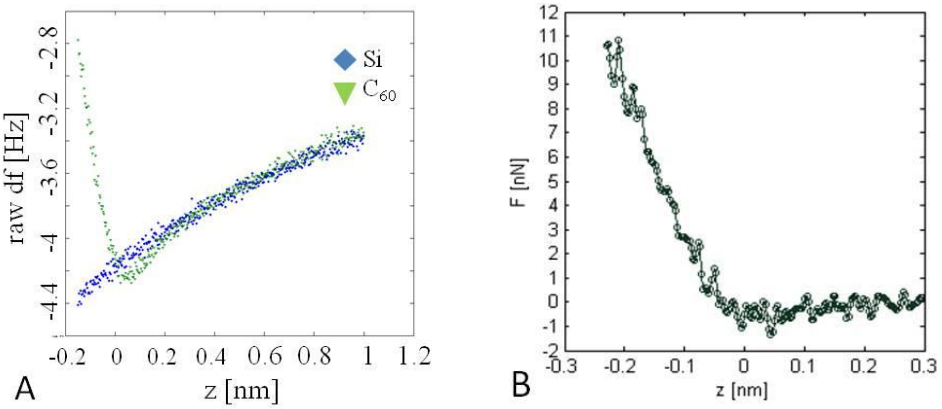

Figure 4-19. (A) Raw *df(z)* spectra recorded above a C_{60} molecule and on the Si surface, respectively. V = 0 V, A = 7 nm, df = -4.14 Hz. **(B)** Short-range force between the tip and a C_{60} molecule calculated from spectra in (A). These measurements were acquired before the manipulation presented in Figure 4-18.

4.4 Summary and Outlook

In summary, high resolution of C_{60} molecules adsorbed on Si(111)-(7x7) was achieved with dynamic STM. Theoretical simulations provided an interpretation of LUMO of C_{60} molecules and, of molecular orientation. A rich variety of intramolecular features were recorded, most likely as a result of a C_{60} probe molecule attached to the tip.

Furthermore, imaging and manipulation of individual C_{60} molecules were performed with qPlus AFM in constant-frequency shift mode, attractive regime. Molecules appeared as bright spherical protrusions. Force spectroscopy was carried out to measure the force of interaction and potential energy between a Si-terminated tip and C_{60} molecules.

Future experiments might be performed to explore the internal structure of C_{60} molecules with dynamic STM at negative bias voltage. However, the cross-talk limits the bias voltage/current range that can be explored for these measurements. Measurements with qPlus AFM could be improved to achieve high

resolution of individual C_{60} molecules and to employ a better technique for controlled manipulation of C_{60} molecules in order to quantify the interaction with Si(111)-(7x7) surface.

5 Sub-molecular Resolution and Orientation of On-tip C_{60} Molecule: Measuring the C_{60}-C_{60} Pair Interaction

5.1 Introduction

End-of-tip characterisation down to the atomic level is an increasingly important aspect of SPM measurements. Scanning probe microscopists are greatly concerned with the tip states that give rise to the features seen in SPM. Characterization of SPM probes with sub-molecular and even so-called "sub-atomic" resolution is essential for force spectroscopy and manipulation experiments. As discussed in Section 2.9.2.11, 'reverse' imaging and tip characterization with SPM at the atomic level were first reported by Giessibl *et al.* [133]. They resolved the charge density arising from atomic orbitals at the tip apex. Schull *et al.* reported the first image of a C_{60} molecule adsorbed at the tip apex with a single bond down [37] or with a hexagon prone [36]. Gross *et al.* demonstrated that a CO molecule can be used as a tip to resolve molecular structures with unprecedented resolution [131]. With a CO-functionalized tip, imaging [136, 167] and discrimination of chemical bonds [130] in molecules was achieved. This high sub-molecular resolution was recorded in AFM, constant-height mode, in the repulsive regime of tip-surface interaction. Based on the same Pauli repulsion principle, sub-molecular resolution of C_{60} molecules was also achieved in AFM by Pawlak *et al.* [128].

In this chapter, high resolution images of a C_{60} molecule adsorbed at the tip apex is presented. Dynamic STM measurements show molecular orbitals for all symmetry orientations of the molecule and its adsorption angle on Si(111)-(7x7) surface. AFM images recorded in the (weak)attractive potential show chemical reactivity close to or at C atom positions in the C_{60} cage. Individual C atoms were resolved, which is not possible in STM. The intermolecular potential for two C_{60} molecules is measured experimentally for the first time.

Si(111)-(7x7) reconstruction proved to be a good choice for this type of experiment due to its electronic and geometric properties. The larger separation between Si adatoms substantially decreases the overlap of sp^3 orbitals of Si adatoms and of orbitals arising from interactions with C_{60}. In addition, the narrow spatial extent and long decay into vacuum of the sp^3 orbital are favourable for probing local specific features on the large C_{60} molecule.

5.2 C_{60} Molecule Transfer to the SPM Tip

The ultimate purpose of the experiments and theoretical calculations described below was to measure the intermolecular pair potential for two C_{60} molecules. This necessitated precise control and characterisation of the apex of the SPM tip – it was essential to prepare and image a tip with a well-defined single molecule termination. For this purpose, a C_{60} molecule was transferred from the surface to the tip by one of several methods: "lateral manipulation", scanning with low feedback gains (Figure 5-1), and force spectroscopy (Figure 5-2).

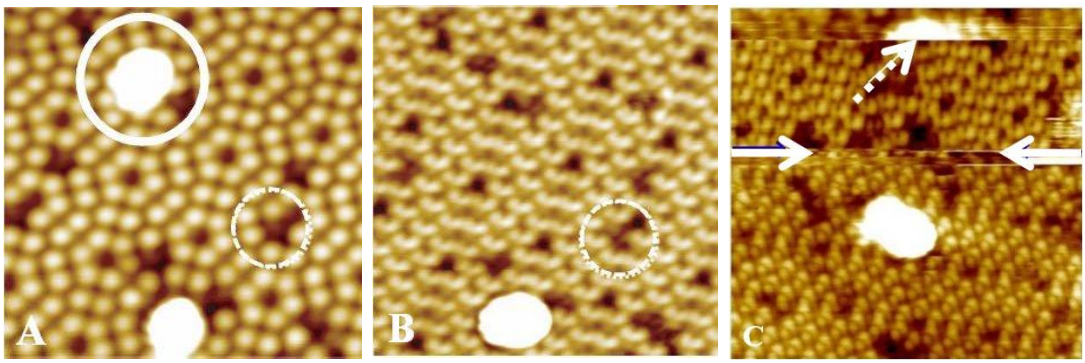

Figure 5-1. Example of picking up a C_{60} molecule during STM scanning. Images were acquired before **(A)** and after **(B)** the pick-up of C_{60} molecule marked by solid circle. The dashed circle highlights the same defect in both images. Note the strong change in atomic contrast in (B) after a single molecule was transferred to the tip apex. **(C)** Dynamic STM image of a different manipulation event. The dashed arrow indicates a C_{60} picked up during normal scanning. Instantaneously, atomic contrast changes to double lobe features. Horizontal, solid arrows mark a shift in molecular orientation. At this point, the two lobe structure on adatoms changes the shape, size and orientation. The pick-up and rotation events are usually associated with discontinuities in the image.

By applying lateral manipulation, the molecule could also be picked up, dropped, or rotated on tip. The orientation of the molecule present at the tip apex

could be switched to two-fold, three-fold or five-fold symmetry. However, a controlled switch of orientation was rather difficult and could only be achieved by a 'trial-and-error' approach under given experimental conditions.

Transfer of a C_{60} molecule to the tip by modifying the (dynamic) STM scanning parameters was the simplest manipulation method. By increasing the current set-point the tip was brought closer to the surface. At the same time, the scan speed was increased and the loop gain was reduced. An example is shown in Figure 4-1A,B. The dramatic change in the shape of the adatoms arises due to the molecule that was transferred to the tip. This phenomenon is best described as "inverse imaging" - the scan provides information not on the electronic structure of the adatoms but on the orbital structure of the apex of the tip.

Depending on the strength of the bond between C_{60} and tip, the molecule can rotate during scanning. The on-tip molecule can also reposition due to strong interaction with the surface. After a molecule was picked up by the tip while scanning, the atomic contrast suddenly changed to two long double lobes (Figure 5-1C). At a certain line, the molecule rotated slightly and the atomic contrast changed again. It retained the double lobe symmetry, with the difference that one lobe is round and the other one has a semispherical shape. In addition, C_{60} could also be transferred to the tip also by vertical manipulation using force spectroscopy (Figure 5-2).

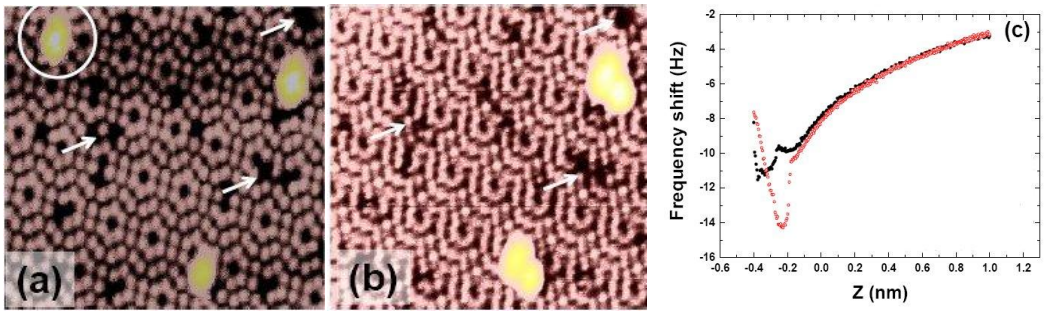

Figure 5-2. Example of vertical transfer of a C_{60} molecule to the tip using force spectroscopy. **(a)** Scan recorded before spectroscopy. **(b)** Scan acquired after spectroscopy. **(c)** spectra acquired above the circled molecule in (a). The transfer of the molecule to the tip is visible on the approach curve (black circles) as a sharp discontinuity. The molecule was removed from the surface.

The moment when a molecule was picked up was indicated by a shoulder in the approach curve (Figure 5-2c). The retraction curve (red circles) is radically different than the approach spectrum. When the molecule was removed, a doubling effect was sometimes produced on molecules and atoms. This effect could create difficulties in distinguishing sub-molecular orbitals from doubling, but with experience was easy to identify.

5.3 Sub-molecular Imaging of on-tip C_{60} with Dynamic STM

Once the molecule was transferred to the tip, a change in the atomic contrast was observed. At this point, the scan was zoomed on a clean silicon area and images with sub-molecular features were recorded (Figure 5-3). It was essential to avoid scanning above molecules on the surface during this process because of the small tip-sample separation required to image the adatoms. The proximity of the tip to the surface meant that scanning a surface-adsorbed C_{60} molecule could induce changes in the position of the on tip-molecule and could result in the loss of sub-molecular resolution.

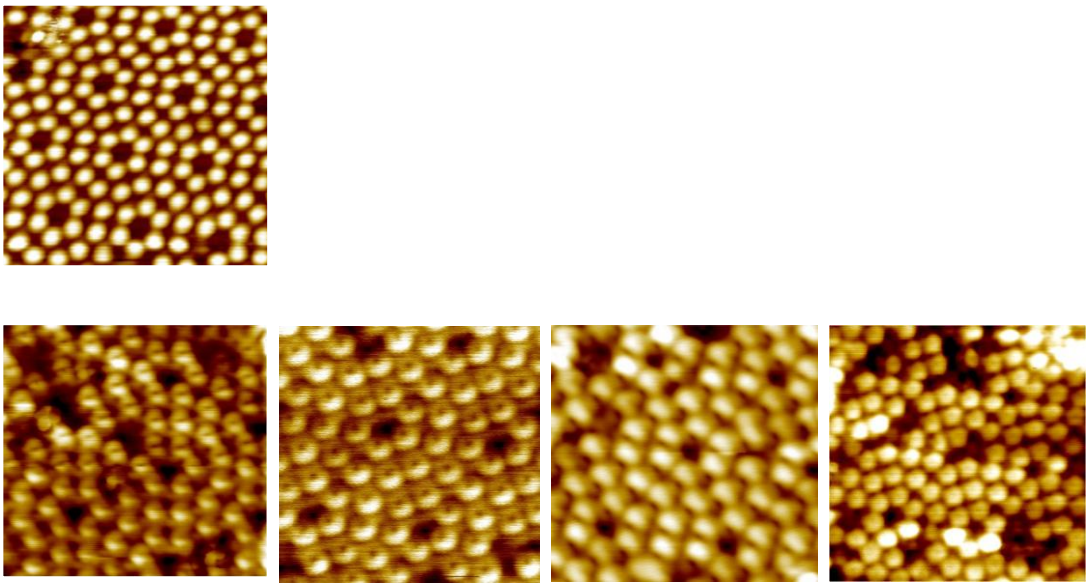

Figure 5-3. Top row: Empty state image of Si(111)-(7x7) reconstruction. Adatoms show conventional round shape image. **Bottom row:** Collection of images demonstrating various features of atomic contrast. These images were recorded after a C_{60} molecule was transferred to the tip. All images in dynamic STM were recorded at positive bias voltage applied to the sample.

For the interpretation of the sub-molecular features observed on the Si(111)-(7x7) surface, Hückel molecular orbital theory calculations were employed. A detailed description of Hückel molecular orbital theory method is presented in Section 2.6. A comparison between theoretical images and dynamic STM data is presented in this section.

Representative images of the two-fold, three-fold, five-fold symmetries and single bond prone geometries are shown in Figure 5-4 below. A molecule oriented with a single bond down shows a significant difference in contrast between two asymmetric lobes, with one lobe much brighter than the other (Figure 5-4A). A tip-adsorbed C_{60} molecule with a double bond prone to the surface also produced a double-lobe adatom shape, more symmetric in this case (Figure 5-4B). However, a change in size, shape and orientation of the lobes could also be seen in the image following the rotation of the molecule during scanning (marked by white arrows in Figure 5-4B). In the case of two-fold symmetry, the Hückel molecular orbital theory predicted two symmetric, elongated lobes for the adatom structure. This was the case when the molecule pointed down with a double bond perpendicular to the surface. However, in experimental dynamic STM images differences between the two lobes were observed. They did not have the same size or brightness. This was dictated by how the C_{60} was oriented and tilted on tip. The interaction was stronger on the side of the brighter lobe.

For the case where the tip-adsorbed molecule is oriented such that a hexagonal face is prone to the (7x7) surface, the (dynamic) STM image shows three lobes per Si adatom (Figure 5-4C). In the three-fold symmetry images, due to molecular tilt, the lobes were often not the same size and they were unequally spaced. There were, however, also cases when the C_3 symmetry axis was almost perpendicular to the surface and the interaction yielded a more symmetric structure (marked by white arrows in Figure 5-4C). When the tip-adsorbed C_{60} molecule was pentagon-prone, the adatoms appear roughly pentagonal in the dynamic STM images (Figure 5-4D). The Hückel molecular orbital theory calculations predict the presence of a sharp node at the centre of the pentagonal structure; this can be seen in the experimental dynamic STM image shown in Figure 5-4D.

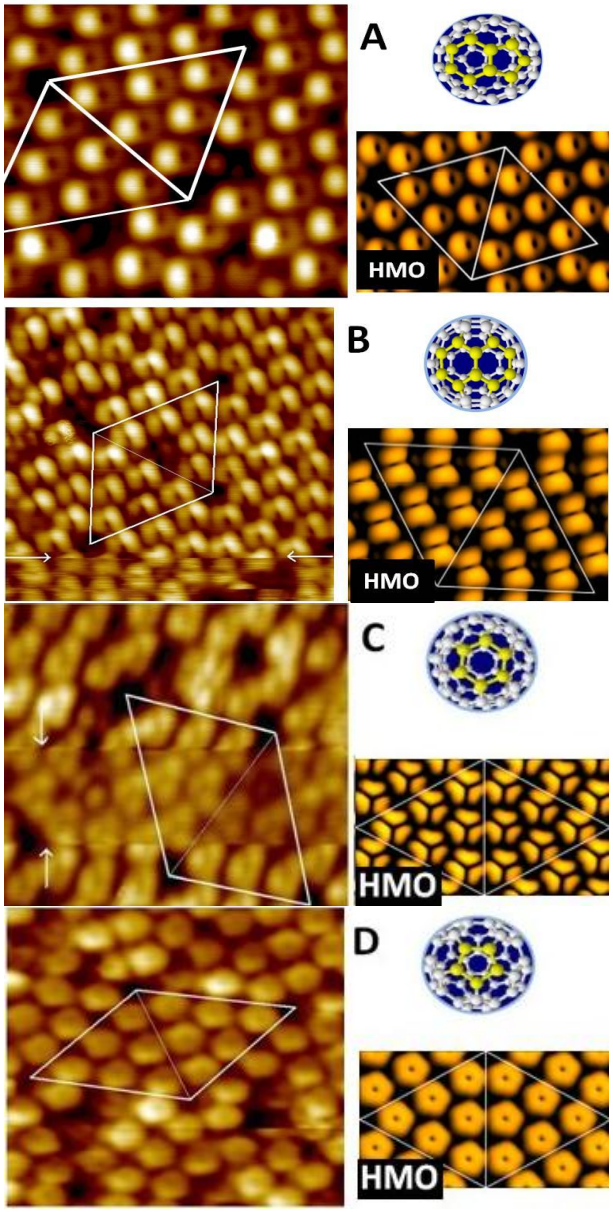

Figure 5-4. Dynamic STM images of Si(111)-(7x7) surface imaged with a C_{60} probe and associated with the Hückel molecular orbital theory simulations. White lines mark the (7x7) unit cell. **(A)** Single bond down A = 0.22 nm, V = 1 V, I = 100 pA. **(B)** C_2-Double bond down, A = 2.8 nm, V = 2.3 V, I = 1.8 nA, df = -32 Hz. **(C)** C_3-Hexagon down, A = 2.7 nm, V = 2.3 V, I = 0.4 nA, df = -70 Hz. **(D)** C_5-Pentagon down, A = 3 nm, V = 2.7 V, I = 1.33 nA, df = -29 Hz. White arrows in (C) mark a few lines when the molecule rotation yields a more symmetric pattern for the three lobes. In (B), white arrows mark a change in the tip-adsorbed molecule's orientation. The two lobes formed at the bottom at the image have different shape and orientation.

We can make the plausible assumption that the rotational/orientational "mobility" of the molecule often seen in the dynamic STM images depends on the type of bonding the C_{60} experiences at the tip apex. Weak bonding, such as a van der

Waals interaction, will lead to relatively low energy barriers for rotation or tilting. The implication is that there is more than one C_{60} molecule at the tip apex – the C_{60} primarily involved in the imaging process is 'back-bonded' to other C_{60} molecules, rather than to silicon or tungsten atoms. The latter would produce significantly higher binding energies and barriers, at best strongly restricting – and, most likely, precluding - molecular mobility at the tip apex.

A comprehensive set of simulated Hückel molecular orbital theory images has been calculated by our collaborators, Dr. Andrew Lakin and Dr. Janette Dunn. These provide an extremely important tool for rapidly discerning the orientation and tilt of a tip-adsorbed molecule (see, for example, Figure 5-5, and Figure 5-6 for experimental images). While a significant subset of the simulated images agrees well with the experimental data, there are some experimental dynamic STM images which seemingly do not have a counterpart in the simulated image set. These most likely arise from situations where either more than one C_{60} is adsorbed at the tip apex and/or a silicon dangling bond at the tip also contributes to the image formation mechanism.

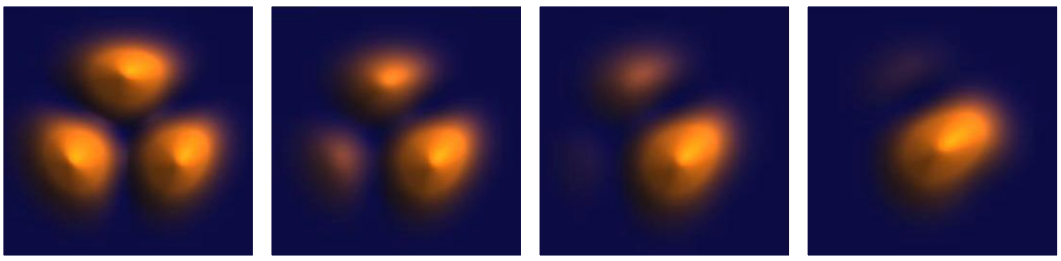

Figure 5-5. Hückel molecular orbital theory images of three-fold symmetry of a C_{60} molecule observed under different adsorption angle. The shape of molecular orbitals differs according to the adsorption angle of the molecule on the tip. From left to right: 0^0, 5^0, 10^0 and 15^0, respectively.

As seen in theoretical and experimental data, the shape and size of the molecular orbitals can change dramatically with the orientation of the molecule. Hückel molecular orbital theory simulations for two- and five-fold symmetry also produced different features for the lobes according to the adsorption angle of the molecule. Many of the simulated structures were observed during these experiments. Images presented in this section were not consecutive scans. It was very difficult to control the adsorption position of the molecule on the tip and often the molecule was

dropped or sub-atomic resolution was lost. Still, during lateral manipulation across a clean Si area, the molecule on the tip shifted the position and/or rotated.

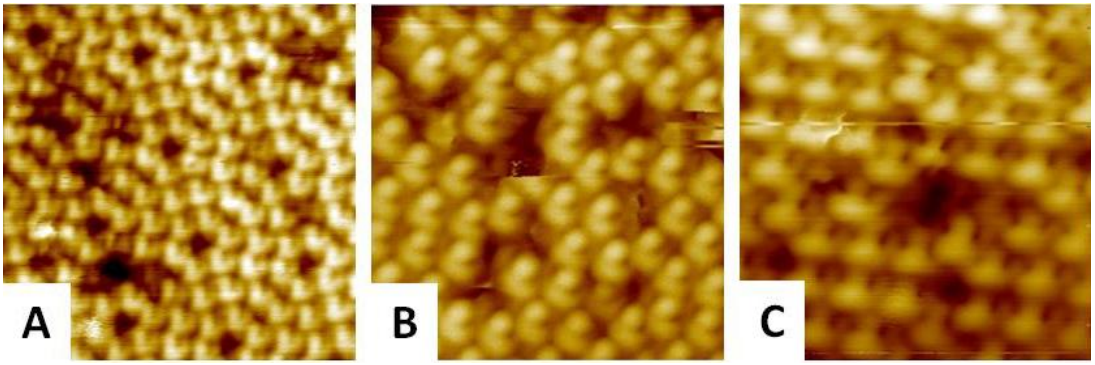

Figure 5-6. Experimental images of potential C_3 symmetry recorded in dynamic STM. Shapes and features of molecular orbitals differ dramatically for each image. The first scan **(A)** could be attributed to the case in which a hexagon is almost perpendicular to the surface. In image **(B)**, simulated Hückel molecular orbital theory images would suggest that the tip-adsorbed C_{60} has a tilt of less than 10^0 away from the surface normal, while image **(C)** most likely arises from a molecular tilt of greater than 10^0.

Various adsorbates or defects on the surface may act as probes in dynamic STM and image the end of the tip. Different dangling bonds have the potential to produce particular orbital 'signatures' in the adatom images. For example, in Figure 5-7, each adsorbate/defect produced very sharp three-fold or six-fold symmetric structures. The six-fold was a very high resolution of the molecule. This type of orbital structure was theoretically predicted using Hückel molecular orbital theory (see insets to Figure 5-7B,C) [74], but it has never been successfully probed in experiments before.

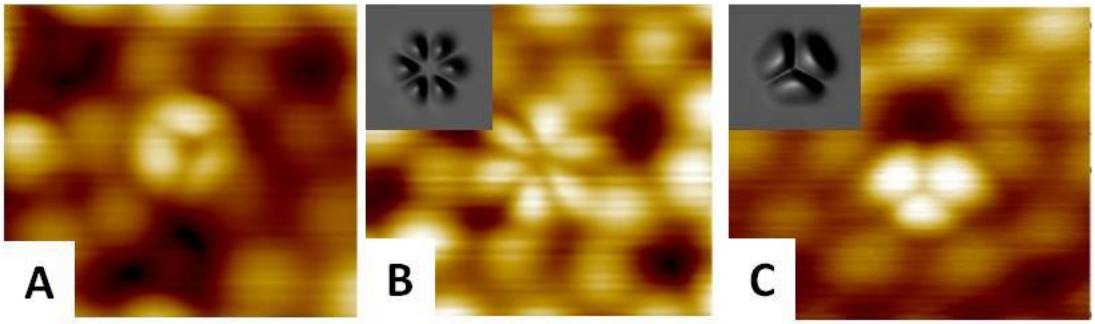

Figure 5-7. Unidentified adsorbates or defects on Si(111)-(7x7) exhibited three- **(A,C)** and six-fold **(B)** patterns. This may be evidence for a hexagon-prone on-tip C_{60}. Insets: Hückel molecular orbital theory, low current simulations for three-fold symmetry of a C_{60} oriented with a hexagon prone to the surface [74].

5.4 Sub-molecular Imaging of on-tip C_{60} with qPlus AFM

If stable scanning conditions were achieved after imaging the on-tip C_{60} in dynamic STM, one could switch to qPlus AFM. The transfer to AFM could affect the molecule's position on the tip and could even cause the molecule to re-adsorb on the surface. This disadvantage occurred because of the necessity of changing the feedback parameter from tunnelling current to frequency shift, to reduce the scan speed and to decrease the voltage to 0 V. The tip-sample separation was altered as well. However, if the molecule was relatively strongly anchored on the tip, as was often the case, then the transition from dynamic STM to qPlus AFM was routine.

The 'acid test' that the "sub-atomic" contrast observed in the qPlus images arises from a tip-adsorbed C_{60} (and not, for example, a silicon cluster) was the acquisition of images showing the pentagonal face of the C_{60} molecule. (This type of symmetry would not be expected for tip apices which were not C_{60}-terminated). The five C atoms of a pentagonal C_{60} face are seen in Figure 5-8A. Note that not all atoms have the same intensity in the image due to the tilt of the tip-adsorbed C_{60} molecule away from the surface normal. Moreover, the intensity of the maxima in one half of the unit cell is stronger, due to the well-known difference in density of states, and thus chemical reactivity, between the faulted and unfaulted halves of the (7x7) unit cell.

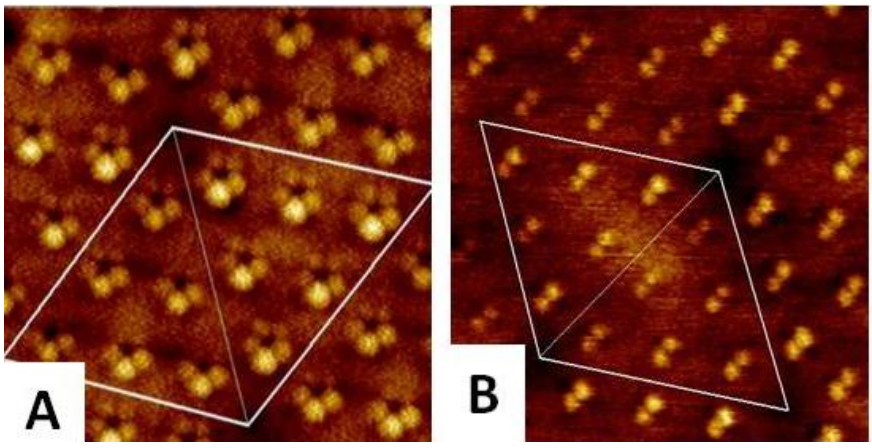

Figure 5-8. AFM images of on-tip C_{60}. White rhombi mark the (7x7) unit cell. **(A)** Five maxima per Si adatom, A = 0.5 nm, V = 0 V, df = -22.3 Hz. **(B)** Two maxima per Si adatom, A = 0.5 nm, V = 0 V, df = -46 Hz.

The five-fold symmetry observed in AFM represents strong evidence that contrast variations observed on adatoms arise from a C_{60} probe and not from a multi-tip or a Si/foreign species-contaminated tip. Local chemical reactivity is most likely the reason for higher resolution in AFM. A variety of other adatom shapes were observed in the qPlus AFM images. Figure 5-8B shows an image where the on-tip C_{60} is adsorbed with either a single or a double bond facing towards the surface. The separation between the maxima is ~180 pm. This value is much larger than the theoretical values proposed for single and double bonds in C_{60} molecule. This difference was a consequence of the interaction between the C_{60} molecule and the Si adatoms, as discussed in Section 5.5 below. (Note that somewhat similar large differences in predicted and measured bond lengths have been reported by Gross *et al.* [130] and rationalised in the context of the relaxation of the AFM tip apex). The size and the intensity of the lobes varied, being a result of adsorption angle of the molecule on the tip, of adatom positions, and of surface defects. The brighter the maximum, the stronger the interaction was between the C_{60} molecule and the Si atom at that point.

A number of direct comparisons between dynamic STM and AFM images were carried out during the course of this work. One of these is shown in Figure 5-9 below. In this case, the on-tip C_{60} was clearly in a pentagon-prone orientation and the FM-AFM image showed five maxima per Si adatom (Figure 5-9A). Because the molecule was slightly tilted some protrusions were brighter. The scanning mode was then switched to dynamic STM (Figure 5-9B).While the pentagonal adatom shape is vaguely visible in the dynamic STM image, it is rather more difficult to discern the node in the orbital structure. A high-pass filter was therefore used to accentuate the image (Figure 5-9C). To check that the orientation of the molecule did not change, the scanning mode was switched back to qPlus AFM. Precisely the same structure as the initial AFM scan was observed (Figure 5-9D). This experiment provides a direct comparison between molecular features seen in AFM, dynamic STM and Hückel molecular orbital theory.

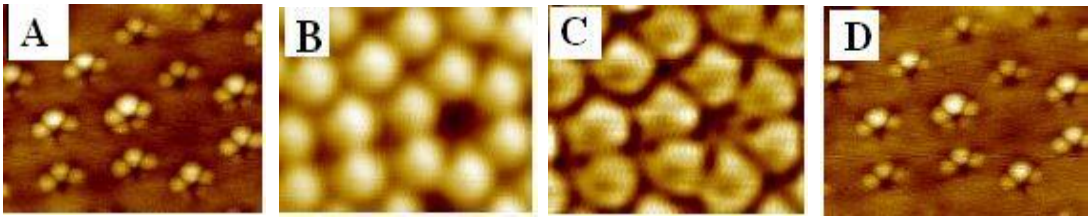

Figure 5-9. Direct switch between AFM and dynamic STM modes allowing comparison between the structures observed for a pentagon prone of the on-tip molecule in both modes. Image **(A)** is the original scan in AFM – five maxima per Si adatom, *df* = -150 Hz. Image **(B)** is the dynamic STM scan of the same area. Image **(C)** is a high pass-filtered version of (B) to accentuate the presence of the node in the orbital. The molecular orientation is double-checked by switching back to AFM (image **(D)**).

A hexagon-prone orientation has not been found to date for qPlus AFM imaging. This is an intriguing result and most likely points to the site-specific reactivity of the tip-adsorbed C_{60} cage with respect to the underlying silicon adatoms. We discuss this in more detail in Section 5.5.

Following the AFM interaction and image formation theory described by Ondracek *et al.* [168] and Hobbs and Kantorovich [166] it is expected that the bright protrusions in this case correspond to the C atom positions in the C_{60} cage. Ondracek *et al.* [168] ran density functional theory simulations to understand whether the contrast observed experimentally in AFM measurements on carbon nanostructures arises from the contribution given by carbon atom positions or from the hollow sites between the atoms. They looked at carbon nanotubes and graphite substrates with tips of different material and various apex configurations. While for a Si-dimer or O-termination, hollow sites yielded stronger attractive forces, for a tungsten or a clean silicon tip with (111) orientation, the maximal force was located at the atomic positions.

Force spectroscopy calculations of Ondracek *et al.* provided information on the nature and magnitude of the forces involved in interaction. It was found that short-range chemical forces were responsible for atomic contrast, but the van der Waals interactions dominated the strength and scale of the total force. These findings could also be relevant to organic molecules with a polycyclic aromatic core. As concluded by Ondracek *et al.* in the case of a clean Si tip, the dangling bond of the

outermost apex atom is highly reactive. In interactions with a C atom of a nanotube, a change in hybridization typically accompanies chemical bond formation.

The DFT simulations of both Ondracek *et al.* and Hobbs and Kantorovich demonstrated that chemical reactivity plays an important role in contrast formation in carbon nanostructures. Therefore, in our case, where we use the highly reactive dangling bond of Si adatoms as a "mini-tip", one might expect strong contrast close to, or at, the carbon atom positions in the on-tip C_{60} molecule. The qPlus sensors used in these experiments had high stiffness properties (~2.6 kN/m) which enabled imaging in dynamic modes at very low oscillation amplitudes. Scanning with low amplitudes increased sensitivity to the short-range chemical forces.

5.5 Contrast Formation in AFM

In order to elucidate the chemical interaction responsible for the high resolution qPlus AFM images shown in, for example, Figure 5-8 and Figure 5-9 above, a combined experimental-theoretical force spectroscopy study was carried out. (The theoretical force-distance curves were calculated by Dr. Samuel Jarvis.) Frequency shift spectra were acquired to provide information on the contrast formation mechanism in the AFM images. Force spectroscopy was carried out between the on-tip molecule and the Si adatom for a number of configurations. Here we will focus on the pentagon-down orientation. Forces were extracted from the experimental frequency shifts using the method described in Section 2.5.3.6. In order to separate the long-range contribution from the short-range interaction, "background" spectra were measured above corner holes, where the short-range contribution is negligible. This procedure was adopted from Lantz *et al.* [163].

Spectra were recorded above the lobe with the highest intensity among the five maxima (crossed in Figure 5-10 inset). Short-range force curves presented here were compared to DFT force spectroscopy. The maximum attractive force found in this experiment was ~1.6 +/- 0.2 nN. DFT calculations predicted a value of ~1.4 nN for this case, consistent with the experimental data. This value is above the

magnitude of a (short-range) van der Waals interaction [168], but in line with an (iono)covalent interaction between Si and C_{60} [106]. In addition to the strong C-Si covalent bond (Figure 5-10b,c), a localised charge transfer occurs from Si to the C_{60} molecule which produces weak ionic bonds [106].

In the experimental force spectroscopy curves, a reproducible "jump" or discontinuity at a threshold tip-sample separation routinely occurred (Figure 5-10a). DFT spectra showed much the same "jump-to-contact" effect (Figure 5-10a) originating from Si-C bond formation. According to the DFT simulations, the Si-C bond is strong, producing significant distortions in the C_{60} cage due to the change in hybridisation of the C atom when bonded to Si (Figure 5-10c).

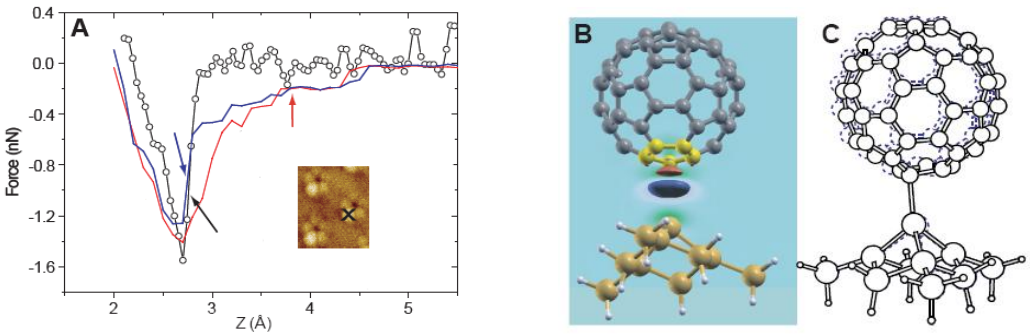

Figure 5-10. (A) Short-range chemical force representing the interaction between the closest C atom to the surface and the brightest maximum on Si adatom (inset). The experimental curve (empty circles), *df* = -18.5 Hz, as well as the curves calculated using DFT for a Si adatom directly below a C atom (red line) and a C-C single bond (blue line) exhibit a "jump-to-contact" effect indicated by the blue and the black arrows. The red arrow indicates the point at *z* = ~3.8Å where the Si-C bond was formed. **(B)** Charge density. **(C)** Ball-and-stick model show theoretical models of C-Si bond formation. Locally the C_{60} cage was deformed.

DFT simulations were also performed for various other orientations of the on-tip C_{60} molecule (hexagon-down, single-bond-down etc…). In all cases, a strong interaction arose at the C atom site; this is the mechanism responsible for contrast formation. From analysis of the DFT force spectra and electronic charge density, contrast in AFM could be achieved only in the weakly attractive force regime, between the point where the spectrum diverges and the point where the "jump-to-contact" occurs. Outside this regime, a stronger chemical bond showed a larger spatial extent, acting outside the perimeter of a C atom. At the same time, this

strong interaction may produce distortions of the C_{60} cage and instabilities in its position, which may explain the difficulties in imaging, and even why a hexagon orientation could not be probed.

5.6 C_{60}-C_{60} Pair Potential

In addition to quantifying the C_{60}-Si bond strength and interaction potential, controlled termination of the AFM tip apex with a C_{60} molecule enables a key measurement: the determination of the C_{60}-C_{60} intermolecular pair potential. This has hitherto not been measured experimentally, although the interaction potential of course underpins a vast amount of the science and technology of fullerenes.

Conversion of the *df(z)* curves to a potential energy plot resulted in remarkably good agreement with the Girifalco potential [167] (Section 2.5.2) in terms of the depth and width of the potential well close to the equilibrium separation. The Girifalco potential arises exclusively from *short-range* dispersion forces (*i.e.* van der Waals interactions). Following determination of the orientation of the on-tip C_{60} molecule, as described in previous sections, the tip was positioned above a C_{60} molecule on the surface and *df-vs-z* spectra were acquired at various spots on the molecule. Small differences in the potential profile and in the depth of the well were observed when the position of the spectroscopic point above the molecule was slightly changed (Figure 5-11). Variations in the magnitude of maximum attractive force (~ 50 meV) across the molecule were in line with the DFT calculations of Tournus *et al.* [169] and arose from electron density at single and double bonds in the C_{60} cage. It is important to note, however, that the agreement with DFT is likely to be entirely fortuitous as the DFT calculations take no account of dispersion interactions. (More recent calculations in collaboration with King's College London, using a van der Waals-DFT code, provide excellent agreement with the Girifalco potential for isolated C_{60} molecules. We are currently investigating how molecular adsorption modifies the potential energy profile).

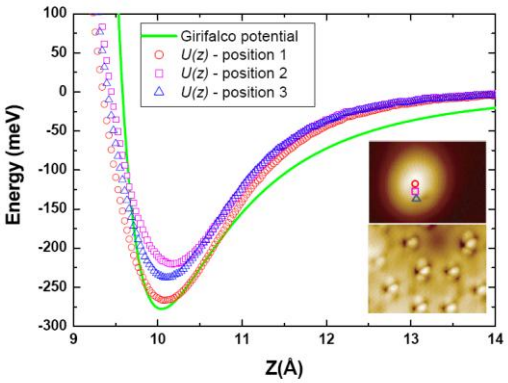

Figure 5-11. C_{60}-C_{60} pair potential energy. The probe is a C_{60} molecule facing with a pentagon down the surface (lower inset). Three *df(z)* spectra were measured at different points on the molecule in the upper inset, *df* = -18.5 Hz. The intermolecular potential energy variation was calculated from these curves and show good agreement (near the equilibrium separations) with the analytical Girifalco potential for the C_{60}-C_{60} interaction (solid green line).

The Girifalco potential was shown to be a very good description of C_{60} interactions when compared to DFT calculations [170]. The potential *U(z)* calculated in this experiment exhibited very good agreement with the Girifalco potential around the equilibrium separation. Differences between the experimental and theoretical data in the repulsive regime (Figure 5-11) almost certainly arise from the relaxation of the molecule-tip and molecule-sample junctions which is not accounted for in the Girifalco potential. This type of effect was previously observed by other research groups for C_{60}-Cu [128] and CO-CO molecule [171] interactions. In the attractive regime of the potential, the differences in the experimental data and the Girifalco potential arise from the dipole moment/change in polarizability resulting from bonding of the C_{60} molecule.

5.7 STM Imaging of C_{60} Molecules with a C_{60} Probe

Hückel molecular orbital theory proved suitable for even more complicated calculations, such as modelling molecular orbitals resulting from the interaction of two C_{60} molecules. In dynamic STM, when a C_{60} molecule is transferred to the tip, Si atoms change their features and C_{60} molecules adsorbed on the surface show a variety of new intramolecular structures.

Hückel molecular orbital theory simulations were used to determine the orientation of C_{60} molecules adsorbed on both the tip and the surface. Sub-molecular features observed on the Si(111)-(7x7) surface played a key role in calculating the orbitals and orientation of the molecule adsorbed on the tip. Once the orientation of the molecule on the tip was determined, the resulting parameters could be used in a 'trial-and-error' method to find the orientation and contribution of the C_{60} molecule adsorbed on the surface. The selection of the best match with experimental images was qualitative (although work is underway to incorporate a more robust matching scheme).

For example, a C_{60}-terminated tip apex facing downward with a single bond slightly tilted yielded the features shown in Figure 5-12b. This sub-molecular structure was checked with Hückel molecular orbital theory simulations to confirm the molecular orientation Figure 5-12a. A C_{60} molecule with a double bond prone to the surface and imaged through an *s* type orbital probe would have the intramolecular structure as calculated in Figure 5-12e. However, the same molecule imaged through a C_{60} probe oriented downward with a single bond slightly tilted produced the sub-molecular features presented in Figure 5-12c,d.

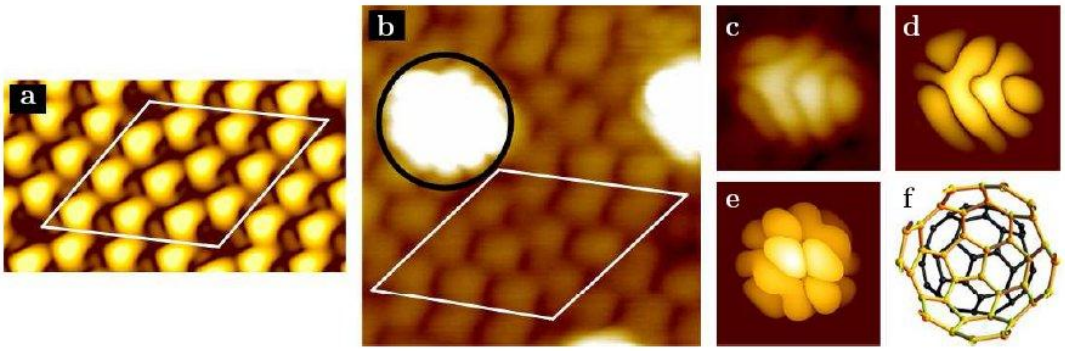

Figure 5-12. Interaction between a molecule with a double bond prone to the surface and a molecule probe facing down with a single bond slightly tilted (ball-and-stick model in **(f)**). **(a)** and **(b)** comparison of theoretical and experimental features observed on Si(111)-(7x7) surface that arise from the probe molecule; **(c)** Dynamic STM image of the molecule marked with black circle in (b). **(d)** The best theoretical match resulted from Hückel molecular orbital theory calculations. **(e)** Calculated molecular orbitals of the C_{60} adsorbed on the surface as if imaged with an *s* type orbital. Imaging parameters: V = 2.3 V, I = 300 pA, A = 1.5 nm.

The convolution of the orbital structure of the on-tip C_{60} molecule with that of the surface-adsorbed molecule produces a wide variety of different patterns of intramolecular contrast. In Figure 5-13 two C_{60} molecules adsorbed on Si(111)-(7x7) and imaged through a C_{60} probe are presented. The C_{60} probe was oriented downward the surface with a double bond, slightly shifted from normal position and produced on Si adatoms an asymmetric double-lobe structure (Figure 5-13a,b,g). For the two C_{60} molecules marked on Figure 5-13g and imaged with the C_{60} probe described above the orientation was calculated with Hückel molecular orbital theory. One molecule was adsorbed to the surface with double bond prone (Figure 5-13c,d) and the other C_{60} molecule with a single bond prone to the surface (Figure 5-13h,i). The theoretical image was constructed considering contribution from a singlet of the HOMO of an on-tip molecule and a singlet of the LUMO of a sample molecule (see also Section 2.6).

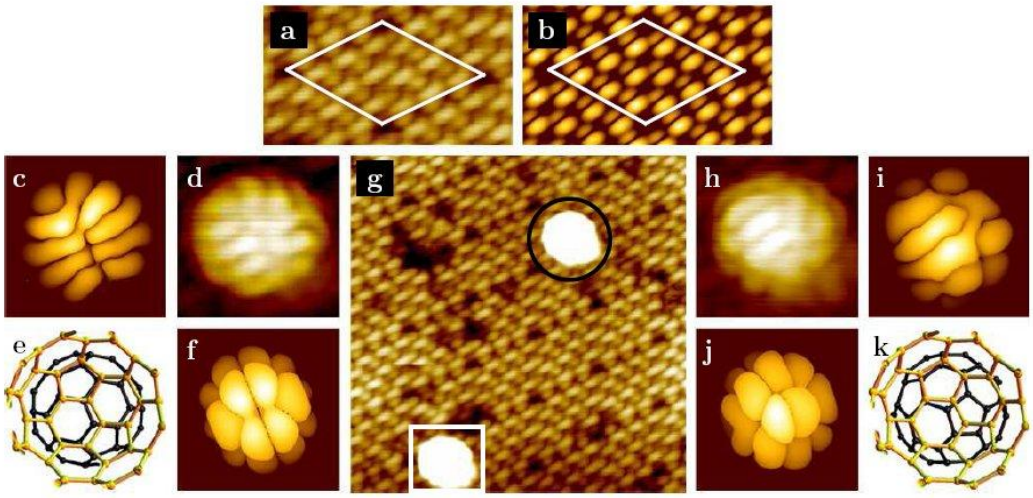

Figure 5-13. (a,g) A C_{60} probe oriented with a double bond down, with the C_2 axis slightly shifted from surface normal, showed nonequivalent double-lobe structure in dynamic STM, as revealed on Si adatoms. **(b)** Hückel molecular orbital theory image of a (7x7) reconstruction calculated for this orientation. **(c-f)** Images of the C_{60} molecule highlighted in black circle in (g), with a double bond prone to the surface. **(h-k)** Images of the C_{60} molecule marked by the white square in (g) with a single bond prone to the surface. **(d, h)** Dynamic STM images. **(c, i)** Simulated images. **(f, j)** Calculated molecular orbitals of the C_{60} adsorbed on the surface as if imaged with an *s* type orbital. **(e, k)** Theoretical models. Imaging parameters: V = 2.4 V, I = 500 pA, A = 1.5 nm.

Orientations of C_{60} molecules adsorbed on Si(111)-(7x7) and imaged with a C_{60} tip, predicted by Hückel molecular orbital theory in this section, were compared to configurations of the C_{60} molecules adsorbed on (7x7) unit cells proposed by Rurali *et al.* [108]. Molecules adsorbed at the M_u site (Figure 5-12b and Figure 5-13g,k) and the R_f binding site (Figure 5-13g,e) were in good agreement with this theory. Therefore the binding site could serve as reference point in further simulations to more rapidly determine the orientation of the C_{60} molecule adsorbed on the surface.

5.8 Summary and Outlook

In conclusion, the highly reactive dangling bond of Si adatoms of (7x7) reconstruction could be used as mini-tips to successfully image various orientations of a C_{60} molecule adsorbed on the tip apex. Hückel molecular orbital theory was employed to provide physical interpretation of the intramolecular structures observed in dynamic STM. Good agreement between theoretical simulations and experiment was found.

Using qPlus AFM in an attractive regime, the chemical reactivity between a silicon dangling bond and a C atom in the C_{60} cage was probed. Force spectroscopy measurements and density functional theory simulations indicate that the formation of an (iono)covalent bond between a C atom and a Si adatom is responsible for the contrast formation mechanism.

All dynamic STM images were recorded at positive bias voltage applied to the sample: therefore, dynamic STM resolved only molecular features arising from HOMO of the on-tip C_{60} molecule. Although future experiments could in principle be carried out at negative bias voltage to reveal orbital characteristics arising from the LUMO of on-tip C_{60} molecule, there are significant constraints with regard to minimising cross-talk between the frequency shift and tunnel current signals which are critically dependent on the magnitude of the bias voltage and the tunnel current. The AFM experiment presented in this chapter could also be repeated in constant-height mode exploiting the repulsive regime of the tip-sample potential.

Using Hückel molecular orbital theory, the orientation and electronic contribution from convoluted orbitals of two C_{60} molecules could also be determined from STM data. The van der Waals interaction between two C_{60} molecules was measured experimentally and found to be in good agreement with the Girifalco potential.

6 Manipulation of C_{60} Molecules on Ag-Si(111)-(√3x√3)R30° using STM

6.1 Introduction

Vertical and lateral manipulation of individual C_{60} molecules for a broad range of systems have been reported in the literature (Section 2.9.2) [115, 116, 118, 120-123, 126]. Controlled manipulation of single molecules was performed with the purpose of building stable and well-defined molecular structures at nanoscale and to characterize surface-adsorbate interactions.

This study focused on manipulation of C_{60} molecules on Ag-Si(111)-(√3x√3)R30° using STM in the VT Omicron system. This experiment was employed as a first step toward manipulation of C_{60} molecules with qPlus AFM at low temperature. The purpose of this experiment was to determine whether controlled positioning of C_{60} molecules was possible on a semiconducting substrate which, unlike the Si(111)-(7x7) and Si(100) surfaces previously used for fullerene manipulation [115, 118, 120, 122, 123], interacted very weakly with the adsorbed molecules.

6.2 Manipulation of C_{60} Molecules on Ag-Si(111)-(√3x√3)R30° at Room Temperature

Controlled manipulation of C_{60} molecules adsorbed on Ag-Si(111)-(√3x√3)R30° was successfully achieved, using the method described in Section 2.9.2 [115, 120-122]. In order to manipulate adsorbates, a threshold force must be reached to surmount the interaction with the substrate [115, 122]. The tip-sample separation was reduced in the close vicinity of the target molecule by decreasing the voltage and by increasing the tunnelling current to ~500 mV and ~1 nA, respectively. For regular scanning, a low current set-point of 50-250 pA was applied to avoid manipulation or removal of the molecule. For values of the tunnelling current higher than 1.5 nA C_{60}

molecules were removed, most likely being transferred to the tip apex during manipulation.

During scanning a considerable number of pick up/drop off events occurred due to the weak interaction of C_{60} molecules with Ag-Si(111)-($\sqrt{3}$x$\sqrt{3}$)R30^o. Molecules were removed or dropped at various spots. It was more difficult to achieve manipulation of molecules bound to surface defects or step edges. Reactive dangling bonds at these sites produce a stronger interaction due, most likely, to covalent bonding with C_{60} molecules. Further increasing the interaction by bringing the tip closer to one of these molecules most often resulted in instability and noise.

The idea was to manipulate a molecule off a defect and transfer it across the surface. If it did not interact with other molecules in its final position then it would diffuse. The starting and final positions were at defects. The experiment focused on manipulation of molecules adsorbed at defects. Therefore, the tip trajectory was set during manipulation to start from a point behind the target molecule and extended to a nearby defect to allow the molecule to bind firmly and remain at the target position (Figure 6-1a,b, 6-2a,b and 6-3a,b). Tunnelling current and height profiles associated with manipulations were not flat (Figure 6-1c,d, 6-2c,d and 6-3c,d). Significant variations were recorded in the tip-sample separation but at room temperature it was not possible to separate them into repulsive and attractive interactions.

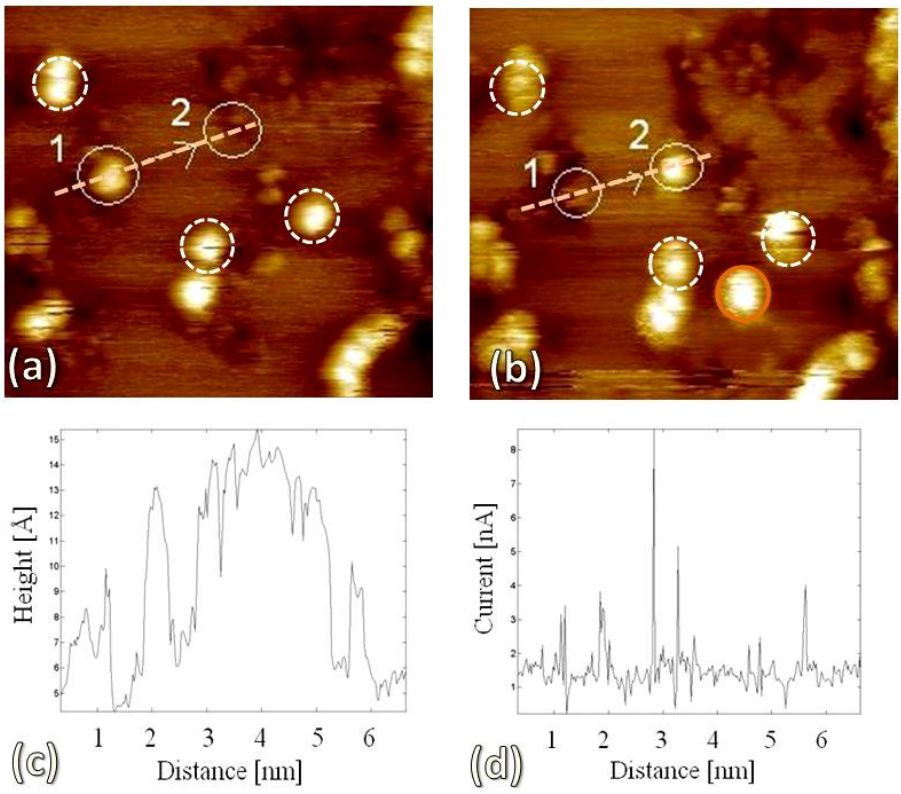

Figure 6-1. Manipulation of a single C_{60} molecule on Ag-Si(111)-(√3x√3)R30°. **(a)** Image recorded before manipulation. **(b)** Image recorded after manipulation. **(c)** Height profile showing tip movement during manipulation. **(d)** Tunnelling current profile measured during manipulation. Dashed, white circles mark reference molecules. Orange, solid circle marks a molecule found on the surface after manipulation. However, other molecules on the terrace did not move. Dashed, orange line marks tip trajectory. The STM tip was positioned close to the molecule found in Position 1. When the tip-sample distance was decreased, due to the strong tip-molecule interaction, the C_{60} molecule from Position 1 followed the tip in the direction indicated by arrow across Ag-Si(111)-(√3x√3)R30° terrace to Position 2. Imaging parameters: 50x50 nm^2, V = 2 V, I = 400 pA. Manipulation parameters: V = 0.4 V, I = 1.1 nA.

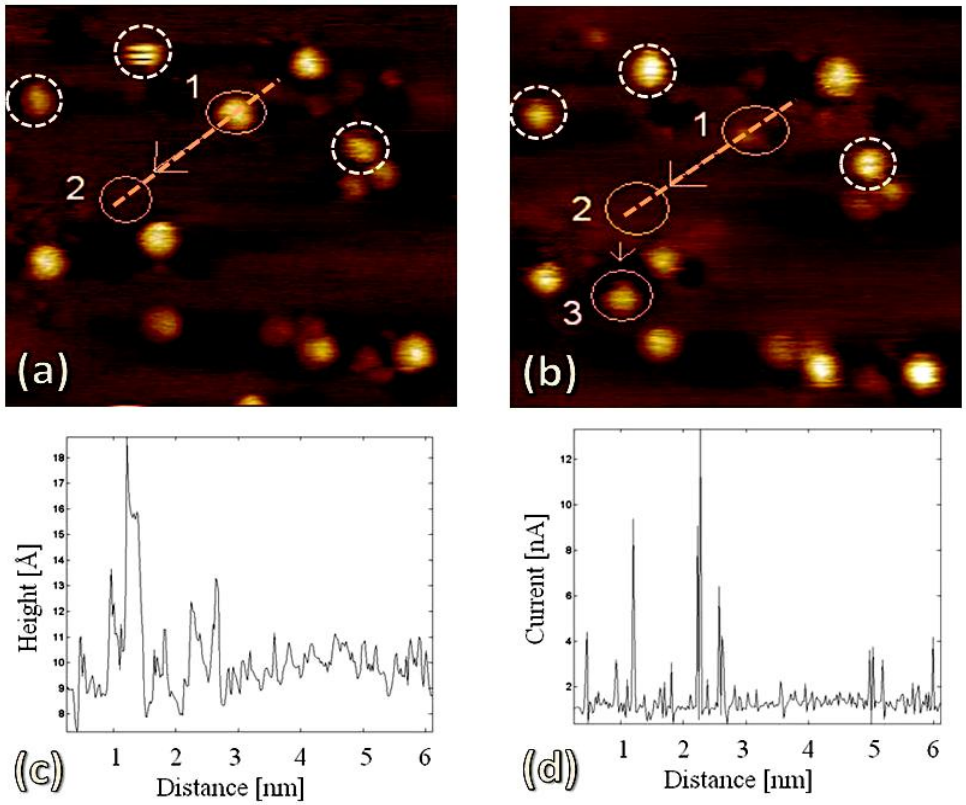

Figure 6-2. Second case of a single C_{60} molecule manipulation on Ag-Si(111)-(√3x√3)R30°. **(a)** Image recorded before manipulation. **(b)** Image recorded after manipulation. **(c)** Height profile showing tip movement during manipulation. **(d)** Tunnelling current profile measured during manipulation. Dashed, white circles mark reference molecules. Dashed, orange line marks tip trajectory. The manipulation procedure followed as presented in Figure 6-1. The molecule was driven from Position 1 to Position 2. At Position 2 the tip retracted. The molecule was then found in Position 3 (image (b)). Several reasons may explain why the molecule could not be found in Position 2 in image (b). The defect edge close to Position 2 might have caused the molecule to reach to Position 3 or the molecule could have been picked up by the tip at some point on the manipulation trajectory and dropped in Position 3 during the check scan. Also another molecule from the tip, different from the molecule picked in Position 1, could have been dropped by the tip in Position 3. Imaging parameters: 45x45 nm^2, V = -2 V, I = 600 pA. Manipulation parameters: V = 0.3 V, I = 1.0 nA.

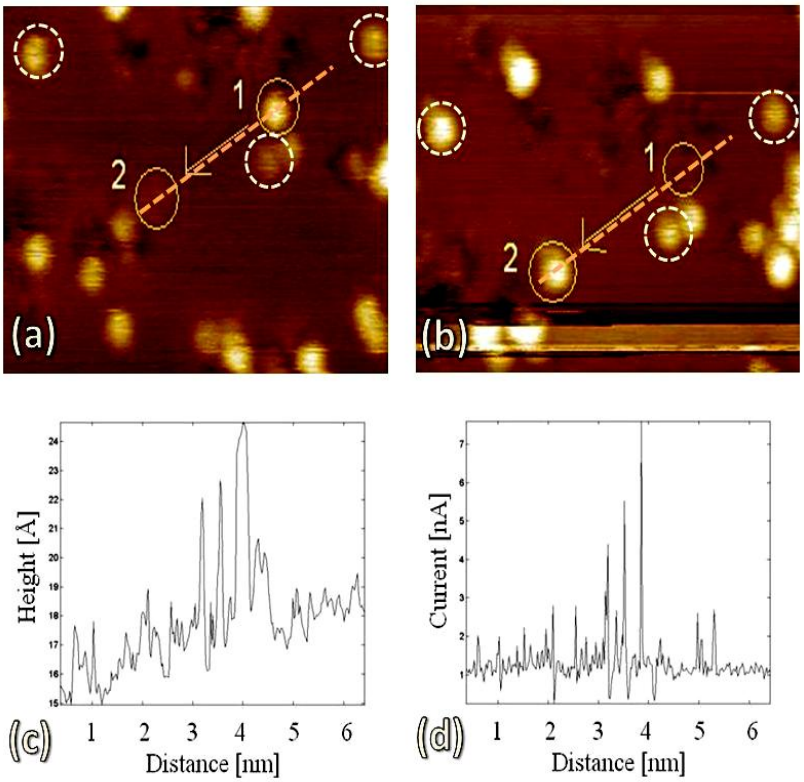

Figure 6-3. A third case of controlled manipulation of a C_{60} molecule on Ag-Si(111)-(√3x√3)R30°. **(a)** Image recorded before manipulation. **(b)** Image recorded after manipulation. **(c)** Height profile showing the tip movement during manipulation. **(d)** Tunnelling current profile measured during manipulation. Dashed, white circles mark reference molecules. Dashed, orange line marks tip trajectory. The molecule was moved from Position 1 to Position 2. Transversal lines at the bottom of image (b) represent instabilities at the tip apex resulted after manipulation. Imaging parameters: 45x45 nm^2, V = -2 V, I = 600 pA. Manipulation parameters: V = 0.3 V, I = 1.0 nA.

6.3 Manipulation of C_{60} Molecular Islands at 100 K

After deposition on Ag-Si(111)-(√3x√3)R30°, C_{60} molecules diffused at room temperature and formed close-packed hexagonal islands. Subsequently, the sample was cooled to 100 K with the tip remaining at room temperature. A number of manipulation attempts were performed at 100 K on Ag-Si(111)-(√3x√3)R30° surface on the variable temperature Omicron system at low temperature in order to remove C_{60} molecules from the island edge and to drag them with the STM tip across the Ag-Si(111)-(√3x√3)R30° surface to a preset spot (Figure 6-4). The results are presented in this section.

Removal of C_{60} molecules from the island edge, by breaking the intermolecular bonds, and their translation in a controllable manner to a specific location were the purpose of this experiment. When the tip was placed above the target molecule, the interaction with the tip was strong enough to pull the molecule with the tip.

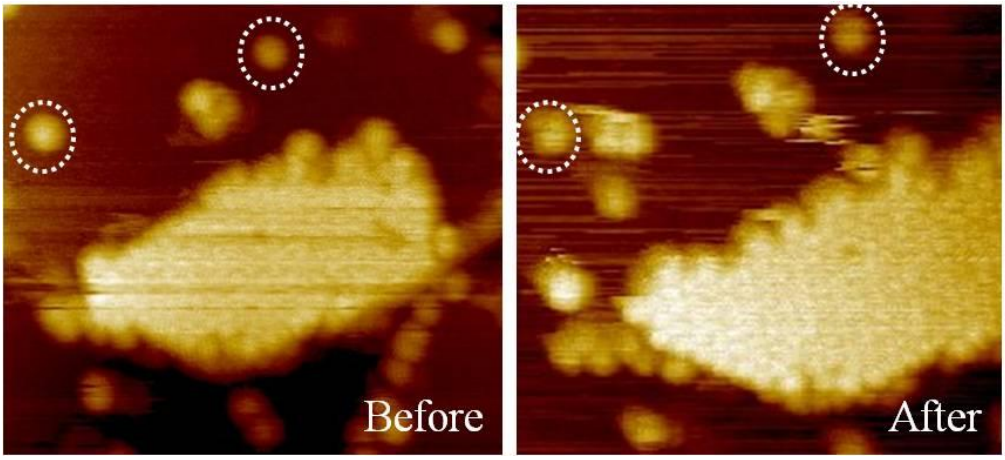

Figure 6-4. C_{60} manipulation at 100 K. Images were recorded before and after manipulation. The island edge was modified by removing molecules and dragging them across the surface. Dashed circles mark two molecules which may be used as reference points. Before manipulation, on the left side of the terrace a small number of molecules can be identified: two single molecules and a cluster of three molecules. After manipulation the number of the molecules on the upper terrace increased by six molecules. The edge of the island was visibly changed. Imaging parameters: 50x50 nm^2, V = 2.8 V, I = 100 pA. Manipulation parameters: V = 1.5-2 V, I = 0.8-1.5 nA.

After several manipulation events modification of the island shape could be observed (Figure 6-5). More precisely, C_{60} molecules were removed from the top-left edge of the island and dragged across the surface. Therefore, molecules were missing from the top-left edge, leaving an empty space. At the same time, the number of the molecules present on the left terrace was significantly increased. Some molecules were picked up from the island edge during scanning or manipulation (Figure 6-5). Bright stripes seen in the image could be the result of a weakly bound molecule that bounces on the tip apex due to interaction with the surface.

C_{60} molecules were either pulled or pushed by the tip. The height profiles shown in Figure 6-6 would suggest that movement of the molecule was via both attractive and repulsive forces, but the sample temperature of 100 K appears to be

still too high for controlled motion of the molecules. This contrasted with previous experiments on C_{60} manipulation on Si surfaces [115, 120-122] where regular hops or rolling was demonstrated due to the character and configuration of bonding with the substrate. Fully controlled manipulation based only on tip-molecule interaction was not achieved; however, the experiment might be improved with a better set of manipulation parameters to assure a constant interaction between the tip and the molecule.

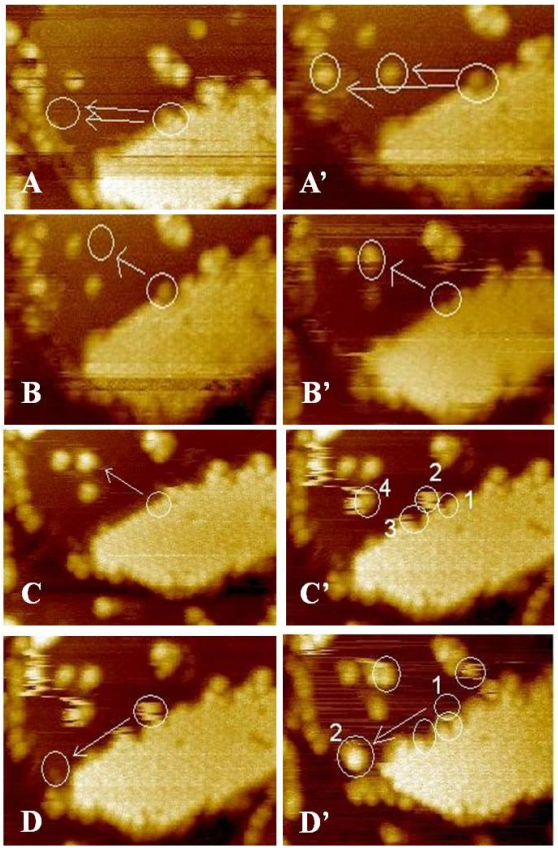

Figure 6-5. Successive manipulation events at 100 K. (A-D) before manipulation. (A'-D') after manipulation. Individual C_{60} molecules were removed from the island edge and translated in the direction indicated by arrows. **(A-A')** Two molecules were removed from the island edge following the tip in two successive manipulation attempts. Imaging parameters: 50x50 nm^2, V = -2.9 V, I = 100 pA. Manipulation parameters: V = -1.5 V, I = 1 nA. **(B-B')** Single molecule manipulated in the arrow's direction. Imaging parameters: 50x50 nm^2, V = -2.9 V, I = 100 pA. Manipulation parameters: -1.5 V, 0.8 nA. In **(C')** and **(D')** more molecules became mobile after lateral manipulation applied on a single molecule. Multiple white circles highlight these molecules or spots where molecules were missing. Therefore, more molecules than manipulation attempts were moved and total number of molecules removed from the island edge cannot be fully appreciated.

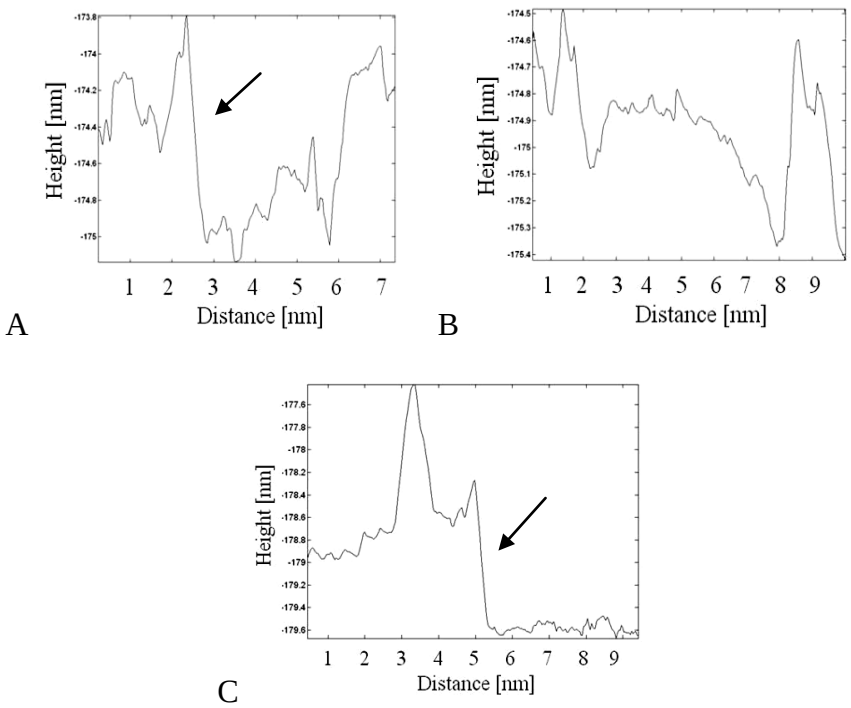

Figure 6-6. Height profiles recorded during the manipulation experiment in Figure 6-5. The **(A)** and **(B)** profiles correspond to Figure 6-5A-A'. Profile **(C)** corresponds to Figure 6-5B-B'. Black arrows indicate a sudden, long drop in the profile. At this point, the tip moved closer to the surface because the C_{60} molecule was pushed laterally away in front of the tip (repulsive manipulation)

Typical ranges for the tunnelling parameters in the experiment presented in this chapter were between 0.8-1.5 nA current and ± 0.3 to ± 2 V bias voltage. The bias voltage used for manipulation at room temperature was mainly positive and the interaction was overall attractive. For manipulation examples at 100 K the bias voltage was negative for most attempts and in some cases clear evidence of repulsive manipulation was recorded. However, due to the small data set, a firm, general conclusion regarding the influence of polarity voltage on the mode of manipulation cannot be drawn.

Significant difficulties occurred due to weak adsorption of the molecules. When one or two molecules were removed from the island edge, neighbouring molecules became mobile and diffused on the surface. This happened more strongly while scanning over the island. On a few occasions, smaller islands even rearranged.

Scanning and manipulation of C_{60} molecules on Ag-Si(111)-(√3x√3)R30° was not trivial, because even at low sample temperature a considerable

number of uncontrolled pick-up/drop-off events occurred. C_{60} molecules could be manipulated when the tip was brought in good state, stable, and rigid. More than one molecule could be manipulated individually in one measurement, until the tip structure changed. Often, the tip-molecule interaction was not strong enough to produce manipulation regardless of the tip-molecule separation or manipulation parameters. In these cases, a tip covered by C_{60} molecules was assumed. Therefore, the interaction between the C_{60} molecules on the tip and the target molecule was too weak to produce manipulation.

In this experiment, all molecules were moved in one attempt. Manipulation trajectories were not set repeatedly back and forward. If the end of the tip was not rigid, instabilities might have occurred during the transition to manipulation when the parameters were modified by a significant order of magnitude or voltage polarity was reversed. Any change in the parameter value automatically adjusted the tip-sample separation, intensity and flow of the tunnelling current between the tip and the sample.

6.4 Summary and Outlook

To conclude, controlled manipulation of single C_{60} molecules on Ag-Si(111)-(√3x√3)R30° was demonstrated. C_{60} molecules were moved across Ag terraces between defective sites. Moreover, individual molecules were removed from the edges of C_{60} islands and translated across the surface. It was not possible to distinguish between attractive/repulsive interaction between tip and C_{60} molecules. Due to the weak adsorption of the molecules on the Ag-Si(111)-(√3x√3)R30°, the tip-molecule interaction could be considered responsible for manipulation process.

Significant difficulties were encountered due to the high thermal energy and mobility of the molecules on the surface and at the tip apex. A considerable number of undesired pick-up and drop-off events of the C_{60} molecules occurred. To overcome these barriers and improve experimental conditions, further manipulation measurements could be performed at low temperature using the Omicron STM/qPlus AFM system.

At low temperature, stability during manipulation might be increased. Resolution of internal structure might provide information on the molecular orientation before and after manipulation. Furthermore, the force of interaction between C_{60} molecules and Ag-Si(111)-(√3x√3)R30^o surfaces might be quantified by performing manipulation with qPlus AFM. These potential results would be compared to the interaction of the C_{60} molecule with a highly reactive surface like Si(111)-(7x7).

7 Conclusions

Scanning probe microscopy has been a powerful technique for imaging organic molecules and surfaces with resolution down to the atomic level. STM and AFM have proven suitable not only for very high resolution topographic and spectroscopic imaging, but also for precisely controlled molecular manipulation. Research carried out during this Ph.D. has revealed new physical and electronic properties of C_{60} molecules interacting with Ag-Si(111)-($\sqrt{3}$x$\sqrt{3}$)R30^{o} and Si(111)-(7x7) surfaces.

Interaction of C_{60} molecules with Si(111)-(7x7) surfaces was investigated at 77 K with the low temperature Omicron system. Imaging, spectroscopy and manipulation were effected using dynamic STM and non-contact AFM with a qPlus sensor. In dynamic STM, intramolecular resolution was probed. Molecular orbital structure was analyzed with Hückel molecular orbital theory data. Most observed sub-molecular features had been previously revealed in experiments or theoretical simulations and were attributed to one of the possible orientations of the adsorbed molecule. However, new intramolecular structures were also recorded. Some of them were only recently predicted in theoretical calculations. Those structures were probed with a C_{60} molecule on the tip apex. Using Hückel molecular orbital theory, simulations of the orientation of both on-sample and on-tip adsorbed molecules, which could have yielded that type of electronic orbital, were determined.

Using qPlus AFM, individual molecules were resolved on Si(111)-(7x7) in frequency modulation mode, attractive regime. They appeared as bright spherical protrusions with an apparent diameter of 1-1.5 nm, depending on the tip radius of curvature. Frequency shift spectra were acquired in order to determine the Si tip-C_{60} molecule force and the potential energy of interaction. By decreasing tip-sample separation, C_{60} molecules could be maintained in a strong interaction with the tip and forced to move in the scanning direction. Before manipulation, *df-vs-z* spectra were acquired in order to approximate the force required to move a C_{60} molecule on the Si(111)-(7x7) surface. More measurements could be performed to develop a more

precise method to manipulate molecules using AFM. Further investigations could be done in constant-height mode so as to achieve sub-molecular resolution of C_{60} molecules on Si(111)-(7x7).

Another set of experiments consisted of imaging Si(111)-(7x7) with a C_{60} molecule on the tip. For this purpose, a molecule was picked up from the surface by lateral or vertical manipulation. As soon as the atomic contrast changed, the scan size was reduced to comprise only a clean area of Si. Sub-molecular features revealed using dynamic STM experiments were consistent with Hückel molecular orbital theory simulations for each of the three symmetry orientations C_2, C_3, and C_5. In each case, the C_{60} molecule was oriented with a double bond, a hexagon, or a pentagon downward, respectively. Shape and size of the electronic structure could be tuned by varying the rotation or adsorption angle of the molecule on the tip.

Very sharp resolution of on-tip C_{60} orbitals was achieved with qPlus AFM, (frequency-modulation, attractive regime of tip-sample potential). Measurements showed two maxima per Si adatom for C_2 and five for C_5. The image of the C_5 orientation, pentagon pointing down, was an AFM image showing five maxima per Si adatom. SIESTA DFT force spectroscopy simulations were performed to understand contrast formation in AFM. These simulations supported the hypothesis that in AFM, atomic contrast in the C_{60} cage was probed and the (iono)covalent bond was the imaging mechanism. Tuning the orbital shape in AFM was not as flexible and rich in variation as in dynamic STM imaging. Future experiments might focus on probing the force of interaction between the on-tip molecule and Si adatoms for C_2, C_3, and C_5 orientations. The aim would be to obtain a force map in each case. In order to run grid spectroscopy, the system should be cooled to 5 K using liquid helium.

Manipulation experiments at 100 K performed on Ag-Si(111)-($\sqrt{3}$x$\sqrt{3}$)R30^o surface showed that C_{60} molecules could be extracted from an island edge and dragged across the surface. The manipulation method was simple and consisted of placing the tip above a molecule and increasing tip-molecule interaction by decreasing the separation. Movement of the molecule, dictated by the interaction of the tip and the surface, was printed in the line profile recorded along the

manipulation trajectory. As read in height and current traces, the motion of the molecules was arbitrary. Most likely due to very weak molecule-surface interaction, the type of molecule movement could not be controlled. The molecule could be moved in an attractive or repulsive mode, *i.e.*, pulled or pushed.

In the VT Omicron system the tip was held at room temperature. For this reason many undesirable molecular pick up/ drop-off events occurred during the manipulation attempts. Manipulation of C_{60} molecules on Ag-Si(111)-($\sqrt{3}$x$\sqrt{3}$)R30^{o} was also performed at room temperature. Height and current traces recorded during manipulation revealed a dominant, attractive interaction between tip and molecule.

Future experiments to manipulate C_{60} on Ag-Si(111)-($\sqrt{3}$x$\sqrt{3}$)R30^{o} could be performed at low temperature. With both tip and sample cooled to 77 K or 5 K, greater control of the manipulation process would be expected. Due to the extremely low temperature, molecular rotation and diffusion would be suppressed and the probability of tip contamination with C_{60} would be dramatically reduced, leading to more consistent spectroscopic results. Ultimately, the goal would be to perform controlled manipulation using qPlus AFM.

Appendix - Ionic Liquid on Au(110)-(2x1)

A.1 Introduction

An ionic liquid [172] is an organic salt composed of ion pair molecules, an anion and the other a cation. Its behavior in bulk or at an interface is rather complicated due to various interactions: Coulomb, van der Waals, dipole-dipole, or hydrogen bonds [173]. Studies have focused on molecular structure, intermolecular interactions, molecular-solid interface, and physicochemical properties of ionic liquids [173]. The interaction of ionic liquids with solid surfaces has been useful for catalysis, electrodeposition, or dye-sensitized solar cells.

Studies of ionic liquids have attracted increased interest as candidates for solvents in chemical synthesis [174] or electrochemistry [175]. Ionic liquids have remarkable properties, such as high conductivities, very low vapour pressures, wide electrochemical windows, novel solvencies, and catalytic behavior [176]. Fine tuning of properties can be obtained with careful selection of the cations and anions and also of the variations in the molecular structure.

Scanning tunnelling microscope investigations on ionic liquids have been several. For example, studies of ionic liquids on Au(100) [176] or Au(111) [174] demonstrated that the interaction could be sufficiently strong to produce surface etching or restructuring. Ionic liquid on Au(100) could form ordered molecular structures with the cation binding to the surface [176]. These measurements were performed under electrochemical control. The interaction of one monolayer of ionic liquid with Au(111) was studied only recently with STM in UHV [177]. Ionic liquid molecules formed short-range ordered structures when frozen at 210 K. These structures could be the result of ion pairs arranged in a double or single layer if both the anion and the cation were bound to the surface. Measurements at higher temperature showed mobility of the ionic liquid.

A.2 Au(110)-(2x1) Sample Preparation

The Au(110) sample used in the experiments was a single crystal substrate. After being ultrasonicated in organic solvents, the sample was mounted on a standard Omicron indirect heating sample holder. Cleaning and the preparation of the Au(110) surface which led to (2x1) reconstruction took place under ultrahigh vacuum conditions.

The surface was prepared by sputtering with Ar ions and annealing. First, the sample was annealed up for at least 30 min at 500^{o} C for outgassing the residual atoms or molecules. Annealing was followed by Ar ion sputtering. The process took ~20-30 min at 1 KeV beam energy. The ion source allowed control of the beam direction and intensity. By sputtering the contaminated top layers were removed.

Sputtering was done using an ISE 5 ion source. Argon gas was introduced via a gas inlet to a gas cell. The gas cell was fitted with an anode-cathode pair. By applying a voltage between the two electrodes a gas discharge was initiated. A longitudinal magnetic field was created by an external permanent magnet. This assured a spiral path for the electrons, and permitted large ion and electron generation. The ion beam was focused in the flight tube toward the sample where the ion current hitting the sample was measured and displayed on the ISE 5 Gun Control. For Ar ion gas a pressure in the range of 10^{-6} mbar was permitted in the chamber. During sputtering the ion pump was switched off due to incompatibility with the argon ions and the gas was pumped down using the turbomolecular pump.

The last step was to anneal the sample for ~30 min at 500^{o} C. Heating the sample was necessary to repair damage caused during sputtering and to obtain the (2x1) reconstruction.

A.3 Ionic Liquid Deposition

For deposition of ionic liquid, an evaporator built by Dr. Richard Foulston, School of Chemistry Nottingham was used. The set-up containing the evaporation source was mounted in an external vacuum arm attached to the

preparation chamber. The set-up consisted of the evaporator, a collimator and an ionisation gauge. A glass vial with ~1 ml of ionic liquid was inserted into the Cu tube of the evaporator. The tube was heated by a tungsten halogen light bulb. A K-type thermocouple was used to measure the temperature.

This evaporation method is called vapour phase deposition. The vapour of ionic liquid passes through a tube where is collimated into a molecular beam. The ionisation gauge is placed between the collimator and sample with the purpose of monitoring the intensity and stability of the flux. When the evaporator was operated at temperatures of 423-523 K, a deposition rate of <1 monolayer/min was achieved.

A.4 Au(110)-(2x1) Reconstruction

Au substrates have been of great interest and have been intensively studied because they offer an inert surface, which allows formation of supramolecular structures in periodic networks. Their application in heterogeneous catalysis and their straight-forward preparation procedure (which yields long-range ordered domains) classify the Au surface as one of the most important systems in surface science.

The (110) surface of an Au crystal builds close-packed rows (1x1) surface [178]. The separation between rows is a_0 = 4.078 Å. By heating the substrate, the rows rearrange into a (2x1) reconstruction [179]. This reconstruction is called missing row model, in which every other row is missing (Figure A-7-1). Distance between the rows in the first layer will become $2a_0$ = 2x4.078 Å.

STM topographic images show large terraces of parallel rows with a high density of atomic steps on the Au surface. Based on STM measurements, domain boundaries formed on Au(110)-(2x1) can be classified after additional or missing rows in the reconstruction. Four main categories were found: solid wall, truncated, solid wall, hollow wall and truncated hollow wall [180].

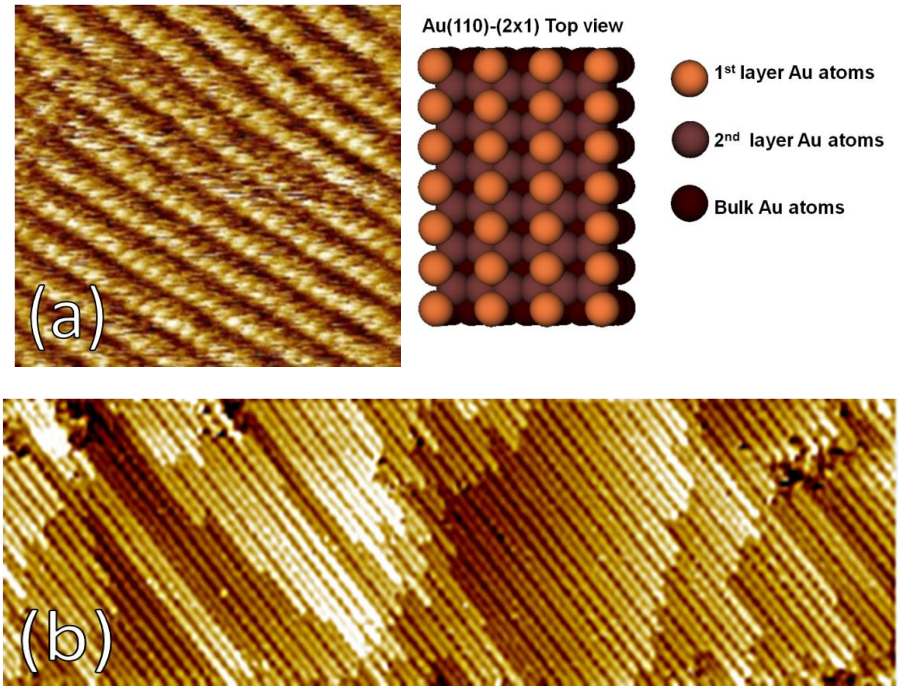

Figure A-7-1. Au(110)-(2x1) surface. **(a)** Atomic resolution. Imaging parameters: 10 nm, -0.6 V, 300 pA and theoretical model of (2x1) missing row reconstruction. **(b)** Au(110)-(2x1) rows and high density of steps. Imaging parameters: cut from 100 nm, -0.2 V, 800 pA.

An Au(110)-(2x1) surface was prepared and imaged with an UHV Omicron STM/AFM system. Large scale images show small scale terraces with row reconstruction and a high density of steps (Figure A-7-1b). Atomic resolution was recorded at room temperature (Figure A-7-1a). Au(110)-(2x1) was used in further experiments for organic molecule deposition. The Au surface provides a very weak interaction with adsorbates allowing free diffusion at room temperature so that molecules can self-assemble in long-range ordered networks.

A.5 Imaging of Ionic Liquid on Au(110)-(2x1) using STM

Experiments presented in this section with 1-ethyl-3-methyllimidazolium bis[(triflouromethyl)sulfonyl]imide $[C_2C_1Im][Tf_2N]$ on Au(110)-(2x1) focused on adsorption and desorption of ionic liquid layers (Figure A-7-2). The aim of this study was to observe the behavior of individual ions at nanoscale in interactions with the crystalline corrugation of the surface. This experiment sought to determine how ultra-thin liquid layers grow and order with the corrugation of the substrate. Au(110)-

(2x1) seemed appropriate for this study due to its weakly reactive and anisotropic surface. The ionic liquid $[C_2C_1Im][Tf_2N]$ was chosen for its electrical conductivity, thermal stability, low reactivity, and low vapour pressure.

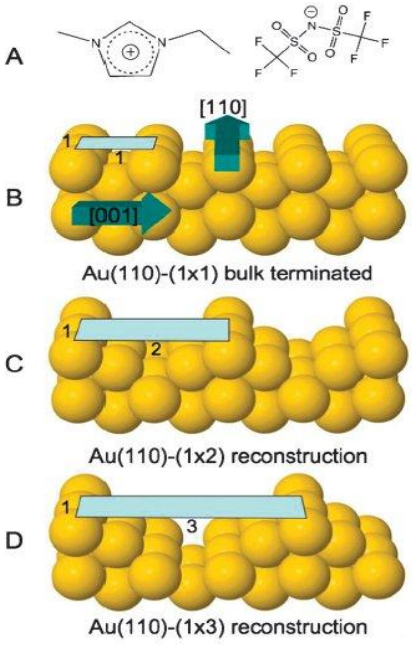

Figure A-7-2. Schematic of **(A)** ionic liquid $[C_2C_1Im][Tf_2N]$ and **(B-D)** possible reconstructions of Au(110) surface. (Figure from [181])

STM measurements at room temperature did not provide useful information because of molecular diffusion, a problem also encountered by Waldmann *et al.* [177]. When the sample was cooled to liquid nitrogen temperature, molecules formed ordered domains aligned along the rows of Au(110)-(2x1) reconstruction in the (110) direction with a separation of (2x1) in the [001] direction (Figure A-7-3). The anion and cation of the ionic liquid appeared as a single entity in a monolayer, confirming the lack of dissociation. $[C_2C_1Im][Tf_2N]$ apparently adsorbed on Au(110)-(2x1) without decomposition.

STM images of different coverage of ionic liquid were recorded at low temperature (Figure A-7-3). At ~128 K ionic liquid adsorbed in the position where it reached the surface producing layer by layer growth. Adsorption at room temperature resulted instead from droplet formation. With time, the energy activation barrier was overcome by ion pairs [182]. These molecules broke the mutual attractive interaction

of their dipoles and dissociated or moved to allow multilayer growth on the surface [182].

For sub-monolayer coverage, the ionic liquid formed 2D islands (Figure A-7-3A). For coverage of about one monolayer, individual "objects" formed rows running parallel to the [110] direction of the (2x1) reconstruction (Figure A-7-3B,C). Anions and cations could not be distinguished on the surface, which may denote that each individual "object" could be a neutral ion pair. Individual "objects" were clearly resolved in both the first and second monolayers. The second monolayer was ordered in the same style, with rows in the direction dictated by the first monolayer (Figure A-7-3D). However, locally, the ionic liquid showed a different organization or a trend toward aggregation.

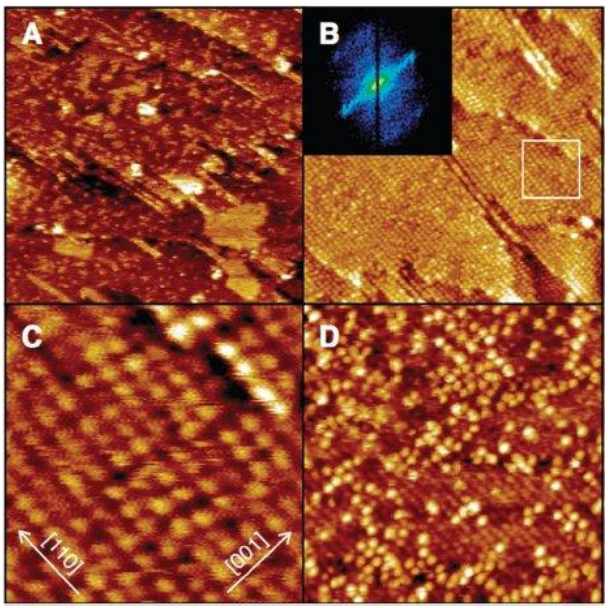

Figure A-7-3. Low temperature STM images showing different coverage of ionic liquid $[C_2C_1Im][Tf_2N]$ on Au(110)-(2x1). **(A)** 2D islands of ionic liquid. **(B)** One monolayer coverage of ionic liquid. Image **C** was a zoom of area marked on image B. The inset in image B was a Fourier transform of the image B indicating one-dimensional ordering of the rows. Image **D** was obtained after deposition of more than one monolayer. Typical scanning parameters: V = 1.7-2 V, I = 100-200 pA.

Domains with particular orientations have not been observed in present STM measurements, the unidirectional orientation of ionic liquid denoting that (2x1) reconstruction of Au surface was still preserved to some extent. A (1x1) surface

would facilitate locally ordered islands. A (2x1) arrangement of ionic liquid was not confirmed with low energy electron diffraction (LEED) measurements at room temperature. LEED data only demonstrated a weak (2x1) periodicity that fades with increasing number of ionic liquid layers. High mobility and disorder of ionic liquid at room temperature on a (1x1) surface could explain this difference. At low temperature a (2x1) ordering of ionic liquid could be induced by local (2x1) reconstruction of the Au(110) surface.

Surface structure was investigated at liquid nitrogen temperature following annealing of the sample and desorption of ionic liquid multilayers (Figure A-7-4). Annealing the sample at ~373 K left about one monolayer of ionic liquid on the surface. The ordering showed close-packed rows of "objects" aligned to [110] direction (Figure A-7-4A). After raising the temperature to ~523 K, the coverage decreased below one monolayer (Figure A-7-4B). The (2x1) rows of ionic liquid in [001] direction exhibited a zigzag structure. Separation between the ionic liquid rows increased to (3x1). No specific ordering of ionic liquid was observed in (3x1) rows. The (3x1) reconstruction of Au substrate dominated over (2x1) after ~1 min annealing at ~553 K (Figure A-7-4C). After ~5 min annealing at the same temperature, the ionic liquid coverage was reduced to isolated patches, leaving a (3x1) reconstructed Au(110) (Figure A-7-4D). This surface morphology was confirmed with LEED and ultraviolet photoelectron spectroscopy (UPS).

Complete removal of ionic liquid occurred at ~600 K. During the desorption process Au surface reconstruction reverted to (2x1). The (3x1) periodicity of Au(110) also changed to (2x1) by electron beam induced dissociation and complete desorption of ionic liquid during LEED measurements. This process sustained the hypothesis that (3x1) reconstruction was formed and maintained by presence of ionic liquid and not by arrangement of ionic liquid on a (1x1) surface.

UPS spectra also demonstrated that ionic liquid adsorbed as neutral ion pairs without dissociation of the covalent bonds within ions. These measurements showed a strong bonding of ionic liquid on Au(110) (chemisorption) and formation of specific interface states. However, no surface charging was recorded.

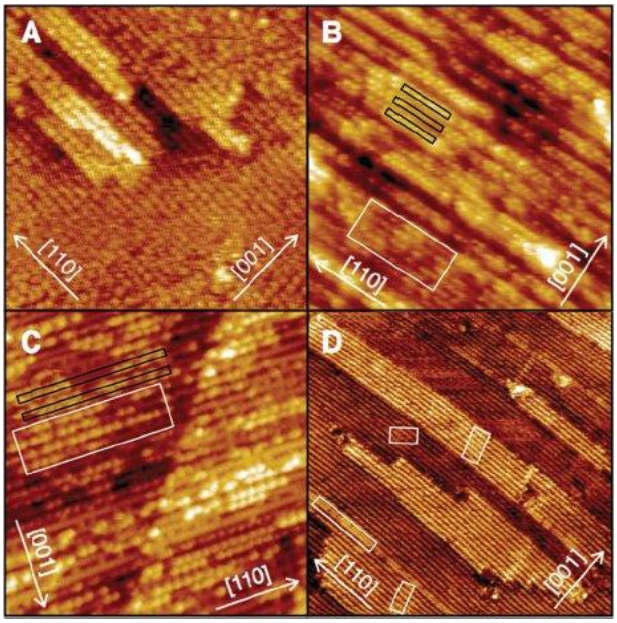

Figure A-7-4. Low temperature STM images of ionic liquid on Au(110) after annealing at various temperatures: **(A)** ~373 K, **(B)** ~523 K for 1 min, **(C)** ~553 K for 1 min, **(D)** ~553 K for 5 min. White rectangles show well-resolved "objects".

A.6 Summary and Outlook

In conclusion, interaction of $[C_2C_1Im][Tf_2N]$ with Au(110)-(2x1) was investigated with STM, LEED, and UPS, via adsorption and desorption mechanisms. Ionic liquid adsorbed unidirectional on Au(111))-(2x1) as a single entity without dissociation of anion-cation pairs, ordered in rows parallel to the surface reconstruction. During desorption at elevated temperatures, the ionic liquid sub-monolayers formed specific interface states with Au(110)-(2x1) inducing the formation of a (3x1) reconstruction. After complete desorption the surface reverted to a (2x1) reconstruction and remained without any residue of the ionic liquid. Future work might involve STM analysis at 77 K of orientation and internal structure of individual ion pairs and their bonding configurations with the substrate.

List of References

[1] Langa, F. and J.-F. Nierengarten, *Fullerenes Principles and Applications*. 2007, Cambridge: The Royal Society of Chemistry.

[2] Shinar, J., Z.V. Vardeny, and Z.H. Kafafi, *Optical and Electronic Properties of Fullerenes and Fullerene-Based Materials*. 2000, New York: Marcel Dekker, Inc.

[3] Andreoni, W., *The Physics of Fullerene-Based and Fullerene-Related Materials*. 2000, Dordrecht: Kluwer Academic Publishers.

[4] Nejo, H., *Nanoeletrodynamics. Electrons and Electromagnetic Fields in Nanometer-Scale Structure*. 2003, Berlin: Springer-Verlag.

[5] Nejo, H., *Nanostructures-Fabrication and Analysis*. 2007, Berlin: Springer-Verlag.

[6] Wang, C. and C. Bai, *Single Molecule Chemistry and Physics*. 2006, Berlin: Springer-Verlag.

[7] Crommie, M.F., C.P. Lutz, and D.M. Eigler, *Science*, 1993. **262**: p. 218.

[8] Eigler, D.M. and E.K. Schweizer, *Nature*, 1990. **344**: p. 524.

[9] Heller, E.J., M.F. Crommie, C.P. Lutz, and D.M. Eigler, *Nature*, 1994. **369**: p. 464.

[10] Mamoharan, H.C., C.P. Lutz, and D.M. Eigler, *Nature*, 2000. **403**: p. 512.

[11] Hla, S.W., K.F. Braun, and K.H. Rieder, *Phys. Rev. B*, 2003. **67**: p. 201402(R).

[12] Hla, S.W., K.F. Braun, B. Wasserman, and K.H. Rieder, *Phys. Rev. Lett.*, 2004. **93**: p. 208302.

[13] Neu, B., G. Meyer, and K.H. Rieder, *Appl. Phys. (RC) A*, 1995. **60**: p. 343.

[14] Bartels, L., G. Meyer, and K.H. Rieder, *Phys. Rev. Lett.*, 1997. **79**: p. 697.

[15] Bartels, L., G. Meyer, and K.H. Rieder, *Appl. Phys. Lett.*, 1997. **71**: p. 213.

[16] Grill, L., F. Moresco, P. Jiang, C. Joachim, A. Gourdon, and K.H. Rieder, *Phys. Rev. B*, 2004. **69**: p. 035416.

[17] Sugimoto, Y., M. Abe, S. Hirayama, N. Oyabu, O. Custance, and S. Morita, *Nature Materials*, 2005. **4**(2): p. 156.

[18] Sugimoto, Y., P. Jelinek, P. Pou, M. Abe, S. Morita, R. Pérez, and O. Custance, *Phys. Rev. Lett.*, 2007. **98**: p. 106104.

[19] Sugimoto, Y., Y. Nakajima, D. Sawada, K. Morita, M. Abe, and S. Morita, *Phys. Rev. B*, 2010. **81**: p. 245322.

[20] Sugimoto, Y., P. Pou, M. Abe, P. Jelinek, R. Perez, S. Morita, and O. Custance, *Nature*, 2007. **446**(7131): p. 64.

[21] Sugimoto, Y., P. Pou, O. Custance, P. Jelinek, M. Abe, R. Perez, and S. Morita, *Science*, 2008. **322**(5900): p. 413.

[22] Amer, M.S., *Raman Spectroscopy, Fullerenes and Nanotechnology*. 2010, Cambridge: RSC Publishing.

[23] Wolf, E.L., *Nanophysics and Nanotechnology*. 2006, Weinheim: Wiley-VCH Verlag.

[24] Meyer, E., Hug Hans Josef, and Bennewitz Roland, *Scanning Probe Microscopy*. 2004, Berlin: Springer-Verlag.

[25] Pradeep, T., *Nano: The Essentials: Understanding Nanoscience and Nanotechnology*. 2008, New Delhi: Tata McGraw-Hill Publishing.

[26] Hornyak, G.L., Tibbals Harry L., Dutta Joydeep, and Moore John J., *Introduction to Nanoscience & Nanotechnology*. 2009, Boca Raton: CRC Press Taylor & Francis Group.

[27] Upward, M.D., P. Moriarty, and P.H. Beton, *Phys. Rev. B*, 1997. **56**(4): p. R1704.

[28] Nakayama, T., J. Onoe, K. Takeuchi, and M. Aono, *Phys. Rev. B*, 1999. **59**(19): p. 12627.

[29] Tsuchie, K., T. Nagao, and S. Hasegawa, *Phys. Rev. B*, 1999. **60**(15): p. 11131.

[30] Hou, J.G., J.L. Yang, H.Q. Wang, Q.X. Li, C.G. Zeng, H. Lin, W. Bing, D.M. Chen, and Q.S. Zhu, *Phys. Rev. Lett.*, 1999. **83**(15): p. 3001.

[31] Pascual, J.I., J. Gomez-Herrero, C. Rogero, A.M. Baro, D. Sanchez-Portal, E. Artacho, P. Ordejon, and J.M. Soler, *Chem. Phys. Lett.*, 2000. **321**(1-2): p. 78.

[32] Schull, G. and R. Berndt, *Phys. Rev. Lett.*, 2007. **99**(22): p. 226105.

[33] Hou, J.G. and K. Wang, *Pure and Applied Chemistry*, 2006. **78**: p. 905.

[34] Hou, J.G., J.L. Yang, H.Q. Wang, Q.X. Li, C.G. Zeng, L.F. Yuan, B. Wang, D.M. Chen, and Q.S. Zhu, *Nature*, 2001. **409**: p. 304.

[35] Yuan, L.F., J.L. Yang, H.Q. Wang, C.G. Zeng, Q.X. Li, B. Wang, J.G. Hou, Q.S. Zhu, and D.M. Chen, *J. Am. Chem. Soc.*, 2003. **125**: p. 169.

[36] Schull, G., T. Frederiksen, A. Arnau, D. Sanchez-Portal, and R. Berndt, *Nature Nanotechnology*, 2011. **6**: p. 23.

[37] Schull, G., T. Frederiksen, M. Brandbyge, and R. Berndt, *Phys. Rev. Lett.*, 2009. **103**: p. 206803.

[38] Sutton, A.P., *Electronic Structure of Materials*. 2004, Oxford: Oxford University Press.

[39] Atkins, P.W., *Physical Chemistry*. 5th ed. 1994, Oxford: Oxford University Press.

[40] Atkins, P. and J.d. Paula, *Physical Chemistry*. 9th ed. 2010, New York: W.H. Freeman and Company.

[41] Tsurumi, T., *Nanoscale Physics for Materials Science*. 2010: Taylor&Francis Group.

[42] Tipler, P.A. and G. Mosca, *Physics for Scientists and Engineers*. 5th ed. 2004, New York: W.H. Freeman and Company.

[43] Attard, G. and C. Barnes, *Surfaces. Edition en anglais*. Oxford Chemistry Primers Series. Vol. 59. 1998, Oxford: Oxford University Press.

[44] Zangwill, A., *Physics at Surfaces*. 1988, Cambridge: Cambridge University Press.

[45] Binnig, G., Rohrer H., *IBM Journal of Research and Development*, 1986. **30**: p. 4.

[46] Stroscio, J.A. and W.J. Kaiser, *Scanning Tunneling Microscopy*. Methods of Experimental Physics. Vol. 27. 1993, London: Academic Press Limited.

[47] Wiesendanger, R., *Scanning Probe Microscopy and Spectroscopy*. Methods and Applications. 1998, Cambridge: Cambridge University Press.

[48] Liboff, R.L., *Introductory Quantum Mechanics*. 3rd ed. 1998, Reading, Massachusetts: Addison Wesley Longman.

[49] Lueth, H., *Quantum Physics in the Nanoworld*. 2009, Berlin: Springer Verlag.

[50] Beck, M., *Quantum Mechanics Theory and Experiment*. 2012, Oxford: Oxford University Press.

[51] Chen, C.J., *Introduction to Scanning Tunneling Microscopy*. 2nd ed. 2008, New York: Oxford University Press.

[52] Tersoff, J. and D.R. Hamann, *Phys. Rev. B*, 1985. **31**(2): p. 805.

[53] Bardeen, J., *Phys. Rev. Lett.*, 1961. **6**: p. 57.

[54] Yao, X., T.G. Ruskell, R.K. Workman, D. Sarid, and D. Chen, *Surf. Sci.*, 1996. **366**: p. L743.

[55] Binnig, G., C.F. Quate, and C. Gerber, *Phys. Rev. Lett.*, 1986. **56**(9): p. 930.

[56] Giessibl, F.J., *Reviews of Modern Physics*, 2003. **75**: p. 949.

[57] Morita, S., R. Wiesendanger, and E. Meyer, *Noncontact Atomic Force Microscopy*. Nanoscience and Technology. 2002, Berlin: Springer-Verlag.

[58] Gan, Y., *Surf. Sci. Rep.*, 2009. **64**(3): p. 99.

[59] Giessibl, F.J., *Phys. Rev. B*, 1997. **56**(24): p. 16010.

[60] Israelachvili, J.N., *Intermolecular and Surface Forces*. 3rd ed. 2011, Amsterdam: Elsevier.

[61] Girifalco, L.A., *J. Phys. Chem.*, 1992. **96**(2): p. 858.

[62] Martin, Y., C.C. Williams, and H.K. Wickramasinghe, *Journal of Applied Physics*, 1987. **61**(10): p. 4723.

[63] Albrecht, T.R., P. Grutter, D. Horne, and D. Rugar, *Journal of Applied Physics*, 1991. **69**(2): p. 668.

[64] Giessibl, F.J., S. Hembacher, M. Herz, C. Schiller, and J. Mannhart, *Nanotechnology*, 2004. **15**(2): p. S79.

[65] Kikukawa, A., S. Hosaka, Y. Honda, and R. Imura, *Japanese Journal of Applied Physics Part 2-Letters*, 1994. **33**(9A): p. L1286.

[66] Nony, L. and A. Baratoff, *Phys. Rev. B*, 2006. **74**(23): p. 235439.

[67] Eator, P. and P. West, *Atomic Force Microscopy*. 2010, Oxford: Oxford University Press.

[68] Sader, J.E. and S.P. Jarvis, *Appl. Phys. Lett.*, 2004. **84**(10): p. 1801.

[69] Majzik, Z., M. Setvin, A. Bettac, A. Feltz, V. Chab, and P. Jelinek, *Beilstein J. Nanotechnol.*, 2012. **3**: p. 249.

[70] Weymouth, A.J., T. Wutscher, J. Welker, T. Hofmann, and F.J. Giessibl, *Phys. Rev. Lett.*, 2011. **106**(22): p. 226801.

[71] Sweetman, A., S. Jarvis, R. Danza, J. Bamidele, S. Gangopadhyay, G.A. Shaw, L. Kantorovich, and P. Moriarty, *Phys. Rev. Lett.*, 2011. **106**: p. 136101.

[72] Sweetman, A., S. Jarvis, R. Danza, J. Bamidele, L. Kantorovich, and P. Moriarty, *Phys. Rev. B*, 2011. **84**: p. 085426.

[73] Chiutu, C., A. Stannard, A.M. Sweetman, and P. Moriarty, *Chem. Commun.*, 2011. **47**: p. 10575.

[74] Hands, I.D., J.L. Dunn, and C.A. Bates, *Phys. Rev. B*, 2010. **81**(20): p. 205440.

[75] Chen, C.J., *Phys. Rev. B*, 1999. **42**(14): p. 8841.

[76] Gross, E.K.U. and R.M. Dreizler, *Density Functional Theory*. NATO ASI. 1995, New York: Plenum Press.

[77] Hohenberg, P. and W. Kohn, *Phys. Rev.*, 1964. **136**(3B): p. B864.

[78] Garcia, R. and R. Perez, *Surface Science Reports*, 2002. **47**(6-8): p. 197.

[79] Solares, S.D., S. Dasgupta, P.A. Schultz, Y.-H. Kim, C.B. Musgrave, and W.A. Goddard, *Langmuir*, 2005. **21**: p. 12404.

[80] Brommer, K.D., M. Needels, B.E. Larson, and J.D. Joannopoulos, *Phys. Rev. Lett.*, 1992. **68**: p. 1355.

[81] Qian, G.-X. and D.J. Chadi, *Phys. Rev. B*, 1987. **35**: p. 1288.

[82] Zhang, H.M., J.B. Gustafsson, and L.S.O. Johansson, *Journal of Physics: Conference Series*, 2007. **61**: p. 1336.

[83] Wilson, R.J. and S. Chiang, *Phys. Rev. Lett.*, 1987. **59**: p. 2329.

[84] Kirchner, E.J.J., E.J. Baerends, G.t. Velde, and E. Vlieg, *Surf. Sci.*, 1995. **330**: p. 113.

[85] Wan, K.J., X.F. Lin, and J. Nogami, *Phys. Rev. B*, 1993. **47**(20): p. 13700.

[86] Watanabe, S., M. Aono, and M. Tsukada, *Phys. Rev. B*, 1991. **44**: p. 8330.

[87] Sato, N., T. Nagao, and S. Hasegawa, *Surf. Sci.*, 1999. **442**: p. 65.

[88] Chen, L., H.J. Xiang, B. Li, A. Zhao, X. Xiao, J. Yang, J.G. Hou, and Q. Zhu, *Phys. Rev. B*, 2004. **70**: p. 245431.

[89] Aizawa, H., M. Tsukada, N. Sato, and S. Hasegawa, *Surf. Sci.*, 1999. **429**: p. L509.

[90] Aizawa, H. and M. Tsukada, *Phys. Rev. B*, 1999. **59**: p. 10923.

[91] Hasegawa, S., X. Tong, C.-S. Jiang, Y. Nakajima, and T. Nagao, *Surf. Sci.*, 1997. **386**: p. 322.

[92] Loenen, E.J.v., J.E. Demuth, R.M. Tromp, and R.J. Hamers, *Phys. Rev. Lett.*, 1987. **58**: p. 373.

[93] Zhang, H.M., J.B. Gustafsson, and L.S.O. Johansson, *Phys. Rev. B*, 2006. **74**: p. 201304(R).

[94] Viernow, J., M. Henzler, F.K. Men, and F.M. Leibsle, *Phys. Rev. B*, 1998. **57**(4): p. 2321.

[95] Gasparov, V.A. and M. Riehl-Chudoba, *Surf. Sci.*, 2007. **601**: p. 5403.

[96] Binns, C., *Introduction to Nanoscience and Nanotechnology*. 2010, Hoboken: Wiley.

[97] Osawa, E., *Kagaku*, 1970. **25**: p. 654.

[98] Davidson, R.A., *Theor. Chim. Acta*, 1981. **58**: p. 193.

[99] Rohlfing, E.A., D.M. Cox, and A. Kaldor, *J. Chem. Phys.*, 1984. **81**: p. 3322.

[100] Taylor, R., *Lecture Notes on Fullerene Chemistry*. 1999, London: Imperial College Press.

[101] Chancey, C.C. and M.C.M. O'Brien, *The Jahn-Teller Effect in C_{60} and Other Icosahedral Complexes*. 1997, Princeton: Princeton University Press.

[102] Moriarty, P., *Rep. Prog. Phys.*, 2001. **64**: p. 297.

[103] LeLay, G., M. Gothelid, V.Y. Aristov, and A. Cricenti, *Surf. Sci.*, 1997. **377-379**: p. 1061.

[104] Sakurai, T. and Y. Watanabe, *Advances in Scanning Probe Microscopy*. 2000, Berlin: Springer-Verlag.

[105] Soler, J.M., E. Artacho, J.D. Gale, A. Garcia, J. Junquera, P. Ordejon, and D. Sanchez-Portal, *J. Phys.: Condens. Matter*, 2002. **14**: p. 2745.

[106] Masenelli, B., F. Tournus, P. Melinon, X. Blase, A. Perez, M. Pellarin, M. Broyer, A. Flank, and P. Lagarde, *Surf. Sci.*, 2003. **532**: p. 875.

[107] Gangopadhyay, S., R.A.J. Woolley, R. Danza, M.A. Phllips, K. Schulte, L. Wang, V.R. Dhanak, and P.J. Moriarty, *Surf. Sci.*, 2009. **603**: p. 2896.

[108] Rurali, R., R. Cuadrado, and J.I. Cerda, *Phys. Rev. B*, 2010. **81**(7): p. 075419.

[109] Neel, N., J. Kroeger, L. Limot, and R. Berndt, *Nano Lett.*, 2008. **8**(5): p. 1291.

[110] Lu, X.H., M. Grobis, K.H. Khoo, S.G. Louie, and M.F. Crommie, *Phys. Rev. Lett.*, 2003. **90**(9): p. 096802.

[111] Hands, I.D., J.L. Dunn, and C.A. Bates, *Phys. Rev. B*, 2010. **82**: p. 155425.

[112] Lu, X.H., M. Grobis, K.H. Khoo, S.G. Louie, and M.F. Crommie, *Phys. Rev. B*, 2004. **70**(11): p. 8.

[113] Wang, H., C. Zeng, Q. Li, B. Wang, J. Yang, J.G. Hou, and Q. Zhu, *Surf. Sci.*, 1999. **442**: p. L1024.

[114] Chen, T., S. Howells, M. Gallagher, L. Yi, D. Sarid, D.L. Lichtenberger, K.W. Nebesny, and C.D. Ray, *J. Vac. Sci. Technol. B*, 1992. **10**(1): p. 170.

[115] Keeling, D.L., M.J. Humphry, P. Moriarty, and P.H. Beton, *Chem. Phys. Lett.*, 2002. **366**(3-4): p. 300.

[116] Moriarty, P., Y.R. Ma, M.D. Upward, and P.H. Beton, *Surf. Sci.*, 1998. **407**: p. 27.

[117] Maruno, S., K. Inamaga, and T. Isu, *Microelectronic Eng.*, 1995. **27**: p. 39.

[118] Beton, P.H., A. Dunn, and P. Moriarty, *Appl. Phys. Lett.*, 1995. **67**: p. 1075.

[119] Cuberes, M.T., R.R. Schlittler, and J.K. Gimzewski, *Appl. Phys. A*, 1998. **66**: p. 669.

[120] Moriarty, P., Y.R. Ma, M.D. Upward, P.H. Beton, and D. Teehan, *Semicond. Sci. Technol.*, 1998. **13**(8A): p. A47.

[121] Dunn, A., P. Moriarty, M.D. Upward, A. Nogaret, and P.H. Beton, *Semicond. Sci. Technol.*, 1996. **11**: p. 1563.

[122] Keeling, D.L., M.J. Humphry, R.H.J. Fawcett, P.H. Beton, C. Hobbs, and L. Kantorovich, *Phys. Rev. Lett.*, 2005. **94**(14): p. 146104.

[123] Dunn, A.W., P.H. Beton, and P. Moriarty, *J. Vac. Sci. Technol. B*, 1996. **14**(3): p. 1596.

[124] Kobayashi, K., H. Yamada, T. Horiuchi, and K. Matsushige, *Appl. Surf. Sci.*, 1999. **140**(3-4): p. 281.

[125] Mativetsky, J.M., S.A. Burke, R. Hoffmann, Y. Sun, and P. Grutter, *Nanotechnology*, 2004. **15**(2): p. S40.

[126] Loske, F. and A. Kuehnle, *Appl. Phys. Lett.*, 2009. **95**(4): p. 04310.

[127] Loske, F., P. Rahe, and A. Kuhnle, *Nanotechnology*, 2009. **20**(26): p. 6.

[128] Pawlak, R., S. Kawai, S. Fremy, T. Glatzel, and E. Meyer, *ACS Nano*, 2011. **5**: p. 6349.

[129] Pawlak, R., S. Kawai, S. Fremy, T. Glatzel, and E. Meyer, *J. Phys.: Condens. Matter*, 2012. **24**: p. 084005.

[130] Gross, L., F. Mohn, N. Moll, B. Schuller, A. Criado, E. Guitian, D. Pena, A. Gourdon, and G. Meyer, *Science*, 2012. **337**: p. 1326.

[131] Gross, L., F. Mohn, N. Moll, P. Liljeroth, and G. Meyer, *Science*, 2009. **325**(5944): p. 1110.

[132] Sedlar, J., I. Andelic, I. Gutman, D. Vukicevik, and A. Graovac, *Chem. Phys. Lett.*, 2006. **427**: p. 418.

[133] Giessibl, F.J., S. Hembacher, H. Bielefeldt, and J. Mannhart, *Science*, 2000. **289**(5478): p. 422.

[134] Herz, M., F.J. Giessibl, and J. Mannhart, *Phys. Rev. B*, 2003. **68**(4): p. 045301.

[135] Caciuc, V., H. Holscher, S. Blugel, and H. Fuchs, *Phys. Rev. Lett.*, 2006. **96**(1): p. 016101.

[136] Gross, L., N. Moll, F. Mohn, A. Curioni, G. Meyer, F. Hanke, and M. Persson, *Phys. Rev. Lett.*, 2011. **107**: p. 086101.

[137] Ternes, M., C.P. Lutz, C.F. Hirjibehedin, F.J. Giessibl, and A.J. Heinrich, *Science*, 2008. **319**(5866): p. 1066.

[138] Bai, C., *Scanning Tunneling Microscopy and Its Applications*. 2nd Revised ed. 1995: Springer.

[139] Zhang, R. and D.G. Ivey, *J. Vac. Sci. Technol. B*, 1996. **14**(1): p. 1.

[140] Ekvall, J., E. Wahlstroem, D. Claesson, H. Olin, and E. Olsson, *Meas. Sci. Technol.*, 1999. **10**: p. 11.

[141] Yu, Z.Q., C.M. Wang, Y. Du, S. Thevuthason, and I. Lyubinetsky, *Ultramicroscopy*, 2008. **108**: p. 873.

[142] Song, J.P., N.H. Pryds, K. Glejbol, K.A. Morch, A.R. Tholen, and L.N. Christensen, *Rev. Sci. Instrum.*, 1993. **64**(4): p. 900.

[143] Ottaviano, L., L. Lozzi, and S. Santucci, *Rev. Sci. Instrum.*, 2003. **74**(7): p. 3368.

[144] Huang, D.H., F. Grey, and M. Aono, *Appl. Surf. Sci.*, 1998. **130-132**: p. 909.

[145] Watanabe, S., M. Aono, and M. Tsukada, *J. Vac. Sci. Technol. B*, 1994. **12**(3): p. 2167.

[146] Cai, C.Z., W.L. Wang, X.Y. Chen, and Q.Q. Shu, *Mater. Phys. Mech.*, 2001. **4**: p. 111.

[147] Huang, D.H., F. Grey, and M. Aono, *Microelectronic Eng.*, 1995. **27**: p. 17.

[148] Tsong, T.T., C.S. Chang, W.B. Su, H.N. Lin, T.C. Chang, and R.L. Lo, *Chinese Journal of Physics*, 1994. **32**(5-11): p. 667.

[149] Moriarty, P. and G. Hughes, *Appl. Phys. Lett.*, 1992. **60**(19): p. 2338.

[150] Nakayama, T., S. Watanabe, and M. Aono, *Surf. Sci.*, 1995. **344**: p. 143.

[151] Uhrberg, R.I.G., H.M. Zhang, T. Balasubramanian, E. Landemark, and H.W. Yeom, *Phys. Rev. B*, 2002. **65**: p. 081305.

[152] Schulte, K., L. Wang, P.J. Moriarty, J. Purton, S. Patel, H. Shinohara, M. Kanai, and T.J.S. Dennis, *Phys. Rev. B*, 2005. **71**: p. 115437.

[153] Upward, M.D., P.H. Beton, and P.J. Moriarty, *Surf. Sci.*, 1999. **441**: p. 21.

[154] Upward, M.D., P.J. Moriarty, P.H. Beton, P.R. Birkett, H.W. Kroto, D.R.M. Walton, and R. Taylor, *Surf. Sci.*, 1998. **405**: p. L526.

[155] Melinon, P., B. Masenelli, F. Tournus, and A. Perez, *Nature Materials*, 2007. **6**: p. 479.

[156] Moriarty, P., *Surf. Sci. Rep.*, 2010. **65**(7): p. 175.

[157] Pellarin, M., C. Ray, J. Lerme, J. Vialle, M. Broyer, and P. Melinon, *J. Chem. Phys.*, 2000. **112**: p. 8436.

[158] Masenelli, B., F. Tournus, P. Melinon, A. Perez, and X. Blase, *J. Chem. Phys.*, 2002. **117**: p. 10627.

[159] Marcos, P., J. Alonso, and M. Lopez, *J. Chem. Phys.*, 2005. **123**: p. 204323.

[160] Lee, J.Y. and M.H. Kang, *Surf. Sci.*, 2008. **602**(7): p. 1408.

[161] Larsson, J.A., S.D. Elliott, J.C. Greer, J. Repp, G. Meyer, and R. Allenspach, *Physical Review B*, 2008. **77**(11).

[162] Leigh, D.F., J.H.G. Owen, S.M. Lee, K. Porfyrakis, A. Ardavan, T.J.S. Dennis, D.G. Pettifor, and G.A.D. Briggs, *Chem. Phys. Lett.*, 2005. **414**(4-6): p. 307.

[163] Lantz, M., H. Hug, R. Hoffmann, P.v. Schendel, P. Kappenberger, S. Martin, A. Baratoff, and H. Guntherodt, *Science*, 2001. **291**: p. 2580.

[164] Sweetman, A., R. Danza, S. Gangopadhyay, and P. Moriarty, *J. Phys.: Condens. Matter*, 2012. **24**: p. 084009.

[165] Sweetman, A., S. Jarvis, R. Danza, and P. Moriarty, *Beilstein J. Nanotechnol.*, 2012. **3**: p. 25.

[166] Hobbs, C. and L. Kantorovich, *Surf. Sci.*, 2006. **600**: p. 551.

[167] Gross, L., F. Mohn, N. Moll, G. Meyer, R. Ebel, W.M. Abdel-Mageed, and M. Jaspars, *Nature Chemistry*, 2010. **2**: p. 821.

[168] Ondracek, M., P. Pou, R. Rozsival, C. Gonzalez, P. Jelinek, and R. Perez, *Phys. Rev. Lett.*, 2011. **106**: p. 176101.

[169] Tournus, F., J.-C. Charlier, and P. Melinon, *J. Chem. Phys.*, 2005. **122**: p. 094315.

[170] Pacheco, J. and J.P. Ramalho, *Phys. Rev. Lett.*, 1997. **79**: p. 3873.

[171] Sun, Z., M. Boneschanscher, I. Swart, D. Vanmaekelbergh, and P. Liljeroth, *Phys. Rev. Lett.*, 2011. **106**: p. 046104.

[172] Wakeham, D., R. Hayes, G.G. Warr, and R. Atkin, *J. Phys. Chem. B*, 2009. **113**: p. 5961.

[173] Hayes, R., S.Z.E. Abedin, and R. Atkin, *J. Phys. Chem. B*, 2009. **113**: p. 7049.

[174] Atkin, R., S.Z.E. Abedin, R. Hayes, L.H.S. Gasparotto, N. Borisenko, and F. Endres, *J. Phys. Chem. C*, 2009. **113**: p. 13266.

[175] Lin, L.G., Y. Wang, J.W. Yan, Y.Z. Yuan, J. Xiang, and B.W. Mao, *Electrochemistry Comm.*, 2003. **5**: p. 995.

[176] Su, Y.-Z., Y.-C. Fu, J.W. Yan, Z.B. Chen, and B.W. Mao, *Angew. Chem. Int. Ed.*, 2009. **48**: p. 5148.

[177] Waldmann, T., H.-H. Huang, H.E. Hoster, O. Hoefft, F. Endres, and R.J. Behm, *ChemPhysChem*, 2011. **12**: p. 2565.

[178] Koch, R., M. Borbonus, O. Haase, and K.H. Rieder, *Appl. Phys. A*, 1992. **55**: p. 417.

[179] Uehara, Y., T. Fujita, and S. Ushioda, *Phys. Rev. Lett.*, 1999. **83**(12): p. 2445.

[180] Rost, M.J., S.B. van Albada, and J.W.M. Frenken, *Surf. Sci.*, 2003. **547**(1-2): p. 71.

[181] Foulston, R., S. Gangopadhyay, C. Chiutu, P. Moriarty, and R.G. Jones, *Phys. Chem. Chem. Phys.*, 2012. **14**: p. 6054.

[182] Kittel, C., *Introduction to Solid State Physics*. 8th ed. 2005: John Wiley and Sons, Inc.

List of Figures

Figure 2-1. Four fundamental bonding configurations. A σ bond can be formed by two *s* orbitals **(a)**, one *s* orbital and one p_x orbital **(b)** or two p_x orbitals **(c)**. A π bond can be built by two p_z orbitals **(d)**.....11

Figure 2-2. Hybrid orbitals **(a)** *sp* with two *p* orbitals left over, **(b)** in-plane sp^2 with 120^o angle between orbitals and one *p* orbital left over, and **(c)** tetrahedral sp^3 with 109.5^o angle between orbitals. 12

Figure 2-3. Distribution of electrons and energy levels for a C atom in its ground state **(a)**, *sp* bonding **(b)**, sp^2 bonding **(c)**, and sp^3 bonding **(d)**. Electrons of *2s* orbital are shared with *2p* orbitals giving rise to the hybrids sp^i. (Figure reproduced from ***lsc.ucdavis****.edu/~holliste/Jim2A/****Hybridization****Carbon.pdf*) 13

Figure 2-4. Tetrahedral arrangement of atoms in a face-centred cubic unit cell of Si and diamond crystals. Dashed blue triangle marks the (111) plane. 14

Figure 2-5. Interaction with a substrate yields significant changes in the energy states of an adsorbate. **(I)** Energy levels in a free molecule. **(II)** Physisorption. **(III-V)** Chemisorption. **(IV)** Charge transfer. **(VI)** Dissociation of the molecule. (Figure reproduced from [43]) 15

Figure 2-6. A simple energy level diagram for a metallic surface and a tip, the tip having a negative bias voltage relative to the surface. With a positive tunnelling voltage (+eV) applied to the sample, electrons from the occupied states in the valence band of the tip travel through the barrier to the unoccupied states of the sample. Φ is the work function of the tip. 16

Figure 2-7. Schematic diagram describing wavefunction's behavior for an electron incident to a barrier $leikz$. Electron's wavefunction decays or varies inside the barrier $DeiKz, D'\ e - iKz$, according to the probability of penetrating the barrier, and has a reflected component $re - ikz$. Transmitted wave is the remaining component of the wavefunction and represents the motion of the electron on the other side of the barrier $teikz$. In this figure V_o is the height of the barrier, $d = z_2\text{-}z_1$ is the width of the barrier, *E* is the energy of the electron, *k* is the wavevector of the wavefunction outside the barrier, *K* is the wavevector of the wavefunction inside the barrier, *l,r,t,D*, and *D'* represent wave amplitude. (Figure after [48]) 17

Figure 2-8. Schematic diagram of the scanning tunnelling microscopy principle. 21

Figure 2-9. Comparison between constant-height mode **(a)** and constant-current mode **(b)** of STM. In constant-current mode the scanner is moved up and down, but the irregular surfaces can be measured with high precision, while the constant-height mode can provide useful information only for very smooth surfaces.....22

Figure 2-10. Scanning tunnelling spectroscopy data acquired on clean Si(100)-(2x1) and on C_{60} molecules deposited on this substrate. Theoretical energy levels calculated for a free C_{60} molecule are compared to the peaks resulted from experimental measurement. Once the molecule is adsorbed on the surface, due to

covalent bonding, its energy levels maintain their position with slight deviation, but they broaden significantly. (Figure from [54]) 25

Figure 2-11. Lennard-Jones potential describing a short-range interaction. 27

Figure 2-12. The total interaction force is composed of the long- and short-range forces. Long-range forces have a smooth monotonic decay. The forces deriving from the chemical bond occur only very close to the sample. In this case, the attractive force increases sharply. 28

Figure 2-13. Example of force versus tip-sample separation curve, measured with AFM. 29

Figure 2-14. Tuning fork vibrated at its resonant frequency with an amplitude, *2A*. *Z* is the minimum tip-sample separation. At distance z_o the fork is not deflected. 31

Figure 2-15. Representation of frequency profile as a function of amplitude. Due to interaction with the substrate a shift in the frequency Δf of the cantilever with respect to resonant frequency f_0 is recorded at constant amplitude *A*. (Figure by Dr Adam Sweetman) 32

Figure 2-16. FM-AFM set-up diagram. 36

Figure 2-17. Diagram of AFM circuit including the PLL block. 37

Figure 2-18. Amplitude versus frequency resonance curve. ω_o is the resonant frequency where the amplitude is maxim. $\Delta\omega$ is the width of the resonance peak. High *Q* factor – sharp narrow tall peak. Low *Q* factor – wide short peak. 39

Figure 2-19. Diagram showing a C_{60} molecule attached to the tip, scanning across a Si(111)-(7x7) surface. Molecules adsorb on the tip/surface with symmetry axis parallel or at an angle to the normal surface. Depending on the molecular orientation, atomic contrast for Si adatoms changes in dynamic STM and qPlus AFM. 46

Figure 2-20. Interaction of two C_{60} molecules. The molecule adsorbed on the tip plays role of a probe and images the molecule adsorbed on the surface. The molecule on the surface is adsorbed with a pentagon down. The five-fold symmetry axis C_5 forms an angle with surface normal. The on-tip C_{60} molecule faces downward with a hexagon tilted from normal axis of the tip. 47

Figure 2-21. Ball and stick model of interaction between a C_{60} molecule and a Si cluster (blue balls). This Si cluster approximates position of a Si adatoms in (7x7) unit cell. (Figure by Dr Sam Jarvis) 53

Figure 2-22. Si(111)-(7x7) DAS model: Top view and side view. 54

Figure 2-23. Si(111)-(7x7). **(a)** 200 nm image shows a step, always seen on a Si sample, good resolution of the unit cells and a domain boundary crossing the terrace. Image recorded at -2 V, 400 pA. **(b)** 40 nm empty states image – dark and bright spots represent missing atoms and adatoms/adsorbates, respectively, all considered defects of the reconstruction. Scanning parameters: 1 V, 20 pA. 55

Figure 2-24. Si(111)-(7x7). **(a)** Empty states image, 10 nm, 1 V, 100 pA; **(b)** Filled states at room temperature, -0.9 V, 1 nA; **(c)** Filled states at 77 K with high resolution of rest atoms, 0.5 V, 0.6 nA. 55

Figure 2-25. Model of honeycomb-chain-trimer. Two Ag triangles (blue balls) form the unit cell of the ($\sqrt{3}$x$\sqrt{3}$) reconstruction. Each Ag 'trimer' is imaged as a bright protrusion in STM. Si 'trimers' are formed by light green balls in the first layer. Dark green balls represent the second layer of Si atoms. 56

Figure 2-26. Ag-Si(111)-($\sqrt{3}$x$\sqrt{3}$)R30^o reconstruction. **(a)** HCT and **(b)** IET room temperature STM images. One Ag 'trimer' gives rise to a maximum. Si 'trimers' are located in the dark centre of each hexagon. Two Ag 'trimers' build a unit cell, the dashed, white rhombus with the vertices on Si 'trimers'. Image parameters: HCT: 10 nm, 0.4 V, 1 nA, IET: 4 nm, -0.2 V, 50 pA. 57

Figure 2-27. (a) Flat Ag terraces and islands on the Ag-Si(111)-($\sqrt{3}$x$\sqrt{3}$)R30^o substrate, 150 nm, -2 V, 10 pA. **(b)** Honeycomb network, 25 nm, -2 V, 100 pA. 58

Figure 2-28. Calculation of band structure for Ag-Si(111)-($\sqrt{3}$x$\sqrt{3}$)R30^o. Depending on the bias voltage employed in STM imaging, tunnelling can be tuned for different surface states S_1, S_2, S_3. Resonance states SR_1 (black arrow) and SR_2 (parallel blue lines) are labelled on the graph. (Figure from [88]).....59

Figure 2-29. Tip state-dependent images of a ($\sqrt{3}$x$\sqrt{3}$) reconstruction of Ag-terminated Si obtain with STM at room temperature. In image **(a)** at 0.2 V, data show parallel lines of individual bright spots. At the dashed line, also marked by white arrows, when the bias voltage is set at -0.2 V, scanning shows again the honeycomb network. Imaging parameters: 10 nm, 500 pA. In image **(b)** the Si 'trimers' were imaged as bright spots. Together with the protrusion of the Ag 'trimers', they form a hexagonal network. Imaging parameters: 7 nm, 0.1 V, 1.5 nA. 60

Figure 2-30. (a) *I(V)* and (b) *dI/dV* spectroscopic profiles of clean Ag-Si(111)-($\sqrt{3}$x$\sqrt{3}$)R30^o. The curves represent the average of three sets of measurements recorded using the same tip and sample. (a) The graph intersects the axes only at the (0,0) point. (b) The curves show a featureless metallic character of the surface. Blue dashed vertical line marks the Fermi level, while the blue arrow shows potential S_1 state. 62

Figure 2-31. Small and large fullerenes. 63

Figure 2-32. Rotation axes and symmetry of C_{60}. 64

Figure 2-33. Energy-level diagram in C_{60}. 65

Figure 2-34. (a1)-(a4) – molecule adsorbed on the faulted half of a (7x7) unit cell on top of three Si adatoms **(a)** imaged at different bias voltages. (a1) *Vs* = -1.8 V, (a2) *Vs* = 1.5 V, (a3) *Vs* = 1.8 V, (a4) *Vs* = 2.5 V; **(b1)-(b2)** – molecule sitting on the corner hole, between six Si adatoms **(b)**. (b1) *Vs* = -1.8 V, (b2) *Vs* = 2.3 V. Electronic features change significantly for different voltages. (Figure from [30]).....67

Figure 2-35. Intramolecular structure of C_{60} on Si(111)-(7x7). Experimental data (a-d) and analog DFT simulations (e-h). Imaging parameters: **(a)** 2 V, 0.2 nA. The molecule has three-fold symmetry and is adsorbed onto Si with a hexagon down; **(b)** -1.5 V, 0.2 nA. The molecule has its two-fold axis perpendicular to

the surface; **(c)** 2 V, 1 nA. The molecule has a pentagon on top, and on the bottom as well; **(d)** -2 V, 1 nA. The molecule has three-fold symmetry, but its axis is tilted by 40°. Corresponding DFT orientation: **(e)** three-fold, **(f)** two-fold, **(g)** five-fold, **(h)** three-fold symmetry axis of the molecule tilted 40°. (Figure from [31]) 68

Figure 2-36. STS spectra recorded on C_{60} molecules adsorbed at sites A, B and C on the Si(111)-(7x7) unit cell. The shift of the main orbitals peaks, HOMO and LUMO, and additional peaks measured in the gap denote a strong electronic contribution from the surface states to interaction with the molecule. Spectrum D is the average of the other spectra. For C_{60} adsorbed on the faulted half of Si(111)-(7x7) unit cell, on top of three Si adatoms, (site A) the gap is the largest (~1.4 eV). For site B, a molecule on the corner hole, the gap is slightly smaller (~1.3 eV). The smallest gap was measured for a molecule adsorbed on top of four adatoms, including the dimer line – site C, and was ~0.8 eV. These values are considerably smaller than the energy gap of free C_{60} (1.6-1.9 eV). (Figure from [113]).....69

Figure 2-37. Single C_{60} molecules imaged on Au(111) at 7 K. Scanning parameters: V = 2.0 V, I = 0.3 nA. The molecule is oriented with a hexagon **(a)**, double bond **(b)**, single bond **(c)**, apex atom **(d)**, and pentagon **(e)** prone to the surface. STS *dI/dV* spectra were acquired at nine different points on a single molecule adsorbed on Au(111). At each point, peaks' height varies depending on the electronic states. In conclusion, density of states is not distributed uniform but varies across the molecule. Tunnelling parameters: V = 2.0 V, I = 1.0 nA. (Figure from [112]).....70

Figure 2-38. C_{60} superstructure. The yellow rhombus is the unit cell formed by 49 molecules. The unit cell has a faulted and an unfaulted half. Arrows highlight the molecules with C_5 **(1)**, C_2 **(2)** and C_3 **(3)** symmetry. They indicate a five-fold symmetry (pentagon up appearing as one-fold (first case)), two-fold symmetry (double bond up (second case)), and three-fold symmetry of C_{60} (hexagon up). Defects seen in the molecular lattice were mainly dark molecules. They appear lower than the other molecules and always in the faulted half of the unit cell. The approximate orientation of each molecule in the mesh of C_{60} assembly is also indicated. (Figure from [32]).....71

Figure 2-39. (a) Model of ($\sqrt{3}$x$\sqrt{3}$) reconstruction. The rhombus unit cell encloses an Ag 'trimer' and a Si 'trimer'. **(b)** Position of C_{60} (circles) on Ag-Si(111)-($\sqrt{3}$x$\sqrt{3}$)R30°. Molecules sit on a Si 'trimer' (the hexagon) or on an Ag 'trimer' (the vertex). (Figure from [27]).....72

Figure 2-40. Ordered domains formed by ~0.8 monolayers of C_{60} on Ag-Si(111)-($\sqrt{3}$x$\sqrt{3}$)R30°. (Figure from [29]) 73

Figure 2-41. (a) Experimental image of C_{60} layers showing the defect distribution. **(b)-(c)** Diagram of the first layer indicating the spacing between molecules and the periodicity of defects, respectively. **(c)** is a schematic representation of the rectangle marked on (a). The two parallelograms on (c) show a local short range periodicity of the defective sites. (Figure from [28]).....74

Figure 2-42. Line scan showing attractive **(a)**, and repulsive **(b)** manipulation. The first arrow indicates the moment when the tip approaches the molecule and the second arrow the point where the molecule is moved. In the repulsive mode (b), the tip is placed near the target molecule, within 2 nm distance. The tip position is lowered by modifying the current set-point or the bias voltage. Next, the tip follows the molecule

profile till the point where the molecule is pushed away by the tip interaction. At this moment, an increase is recorded in the tip-sample separation profile. The feedback loop then drives the tip towards the sample surface. (Figure from [115]). 75

Figure 2-43. Manipulation of C_{60} on Si(100)-(2x1). **(a)-(c)** Parallel to the dimer rows, **(d)-(e)** Perpendicular to the dimer rows, **(f)** An array of C_{60} formed by positioning individual molecules. The white arrows show the direction of the tip trajectory. **(e)** Indicates a small deviation of the molecule from the perpendicular direction. This lateral displacement from the set trajectory shows the natural trend of the molecule to relax in the potential well along the dimer rows. **(f)** Possibility to form ordered pattern is illustrated, such as molecular arrays, based on the molecule translation along or across the rows of Si(100)-(2x1). Manipulation parameters were -1.0 V bias voltage and 1.0 nA tunnelling current. The imaging was acquired at -3.5 V and 0.1 nA. (Figure from [120]).....76

Figure 2-44. Manipulation of C_{60} molecules by "sweeping" method on Si(111)-(7x7). Labels help to track the molecules, showing how their positions changed from the initial scan (a). The pattern was built with five segments in the shape of letter '*S*'. Manipulation parameters: -0.4 V, 4 nA. (Figure from [118]) 77

Figure 2-45. Individual C_{60} molecules resolved with non-contact AFM on Au(111) **(a)** and Si(111)-(7x7) **(b-c)**. (Figure (a) from [125] and (b-c) from [124]).....78

Figure 2-46. (a) Sub-molecular contrast of C_{60} using qPlus AFM, in constant-height mode, at 5 K. Only intramolecular structure of C_{60} molecules in the second layer (2) could be resolved. **(b)** Force spectra acquired on several points on a single C_{60} molecule. (Figures taken from ref. [128]).....79

Figure 2-47. Bond discrimination in a hexagon ring of a C_{60} molecule using AFM. **(a)** Stick model of the C_{60} cage showing single and double bonds. Inset: STM image of the C_{60} molecule which confirmed its three-fold orientation on Cu(111). **(b)** AFM image of the same C_{60} molecule with two types of bonds in the hexagon, shorter bonds alternating with longer bonds. (Figures from [130]).....80

Figure 2-48. (a) AFM image of Si(111)-(7x7) surface. Each adatom exhibits sub-atomic 'double lobe' semispherical features. **(b)** Theoretical model representing the interaction between one sp^3 orbital of a Si adatom and two free, dangling bonds of the Si atom on the tip end. (Figure from [133]) 81

Figure 2-49. Dynamic STM scan of a Si(111)-(7x7) surface imaged with a samarium tip. Sub-atomic features reveal the structure of the samarium *f* orbital tilted at 37°. A schematic model shows the interaction between an *f* orbital and a p_z orbital. As explained by Bardeen [53], both tip and sample contribute to the tunnelling junction. Current recorded is a convolution of the electronic states of the two electrodes. Therefore, the sharp dangling bond of the Si adatoms maps the apex of the tip. (Figure from [134]) 81

Figure 2-50. STM images of on-tip C_{60} molecule resolved by Au/Cu adatoms. **(a)** Hexagon down orientation of on-tip C_{60}. **(b)** Single bond down orientation of C_{60} adsorbed on the tip. **(c-f)** Various orientations of on-tip molecules imaged after controlled rotation by applying a high set-point current. **(g)** Adatoms imaged with a metal tip. **(h)** The same adatoms imaged with a C_{60} tip, showing three-fold symmetry. (Figures from [36, 37]).....82

Figure 2-51. Close-packed island of C_{60} on Au(111). **(a-e)** Consecutive scans at room temperature with non-contact AFM. With every scan the molecular island changed its shape after losing a few molecules. **(f-j)** Schematic of the molecular island. (Figure from [125]) 83

Figure 2-52. Manipulation of the C_{60} inside a close-packed island on rutile TiO_2(110). The dotted circle marks a defect (a missing molecule) used as reference point. Image **(a)** was taken before the manipulation. Image **(b)** shows the result of the manipulation. **(a)** The bright molecular segments are domain boundaries. The three full white circles indicate three molecular rows separating the domain boundaries at the bottom of the image. **(b)** A square hole in the center of the image resulted from removal of twelve C_{60} molecules from the island and five molecules from the domain boundary. At the same time, domain boundaries at the right were shifted by one molecular row, so the separation between the boundaries at the bottom of the image is two molecular rows marked by white circles. (Figure from [126]) 84

Figure 2-53. Interaction between an AFM tip and an adsorbate on the surface. F is the total force. F_x is the lateral force in the x direction. F_z is the remaining vertical force after the background force F_B was removed. (Figure from [137]).....85

Figure 3-1. Omicron UHV VT AFM set-up (front view and side view). The system consisted of a transfer chamber and an STM/AFM chamber. To achieve UHV, the VT system was fitted with four pumps through the transfer chamber. 86

Figure 3-2. The head of the STM/AFM. The tip holder was mounted on the piezo tube scanner and the sample holder was inserted into the sample stage. 87

Figure 3-3. Schematic set-up for sample cooling on the VT Omicron STM/AFM. 88

Figure 3-4. Omicron LT STM/ qPlus AFM. 92

Figure 3-5. In-house LabView software used to measure resonant frequency, f_0, and quality factor, Q, of tuning fork (f_0 = 22275 Hz. Q = 9526).....94

Figure 4-1. Schematic diagram of adsorption sites within a (7x7) unit cell. (Figure reproduced from [108]) 97

Figure 4-2. C_{60} molecules adsorbed on Si(111)-(7x7). Dynamic STM images recorded with a qPlus sensor at 77 K. **(A)** Intramolecular features show different orientations. V = 2.3 V, I = 2 nA. **(B)** Molecules adsorbed at corner holes have a lower apparent height than the others (marked by white circles). V = 2.8 V, I = 400 pA, A = 6.2 nm. Weakly bound molecules appear fuzzy during scanning. 98

Figure 4-3. (A-E) Dynamic STM images of single C_{60} molecules. Hückel molecular orbital theory simulations showing orientations which produce images closest to those observed in experiment. molecular orientation **(A'-D')**. **(A)** A pentagon prone to the surface, 2.57 V, 200 pA, A = 8 nm. **(A')** LUMO. **(B)** A hexagon prone to the surface, 2.9 V, 300 pA. **(B')** LUMO+1 [74]. **(C)** A double bond prone to the surface, 2.9 V, 300 pA. **(C')** LUMO+1 [74]. **(D)** A single bond prone to the surface, 2.57 V, 200 pA, A = 8 nm. **(D')** LUMO.

(E) An apex atom prone to the surface. 2.8 V, 400 pA, *A* = 6.2 nm. **(E')** simulation, 2.5 V [30]. A tip doubling effect can be noticed in all images due to a C_{60} molecule on the tip.....101

Figure 4-4. Dynamic STM images of C_{60} molecules **(A-E)**. Various internal features compared to Hückel molecular orbital theory images **(A'-E')**. A hexagon prone to the surface: **(A)** 2.1 V, 300 pA **(A')** LUMO. **(B)** 2.3 V, 2 nA. **(B')** LUMO. **(C)** 2.3 V, 2 nA. **(C')** LUMO. A single bond prone to the surface: **(D)** 2.1 V, 300 pA. **(D')** LUMO. A double bond prone to the surface: **(E)** 1.6 V, 400 pA. **(E')** LUMO. A tip doubling effect can be noticed in all images due to a C_{60} molecule on the tip. 102

Figure 4-5. Dynamic STM images of C_{60} molecules **(A-E)**. Associated simulation images **(A'-E')**. A hexagon prone to the surface: **(A)** 2.1 V, 300 pA. **(A')** *dI/dV* map, 1 V [112]. **(B)** 2.1 V, 300 pA. **(B')** *dI/dV* map, 0.8 V [161]. A single/double bond prone to the surface: **(C)** 2.1 V, 300 pA. **(C')** DFT -0.4 V [160]. **(D)** 3 V, 300 pA. **(D')** DFT, -0.4 V [162]. Unidentified orientation: **(E)** 2.1 V, 300 pA. **(E')** DFT 1.5 V [162]. A tip doubling effect can be noticed in all images due to a C_{60} molecule on the tip. 103

Figure 4-6. A pentagon prone to the surface: **(A)** 2.3 V, 300 pA, **(A')** DFT 0.3 V [160]. A hexagon prone to the surface: **(B)** 2.1 V, 300 pA, **(B')** DFT, -0.4 V [162]. **(C-F)** Dynamic STM images of C_{60} molecules: unidentified orientations. Probably, these images are the result of imaging with a C_{60} probe.....104

Figure 4-7. qPlus AFM images of Si(111)-(7x7). (a) 6x6 nm^2, *df* = -7.5 Hz, *V* = 0 V, *A* = 1 nm. (b) 5x5 nm^2, *df* = -26 Hz, *V* = 0 V, *A* = 2 nm. Tip-sample separation was decreased in image (b) to achieve sharper resolution. Unfortunately, this often resulted in strong interactions or contact with the surface leading to a total loss of resolution. 105

Figure 4-8. Force curve measured above Si adatoms. Short-range chemical force curve indicated a maximum attractive force at ~2 nN. The inset shows a long-range frequency shift curve acquired above a corner hole on Si surface. Imaging parameters: *df* = -21.6 Hz, *V* = 0 V, *A* =1 nm.....106

Figure 4-9. AFM images of individual C_{60} molecules, recorded at 0 V bias voltage. **(a)** 15x15 nm^2, *A* = 6.4 nm, *df* = -10.5 Hz. **(b)** 8x8 nm^2, *A* = 1 nm, *df* = -59 Hz.....107

Figure 4-10. (A)-(B) Dynamic STM images 9x6 nm^2 , *V* = 2.3 V, *I* = 300 pA, *A* = 6 nm, *df* = -59 Hz. **(A)** *Z* image showing topography. **(B)** Frequency shift image. **(C)** AFM *Z* image recorded on the same area in constant-frequency shift mode, *V* = 0 V, *A* = 1 nm, *df* = -11 Hz. A great difference was evident between the *df* image in D-STM and the AFM *Z* image due to cross-talk. The *df* measured by PLL in dynamic STM was on the order of tens of Hz, much higher than in AFM, due to the bias voltage of more than 2 V. Therefore, the tunnelling current apparently dominated the force of interaction producing *df* images as seen in (B). 108

Figure 4-11. (a) AFM topography *Z* image, forward scan, constant-frequency shift mode, 6.6x4.8 nm^2, *V* = 0 V, *A* = 1 nm, *df* = -18 Hz. **(b)** *df* image, backward scan, pseudo-constant height/contact mode. Above the horizontal line the *df* set-point was increased to -18.75 Hz. Molecules appeared sharper and sub-molecular contrast was more intense.....109

Figure 4-12. When the tip was positioned above the molecule the interaction consisted of contribution of both short- and long-range forces. (Figure reproduced from [166]).....110

Figure 4-13. (A) Raw *df(z)* spectra measured above clean Si, *df* = -4.14 Hz. **(B)** Raw *df(z)* spectra measured above a C_{60} molecule, *df* = -4.14 Hz. **(C)** Spectrum obtained from the curve in (B) after subtraction of the *df* spectrum measured on Si. The short-range chemical force was calculated from (C).....111

Figure 4-14. (a) Experimental short-range force versus *z* spectra acquired with qPlus AFM above C_{60} molecules labelled in the inset, *df* = -3.65 Hz. **(b)** Binding energy was calculated in the lower graph for each of the molecules *A*, *B* and *C*. 112

Figure 4-15. (a) Frequency shift spectra showing the strong dependence of Si-C_{60} bonding on the structure of the apex of the tip, *df* = -15.4 Hz. Arrows indicate the approach and retraction *df(z)* curves. The hysteresis observed in spectra denotes rearrangement of the atoms on the tip. Spectra were recorded on the molecule presented in the dynamic STM image in the inset in (b). **(b)** Force calculated from the (iii) and (iv) *df(z)* curves shown in (a). Inset: height profile of the same C_{60} molecule.....113

Figure 4-16. Manipulation of a C_{60} molecule with AFM. Images showing a C_{60} molecule moved from Position 1 to Position 2. Imaging parameters: *A* = 7.2 nm, *V* = 0 V, 9x9 nm^2 image size. First image **A** was recorded at *df* = -6.1 Hz. Second, image **B** was recorded by decreasing the tip-surface separation by changing the set-point to -6.25 Hz. The C_{60} molecule located in Position 1 was removed by the tip. In the positions marked with rectangles the molecule appeared to interact repeatedly with the tip, four times. At the line indicated by the white arrow, the *df* set-point was reduced to -6.1 Hz and the molecule was released in Position 2. Scanning followed well. Image **C** was a check scan. In this image, the molecule disappeared from Position 1 and it was located in Position 2 just at the spot where the set-point was set back to its initial value. (Image A was recorded downward. Image B was recorded upward and stopped after the molecule dropped. Image C was recorded upward after restart.) 114

Figure 4-17. (A) Raw *df(z)* spectra acquired on C_{60} molecules and on clean Si surfaces. *V* = 0 V, *A* = 7.2 nm, *df* = -6.1 Hz. **(B)** Force versus *z* curve showing the short-range interaction between the tip and a C_{60} molecule calculated after subtraction of the *df* taken on Si from the *df* taken on C_{60}. These spectra were recorded before the manipulation presented in Figure 4-16. 115

Figure 4-18. An example of manipulation of a C_{60} molecule with AFM. The molecule was moved from Position 1 to Position 2. A rounded rectangle surrounds a black spot on a C_{60} molecule. Imaging parameters: *A* = 7 nm, *V* = 0 V, *df* = -4.14 Hz, 8x8 nm^2 image size. (Description of figures in text.) 116

Figure 4-19. (A) Raw *df(z)* spectra recorded above a C_{60} molecule and on the Si surface, respectively. *V* = 0 V, *A* = 7 nm, *df* = -4.14 Hz. **(B)** Short-range force between the tip and a C_{60} molecule calculated from spectra in (A). These measurements were acquired before the manipulation presented in Figure 4-18. 117

Figure 5-1. Example of picking up a C_{60} molecule during STM scanning. Images were acquired before **(A)** and after **(B)** the pick-up of C_{60} molecule marked by solid circle. The dashed circle highlights the same defect in both images. Note the strong change in atomic contrast in (B) after a single molecule was transferred to the tip apex. **(C)** Dynamic STM image of a different manipulation event. The dashed arrow indicates a C_{60} picked up during normal scanning. Instantaneously, atomic contrast changes to double lobe features. Horizontal, solid

arrows mark a shift in molecular orientation. At this point, the two lobe structure on adatoms changes the shape, size and orientation. The pick-up and rotation events are usually associated with discontinuities in the image...120

Figure 5-2. Example of vertical transfer of a C_{60} molecule to the tip using force spectroscopy. **(a)** Scan recorded before spectroscopy. **(b)** Scan acquired after spectroscopy. **(c)** spectra acquired above the circled molecule in (a). The transfer of the molecule to the tip is visible on the approach curve (black circles) as a sharp discontinuity. The molecule was removed from the surface.....121

Figure 5-3. Top row: Empty state image of Si(111)-(7x7) reconstruction. Adatoms show conventional round shape image. **Bottom row:** Collection of images demonstrating various features of atomic contrast. These images were recorded after a C_{60} molecule was transferred to the tip. All images in dynamic STM were recorded at positive bias voltage applied to the sample. 122

Figure 5-4. Dynamic STM images of Si(111)-(7x7) surface imaged with a C_{60} probe and associated with the Hückel molecular orbital theory simulations. White lines mark the (7x7) unit cell. **(A)** Single bond down A = 0.22 nm, V = 1 V, I = 100 pA. **(B)** C_2-Double bond down, A = 2.8 nm, V = 2.3 V, I = 1.8 nA, df = -32 Hz. **(C)** C_3-Hexagon down, A = 2.7 nm, V = 2.3 V, I = 0.4 nA, df = -70 Hz. **(D)** C_5-Pentagon down, A = 3 nm, V = 2.7 V, I = 1.33 nA, df = -29 Hz. White arrows in (C) mark a few lines when the molecule rotation yields a more symmetric pattern for the three lobes. In (B), white arrows mark a change in the tip-adsorbed molecule's orientation. The two lobes formed at the bottom at the image have different shape and orientation. 124

Figure 5-5. Hückel molecular orbital theory images of three-fold symmetry of a C_{60} molecule observed under different adsorption angle. The shape of molecular orbitals differs according to the adsorption angle of the molecule on the tip. From left to right: 0^0, 5^0, 10^0 and 15^0, respectively. 125

Figure 5-6. Experimental images of potential C_3 symmetry recorded in dynamic STM. Shapes and features of molecular orbitals differ dramatically for each image. The first scan **(A)** could be attributed to the case in which a hexagon is almost perpendicular to the surface. In image **(B)**, simulated Hückel molecular orbital theory images would suggest that the tip-adsorbed C_{60} has a tilt of less than 10^0 away from the surface normal, while image **(C)** most likely arises from a molecular tilt of greater than 10^0. 126

Figure 5-7. Unidentified adsorbates or defects on Si(111)-(7x7) exhibited three- **(A,C)** and six-fold **(B)** patterns. This may be evidence for a hexagon-prone on-tip C_{60}. Insets: Hückel molecular orbital theory, low current simulations for three-fold symmetry of a C_{60} oriented with a hexagon prone to the surface [74]. 126

Figure 5-8. AFM images of on-tip C_{60}. White rhombi mark the (7x7) unit cell. **(A)** Five maxima per Si adatom, A = 0.5 nm, V = 0 V, df = -22.3 Hz. **(B)** Two maxima per Si adatom, A = 0.5 nm, V = 0 V, df = -46 Hz. 127

Figure 5-9. Direct switch between AFM and dynamic STM modes allowing comparison between the structures observed for a pentagon prone of the on-tip molecule in both modes. Image **(A)** is the original scan in AFM – five maxima per Si adatom, df = -150 Hz. Image **(B)** is the dynamic STM scan of the same area. Image **(C)** is a high pass-filtered version of (B) to accentuate the presence of the node in the orbital. The molecular orientation is double-checked by switching back to AFM (image **(D)**). 129

Figure 5-10. (A) Short-range chemical force representing the interaction between the closest C atom to the surface and the brightest maximum on Si adatom (inset). The experimental curve (empty circles), *df* = -18.5 Hz, as well as the curves calculated using DFT for a Si adatom directly below a C atom (red line) and a C-C single bond (blue line) exhibit a "jump-to-contact" effect indicated by the blue and the black arrows. The red arrow indicates the point at *z* = ~3.8Å where the Si-C bond was formed. **(B)** Charge density. **(C)** Ball-and-stick model show theoretical models of C-Si bond formation. Locally the C_{60} cage was deformed. 131

Figure 5-11. C_{60}-C_{60} pair potential energy. The probe is a C_{60} molecule facing with a pentagon down the surface (lower inset). Three *df(z)* spectra were measured at different points on the molecule in the upper inset, *df* = -18.5 Hz. The intermolecular potential energy variation was calculated from these curves and show good agreement (near the equilibrium separations) with the analytical Girifalco potential for the C_{60}-C_{60} interaction (solid green line).....133

Figure 5-12. Interaction between a molecule with a double bond prone to the surface and a molecule probe facing down with a single bond slightly tilted (ball-and-stick model in **(f)**). **(a)** and **(b)** comparison of theoretical and experimental features observed on Si(111)-(7x7) surface that arise from the probe molecule; **(c)** Dynamic STM image of the molecule marked with black circle in (b). **(d)** The best theoretical match resulted from Hückel molecular orbital theory calculations. **(e)** Calculated molecular orbitals of the C_{60} adsorbed on the surface as if imaged with an *s* type orbital. Imaging parameters: *V* = 2.3 V, *I* = 300 pA, *A* = 1.5 nm.....134

Figure 5-13. (a,g) A C_{60} probe oriented with a double bond down, with the C_2 axis slightly shifted from surface normal, showed nonequivalent double-lobe structure in dynamic STM, as revealed on Si adatoms. **(b)** Hückel molecular orbital theory image of a (7x7) reconstruction calculated for this orientation. **(c-f)** Images of the C_{60} molecule highlighted in black circle in (g), with a double bond prone to the surface. **(h-k)** Images of the C_{60} molecule marked by the white square in (g) with a single bond prone to the surface. **(d, h)** Dynamic STM images. **(c, i)** Simulated images. **(f, j)** Calculated molecular orbitals of the C_{60} adsorbed on the surface as if imaged with an *s* type orbital. **(e, k)** Theoretical models. Imaging parameters: *V* = 2.4 V, *I* = 500 pA, *A* = 1.5 nm. 135

Figure 6-1. Manipulation of a single C_{60} molecule on Ag-Si(111)-($\sqrt{3}$x$\sqrt{3}$)R30°. **(a)** Image recorded before manipulation. **(b)** Image recorded after manipulation. **(c)** Height profile showing tip movement during manipulation. **(d)** Tunnelling current profile measured during manipulation. Dashed, white circles mark reference molecules. Orange, solid circle marks a molecule found on the surface after manipulation. However, other molecules on the terrace did not move. Dashed, orange line marks tip trajectory. The STM tip was positioned close to the molecule found in Position 1. When the tip-sample distance was decreased, due to the strong tip-molecule interaction, the C_{60} molecule from Position 1 followed the tip in the direction indicated by arrow across Ag-Si(111)-($\sqrt{3}$x$\sqrt{3}$)R30° terrace to Position 2. Imaging parameters: 50x50 nm^2, *V* = 2 V, *I* = 400 pA. Manipulation parameters: *V* = 0.4 V, *I* = 1.1 nA.....140

Figure 6-2. Second case of a single C_{60} molecule manipulation on Ag-Si(111)-($\sqrt{3}$x$\sqrt{3}$)R30°. **(a)** Image recorded before manipulation. **(b)** Image recorded after manipulation. **(c)** Height profile showing tip movement during manipulation. **(d)** Tunnelling current profile measured during manipulation. Dashed, white circles mark reference molecules. Dashed, orange line marks tip trajectory. The manipulation procedure followed

as presented in Figure 6-1. The molecule was driven from Position 1 to Position 2. At Position 2 the tip retracted. The molecule was then found in Position 3 (image (b)). Several reasons may explain why the molecule could not be found in Position 2 in image (b). The defect edge close to Position 2 might have caused the molecule to reach to Position 3 or the molecule could have been picked up by the tip at some point on the manipulation trajectory and dropped in Position 3 during the check scan. Also another molecule from the tip, different from the molecule picked in Position 1, could have been dropped by the tip in Position 3. Imaging parameters: 45x45 nm^2, V = -2 V, I = 600 pA. Manipulation parameters: V = 0.3 V, I = 1.0 nA. 141

Figure 6-3. A third case of controlled manipulation of a C_{60} molecule on Ag-Si(111)-($\sqrt{3}$x$\sqrt{3}$)R30^o. **(a)** Image recorded before manipulation. **(b)** Image recorded after manipulation. **(c)** Height profile showing the tip movement during manipulation. **(d)** Tunnelling current profile measured during manipulation. Dashed, white circles mark reference molecules. Dashed, orange line marks tip trajectory. The molecule was moved from Position 1 to Position 2. Transversal lines at the bottom of image (b) represent instabilities at the tip apex resulted after manipulation. Imaging parameters: 45x45 nm^2, V = -2 V, I = 600 pA. Manipulation parameters: V = 0.3 V, I = 1.0 nA. 142

Figure 6-4. C_{60} manipulation at 100 K. Images were recorded before and after manipulation. The island edge was modified by removing molecules and dragging them across the surface. Dashed circles mark two molecules which may be used as reference points. Before manipulation, on the left side of the terrace a small number of molecules can be identified: two single molecules and a cluster of three molecules. After manipulation the number of the molecules on the upper terrace increased by six molecules. The edge of the island was visibly changed. Imaging parameters: 50x50 nm^2, V = 2.8 V, I = 100 pA. Manipulation parameters: V = 1.5-2 V, I = 0.8-1.5 nA. 143

Figure 6-5. Successive manipulation events at 100 K. (A-D) before manipulation. (A'-D') after manipulation. Individual C_{60} molecules were removed from the island edge and translated in the direction indicated by arrows. **(A-A')** Two molecules were removed from the island edge following the tip in two successive manipulation attempts. Imaging parameters: 50x50 nm^2, V = -2.9 V, I = 100 pA. Manipulation parameters: V = -1.5 V, I = 1 nA. **(B-B')** Single molecule manipulated in the arrow's direction. Imaging parameters: 50x50 nm^2, V = -2.9 V, I = 100 pA. Manipulation parameters: -1.5 V, 0.8 nA. In **(C')** and **(D')** more molecules became mobile after lateral manipulation applied on a single molecule. Multiple white circles highlight these molecules or spots where molecules were missing. Therefore, more molecules than manipulation attempts were moved and total number of molecules removed from the island edge cannot be fully appreciated. 144

Figure 6-6. Height profiles recorded during the manipulation experiment in Figure 6-5. The **(A)** and **(B)** profiles correspond to Figure 6-5A-A'. Profile **(C)** corresponds to Figure 6-5B-B'. Black arrows indicate a sudden, long drop in the profile. At this point, the tip moved closer to the surface because the C_{60} molecule was pushed laterally away in front of the tip (repulsive manipulation) 145

Figure A-7-1. Au(110)-(2x1) surface. **(a)** Atomic resolution. Imaging parameters: 10 nm, -0.6 V, 300 pA and theoretical model of (2x1) missing row reconstruction. **(b)** Au(110)-(2x1) rows and high density of steps. Imaging parameters: cut from 100 nm, -0.2 V, 800 pA. 154

Figure A-7-2. Schematic of **(A)** ionic liquid [C_2C_1Im][Tf_2N] and **(B-D)** possible reconstructions of Au(110) surface. (Figure from [181]) 155

Figure A-7-3. Low temperature STM images showing different coverage of ionic liquid [C_2C_1Im][Tf_2N] on Au(110)-(2x1). **(A)** 2D islands of ionic liquid. **(B)** One monolayer coverage of ionic liquid. Image **C** was a zoom of area marked on image B. The inset in image B was a Fourier transform of the image B indicating one-dimensional ordering of the rows. Image **D** was obtained after deposition of more than one monolayer. Typical scanning parameters: V = 1.7-2 V, I = 100-200 pA. 156

Figure A-7-4. Low temperature STM images of ionic liquid on Au(110) after annealing at various temperatures: **(A)** ~373 K, **(B)** ~523 K for 1 min, **(C)** ~553 K for 1 min, **(D)** ~553 K for 5 min. White rectangles show well-resolved "objects". 158